A computational and semi-analytical study of laminar, standing hydraulic jumps

A Thesis

Submitted for the Degree of

DOCTOR OF PHILOSOPHY

in the Faculty of Engineering

by

RATUL DASGUPTA

ENGINEERING MECHANICS UNIT
JAWAHARLAL NEHRU CENTRE FOR ADVANCED SCIENTIFIC RESEARCH
(A Deemed University)
Bangalore – 560 064

JUNE 2011

DECLARATION

I hereby declare that the matter embodied in the thesis entitled "**A computational and semi-analytical study of laminar standing hydraulic jumps**" is the result of investigations carried out by me at the Engineering Mechanics Unit, Jawaharlal Nehru Centre for Advanced Scientific Research, Bangalore, India under the supervision of Prof. Rama Govindarajan and that it has not been submitted elsewhere for the award of any degree or diploma.

In keeping with the general practice in reporting scientific observations, due acknowledgment has been made whenever the work described is based on the findings of other investigators.

Ratul Dasgupta

CERTIFICATE

I hereby certify that the matter embodied in this thesis entitled "**A computational and semi-analytical study of laminar standing hydraulic jumps**" has been carried out by Mr. Ratul Dasgupta at the Engineering Mechanics Unit, Jawaharlal Nehru Centre for Advanced Scientific Research, Bangalore, India under my supervision and that it has not been submitted elsewhere for the award of any degree or diploma.

Prof. Rama Govindarajan
(Research Supervisor)

Acknowledgements

Phew! cannot believe that I am submitting my PhD thesis. It just seems the other day, that I was standing in front of a puzzled interview committee trying to explain why was I interested in leaving Infy for research. Five years at Byatarayanapura is over and its time to say thank you. I will remain grateful to,

Dada, the person without whose support and encouragement, I would have probably never come back to academics. He's my lighthouse in the open ocean.

Prof. J. Dey, IISc, Aerospace Dept., for introducing me to research and for giving me an opportunity on many weekends to come to IISc to his laboratory. Dull and boring Infosys weekends would suddenly become enjoyable, everytime I went to his lab or to IISc.

Prof. Rama Govindarajan, advisor and a close friend, for suggesting this wonderful problem, for her numerous contributions to this thesis, for many scientific ideas related to the problem, discussions and debates on the problem, support, effort, for her patience with my slow progress and for the freedom. I will always remember the freedom that I got durng my PhD because of which I could read and learn many things. On the personal side, she has been hugely generous, supportive and kind in times of mental distress and also a mentor. I would also like to thank her for helping us build an EMU library almost from scratch.

Dr. Gaurav Tomar, IISc, Mech. Engg, for all the help in GERRIS. VOF is a nightmare, the simulations were difficult and it would have been impossible without his help. He was Godsend.

Prof. Roddam Narasimha, JNCASR for giving me some of his time for discussions. I truly enjoyed them.

Prof. K. R. Sreenivas, JNCASR for help and discussions related to the experiments.

Miss V. K. Ponnulakshmi, for being a natural and constant supply of entertainment, happiness and even more happiness for her GODs and other lesser mortals. May her tribe increase manyfold.

Harish and **Anubhab** for all the fun we had (sometimes at the cost of Harish) and for all the eating sessions, terrace-top parties etc. Anubhab once again, for discovering Ponnulakshmi.

Dheeraj, **Sumesh**, **Saikishan** and **Croor Singh** for help with my thesis.

Vishwanath, for his experiments, universal critical-value theory and the rava-idlis at Shanthi-Sagar.

To labmates **Srikanth**, **Vivekanand**, **Gayathri**, **Rakshith** and once again **Dr. Vishwanath K. P. Shady Shastry** (Jumping Postdoc, Phd, MSc, BSc, XII, X...VI....I...KgII....Nursery etc.). We had a lot of fun with and mostly at the cost of Dr. Shastry.

Communist **Rahul**, **Krithika**, **Aditya**, **Rajaram**, **Vivek Prakash**, **Ashish**, **Vijay**, **Priyanka**, **Pinaki**, **Kaushik**, **Rajapandiyan**, **Dinesh**, **Alakesh** at IISc and many others whose names, I may have forgotten.

Ravi, my piano teacher for his lessons, for teaching me Fur Elise, and many other things about music. For giving me opportunities that I never imagined I would get, even in my wildest dreams.

Ma, **Bapi** and **Didi** for everything. **Sonai**, for a new begining.

Manikandan, and many other people who kindly sent me papers I did not have access to.

The Supreme Being who lies above the narrow confines of any man-made religion.

Abstract

A layer of fluid with a free-surface which is initially supercritical (local Froude $Fr > 1$), displays a near discontinuity in film-thickness at a location where the Froude number becomes unity. This is better known as the hydraulic jump and has attracted the attention of civil engineers for a very long time (Bidone [1819]). The circular analogue of this was first noticed by Rayleigh [1914]. The phenomenon is robust and occurs in laminar and turbulent flows. It also manifests itself in the form of tidal bores in rivers where the height discontinuity front travels with a certain speed, and is thus referred to as a travelling jump.

The objective of this thesis is to study the laminar standing hydraulic jump in planar and circular geometries. The thesis is divided into seven chapters. The work and the results pertianing to each of the chapters are as follows:

- In Chapter 1, we present a one hundred year literature survey of circular jumps with some discussion on planar jumps as well. A series of questions are posed and we record our comments on every reference that is discussed. These comments summarise the significance of the work and limtations, if any.

- We study weak hydraulic jumps in Chapter 2. We review the shallow-water assumption and the vertical averaging approach that is traditionally used to study hydraulic jumps and provide a criticism of latter. We then propose instead an exact approach, involving a transformation of the boundary-layer shallow-water equations (BLSWE). The equations are derived in this coordinate system for planar and circular geometries. The solution procedure is novel and it involves solving the governing partial differential equation as a parametric ordinary differential equation. This provides jump-like transitions in the neighbourhood where the Froude number is unity. In the limit of high and low Froude number, the equation admits similarity solutions

of different kinds. An analysis of this equation reveals the inadequacy of shallow-water theory in the jump neighbourhood. We obtain multiple solutions downstream of the jump, one with a separated profile and another with an attached profile. The separated profile becomes increasingly unrealistic downstream. Instability of the separated profile is conjectured to be the reason for the reattachment, and for the transition to the later solution. Preliminary stability studies conducted by [Ramadurgam, 2010] are in agreement with this conjecture. The results are compared with experiments and vertically averaged models. Our results show an improvement over the vertically averaged models in the near-jump region and downstream. In the near jump region, dispersive effects may not be neglected.

- In Chapter 3, we study jumps in planar geometries computationally and analytically. It is found that even for a weak jump, the BLSWE is inadequate in the near-jump region. The full Navier-Stokes equations are integrated and an equivalent depth-averaged equation is derived. Using this equation and we find that for a strong jump in the near-jump region, at the two lowest orders in an appropriate expansion, no terms from the shallow-water equation enters the governing equation. In this region, the dominant terms come from viscous and disspative terms from the vertical momentum equation. In the region upstream of the jump, the BLSWE si found to be a good approximation. For the region downstream of the jump, if a flat region occurs, the BLSWE is found to describe this well. A train of downstream waves are found to appear at high Reynolds numbers and a model equation is proposed for the same. Downstream boundary condtions are found to have a weak influence on the jump location if the domain is sufficiently long. Increasing viscosity or gravity pushes the jump upstream while making it steeper. Rayleigh's shock criterion works well for weak jumps but underpredicts the jump height for strong jumps.

- In Chapter 4, we present computational results on circular jumps. It is shown that circular jumps without separation are possible. contradicting Tanis hypothesis about the mechanism of jump formation Tani [1949]. We present qualitative results on the circular jump. Surface-tension is found to have a strong influence on the jump structure but a negligible influence on its radial

location. The downstream boundary condition can significantly affect separation underneath the jump but its location is found to have a mild influence on the jump radius. Time-evolution of jump formation reveals that in the absence of viscosity, wave-breaking continues unabated. A paradox related to Rayleigh's shock criterion in a circular geometry is discussed.

- In Chapter 5, we study the effect of momentum-flux on the circular hydraulic jump. The existing scaling relation proposed by [Bohr *et al.*, 1993] does not contain any dependence of momentum flux on the radius of the jump. Using physical reasoning we motivate why momentum flux can affect the jump radius. The experiments reported here are conducted in collaboration with Dr. Vishwanath Shastry and Prof. K. R. Sreenivas. The experimental results show that momentum flux can significantly influence the jump radius. Using a combination of data obtained from Navier-Stokes simulations and experiments, we attempt to obtain an empirical relation for the jump radius in terms of the impingement Froude and Reynolds number. This relation shows a definite dependence of the jump radius on the momentum flux.

- In Chapter 6, we study surface-tension driven jumps at small-scales in the absence of gravity. Vertically averaged shallow-water equations including surface-tension are derived and for certain initial conditions, a divergence in height is predicted. This singularity is analogous to the one obtained from depth-averaged models of gravity-driven jumps. The motivation for this work arises from experimental finding of cup-shaped structures formed out of solidification of impinging molten-metal droplets on a substrate. The analytical results are consistent with the observations. We also present some analytical results for droplet spreading which are a generalisation of the models available in literature.

- Chapter 7 - A code has been developed to implement the Volume-Of-Fluid (VOF) method used for simulating free-surface flows. A detailed description is provided for the implementation of the interface reconstruction algorithm LVIRA Puckett *et al.* [1997]. We also describe the implementation of the advection algorithm. Standard benchmark tests for validating the code are presented. This chapter is written to assist anyone who is interested in a numerical implementation of these techniques.

List of Publications

- "Gravity-free hydraulic jumps and metal femtoliter cups", M. Mathur, R. Dasgupta *et. al.*, Phys. Rev. Lett., 2007, 98, 164502.
- "Non-similar solutions of the viscous shallow-water equations governing weak hydraulic jumps", R. Dasgupta and R. Govindarajan, Phys. Fluids (In Press), 2010.
- "Study of a lid-driven cavity in an axisymmetric geometry", R. Dasgupta and R. Govindarajan, Proc. IUTAM Sympoisum - Unsteady Separated Flows and their Control, 2007, Corfu, Greece.

Contents

Abstract **vii**

1 Introduction and Literature Review **1**

1.1 Introduction 1

1.1.1 The shape of a wave 3

1.1.2 Relating the travelling and the standing jump 7

1.1.3 Approach 2 - Wave trapping 10

1.2 Literature review of circular hydraulic jumps 12

1.3 List of references which could not be accessed 82

1.4 Discussion 84

2 Weak hydraulic jumps: A semianalytical study **91**

2.1 Shallow-water assumption 91

2.2 Inviscid shallow-water equations 93

2.2.1 Planar 93

2.2.2 Circular 94

2.3 Viscous shallow-water equations 95

2.3.1 Planar 96

2.3.2 Circular 97

2.3.3 Derivation of the BLSWE from the Navier-Stokes equations 97

2.3.4 Vertical averaging of the BLSWE 100

2.3.5 Viscous to inviscid transition of the vertically averaged solution 105

2.4 Transformation of the BLSWE 109

2.4.1 In a planar geometry 109

2.4.2 Analysis and numerical results - Planar Geometry 111

2.4.3 In a circular geometry 121

2.4.4 Analysis and numerical results - Circular geometry 122
2.5 Comparison with results from self-similar profiles, Pohlhausen profiles and Experiments 123
2.6 Conclusion 127

3 Computational and analytical results on the PHJ 129
3.1 Introduction 129
3.2 The geometrical model and the simulations 131
3.2.1 Numerical Method 131
3.2.2 Computational Domain and Boundary Conditions 133
3.3 Results from simulations 134
3.3.1 Comparisons of the simulations with shallow water theory . 138
3.3.2 The change in height and the Rayleigh shock criterion . . . 146
3.4 The depth-averaged Navier-Stokes equation 151
3.4.1 The near-jump region J 154
3.4.2 A model for the undular region U 156
3.5 Conclusion 158
3.6 Depth averaged Navier-Stokes equation 159

4 Computational results on the CHJ 163
4.1 Introduction 163
4.2 Numerical Modelling 166
4.3 Computational Results 170
4.3.1 Effect of gravity, viscosity and surface-tension 174
4.4 Comparisons 175
4.4.1 Comparison between planar and circular geometries 175
4.4.2 Comparison with BLSWE 181
4.4.3 Effect of downstream boundary conditions 184
4.5 Undular jumps - Radial KdV like equation 185
4.6 Some other qualitative studies 189
4.6.1 Initial-value problem of circular jump formation 189
4.6.2 Inviscid wave-breaking 191
4.7 Conclusion 191

5 Effect of momentum flux on the CHJ **193**
5.1 Scaling laws for the radius of the CHJ . . . 193
5.2 Momentum-flux . . . 195
5.2.1 Dimensional analysis . . . 196
5.2.2 Experiments . . . 198
5.3 Simulations . . . 201
5.4 Results and Discussion . . . 201
5.4.1 Determining the exponents . . . 202
5.5 Comparisons with previous experiments . . . 204
5.6 Conclusion . . . 206

6 Surface tension driven jumps **213**
6.1 Introduction . . . 213
6.1.1 Analysis for a jet . . . 213
6.1.2 Analysis for a drop . . . 222
6.2 Conclusion . . . 228

7 The Volume-Of-Fluid Method **229**
7.1 The Volume-Of-Fluid(VOF) method . . . 229
7.2 The Basic Steps in VOF . . . 229
7.3 LVIRA - An interface reconstruction algorithm [Pilliod & Puckett, 2004] . . . 231
7.3.1 Step A - Intial guess of slope . . . 233
7.3.2 Step B - Fit a Straight line . . . 234
7.3.3 Step C - Calculate the perpendicular distance . . . 235
7.3.4 Step D - Extrapolate line and calculate sum of squares . . . 235
7.3.5 Step D - Rotate line . . . 236
7.4 Advection . . . 236
7.5 Benchmark tests . . . 237
7.5.1 Translation test . . . 238
7.5.2 Solid body rotation test . . . 238
7.5.3 Shear test . . . 240
7.6 Coupling the interface with Navier-Stokes . . . 242
7.7 Conclusion . . . 244

References **245**

CHAPTER 1

INTRODUCTION AND LITERATURE REVIEW

1.1 Introduction

Hydraulic jumps have a very old history. They were perhaps first described by Leonardo Da Vinci in the 16th century [Hager, 1992]. They have now persisted in hydraulics literature for almost two centuries (see e.g. [Bidone, 1819]) and are known to occur in myriad forms and geometries. In nature one can see jumps which can be standing or travelling (bores), laminar or turbulent, radial or planar, weak or strong, undular or smooth, circular or polygonal, with or without surface rollers etc. A collage of pictures in figure 1.1 created from numerous online resources serves as a pictorial illustration of the ubiquity and complexity of this phenomenon. In what follows, the acronyms PHJ and CHJ refer to planar hydraulic jump and circular hydraulic jump respectively.

Hydraulic jumps are frequently described as shocks [Stoker, 1992] and like shocks they are strongly connected to nonlinear waves. The mathematical analogy between a hydraulic jump and a shock arises from the possibility to transform the inviscid equations of compressible flow to those of the shallow-water theory. In the one-dimensional unsteady case, this transformation seems to be have been first found by Riabouchinsky [1932] and in the two-dimensional steady case by Preiswerke [1938, 1940]. Just as shocks in compressible flow can be either stationary or travelling (with respect to, say, the lab frame of reference), both stationary and travelling jumps can be easily seen under natural conditions. The traditional textbook approach [Stoker, 1992] treats the travelling and the standing jump as arising out of the same basic physical mechanism viz. nonlinear steepening of finite-amplitude waves. This mechanism and how it leads to a travelling jump, is reasonably well-understood in quantitative terms. In contrast the effect of nonlinear steepening on the formation of a standing jump is at best only qualitatively understood and we return to this point later.

In order to appreciate these physical mechanisms better, it is useful to review

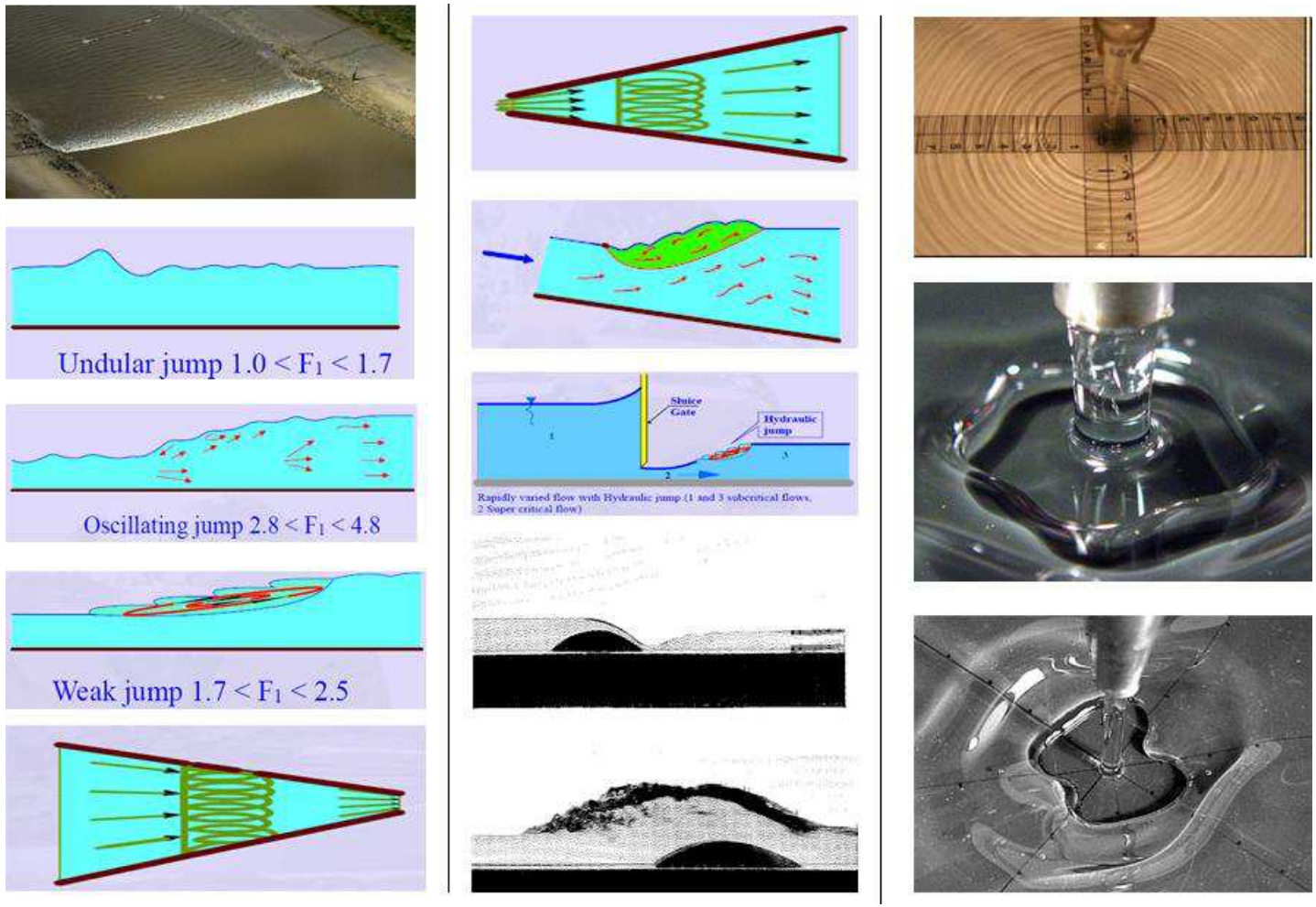

Figure 1.1: A collage of pictures of hydraulic jumps obtained from various online resources available freely on the internet. Starting from the first image at the top left corner and reading from top to bottom, the first image is obtained from Wikipedia [2010] and shows a tidal bore. The next seven images are obtained from Thandaveswara [2010] and these are illustrations of standing jumps in planar geometries. The next two images are of jumps over obstacles obtained from experiments reported in Shapiro [2008]. The next image is that of a circular jump obtained from the experiments of Vishwanath [2010]. The last two images are those of polygon and butterfly-shaped jumps obtained from Aristoff [2010].

two basic concepts related to wave propagation viz. nonlinearity and dispersion. We will discuss these two effects in context of how they influence the "shape" of a wave. An understanding of these two concepts in turn leads us to a physical picture of how and why travelling jumps arise. This in turn can provide a qualitative understanding of the physical mechanism of formation of a standing hydraulic jump. We start with a discussion of nonlinear and dispersive effects on a surface gravity wave. For simplicity, we ignore surface-tension effects through most of this thesis. We will however study its effect on gravity-driven jumps in Chapter 4. A study of jumps driven by surface-tension alone will also be reported in Chapter 6 of this thesis.

1.1.1 The shape of a wave

Linear nondispersive waves

We start with the one-dimensional unsteady, inviscid, shallow-water equations. The horizontal (x) component of velocity is u and the depth of the film is h.

$$\begin{aligned} h_t + hu_x + uh_x &= 0, \\ u_t + uu_x + gh_x &= 0, \end{aligned} \tag{1.1}$$

Any constants, $u = U_0$ and $h = H_0$ are solutions of these equations. We perturb these uniform states such that

$$\begin{aligned} u &= U_0 + \hat{u}(x,t), \\ h &= H_0 + \hat{h}(x,t), \end{aligned} \tag{1.2}$$

Substituting equations 1.2 in equations 1.1 and neglecting all nonlinear terms in $\hat{u}$ and $\hat{h}$, we obtain the system

$$\begin{aligned} \hat{u}_t + U_0\hat{u}_x + g\hat{h}_x &= 0, \\ \hat{h}_t + H_0\hat{u}_x + U_0\hat{h}_x &= 0, \end{aligned} \tag{1.3}$$

Equations 1.3 have linear operators with constant coefficients acting upon $\hat{u}$ and $\hat{h}$. These operators commute and hence one can eliminate either $\hat{u}$ or $\hat{h}$ to obtain a higher order partial differential equation in either of the independent variables. We eliminate $\hat{u}$ to obtain the system

$$\hat{h}_{tt} + 2U_0\hat{h}_{xt} + \left(U_0^2 - gH_0\right)\hat{h}_{xx} = 0, \tag{1.4}$$

Equation 1.4 is a linear wave equation. It is hyperbolic for all values of U_0 and can be solved using the standard method of characteristics. We define a transformation

$$\begin{aligned} \zeta &= x - (U_0 + \sqrt{gH_0})t, \\ \phi &= x - (U_0 - \sqrt{gH_0})t, \end{aligned} \tag{1.5}$$

Using these transformations from equation 1.5 in equation 1.4, it reduces to

$$\bar{h}_{\phi\zeta} = 0, \tag{1.6}$$

which can be integrated to obtain

$$\hat{h} = \underbrace{f_1\left(x - (U_0 + \sqrt{gH_0})t\right)}_{\text{Downstream propagating component}} + \underbrace{f_2\left(x - (U_0 - \sqrt{gH_0})t\right)}_{\text{Upstream propagating component}}, \tag{1.7}$$

This predicts that any initial disturbance can split into two parts, one of which propagates upstream with a speed $\sqrt{gH_0}$ with respect to an observer moving with the speed U_0 and another downstream with the same speed with respect to the same observer. The functions f_1 and f_2 are determined from initial data. We observe that the "shape" of f_1 and f_2 do not change in time and the profiles just get translated in space. To understand why the "shape" of f_1 or f_2 doesn't change, it is useful to look at the dispersion relation of equation 1.4, which predicts that *all* Fourier modes travel with the same speed irrespective of their wavelength. The physical consequence of this is easily understood. Since all Fourier mode travel with the same speed, they maintain their relative phases with respect to each other thus adding up to produce a resultant profile which as a whole merely translates with a given velocity. Thus in nondispersive linear wave equation, the shape of the profile does not change, due to the absence of nonlinear and dispersive

effects. The inclusion of dispersive effects in the linear wave-equation alters this situation. (It is well-known see e.g. [Stoker, 1992], that dispersive effects arise from the deviations of pressure from hydrostatic). In a dispersive linear wave equation, while the individual Fourier modes still travel undistorted, their superposition gives the impression of a wave-form whose shape changes with time. This is because each mode travels with its own unique speed and thus their relative phases keep changing with time. As a consequence, in a linear dispersive system at long times, the individual Fourier modes tend to *disperse* i.e. separate out. Additionally, dispersion also causes the rear part of a localised elevation to steepen. To see this physically, we take the example of a deep-water wave - here the dispersion relation predicts that long waves (with gentle slopes) travel faster while short waves (with steep slopes) lag behind. The presence of waves with gentler slopes at the front and steeper slopes at the rear causes the sum of the Fourier modes to develop steep slopes in the rear when compared to the front. It should be noted that in a linear dispersive medium, the individual Fourier modes *do not* change shape. Due to different velocities for each mode, the summation of the modes gives the impression of a waveform whose shape changes as it travels. The solution of the initial-value problem of water-waves for the evolution of an arbitrary initial disturbance in a dispersive medium (e.g. in deep water) is known as the Cauchy-Poisson problem and the interested reader is referred to [Debnath, 1994] for a discussion. In a manner similar to dispersion, nonlinear effects can also change the shape of a wave albeit in an opposite sense. We next see the effect of nonlinearity in a nondispersive system.

Nonlinear nondispersive waves

Instead of perturbing the flow about a constant state as in the previous section, we instead rewrite the governing equations 1.1 using the transformation $c = \sqrt{gh}$ ([Stoker, 1992])

$$\begin{aligned} u_t + uu_x + 2cc_x &= 0, \\ 2c_t + cu_x + 2uc_x &= 0, \end{aligned} \tag{1.8}$$

Adding and subtracting equations 1.8, we obtain in characteristic form

$$\begin{aligned}[(u+2c)_t + (c+u)(u+2c)_x] &= 0, \\ [(u-2c)_t + (c-u)(u-2c)_x] &= 0,\end{aligned} \tag{1.9}$$

Using the method of characteristics [Stoker, 1992], the system 1.9 can be numerically solved and the conclusions are well-known. The main effect of nonlinearity is a progressive deformation of the inital wave-profile. If we start with a localised elevation, then the higher parts of elevation travel faster than the lower parts and the waveform thus progressively deforms into a discontinuous step-like profile as shown in figure 1.2. Mathematically, this corresponds to an intersection of two or more characteristic curves of the the same family on the $x-t$ plane, leading to multivaluedness in the independent variable. This phenomenon is popularly known as nonlinear steepening and is the basic physical mechanism through which travelling jumps or bores are understood to form. Nonlinear effects can thus be used to account for some of the observed phenomena like wave-breaking etc. It should be noted that as steepening proceeds to produce an infinite slope in the height-profile, the governing equations themselves become invalid in the near vicinity of the step-like profile. In this local neighbourhood, dispersive effects become relatively important and thus need to be considered. We have thus seen that dispersion and nonlinearity, both affect the shape of a wave. Nonlinear effects can progressively steepen the front of a localised elevation while dispersive effects can produce a steepening of the rear. Give this physical picture, it is perhaps not surprising that a balance between these two competing effects can be reached. The resulting waveform represents a nonlinear dispersive wave whose shape remains fixed while it just translates in space, in an manner analogous to the linear nondispersive waveform that we saw earlier. The well-known KdV equation represents such a balance between weak nonlinearity and weak dispersion. Expectedly, it admits solutions which are waves which translate unchanged in shape and are known as cnoidal waves [Benjamin & Lighthill, 1954].

We have a rough physical understanding of how a travelling jump or a bore arises. For such a jump, in the near jump region, dispersive effects (neglected elsewhere in the domain) become relatively important and the structure of the jump itself can represent a balance between dispersive smoothening and nonlinear

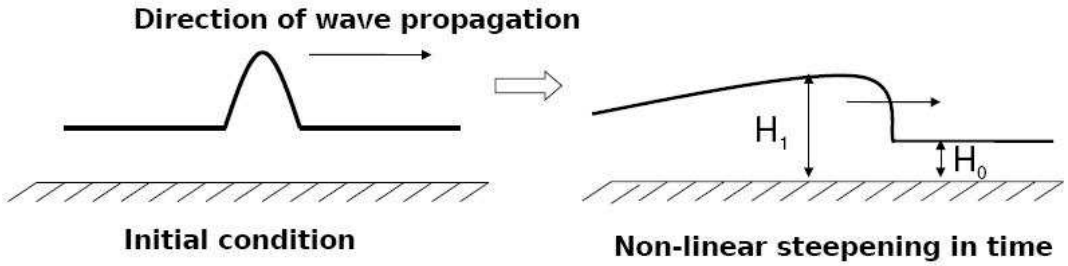

Figure 1.2: A pictorial illustration of how a travelling jump arises - As the waveform propagates from left to right, it steepens into a step like profile shown in the right, due to nonlinear effects. The velocity of propagation of the step like profile can be calculated from the shock criterion of [Rayleigh, 1914].

steepening (Dispersive shock waves have a large literature and continue to be a very active area of research. A good summary/pedaogical article by Hoefer & Ablowitz [2009] is available freely online). In the next section, we start with a discussion of the connection between travelling and standing jumps. The ideas of nonlinear steepening and dispersion and how they are traditionally thought to be related to a standing jump will become clearer through this discussion.

1.1.2 Relating the travelling and the standing jump

There are two ways in which one can think of travelling and standing jumps as being one and the same phenomenon. The first approach is mathematical while the second approach uses physical arguments. We describe them in detail below.

Approach 1 - Galilean Transformation

The first approach is a mathematical one that relies on a Galilean transformation from a lab frame of reference to a jump/bore attached frame. This approach is very standard and is used in many textbooks as a classical explanation for the equivalence between standing and travelling jumps [Stoker, 1992]. It is intuitively evident, but is instructive to describe, as is done briefly here. Consider in figure 1.3 a travelling hydraulic jump/bore modelled as a mathematical discontinuity which propagates unchanged in shape with a velocity U. The fluid velocities upstream and downstream of the bore u_1, u_2 as well as the velocity of the bore itself U, are all measured with respect to the bottom wall. It was shown by Rayleigh that mass

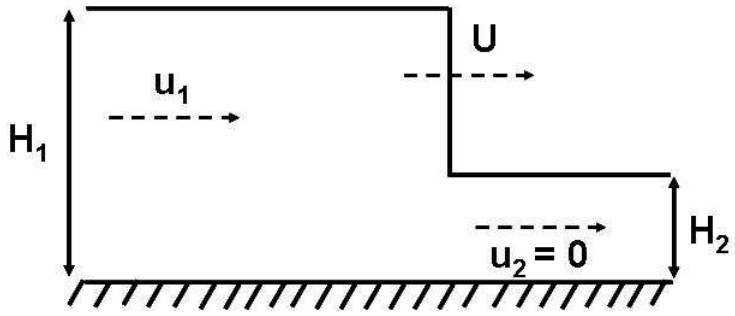

Figure 1.3: A travelling hydraulic jump also known as a *bore*. The illustration indicates a bore moving with constant velocity into still water with a velocity U with respect to the bottom wall.

and momentum conservation equations written across the bore can be satisfied simultaneously but energy cannot be conserved [Rayleigh, 1908, 1914]. Mass and momentum will provide two independent equations and we have five unknowns u_1, u_2, U, H_1 and H_2. Thus if we treat any three of these as independent variables, the other two are determined by mass and momentum conservation. We take for our purpose H_1, H_2 and u_2 to be specified. This corresponds to the case of a tidal bore of fixed depths upstream and downstream moving into stationary water ahead of it ($u_2 = 0$). Thus u_1 and U are determined by the mass and momentum equations. We write these equations in the frame of reference attached to the bottom wall. We restrict ourselves to inviscid shallow-water theory implying that we assume hydrostatic pressure and neglect viscosity

$$\begin{aligned} (u_1 - U)H_1 &= (u_2 - U)H_2, \\ (u_2 - U)^2 H_2 + \frac{gH_2^2}{2} &= (u_1 - U)^2 H_1 + \frac{gH_1^2}{2}, \end{aligned} \tag{1.10}$$

Equations 1.10 are the mass and momentum flux relations written across the discontinuity. We treat H_1, H_2 and u_2 as independent variables, set $u_2 = 0$ and thus obtain

$$\begin{aligned} U &= \sqrt{g\frac{H_1}{H_2}\left(\frac{H_1 + H_2}{2}\right)}, \\ u_1 &= U\left(1 - \frac{H_2}{H_1}\right), \end{aligned} \tag{1.11}$$

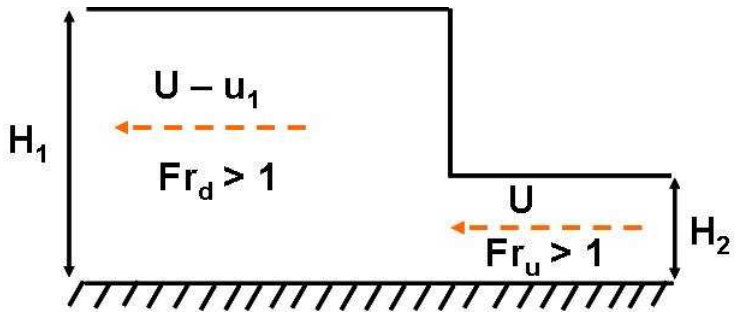

Figure 1.4: The travelling hydraulic jump of figure 1.3 becomes a standing hydraulic jump due to a Galilean transformation to a frame where the bore is stationary. Fr_u and Fr_d represent the upstream and downstream Froude number respectively. It is seen that in this frame of reference, the travelling jump has $Fr_u > 1$ and $Fr_d > 1$. The flow in this coordinate frame is from right to left, but the direction of flow through most of the thesis will be from left to right.

We now do a Galilean transformation and go to a frame of reference moving with velocity U with respect to the bottom wall. In this frame, the the bore appears stationary and the velocities ahead and behind the bore are U and $U - u_1$ with the directions as indicated in figure 1.4. Although we have depicted $H_1 > H_2$ in figure 1.3 and 1.4, this fact has not been used as yet in deriving equations 1.11. If we assume now that $H_1 > H_2$, then by a slight rearrangement, we have the following

$$\begin{aligned} U &= \sqrt{gH_2}\sqrt{\frac{1}{2}\frac{H_1}{H_2}\left(1+\frac{H_1}{H_2}\right)}, \\ \Rightarrow Fr_u \equiv \frac{U}{\sqrt{gH_2}} &= \sqrt{\frac{1}{2}\frac{H_1}{H_2}\left(1+\frac{H_1}{H_2}\right)} > 1, \end{aligned} \tag{1.12}$$

where Fr_u is the upstream Froude number. Similarly, we have

$$\begin{aligned} U - u_1 &= U\left(\frac{H_2}{H_1}\right), \\ \Rightarrow Fr_d \equiv \frac{U-u_1}{\sqrt{gH_1}} &= \sqrt{\frac{1}{2}\frac{H_2}{H_1}\left(1+\frac{H_2}{H_1}\right)} < 1, \end{aligned} \tag{1.13}$$

where Fr_d is the downstream Froude number. It is seen from figure 1.4 that the Galilean transformation reduces the travelling jump to a stationary jump. As seen from equations 1.12 and 1.13 that upstream and downstream of the jump, the re-

spective Froude numbers Fr_u and Fr_d are greater and less than unity respectively.

1.1.3 Approach 2 - Wave trapping

The second approach is more of a qualitative description and does not rely on a Galilean transformation to begin with. We go back to the solution 1.7. Let us imagine a uniform flow which by some inviscid mechanism (e.g. geometry) is able to transition from being supercritical ($Fr > 1$) to subcritical ($Fr < 1$). In the supercritical part of such a flow, we see from solution 1.7, that both upstream and downstream propagating parts of any surface disturbance get swept downstream with respect to the wall. This is because for $Fr \equiv U_0/\sqrt{gH_0} > 1$, both $U_0 + \sqrt{gH_0}$ and $U_0 - \sqrt{gH_0}$ are positive quantities. However, in the subcritical part of the flow i.e. $Fr < 1$, $U_0 + \sqrt{gH_0}$ is positive while $U_0 - \sqrt{gH_0}$ becomes now negative implying that this component of the disturbance now propagates upstream with respect to the wall. Thus the upstream propagating component of any disturbance created anywhere in flow, gets *trapped* at the critical $Fr = 1$ location, during a supercritical to subcritical transition. If we reverse the flow scenario and repeat the above argument for a flow transitioning from subcritical ($Fr < 1$) to ($Fr > 1$), we find that no such wave-trapping occurs for such a transition. This wave-trapping mechanism has been used many times to explain why a jump forms, and yet the arguments are very qualitative. On could think of many obvious questions which merit attention. How is this wave-trapping related to formation of a stationary jump? Can this wave-trapping mechanism provide the equivalence that a Galilean transformation provides between the travelling and standing jump i.e. can we show that wave trapping also occurs in a travelling jump? These are difficult and still open questions and we know of no study where such questions have been answered in a quantative and altogether satisfactory manner. A qualitative answer to the former question usually goes like this (see e.g. Rhines [2010]) - The trapping of waves at the critical location gives an indication that “smooth” transition through the critical Froude number is unlikely. The trapping leads to piling of upstream propagating waves until the wave amplitude becomes large compared to the depth, and non-linearity then deforms it into a step-like profile. The absence of this wave-trapping mechanism for subcritical to supercritical transition lends some

more weight to the argument, as these transitions are known to occur smoothly.

Returning to the second question of equivalence between travelling and standing jumps in this wave-trapping approach, it is possible [Stoker, 1992] to show wave-trapping even for a travelling jump. We return to the travelling jump of figure 1.3 and examine two linearised disturbances - one of which is created behind the jump and one ahead of it. The disturbance which is created ahead of the bore is created in still water. It thus splits into an upstream and a downstream component both of which move in opposite directions with the speed $\sqrt{gH_2}$. We are interested in the component which moves in the positive direction (left to right) and it is easy to see from equation 1.12 that the bore overtakes this disturbance because with respect to the wall, the bore moves with a speed U which is greater than $\sqrt{gH_2}$. Similarly, downstream of the bore there is a positive fluid velocity u_1 given by equation 1.12. Any disturbance created here splits into two components. The upstream propagating component's behaviour is not predictable without specifying the values of H_1 and H_2. We are more interested in the downstream propagating component's behaviour and whether this component moving with a speed $u_1 + \sqrt{gH_1}$ can *catch up* with the bore which is moving with a speed U, both speeds being measured with respect to the wall. It can be shown that for $H_2/H_1 > 1$, the ratio $(u_1 + \sqrt{gH_1})/U$ is also > 1. We thus have a situation where any left to right moving disturbance created ahead of the bore moves slower than the bore and a similar disturbance created behind the bore, moves faster than the bore. Thus disturbances created behind the bore *catch up* with it while the bore itself *catches up* with any disturbance created ahead of it. In other words if one does a Galilean transformation and goes to a frame where the bore is at rest, we will see that the disturbances ahead and behind the bore all getting focussed onto the bore. This is the equivalent of the wave-trapping mechanism discussed for a standing jump as applicable for a bore.

Having examined the physical consequences of nonlinear steepening and how it relates to hydraulic jumps, it is also useful to examine the consequences of dispersion. If we imagine the standing jump as an upstream propagating nonlinear wave, trapped at the critical Froude location, the question arises as to what counteracts non-linear steepening. Indeed if the profile were to steepen indefinitely, then the step-like shape would be unstable as the slightest perturbation would cause it to

topple over and break. This is where dispersion becomes important. As we saw in earlier sections dispersion can counteract nonlinear steepening and produce a solitary wave. Similarly in hydraulic jumps, dispersion can locally become important in the near jump region and play a role in arresting any further steepening of the wave profile. With the rough picture that emerges from this discussion we conclude our discussion of the hydraulic jump from a wave point of view.

1.2 Literature review of circular hydraulic jumps

We next perform a literature review. An enormous literature exists on planar standing jumps and reviews of known results have appeared periodically ([Rajaratnam, 1967],[Chanson, 2009]), also see lecture notes of Thandaveswara [2010]). Until the early part of the twentieth century, almost all theoretical studies of hydraulic jumps used inviscid, irrotational, long-wave equations. It was only much later that viscosity began to be explicitly included in the governing equations, and the importance of the same appreciated. We are not aware of a corresponding review of circular hydraulic jumps, so we take it up in some detail in this chapter. The circular hydraulic jump was probably first mentioned in the literature by Rayleigh [1914] and has attracted renewed interest and attention in recent years. It is visually simple and one can see it readily in a kitchen sink. Despite its apparent simplicity and ease of reproducibility, the physics of the circular hydraulic jump has proved hard to understand and analyse. There are many questions that can be asked regarding jump formation. Many of these questions are relevant for planar jumps as well. We list some of them below not in any particular order, and these should help the reader to appreciate the literature review better. This thesis has been influenced by this list of questions, some of which are partially or fully answered in later chapters.

1. The circular hydraulic jump is known to be associated with a surface and/or a bottom separated eddy. This bottom eddy has been suggested as a necessary condition for jump formation [Tani, 1949]. Is the bottom eddy the cause of the jump? Can we obtain obtain a steady circular hydraulic jump without any separation at the bottom or at the free-surface?

2. The analogy between a planar hydraulic jump and a shock suggests that jump formation owes its origin to non-linear steepening of waves. This is

supposed to happen at a location where the Froude number goes through unity (transitioning from $Fr > 1$ to $Fr < 1$). Can such a Froude number criterion be obtained for the circular hydraulic jump as well? Is it possible to explain the physical mechanism by which jumps form from a nonlinear steepening perspective in quantitive terms? Why can the inviscid transition from $Fr > 1$ to $Fr < 1$ not happen smoothly? What is the role of viscosity in this transition?

3. Scaling relationships have been proposed in literature [Bohr *et al.*, 1993],[Chang *et al.*, 2001] which predict the radius of the circular hydraulic jump in terms of experimentally controllable parameters. How accurate are these? Are improvements over these possible? Are there additional parameters which have not been considered and which can strongly influence the jump radius?

4. Are there any qualitative differences between planar and circular jumps or between travelling and stationary jumps?

5. Can we obtain a steady circular hydraulic jump or a planar hydraulic jump from purely inviscid equations? Can non-linear steepening be counter-balanced by dispersion to give a steady jump-like profile without invoking any viscosity? Do the jump relationships given by Rayleigh for planar jumps work for viscous jumps?

6. Shallow-water theory is widely used for describing jumps. Is shallow-water theory suffcient for describing these jumps? In other words, is hydrostatic pressure ever a good assumption for the entire flow? Can any theory which neglects streamline curvature account for a phenomenon which needs streamline curvature to arise?

7. What is the role of the wall-vorticity in jump-formation? In experiments it is reported that the boundary-layer reaches the free-surface upstream of the jump and theoretical work uses this as a guide [Godwin, 1993] to locate the jump. Is this a necessary condition? Is there a parameter regime where there exists a steady circular hydraulic jump and the boundary layer has not reached the free-surface at the jump location?

8. Most theoretical studies in recent years assume a fully viscous film. In such

a viscous film, there is neither so distinct a "boundary layer" nor any "outer inviscid irrotational flow". The traditional idea, of a boundary layer separating under the influence of an adverse pressure gradient imposed by the outer flow, does not directly apply here. How does one then conceptually think of separation occuring in such thin film viscous flows [Bowles & Smith, 1992]?

9. What is the role of downstream boundary conditions in the formation of the circular hydraulic jump. Controlling the outer depth sometimes causes the jump to lose its circular symmetry [Bohr *et al.*, 1996]. The outer depth also affects the size of separated eddy at the bottom / top and the radius of the jump. Why does the outer-boundary influence the jump structure and its radius so strongly?

10. What is the role of the air boundary layer above the jump (see [Sreenivas *et al.*, 1999])? Does it have a strong influence on the circular hydraulic jump, its radius, its structure?

11. The traditional approach of vertical averaging of viscous shallow-water equations leads to ordinary differential equation governing the evolution of film thickness. The solutions of these evolution equations behave unphysically in the jump neighbourhood, predicting singularities in the derivative of the film height instead of a jump. Why do these singularities arise? Do they arise due to truncation of terms in the Navier-Stokes equations or are they due to accompanying assumptions? Can we identify the neighbourhood of the singularity as the location of the jump? How can the region downstream of the singularity be described in this framework?

12. What is the role of surface-tension in the circular hydraulic jump [Bush & Aristoff, 2003]? Can surface-tension play an analogous role to gravity at small scales and cause a hydraulic-jump? Can capillary waves steepen to produce a shock like discontinuity? Is separation possible at small-scales as well? What is the role of geometry at these scales?

13. How well is the structure of the flow in the near-jump region and the region far upstream and downstream, known? Are results from numerical simulations available in plenty?

In the literature survey that follows, it will become clear that attempts have been made to answer many of these questions. In some cases, the answers are fairly clear while in other cases the conclusions remain unclear and debatable. In this thesis, we will concern ourselves with obtaining at least partial answers to some of the outstanding questions. Despite the renewed focus on studying circular hydraulic jumps in recent years, known results on circular hydraulic jumps have not been systematially reviewed in the literature. So as mentioned earlier, we start with a summary of studies on circular hydraulic jumps . Every attempt has been made to make the literature survey exhaustive. However, in a few instances references could not be accessed due to their not being published in easily accessible journals or due to other constraints, and we list these references as well. A few references on planar hydraulic jumps have also been reviewed because the conclusions and techniques are relevant for the circular case as well.

In what follows, studies are listed in a chronological order starting with the earliest while restricting our attention mostly to laminar circular jumps. At the end, we will try to summarise known results for the circular hydraulic jump. Whenever we qualify a reference as *"the first to..."*, this should be taken with the caveat that this claim is only to the best of our knowledge.

1. [**Rayleigh, 1908, 1914**]:
   The 1914 paper is the first place in literature where the circular hydraulic jump finds mention, although no analysis was presented. The focus in both the papers was on planar jumps and to treat the same as a mathematical discontinuity in height and obtain relations for flux of mass, momentum and energy on either side of the discontinuity using inviscid shallow-water assumptions. The main conclusions were the impossibility of energy flux being continuous across the jump and the impossibility of a negative jump.

   Comments:
   The 1908 and the 1914 work introduced the well-known Rayleigh shock criterion. This criterion is used extensively even in recent literature in shock-fitting techniques. The validity of this criterion becomes suspect in the case of strong jumps where streamline curvature effects are large and hence hydrostatic pressure might not be appropriate. Additionally, there is a discontinuity in energy flux, which is partially a result of neglecting viscous dissipation

through work done at the wall by wall-shear. The impossibility of a negative jump as shown in this paper is a valid conclusion as negative jumps are generally never observed (see Gribbon & Cope [1963]). There was a mistake in the energy flux expression in the 1908 paper which was corrected in the 1914 paper. Applying the Rayleigh shock criterion to a circular geometry leads to some unexpected results and these will be discussed in Chapter 4.

2. [**Tani, 1949**]:
   This is mainly a theoretical work with a small experimental part. The main results are:

   - Introduced and analysed the boundary-layer shallow-water equations independently on the same lines as was done earlier by Kurihara [1946].
   - A first order ordinary differential equation for height and radius was obtained by vertically averaging of the boundary-layer shallow-water equations (BLSWE). The solution to this ordinary differential equation gives height-profiles which were spirals. No jump-like height profiles were obtained. Introduced the idea that circular hydraulic jumps occur due to boundary layer separation at the wall.
   - In another approach to solving the BLSWE, the author uses an assumption that the slope of the streamlines varies linearly from being 0 at the wall to h' at the free-surface (for a steady flow). Using Weirstrass elliptic functions, the resultant equations are solved and height profiles obtained. No vertical averaging is performed here. The results obtained in this approach are qualitatively similar to those obtained from vertical averaging and the solution fails at the location of separation. Some experimental results are also reported for a comparison of predictions of the location of separation (taken to be the jump radius) to experimental jump radius. Forty percent deviations are reported and the author does not analyse the reasons for this in detail.

   Comments:
   This work is important in that it introduced the boundary-layer shallow-water equations. We will study these equations in great detail in Chapter 2. However, one of the principal conclusions of this work is incorrect. The cause

of hydraulic jumps is attributed to flow-separation, thus implying that the physical mechanism of jump formation owes its origin to separation. As we will see in later chapters, the standing hydraulic-jump in planar and circular geometry is a standing shock which does not rely on flow-separation for its existence. The existence of jumps without separation has been hinted at in literature for some time, see e.g. Craik et al. *[1981]; Watanabe* et al. *[2003]. We will also study the BLSWE in great detail for both circular and planar geometries in Chapter 2. It is perhaps not surprising that both the approaches described above lead to qualitatively similar answers because it can be easily shown [Watanabe* et al.*, 2003] that assuming a self-similar velocity profile is also equivalent to the assumption that the slope of the streamlines varies linearly from the wall to the free-surface.*

3. [**Benjamin & Lighthill, 1954**]:
   This is not a direct study of hydraulic jumps. The authors propose that the wave-train which appears downstream of a standing/travelling jump, are cnoidal waves which can be modelled using the KdV equation. It is argued that the loss of energy which occurs across a Rayleigh shock can be explained by the energy needed to create downstream waves. However this net energy loss is found not to become exactly zero even in the presence of downstream waves. The appearance of downstream undulations are governed by the roots of a cubic in the KdV equation. It is argued that only when the cubic contains three real roots, can a train of waves can appear downstream of the jump.

   Comments:
   While the steady KdV equation can be integrated in terms of elliptic functions, these authors offer an alternative approach to the solution. The equation is expressed as the kinetic and potential energy of a particle of total energy zero, trapped in a potential well with a cubic potential. The number of real roots of this cubic determine an oscillatory solution while a repeated real root, determines a solitary wave.

4. [**Gribbon & Cope, 1963**]:
   This is an experimental study where liquid helium is pushed from below through an orifice into a horizontal plate. A hydraulic jump seems to be formed although the illustrations in the paper make it seem like a negative

jump (Hydraulic drop).

Comments:

Although the authors do not discuss much about jumps, we record this reference here because this is the first experimental study of hydraulic jumps with liquid helium. A similar and more detailed study of the circular hydraulic jump with a liquid helium impinging jet was done many years later in Rolley et al. *[2007].*

5. [**Watson, 1964**]:
   A theoretical study with a small experimental contribution. Both laminar and turbulent flows are studied, the later using eddy viscosity. Planar and circular geometries are studied. The flow (including the impinging jet) is divided into different regions as following:

   - A region close to the impinging jet, where the presence of the free-surface is not felt and Homann's similarity solution is valid [Homann, 1936].
   - A region where the boundary-layer thickness is very small and the Blasius similarity solution is valid. Here too the free surface is not felt.
   - A region far-away from the jet but much upstream of the jump, where the boundary layer has already reached the free-surface. In this region a similarity solution without gravity was obtained. The velocity profile can be expressed in terms of a Jacobian elliptic function and it is found that the height profile is $h = \frac{\pi}{\sqrt{3}}\nu(x+l)/Q$ where l is a constant of integration. This is equivalent to

   $$h'Re \equiv \frac{dh}{dx}\frac{Q}{\nu} = \frac{\pi}{\sqrt{3}} \simeq 1.8128, \tag{1.14}$$

   where $Re = Q/\nu$. Similarly, in a circular geometry the film thickness is predicted as $h = \left(2\pi^2/3\sqrt{3}\right)\nu(r^3+l^3)/Qr$ which gives

   $$Re(h' + h/r) \simeq 1.8128 \tag{1.15}$$

   where $Re \equiv Q/2\pi r\nu$.
   - Since gravity is neglected, it is no surprise that no jump-like solutions are obtained for h, which grows monotonically with streamwise distance

for both planar and circular geometries.

- The location of the jump is given by two implicit formulae - One which assumes that the boundary layer reaches the free-surface *before* the jump and another which assumes that the boundary layer reaches the free-surface *after* the jump. Both these formulae depend on the outer depth. The experiments were conducted to check the implicit relation proposed and these show considerable scatter.

Comments:

This was the earliest attempt at modelling the flow by dividing the flow into multiple regions. The existence of a similarity solution in the absence of gravity is an important result. Note however that no jump-like transitions were obtained for the height-profile. The two implicit relations for quantities across the jump were later improved upon by Bush & Aristoff [2003]. The gravity-free similarity solution is indeed realized at high enough local Froude numbers as we will see later in our simulations.

6. [**Olsson & Turkdogan, 1964**]:
   An experimental study of the circular jump where the effect of surface-tension is highlighted. If the water falling over the edge of the plate under gravity is treated like a projectile, then the shape of the surface created by the falling water all around the plate is expected to be parabolic. It is shown that this is not so and the difference is ascribed to surface-tension. Using high-speed photography of around 2000 frames/sec, remarkable for that time, it was concluded that the surface velocity is a constant upto the hydraulic jump. It is also claimed that the radius at which the boundary layer reaches the free-surface as predicted by Watson [1964], is incorrect. The fraction of kinetic energy lost to surface-energy is claimed to be large.

   Comments:

   This was one of the earliest works to highlight the effect of surface-tension on the circular hydraulic jump. One of the conclusion, that the velocity of the free-surface is a constant, was found to be incorrect in later experiments by Stevens & Webb [1992] and Watanabe et al. *[2003].*

7. [**Hsieh, 1967**]:
   A theoretical study of the vertically integrated Navier-Stokes equations. The aim of this report is to provide an explanation for the role of viscosity in the supercritical to subcritical transition. The author however neglects some terms in a rather heurisitic fashion. The resultant ordinary differential equation is analysed for its fixed points. It is shown that a subcritical flow is stable and a supercritical flow is unstable in the presence of viscosity. The author uses this as a physical motivation for why a supercritical flow transitions to being subcritical. There are other results in this report on shocks and vortex breakdown which we do not discuss here.

   Comments:
   This is an interesting work, which due to its not being published, has never been cited before in the hydraulic jump literature. We are happy to bring to attention this reference here. Hydraulic jumps are studied here only in a planar geometry. The method of vertical averaging that we follow in Chapter 3 of this thesis, is borrowed from this work. The author had used this method to obtain an approximate equation for the height profile, but we rewrite the complete Navier-Stokes equations in terms of an evolution equation for the height profile.

8. [**Koloseus & Ahmad, 1969**]:
   A theoretical and experimental study. The main findings are:

   - The height profile in the "width" of the jump is assumed to be linear and pressure to be hydrostatic. Using mass and momentum equations, a relationship is derived relating the depth ratios, the radius ratios before and after the jump and the incoming Froude number. This expression becomes identical to the criterion of a planar Rayleigh shock for a circular jump with zero width.
   - Adding a head loss term to the energy equation, an expression is derived relating the head loss ratio to the incoming Froude number and the depths after and before the jump. Assuming the width of the jump to be zero, here too we recover the planar expressions for head loss as derived by [Rayleigh, 1914].

- The "width" of the jump is obtained as a function of incoming Froude and radius ratios from experimental data. This width is reported to be much smaller for circular jumps when compared to planar jumps.

Comments:

This work is of civil engineering interest. The aim is to derive relationships for a circular jump analogous to a planar jump and compare them between the two geometries. Our numerical simulations also show that circular jumps are usually steeper than planar jumps and thus have a smaller width.

9. [**Arbhabhirama & Wan, 1975**]:
This is an experimental and semi-analytical study. The main results are:

- Expressions for momentum, energy flux across the jump and height profiles are obtained for laminar and turbulent jumps. As in all the work discussed so far, except Hsieh [1967], these make the assumption of hydrostatic pressure. The finite width of the jump assumes the height profile to be linear. An empirical expression is obtained from experiments for height-profile in the near-jump region.
- The validity of these expressions are checked by comparsion with experiments. Comparisons are also made with the results of Watson [1964].

Comments:

This work builds up on the earlier discussed work of Koloseus & Ahmad [1969]. There are some free-surface velocity measurements reported in this reference.

10. [**Labus, 1977; Labus & DeWitt, 1978**]:
These are numerical and experimental studies on jets impinging on finite diameter plates in free fall i.e. nearly zero gravity. The experiments were conducted in a drop-tower. This has some relevance for the circular hydraulic jump because far upstream of the jump, where the local Froude number is very high, the flow locally can be aproximated as a zero-gravity problem, where the similarity solution of [Watson, 1964] is relevant. The main results reported are:

- An order of magnitude estimate of the terms in the Navier-Stokes equation is used to provide a criterion for deciding when viscous effects can be neglected in the impingement region. This criterion depends on the non-dimensional ratio of jet diameter to plate radius.
- Experiments are reported where a liquid jet impinging on a plate is observed inside a drop tower. Three flow regimes are identified depending on the jet velocity viz. inertia dominated, surface-tension dominated, and transitional where both effects are important.
- The inviscid, irrotational Euler's equation without gravity are solved numerically with and without surface-tension to obtain the free-surface shape.
- Good match is reported in the inertia dominated regime between numerical and experimental results. No quantative comparisons could be obtained in the surface-tension regime because the experimental results did not reach a steady state. However qualitative similarities are reported.

Comments:

Though this was not a direct study of the circular hydraulic jump, this work is relevant to discuss here, since a drop-tower was used later by Avedesian & Zhao [2000] to study the effect of lowering of gravity on the circular hydraulic jump. Morever the impingement region is of interest.

11. [**Ishigai *et al.*, 1977**]:
An experimental work on the circular jump. The jump is categorised into four different types based on the upstream Froude's number Fr. The classification is reproduced below.

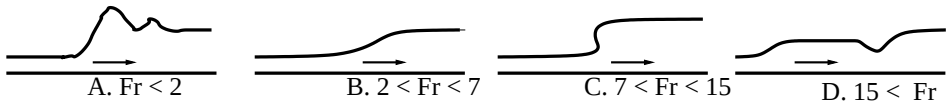

Comments:

This study has a sentence in the opening paragraph where it is claimed that "the hydraulic jump occurs by the interference of the film flow with the water at the periphery of the plate". This statement is not always true. In high

speed photography experiments conducted by us to study the transients leading to the formation of the circular hydraulic jump, we found that the jump forms and even reaches a steady radius much before the fluid reaches the plate edge. This paper was one of the earliest which, although briefly, examined the interactions of two hydraulic jumps and categorised them into different types based on the inter-jet distance. This work was built upon and continued later in the study by [Kate et al.*, 2007a]. The jump of type A represents an undular jump in a circular geometry and the existence of this type of jump has been doubted in Craik* et al. *[1981]. Also see Thorpe & Kavcic [2008]. This was also one of the first studies which doubted Tani's hypothesis that separation was the cause of the jump although the reasoning followed by the authors to arrive at this conclusion appears hazy.*

12. [**Nakoryakov *et al.*, 1978**]
    This is an experimental and theoretical study. The main results relevant to hydraulic jumps are:

    - The theoretical study divides the flow on the lines of Watson [1964] and obtains formulas for friction factor etc.
    - Demonstration of separated flow and subsequent reattachment underneath the jump by making measurements of wall-shear stress using an electrodiffusion method.
    - Dependence of the radius of the jump on the edge conditions of the finite plate. The location of separation was experimentally shown to be sensitive to whether the plate edge was rounded or sharp.
    - Experimental evidence that the average flow speed is close to the inviscid wave speed near the jump.

    Comments:
    This was the first experimental confirmation of flow-separation and reattachment underneath the circular hydraulic jump.

13. [**Craik *et al.*, 1981**]:
    An experimental study. Film thickness measurements where made using a ligh absorption technique. The main findings are:

- The depth of fluid as it exits the plate is externally controlled. The circular jump becomes non-axisymmetric and unstable as this outer depth is increased.
- Experimental confirmation of a separated eddy underneath the jump.
- The separated eddy underneath the jump shortens and vanishes as the outer depth is increased. Increasing the outer depth also triggers an instability causing the jump to lose its axisymmetry and stability and the jump radius starts decreasing until it eventually "closes" and disappears.
- The onset of the oscillatory instability of the jump is associated with the disappearance of the eddy.
- The oscillatory instability of the jump causes it to sometimes have a distinct azimuthal wave-number.
- A critical local Reynolds number of around 147 was identified for the onset of instability.

Comments:

This was one of the early works to doubt Tani's hypothesis [Tani, 1949] that the jump was due to flow separation. However, no experimental evidence of circular jumps ***without*** *separation was presented. The shortening of the eddy length as the outer depth was increased is posed as an unanswered question.*

14. [**Lawson *et al.*, 1983**]: A combination of theoretical and experimental work. Some of the main results reported are:

- An equation is derived for the depth ratio upstream and downstream of the jump, from mass and momentum conservation assuming a linear height profile in the jump-width. An empirical friction-loss term is added to this equation. It was found that the empirical form of the friction used can significantly influence the jump location. This equation is solved to obtain the depth ratios before and after the jump, for given values of the radius ratio and the downstream Froude number.
- Experimental results are compared with the theoretical results obtained above. The authors report that the assumption of a linear height profile

in the width of the jump compares favourably with experiments. It is also reported that the width of the jump is independent of the upstream Froude number.

Comments:

This builds upon the earlier work of [Koloseus & Ahmad, 1969] and, like [Koloseus & Ahmad, 1969], also takes a civil engineering perspective with an aim of coming up with design charts for the circular hydraulic jump. Note that the theoretical analysis and the experiments correspond to a upward facing jet discharging into an orifice on a plate. This is in contrast to impinging jet experiments which are typically used to produce a circular hydraulic jump. The authors model the upstream region of the jump as being of constant thickness. Other works including our axisymmetric Navier-Stokes simulations reported in Chapter 4, find that this is not strictly true.

15. [**Azuma & Hoshino, 1984**]:
This is a three-part experimental, and partly theoretical study of thin-film radial flows and hydraulic jumps. Two kinds of thin-film flows are studied - one formed by an impinging jet and another formed by a jet hitting a plate from below. In the first part, the stability and transition to turbulence is studied. The second part consists of film-thickness measurements and the third comprises velocity-profile measurements. The three parts are summarised below:

    - In the first part of this study, the experiments use a jet impinging on the upper surface of a plate and an inverted jet hitting the lower surface of a plate. The resulting transition to turbulence in radial film flow is studied. Surface waves are categorised qualitatively as roll waves, Rayleigh Taylor waves, ripple waves, lattice shaped waves, sandpaper-like waves etc. A detailed qualitative description of the transition to turbulence is provided. Data is reported for the variation of dimensionless transition radius versus Reynolds number, the transition local Reynolds number etc.
    - The second part of the study measures the film thickness for the experimental setup described earlier. The measured profiles are compared to the predictions of Watson [1964] and Ishigai *et al.* [1977].

- Velocity profiles are measured using a Laser doppler Velocimeter. Aluminium powder is used as scattering particles. It is claimed that the velocity profile in the region upstream of the jump where the boundary layer is growing is modelled well by a fourth-order polynomial. In the fully viscous part of the film, the velocity profiles gradually approaches the gravity-free similarity solution of Watson [1964].

Comments:

This is one of the early studies on the circular hydraulic jump where velocity-profiles were obtained experimentally. This is also among the first experimental studies of the transition to turbulence in a thin liquid film in the context of hydraulic jumps. The study of transition to turbulence in the context of hydraulic jumps was later carried out also by Cholemari [1998].

16. [**Vasista, 1989**]:
    An experimental study designed to test the theoretical predictions of [Watson, 1964]. In the few experimental results reported, very limited agreement is said to have been obtained with the predictions of Watson [1964]. Part of the disparity is reported to be due to the flow becoming turbulent upstream of the jump and due to the appearance of upstream waves.

    Comments:

    The experiments reported in this thesis were carried forward in the subsequent extensive experimental study by Liu & Lienhard [1993]. The description of the experiment in Liu & Lienhard [1993] where it is described very briefly, is given in greater detail in this thesis.

17. [**Thomas *et al.*, 1990**]:
    This is a numerical study of the boundary-layer shallow-water equations using vertical averaging and modelling the skin-friction term. Although the unsteady term is retained in the momentum equation, the numerical procedure uses pseudo-transients and hence time evolution to the steady state is not time-accurate. Both planar and circular geometries are studied, in the latter case the effect of a solid body rotation is also added. Some of the main results are :

- Due to the analogy between compressible flows and shallow-water theory, the numerical technique used to solve the governing equations is borrowed from compressible flow. A downstream boundary condition is imposed in the form of Froude number being equal to unity.
- For simulations with gravity, a hydraulic jump is found to occur somewhere in the domain in both geometries. In the case of zero gravity, it is found that the flow remains supercritical throughout the domain and no jump is obtained.

Comments:

Although a solution of the the initial value problem for jump formation has been presented, the data regarding the time-evolution to steady-state should be interpreted with caution. This is not a full numerical solution of the unsteady boundary-layer shallow-water equations and the governing equations are only quasi-steady.

18. [**Rahman *et al.*, 1991*a***]:
This is a computational study of turbulent jumps and we describe it briefly here. Two kinds of numerical studies are reported viz. (a) Simulation of the Reynolds averaged Navier-Stokes equations with the $k - \epsilon$ model for turbulence modelling (b) Vertical averaging of the BLSWE assuming a uniform profile (as turbulent flows are being modelled) and assuming a model for the friction factor, an unsteady momentum equation is derived which is then solved using the MacCormack predictor-corrector method. Some artificial viscosity is added to damp numerical oscillations occuring near the jump. The simulations are carried out for both planar and circular geometries and comparisons are made between the simulations and some earlier experimental data. Good match is reported for the simulations. For certain parameter ranges, the averaged solution predicts a radius/location of the jump which is substantially larger than the ones seen in simulations. Some velocity profiles upstream and downstream of the jump are also provided.

Comments:

Although the authors include time-dependence in their vertically averaged model, this is only a quasi-steady calculation. Due to vertical averaging the film thickness and the average velocity appear in the continuity equation and

the authors neglect the time variation of the film-thickness compared to that of the average velocity.

19. [**Rahman *et al.*, 1991*b***]:
This is a theoretical study of laminar jumps in both planar and circular geometries. Equations for the evolution of height with radius are derived assuming a uniform velocity profile and a friction factor, or a parabolic velocity profile. The main results are:

    - In the absence of gravity, the film thickness may increase or decrease depending on the friction factor and the solution is single-valued at any radius.
    - In the presence of gravity, the solution is multi-valued at any radius - one solution is supercritical ($Fr > 1$) while the other is subcritical ($Fr < 1$)
    - The solution has a singular point beyond which there is no solution.

    Comments:
    As is usual, the technique of vertical averaging assuming a parabolic velocity profile leads to multiple solutions at a given spatial location, but no jump-like transition between these is predicted.

20. [**Gharangik & Chaudhry, 1991**]:
This is a numerical study of hydraulic jumps in rectangular inclined channels, using the Boussinesq equations. The authors solve the partial differential equation governing the evolution of film-thickness in space and time. This Boussinesq terms are the non-hydrostatic terms for pressure. Three different numerical schemes viz. a second order accurate and two fourth order accurate ones, with and without Boussinesq terms, are tested. The initial conditions are chosen to be such that the flow is supercritical throughout the domain and the initial-value problem is solved numerically. The outer depth is controlled in these simulations and it is found that the jump originates downstream and moves upstream until it reaches its steady-state location. Some oscillation about the steady-state location is reported. Experiments are conducted to compare with the height profiles obtained from the numerical solutions. Good agreement is reported for the fourth order model.

Comments:

The authors correctly recognise the importance of the Boussinesq terms (dispersive terms) for calculating the near-jump profile. However, the effect of the Boussinesq term on the jump radius is found to be negligible. This observation is consistent with the fact that shallow-water models can be used to obtain reliable estimates of the jump radius despite the fact that most of these models do not do a good job in predicting the near-jump height profile. The near-jump region is not studied in detail in this reference.

21. [**Khalifa & McCorquodale, 1992**]:
The authors report simulations of the radial jump in a diverging sector. The wall-shear is modelled and a technique known as the strip-integral method is used. This technique splits the flow into three parts and vertical averaging is then used to simplify the governing equations into a set of ordinary differential equations. Additionally, the mean flow is also modelled. Some results from these simulations are compared with experiments e.g. the depth ratio before and after the jump, surface-velocities, the length of the jump etc. and good agreement is claimed.

    Comments:

    This was one of the early turbulent simulations of the radial jump. Note however that this is not a Navier-Stokes simulation in the sense that there is modelling involved, of the wall-friction terms. Additionally pressure is assumed to be near hydrostatic in the sense that it is decomposed into a laminar hydrostatic part and a non-hydrostatic part due to turbulent fluctuations alone.

22. [**Stevens & Webb, 1992**]:
An experimental study of impinging liquid jets with very limited relevance towards hydraulic jumps.

    - Two sets of experiments are conducted - one with the jet impinging on a vertical plate (parallel to gravity) and another on a horizontal plate (perpendicular to gravity). The difference between the two experiments helps to identify those regions of the flow where gravity is important from those reigons where it is not. At small radii after impingement, gravity is found to be insignificant.

- Mean free-surface velocities before and after impingement are reported. For the impinging jet, the mean free-surface velocity increases from being zero at the nozzle exit to almost the centerline velocity as the jet falls downward. The distance over which this transition happens is reported and it is found that for small jet Reynolds numbers (based on the nozzle diameter), this transition is rapid.
- The mean free-surface velocities after impingment normalised by the average jet velocity is plotted against the radial distance nondimensionalised by the nozzle diameter. It is found that this data collapses into a single band which can be approximated as a parabola and a straight line for different ranges of r/d. The measured free-surface velocity data is compared to the analytical predictions of [Watson, 1964] and it is found that the free-surface velocity differs from the centerline jet velocity before impingment and does not become constant with radial distance, as was assumed earlier by [Olsson & Turkdogan, 1964].
- Some calculations of the depth-profile are reported assuming an parabolic velocity-profile.

Comments:

This work does not strictly pertain to laminar jets (and jumps) as the jet Reynolds number is $O(50000)$ *and turbulent fluctuations are significant. However, some of the results e.g. about the mean free-surface velocities remain valid for laminar jets as well.*

23. [**Varella, 1992**]:
This is an analytical study of wave evolution on radial film-flows. Although not a direct study of the circular hydraulic jump, it bears a strong connection.

- The initial-value problem for the radial shallow-water equations are solved numerically and jump formation is reported.
- Stability of long waves including dispersive and surface-tension effects is analysed.
- An equation is derived which governs the evolution of nonlinear, dispersive, long wavelength waves in a radial geometry. This is a rich equation

which contains many other well-known equations as its subsets. This equation admits cnoidal and solitary wave solutions.

Comments:

This is an unpublished work which to the best of our knowledge has not been cited before in literature. We are grateful to Prof. Peter J. Schmid (LadHyX, France) for bringing this work to our attention. This is one of the earliest studies on wave evolution on radial film flow. The initial-value problem of perturbing a supercritical flow is numerically solved using a shock-capturing scheme. However, the authors seem to report formation of a steady jump-like transition in the numerical solution to the initial value problem invoving the radial shallow-water equations. This does not seem to be correct because the steady, inviscid, irrotational radial shallow-water equations do not admit a jump-like transition.

24. [**Liu, 1992; Liu & Lienhard, 1993**]:
An experimental study of the circular jump. The focus is on studying the deviations of circular jumps from planar jumps. The main conclusions are:

- The classical Rayleigh shock criterion between the upstream and downstream depth, which is used extensively for planar jumps is shown to be invalid for circular jumps at high upstream Froude numbers. It is argued that the failure of this relation is due to dominance of surface-tension in thin-film flows rather than due to axisymmetric geometry. It is also argued that the same phenomenon should be observed in planar jumps if the film-thickness is made small.
- Categorisation of the jump based on steadiness, number of rollers, Weber number etc, instabilities.
- An attempt is made to express the non-dimensional radius of the jump as a function of other non-dimensional paramters but the functional form is not investigated.
- A subtype of Type II jump is reported (see figure 1.5)

Comments:

This is one of the early classifications of the different types of hydraulic jumps

based on non-dimensional parameters. The authors report an extensive parametric study of the different types of jumps based on the jet Reynolds, jet Froude, Weber number based on the film thickness after the jump and. The data reported here can be very useful for guiding numerical simulations of the circular jump.

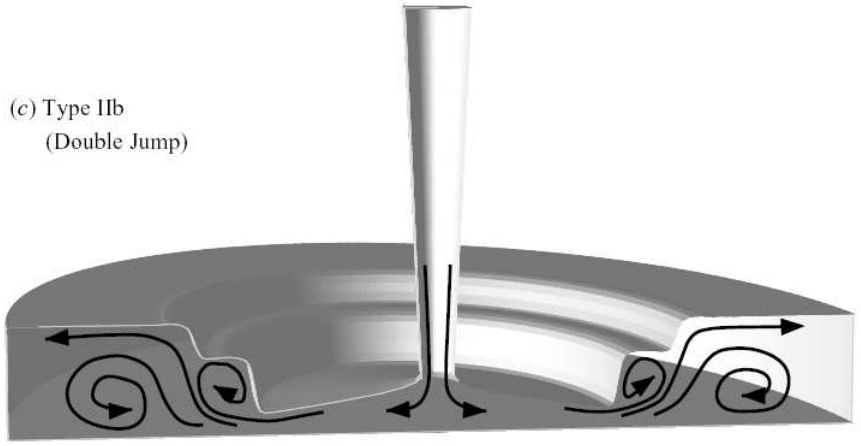

Figure 1.5: Pictorial illustration of Type IIb "double "jump. Reproduced from [Bush *et al.*, 2006]

25. **[Bowles & Smith, 1992; Gajjar & Smith, 1983]**:
These are analytical studies of jumps in both planar and circular geometries. Both studies are related and we summarise them together here. In the first reference, the authors deal with the problem of a developing boundary-layer for an $O(1)$ incident Froude number. The second reference studies the case of an incident fully developed flow for an $O(1)$ incident Froude number. Assuming that the length-scale over which the flow re-adjusts is long compared to its depth, these authors provide a derivation of the BLSWE in primitive variables. These equations are interactive in the sense that the pressure is not prescribed but has to be determined as part of the solution. For large incident Froude numbers, the length-scale of interaction shortens and streamline curvature and surface-tension effects neglected earlier, now become important and new governing equations are derived. The authors solve a linearised forced-interaction problem for flow over an obstacle. Finally the

complete nonlinear free-interaction problem for large incident Froude numbers and short length-scales of interaction, is solved numerically and some of the results are compared with experiments.

Comments:
These were among a series of studies which looked at hydraulic jumps using interactive boundary layer equations, instead of using the vertical averaging technique. The original work was primarily motivated by the some of the experimental findings of [Craik et al.*, 1981]. The basic conclusion of all these studies is that the hydraulic jump is a kind of viscous-inviscid interaction forced by downstream conditions. Here viscous inviscid interaction refers to the interplay between hydrostatic pressure changes generated by the displacement of the free-surface and viscous effects at the wall. When the downstream conditions are explicitly included in the solution, it becomes a forced interaction problem otherwise it is labelled as free-interaction. Also see the first section of Bowles & Smith [1992] for a very nice and crisp summary of the work done in all of these references. Note that the assumption of shallow-water conditions becomes suspect when* $Fr \sim O(1)$.

26. [**Bohr *et al.*, 1993**]:
This is an important analytical work with a small experimental part at the end. The main conclusions are:

- Inviscid shallow-water equations cannot be used to obtain a scaling relationship for the radius of the jump.
- The vertically averaged viscous shallow-water equations with a self-similar velocity assumption lead to a first order ordinary differential equation. Some of these solutions are identified as inner solutions and others as outer solutions. The outer solutions show a negative infinity in slope at a certain radial location and this radius is identified as corresponding to the plate edge in experiments where the fluid falls off the plate.
- The solutions cannot be continued to arbitrary radius for any initial condition. Further, the solutions to this ordinary differential equation spiral around to a critical point, so the height profiles do not show any jump-like transitions.

- By fitting a Rayleigh shock, between the inner and outer solutions, the radius of the circular hydraulic jump is predicted to scale as $Q^{\frac{5}{8}}\nu^{\frac{-3}{8}}g^{\frac{-1}{8}}$. This happens to the radial length scale of the critical point of the ordinary differential equation discussed earlier.
- Experiments are conducted to validate the scaling relationship predicted for the jump radius, and reasonable agreement is obtained at high flow rates. At low flow-rates, corrections are discussed.
- The problem of lack of asymptotic solutions to the vertically averaged equations is shown to be cured when non-hydrostatic effects of pressure are added.

Comments:

The first reliable scaling relationship for the jump radius was obtained in this work. The lack of asymptotic solutions at large radius for the solutions of the ordinary-differential equation was proved rigorously in this study. The discontinuity in the radial momentum-flux was first pointed out in this work and we discuss this in greater detail in Chapter 4.

27. [**Stevens & Webb, 1993**]:
An experimental study of the thin-film flow formed from an impinging jet. Velocity-profiles measurements are made for the thin-film using laser-Doppler velocimetry. Some comparisons are reported with previously known analytical results. The Reynolds number for these experiments based on the average jet velocity and jet diameter is $O(50000)$. Nozzle diameters of various sizes are used and the ratio of the impingement height to the nozzle diameter is maintained constant for all experiments with one exception. The main conclusions are:

- For $r/d << 2.5$, where d is the nozzle diameter and r is the radial coordinate, the maximum of the velocity occurs closer to the wall rather than to the free-surface. This maximum shifts towards the free-surface with increasing values of r/d. Additionally, the velocity above this maximum is not uniform.
- At small values of r/d, the experimentally calculated profiles show substantial deviations from that of Watson [1964], a parabolic, cubic or

a quartic. At large values of r/d, due to the thinness of the film, a sufficiently large number of data points were not obtained.

- Film-thickness measurements are made and compared with the analytical predictions of Watson [1964] in laminar and turbulent flow and good agreement is reported at small values of r/d. Turbulence intensities are reported across the film. It is observed that these intensities are higher near the wall and grow with radial distance.

Comments:

Velocity profile measurements are very difficult for thin-film flows and there are not many studies in literature on hydraulic jumps which report measurements of velocity-profiles with a high degree of accuracy. Some of the associated difficulties associated with these measurements are discussed in this work.

28. **[Siwon, 1993]**:
An experimental comparison of films formed by a gas-liquid spray jet / liquid jet impinging on a plate. The central focus of this work is not the circular hydraulic jump. However some film thickness measurements are made which are relevant for jumps. These measurements are made using a flush mounted conductance probe which is reported to be especially suitable for gas-liquid jets. The main conclusion are:

- No film thickness measurements are made in the impingement region because of experimental set-up limitations.

- The film thickness away from impingement point for a gas-liquid spray is an order of magnitude less than that of a liquid jet.

Comments:

It is not clear whether a circular hydraulic jump is formed from an impinging gas liquid spray. The author reports the formation of circular hydraulic jump only for a liquid jet and height profiles for a gas-liquid impinging spray do not show any jump. It is not immediately clear why this should be so but it could be due to reduced gravity effects in the latter.

29. [**Godwin, 1993**]:
Viscosity is claimed to be a crucial ingredient for jump-formation. Predicts a scaling relationship for the radius of the jump based on a postulate that the jump happens when the boundary-layer reaches the free-surface. the basis for this postulate is not discussed, but this has been used by others later. The scaling relationship for the radius of the jump r_j is predicted as $Q^{\frac{1}{3}}\nu^{\frac{-1}{3}}a^{\frac{2}{3}}$ in terms of volume flow-rate Q, kinematic viscosity ν and nozzle radius a. The radius of the jump is predicted to be independent of gravity. Using some heuristic dimensional reasoning. the authors also argue that the radius of the jump is independent of fluid density.

Comments:
The radius of the jump being independent of gravity is an erronous conclusion. Experiments conducted by Avedesian & Zhao [2000] showed that lowering gravity pushes the circular hydraulic jump radially outward. Our results too show a delayed and weaker jump with lower gravity. The conclusion that the jump happens where the boundary layer reaches the free-surface has been shown to be incorrect later by Watanabe et al. *[2003]. The scaling with the other parameters too is not in line with Bohr* et al. *[1993]*

30. [**Chippada *et al.*, 1994**]:
This is a numerical simulation of turbulent planar jumps using the Reynolds averaged Navier-Stokes equations and the $k-\epsilon$ model for closure. The downstream boundary height is imposed as obtained from Rayleigh's shock criterion by specifying the inlet Froude number. Hydraulic jumps with inlet $Fr = 2$ and $Fr = 4$ are simulated with undeveloped and fully-developed profiles at the inlet. Jumps with and without downstream undulations are reported.

Comments:
The authors make the remark "the nature of the hydraulic jump is mostly dependent on the upstream conditions and the effect of downstream boundary condition is mostly on the location of the jump". In our simulations too, we find that the downstream boundary conditions affect the location of the jump. When the downstream boundary condition is imposed in the form of an obstacle, it influences the height-profile downstream of the as well as the jump

location. Note however that in our simulations the presence of the obstacle is not necessary for the existence of the jump. For certain inlet Froude numbers, it is reported that no steady state was reached. It is interesting to note that the authors report simulation of jumps without separation in a planar geometry.

31. [**Buyevich *et al.*, 1993; Buyevich & Ustinov, 1994**]:
The analytical study of the circular hydraulic jump is common between the two references and hence they are reviewed here together. The second work contains some additional heat transfer studies which are of engineering significance. This is an analytical study of the circular hydraulic jump using the vertical averaging method. The region with a growing boundary layer and the region of the full viscous flow are modelled using the Karman-Pohlhausen technique assuming a cubic velocity profile. Separate equations are derived for the two regions. These equations govern the evolution of boundary layer and film thickness with radial distance. Their numerical solutions show a singularity at a finite radial distance. Shock fitting technique is used to connect "inner" and "outer" solutions using mass and momentum conservation relations. An approximate viscous solution for the impingement region is proposed. The effect of increase of the radius of the plate/disk on the radius of the circular hydraulic jump is discussed.

Comments:
Although the authors clearly mention in the opening section of the paper that the physical mechanism which causes the appearance of a jump remains unclear, they later seem to incline towards the Tani [1949] point of view, that separation is the cause of the same, as seen from later remarks.

32. [**Middleman, 1995**]:
This is a book on axisymmetric free-surface flows. The circular hydraulic jump is one of the problems considered in Chapter 5. The approach here is more in the spirit of explaining some of the known results in greater detail, especially those of Watson [1964], rather than presenting new results. Some experimental data is reported for comparisons with the theoretical predictions.

Comments:
Chapter 5 of this book gives a good introduction to the problem. Some of the

analysis reported here could be related to the work of Errico [1986] although this reference was inaccessible for us.

33. [**Rao & Arakeri, 1998; Rao, 1994**]:
A experimental and analytical study using integral methods for radial film flows formed by impinging jets on axisymmetric surfaces like flat plates, cones and spheres and on planar surface. The main results are:

    - In the region upstream of the jump, where the boundary layer has not reached the free-surface, expressions for evolution of film and boundary-layer thickness are derived. These assume a cubic velocity profile with constant coefficients.
    - In the region where the boundary-layer is fully developed, assuming a variable coefficient cubic velocity profile, the integral momentum equation is solved as an initial value problem for a given jet Froude to determine the evolution of velocity profile and the film-thickness. The derivative of the height-profile displays a singularity at separation.
    - A downstream edge boundary condition is proposed based on the minimisation of energy. This leads to a critical Froude at the edge which is used as a boundary condition for the flow downstream of the jump. Using this boundary condition, the energy integral equation is solved downstream of the jump as a two-point boundary-value problem. Here the velocity-profile considered has constant coefficients.
    - As in earlier work, the solutions upstream and downstream of the jump do not transition smoothly from one to the other and a discontinuity is fitted to locate the jump. The location of this discontinuity is taken as the location of separation.
    - Momentum balance across the jump generalises the approach of [Rayleigh, 1914] to include the work done by the wall-shear.
    - Experiments are conducted for the circular hydraulic jump. Radius, height-profile and separation-length are reported. Results are presented for the effect of plate radius and edge conditions, nozzle height, volume flow-rate on the jump radius. The jump radius displays a small sensitivity to the plate radius but is found to display negligible sensitivity

to the nozzle height. It also shows a very strong sensitivity to the edge conditions. The length of the separation bubble is reported to increase with increasing volume flow-rate. These waves are found to be affected by both surface-tension and gravity.

- The results obtained from integral methods with an assumed velocity profile agree reasonably well with experimental results upstream of the jump. The match in the downstream region is reported to be poor.
- Experiments are conducted to study the wave structure in the laminar turbulent transition. It is found that downstream of the jump, the ratio of average wavelength (spatial average) to the average depth of the fluid lies in between the shallow and deep water limit. The phase speed of the waves downstream of the jump depend on the wavelength, and hence these waves are dispersive. Upstream of the jump, no waves are seen for flow rates less than 4 litres/min. For higher flow rates, concentric waves are reported upstream which owe their origin to a Rayleigh instability of the jet (see [Cholemari, 1998]). An alternative surface wave route for transition to turbulence (different from $T-S$ waves) is found which involves a breakdown of surface waves. This transtion happens through formation of radial streaks.

Comments:

This is one of the most detailed experimental studies of different aspects of the circular hydraulic jump (similar to the extensive experimental parametric study by Liu & Lienhard [1993]). Since the problem in its laminar steady state offers enough theoretical difficulty, there has not been much focus on studying the stability and transition to turbulence in the circular hydraulic jump. This is also one of the few studies (another and an earlier study being that by Azuma & Hoshino [1984]), where this aspect of the problem has been looked at. Wave evolution on a radial flowing film has also been studied earlier by Varella [1992].

34. [**Lemos, 1996**]: This work is not directly related to the circular hydraulic jump but is reviewed here because it uses the Volume-Of-Fluid (VOF) method to simulate travelling hydraulic jumps/bores using the 2D Navier-Stokes equations. The volume-of-fluid method provides an accurate technique for

modelling interfacial flows. Three interfacial flows are simulated for evaluating the abilities of four different computational schemes viz. the evolution of a solitary wave, the formation of an undular bore and the development of a travelling jump which displays wave-breaking at the propagating front. The work then focusses on numerical issues and we do not discuss them here.

Comments:
All Navier-Stokes simulations reported in this thesis use the Volume-Of-Fluid method for simulating hydraulic jumps. In Chapter 7, we provide a detailed description of the technique.

35. [**Higuera, 1994, 1997**]:
A numerical solution of the boundary-layer shallow-water equations (BLSWE). The first reference discusses this in a planar geometry while the second reference extends the analysis to a circular geometry. The main results are:

- As we discuss in Chapter 2, it was perhaps first recognised in this work that the height-profile upstream of the jump, is not affected by gravity. Watson [1964] had provided the zero-gravity similarity solution earlier ($Fr \to \infty$) but it was recognised here for the first time that this similarity-solution is indeed manifested in the solution upstream of the jump.
- The ellipticity of the BLSWE (despite the boundary-layer assumption) was pointed out. It was therefore argued that the prescription of a downstream boundary condition is essential, and determines the dynamics. The numerical solution to the planar BLSWE shows the presence of jumps with and without separation at the wall. An asymptotic analysis is carried out for a high Froude number to describe the inner structure of the jump. The near jump flow structure is split up into five parts and each part is analysed separately.
- A similar asymptotic analysis is carried out for strong jumps in a circular geometry in the limit of large upstream Froude number and large Reynolds number. The numerical solution to the BLSWE in a circular geometry is compared to the analysis and good match is reported. Some comparisons with experiments are also reported.

Comments:

This study builds upon the analysis of Bowles & Smith [1992] (who studied the flow structure at the leading edge of the jump labelled here as the interaction region) and extends the analysis to the region downstream. This was an early attempt at solving the BLSWE using a procedure different from the usual vertical averaging procedure. We will discuss this work and compare our results with the the ones obtained here in Chapter 2. This is also the only reference we know of where the author has reported a Type-II jump (without separation at the wall) in a planar geometry. The author also presents a boundary condition at the edge of the plate where the boundary-layer approximation breaks down and the flow becomes critical. The critical boundary condition has also been used in other studies like Bohr et al. *[1993] etc. We show in Chapter 2 that the BLSWE may be solved locally, and the solution does not depend on the downstream boundary condition. This is one of the very few studies where the flow-structure of the jump is analysed. More near-jump studies through analytical and numerical methods are necessary to resolve the dominant physics in the near-jump region. We make such an attempt in Chapter 3 using the method of vertical averaging for the complete Navier-Stokes equations.*

36. [**Blackford, 1996**]:
This work continues from [Godwin, 1993]. Using a control-volume approach and a drag coefficient, an evolution equation for the film thickness is derived. However, this evolution equation does not have a jump-like solution. Instead a jump-like profile is obtained by artificially increasing the drag coefficient once the boundary-layer reaches the free-surface.

Comments:

In all these models where it is hypothesized that the jump occurs where the boundary-layer reaches the free-surface, no physical reasoning is provided.

37. [**Murtuza, 1996**]:
This is an analytical and experimental study of evolution of waves on radial flows. It builds upon the earlier work by Azuma & Hoshino [1984] and Rao [1994]. The main results are:

- Vertically averaged mass and momentum equations are derived (including surface-tension) with the assumption that the local film-thickness

does not vary significantly due to the radial geometry and thus can be assumed constant. This makes the analysis local. These equations are perturbed about the local state, linearized for the disturbances and a dispersion relation is derived assuming normal modes. This relation predicts amplification for waves of certain wavelength, which for the range of experimental parameters reported here, is of the order of 1 m. The dispersion relation predicts the phase speed for infinitely long waves to be twice the surface-velocity of the film.

- An inviscid nonlinear analysis is carried out to look for waves of permanent form in a radial geometry. Solitary (inverted hump) and cnoidal solutions are reported. Here too, the analysis is local and the effect of radial geometry is not considered.
- An unsteady equation for the evolution of film-thickness is derived from the vertically averaged mass and momentum equations.
- The flow is perturbed using a drop-weight mechanism which generates pressure impulses to the jet and thus generate waves in the radial thin film. Experiments are conducted to meaure wave-speeds and wave-profile. Measurements are reported on the ratio of wave-speed to the surface velocity predicted by Watson [1964] and some agreement is obtained. It is found that the phase speed of the observed waves are $3-4$ the mean flow speed at the surface. The solitary-wave solution predicted theoretically was not observed in experiments. The wavelength of waves observed in experiments lie in a range which make them capillary rather than gravity waves.
- Flow visualisation shows that two waves are formed for every impulse to the jet. The reason for this is not understood. The waves becomes non-axisymmetric as they travel outwards and this transverse breakdown is believed to lead to turbulence. This transition may happen upstream or downstream of the jump depending on the flow-rate.

Comments:

Prior work on the evolution of linear/nonlinear waves on a radial film flow include that of Azuma & Hoshino [1984]; Rao [1994]; Varella [1992]. The possibility of solitary waves in a radial thin-flim flow or the appearance of

a cnoidal wave-train downstream of a circular jump are interesting problems which need further study. We present and discuss a new radial KdV-like equation in Chapter 4.

38. [**Avedesian, 1996; Avedesian & Zhao, 2000**]:
Experiments on the circular hydraulic jump at low gravity conducted using a drop-tower. The main results are:-

    - Reducing gravity pushes the jump dowsntream.
    - Jumps become gentler at low gravity.
    - The fluid depth at the exit of the plate is called the outer-height and this is varied during experiments. There seems to be no effect of changing the outer height on the radius of the jump, at low gravity. A heuristic explanation is provided for this using a balance between viscosity and inertia.
    - Some measurements of the radius of the jump are reported at low and normal gravity, and comparisons are made with the predictions of [Watson, 1964]. For normal gravity, the experimental results agree more with Waton's predictions of a developing boundary-layer. For low gravity, the agreement is closer to the predictions of a developed boundary-layer.

    Comments:
    In our Navier-Stokes simulations reported in Chapter 4, we too find that decreasing gravity makes the jumps gentler and pushes them downstream. The scaling relation of Bohr et al. *[1993] predicts the jump radius to become arbitrarily large at zero gravity. This prediction is consistent with the experimentally observed trend in the current work. Also see Phillips [2008] for a related study.*

39. [**Bohr *et al.*, 1996; Ellegaard *et al.*, 1996**]:
The main results are

    - This study experimentally categorises circular jumps as Type I and Type II (see figure (1.6) and (1.7). By changing the outer depth of the fluid a transition and a breakage of circular symmetry was observed using a viscous fluid like ethylene glycol. Type I jumps correspond to having a

separated eddy underneath the jump. Type II jumps correspond to having an additional surface eddy as well. The transition to Type II jump from Type I is thought to be akin to wave-breaking. This transition is reported to be reversible and free from hysteresis.

- A simulation of axisymmetric Navier-Stokes equations is also attempted although the free-surface was not computed, but instead determined from experiments and held fixed. The authors report simulations of both Type I and Type II jumps in this way. The boundary conditions used are that of a stress-free interface.
- Some surface velocity measurements are also reported experimentally for Type-I jumps. Before the jumps the surface-velocity is found to decrease linearly with radial distance.

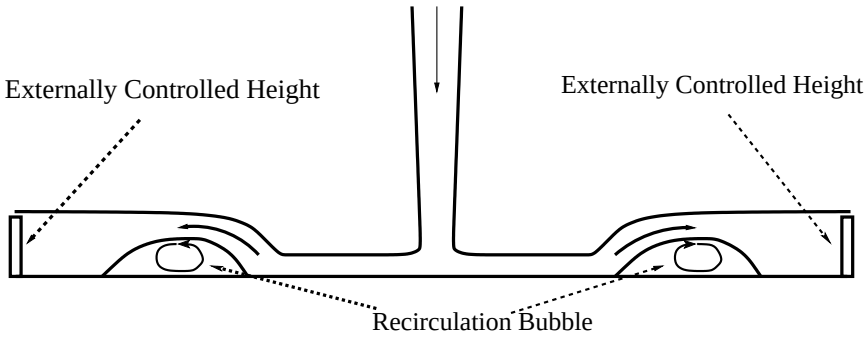

Figure 1.6: A cartoon of a Type-I jump

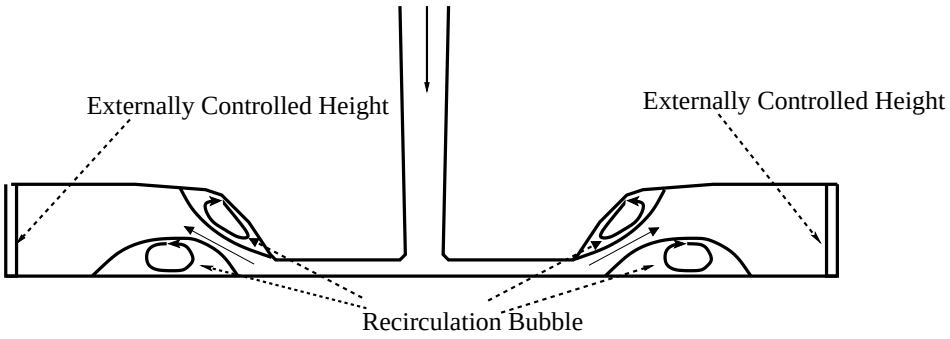

Figure 1.7: A cartoon of a Type-II jump

Comments:

The authors include a simplified discussion of the Goldstein singularity at

separation. Type-I and Type-II jumps are both associated with separation (see figure 1.6 and 1.7). We will see in Chapter 4 that circular jumps without separation are also possible, which we label as Type-0.

40. **[Bloom, 1997]**:
The author studies the circular hydraulic jump theoretically and experimentally.

    - The theoretical study solves the ordinary differential equations (for evolution of film-thickness) derived earlier by Bohr *et al.* [1993] and Blackford [1996] and discusses the solutions in some detail. Some heuristic mathematical reasoning for flow separation that occurs underneath the jump is provided. A simplified stability analysis is also attempted to understand the loss of azimuthal symmetry of the jump when the flow rate is increased. The author also discusses the model of [Watanabe *et al.*, 2003].
    - In the experimental part, comparisons are made between experimentally obtained results and the radius predictions of Godwin [1993] and Bohr *et al.* [1993]. The author concludes that the radius predictions of Bohr *et al.* [1993] agree better with the experiments than those of Godwin [1993], although neither fit appears to be too good. Some film-thickness measurements are also reported.

    Comments:
    This is a part of an undergraduate study. The work has not been published and is freely available online. In the experimental part of the work, the author reports having unsuccessfully attempted Navier-Stokes simulations of the jump but the reasons for failure are not discussed. Attempts made to measure velocity profiles were not successful and the author discusses the details of the problems associated with the experiments.

41. **[Hansen *et al.*, 1997]**:
An experimental and theoretical study.

    - Experiments are conducted to validate the scaling relationship of Bohr *et al.* [1993]. It is reported that the exponent of volume flow-rate in the

scaling relationship for the radius varies from 0.77 to 0.72 with varying viscosities of the working fluid. The authors observe an effect of the nozzle radius on the jump location but report it as being small. We will discuss this is greater detail in Chapter 5.

- The laminar standing hydraulic jump becomes unstable and starts oscillating as the flow rate increases. At high flow rates, the oscillating jump acts as a source of waves. The power spectrum of the height fluctuations due to surface-waves is measured experimentally. The spectrum shows an interference pattern when a reflector is inserted downstream of the jump. The amplitude of interference oscillations decreases with increasing frequency caused mainly due to viscosity. The hydraulic jump is modelled as a spatially uncorrelated broadband source and this helps in interpreting the interference pattern observed.
- A dispersion relation is derived for damped capillary-gravity waves.

Comments:

Some results reported in this work are discussed later in Chapter 5 in terms of the effect of momentum-flux on the radius of the circular jump. These authors too observed such an effect but did not quantify it. The appendix of this reference contains a derivation of the dispersion relation for linearised viscous capillary-gravity waves. A similar relation albeit for linearised gravity waves is also derived in Johnson [1997]. These viscous dispersion relations can be useful to formulate the definition of Froude number for a viscous flow, where the distinction between supercritical and subcritical flow (from a wave propagation perspective) is not apriori clear (also see Watanabe et al. *[2003] for a discussion on this.).*

42. [**Bohr *et al.*, 1998**]:
A combined theoretical and experimental study. Height profile measurements are made using the contact method. The main results are:

- If the mass and momentum equations (boundary-layer shallow-water equations) were to be non-dimensionalised using vertical and horizontal scales such that the equations become independent of Q, ν and g, then the horizontal length scale would be $Q^{\frac{5}{8}}\nu^{\frac{-3}{8}}g^{\frac{-1}{8}}$. It is argued that this

is the scale for the radius of the hydraulic jump.

- In the earlier works [Bohr *et al.*, 1993; Ellegaard *et al.*, 1996] the inability to integrate the boundary-layer equations (assuming a hydrostatic pressure gradient) through the point of separation was a major impediment to obtaining jump-like profiles. Here, an averaging model is suggested which can be taken through the point of separation without encountering Goldstein-type singularities. This model is discussed in detail in later references [Bohr *et al.*, 1997; Watanabe *et al.*, 2003].

Comments:

The transition from Type-I to Type-II jumps happens through a wave-breaking mechanism discussed in this reference. Wave-breaking even otherwise was also observed in some of our low Reynolds number simulations of planar jumps, although we have not observed formation of Type-II kind of jumps in a planar geometry (see the last section in Higuera [1994] where a Type-II like jump is reported in a planar geometry). In our case, the wave breaking gives rise to an unsteady flow which is periodic in some cases.

43. [**Ellegaard *et al.*, 1998, 1999**]:
The experimental discovery of polygonal hydraulic jumps. The authors report that for a highly viscous fluid the circular hydraulic jump breaks its circular symmetry and deforms into stable polygons when the externally controlled height at the edge of the plate is increased. The main findings are:

    - A phase diagram is obtained for the number of sides of stable polygons plotted for external height versus nozzle height and volume flow-rate. Polygons upto 10 sides are reported in the phase diagrams. The observation of multiple stable polygons for the same values of flow parameters is reported.
    - A heuristic model is proposed for the polygons although details of the model are not discussed here (see [Hansen *et al.*, 2002]). The roller is statically balanced horizontally by the difference between the hydrostatic pressure forces from the two sides and shear from the main flow. Assuming a simple line-tension model for the circumference, and treating the problem as one of minimisation of circumference, some of the

features observed in experiments are reproduced by the model E.g., the azimuthal variation of width of the roller is inversely proportional to the azimuthal variation of mass flux through the roller. For more details of the model see [Hansen *et al.*, 2002].

Comments:

The discovery of symmetry-breaking in circular hydraulic jumps has infused new interest into this century old problem. Despite many papers being published since this work, a satisfactory theory which explains every aspect of polygon formation has not been obtained so far. One of the probable reasons for this could be the lack of simple mathematical models for Type-II jumps from which polygonal jumps are known to arise. It is now known that the symmetry-breaking is related to surface-tension [Bush et al.*, 2006]. The study cited above [Hansen* et al.*, 2002], where the line-tension model is discussed, is written in Danish and hence we were unable to understand the details of the model.*

44. **[Putkaradaze, 1997]** :
This is a PhD work and the first two chapters are relevant for circular hydraulic jumps. These are described below:

- the first chapter gives an introduction to boundary-layer theory and discusses the Goldstein singularity at separation. A brief description of the solution of the boundary layer equations which do not become become singular at the point of separation (marginal separation) is provided. A brief description of the Karman-Polhausen integral method is given.
- The author provides a brief description of the experiments including polygon formation. The Tani-Kurihara equations and their solution alongwith the scaling of Bohr *et al.* [1993] is also reviewed. The remaining part of this Chapter contains an expanded version of the methods and the results contained in Watanabe *et al.* [2003].

Comments:

The results and analysis contained in Watanabe et al. *[2003] is explained in greater detail in this thesis. The author also makes an attempt at developing a model for the Type-II jump.*

45. [**Dingwei *et al.*, 1998**]:
This work is a numerical analysis and builds upon the study of Stevens & Webb [1992]. The authors report that they solve the axisymmetric Navier-Stokes equations (see comments below). The main results reported are:

- The jump radius is found to be an increasing function of the impingement height. It is also reported that that a change of nozzle radius has no effect on the radius of the jump.
- A scaling relation is obtained numerically for the jump radius (r_j) and its dependence on the Reynolds number (Re_z) defined using the jet velocity and the nozzle height. This dependence is given as $r_j \sim 1.5103 Re_z^{0.0037}$.
- Some comparisons between the results of [Buyevich & Ustinov, 1994; Watson, 1964] and the present computations are reported.

Comments:
The computational technique used for the simulations is not explained in great detail. The authors report some effect of the nozzle height on the jump radius wihch is presumably a momentum flux effect. However, no attempt is made to explain this dependence. We explore this in more detail in Chapter 5 where we study the effect of momentum flux on the circular hydraulic jump.

46. [**Cholemari, 1998; Cholemari & Arakeri, 2005**]:
These works build upon the earlier studies by Murtuza [1996]; Rao & Arakeri [1998, 2001]; Rao [1994]. Some of them are not direct studies of the circular hydraulic jump but are relevant for studying the stability and transition to turbulence occuring in the context of hydraulic jumps. The authors perform a local stability analysis by neglecting the effects of the radial curvature and assuming the flow to be locally planar. Theoretical and numerical results obtained are compared with experiments and a good match is reported. The main results are:

- The boundary-layer shallow-water equations are vertically integrated and a single unsteady partial differential equation is derived relating the mean velocity to the film-thickness. This equation is supplemented by simplified boundary-conditions which include surface-tension. The mean velocity and the film-thickness are assumed to be slowly varying in the

streamwise direction and a temporal stability analysis is performed using normal modes.

- The slowly-varying mean flow is taken to be the gravity-free solution of [Watson, 1964].
- It is found that the phase speed of normal modes is strongly affected by surface-tension. Radial geometry, gravity and viscosity are found to have very little effect.
- The waves are mostly unstable and the radial geometry is found to have a dominant effect on this instability. Surface-tension and gravity have mild stabilizing effects and viscosity is mildly destabilizing.
- Experiments are conducted for measuring wave speed and amplitude. The waves are formed from perturbations introduced on the jet. Measurment are made for a single isolated and for periodic perturbations. The former shows good agreement while the latter shows moderate agreement with the theoretical predictions.

Comments:

There are not many detailed studies in literature on the stability of the radial film-flow in the jump. The strong variation of the mean-flow in the streamwise direction indicates that non-parallel effects are very important and need to be considered. Due to the lack of extensive Navier-Stokes simulations in the literature, the mean flow is not known well-enough. In Chapter 2, we hypothesize that the instability of the separated profile at the jump is a key reason for the reattachment of the flow downstream. A verification of this conjecture requires a global stability analysis.

47. [**Naraghi *et al.*, 1999**]:
This is mainly an experimental study with a brief theoretical part. The effect of variation of nozzle diameter and nozzle impingement height on the radius at impingement and the jump radius is studied. Some of the main results are:

- The ratio of the radius of the jet at impingement to the nozzle diameter approaches a constant value for large enough values of the ratio of nozzle

height to nozzle diameter. The value of this constant depends on the jet Reynolds number.

- The nozzle height has an effect on the jump radius and so does the nozzle diameter. Increasing the nozzle height increases the jump radius.
- The analytical model follows the standard vertical averaging approach of the BLSWE to derive equations for evolution of film thickness. These use cubic velocity profiles with constant coefficients and predict a singularity at a finite distance in the height profile.

Comments:

This study is very relevant to the results presented in Chapter 5. However the authors do not provide any physical motivation for the observed dependence of the radius of the circular hydraulic jump on the nozzle height and diameter. This effect can be explained using the idea of momentum-flux as we do in Chapter 5.

48. [**Sreenivas *et al.*, 1999**]:
This is not a study of the circular hydraulic jump but of a phenomenon which occurs in the presence of one. A new observation is reported where liquid drops can be levitated on the top of circular jumps. The effect of the air-boundary layer is crucial here. The main results are:

    - Large drops of liquid can be supported on the air film created above a hydraulic jump within the jump radius. These drops are locally stable and their weight is supported by the bearing pressure created in the thin air boundary-layer.
    - The drop is itself in a state of internal motion due to the shear-stresses exerted by the air-film. The surface velocity of the drop can be estimated by balancing the dissipation inside the drop to the rate of external work done on the drop. The estimate compares favourably with experiments
    - The shape of the drop is determined by an interplay of large number of factors like inertia, gravity, surface-tension and viscosity. Drops of alcohol could not be levitated due to their high solubility and high rates of evaporation.
    - It is proposed that only a thin film can suppport drops.

Comments:

This the only study in the circular hydraulic jump literature that pays attention to the air boundary layer above the jump. The effect of this air boundary layer on the structure and mechanics of jump formation is an unexplored area as yet.

49. [**Brechet & Neda, 1999**]:
An experimental and theoretical study. The experiment predicts the exponents for the power law governing the radius of the circular hydraulic jump as $Q^{0.703}\nu^{-0.295}$. Other results are:

- A scaling relationship for the radius of the jump is proposed using both viscous and inviscid analysis.
- For inviscid jumps, imposing a discontinuity and balancing momentum across the discontinuity, the radius of the circular hydraulic jump is predicted to go as $4Q^2\sqrt{\frac{\pi^2 gd}{8Q^2}+\frac{1}{A^4}}/\left(\pi^2 gH^2\right)$. Here Q is the volume flow-rate, ν is the kinematic viscosity, g is the acceleration due to gravity, A is the nozzle-diameter, H is the outer-depth after the jump, d is the nozzle-height.
- For viscous jumps, the radius of the jump is predicted to scale as $Q^{\frac{2}{3}}d^{\frac{-1}{6}}\nu^{\frac{-1}{3}}g^{-1/6}$. This scaling relationship is obtained by imposing the constraint that the boundary layer reaches the free-surface at the location of the circular hydraulic jump. Some comparisons with experiments and the scaling relationship of Bohr *et al.* [1993] are also reported. Nozzle height is reported to have a negligible effect on the jump radius.
- The authors propose a heuristic model which treats the jump as an instability of the flow.

Comments:

Note that the exponent of Q is not very different from the value $5/8$ *predicted by Bohr* et al. *[1993]. Both Godwin [1993] and this work make the same assumptions that the jump occurs where the boundary layer reaches the free surface and yet they obtain a different scaling relation for the radius of the jump. The difference between this work and that of Godwin [1993] is that the* $Fr = 1$ *criterion is used by the presents author but not by Godwin [1993].*

Thus, gravity does not enter the scaling relationship of Godwin [1993]. Additionally, Godwin [1993] takes the film thickness $h \sim 1/r$ whereas the present author takes it to be $h \sim r^2$. As seen in the later dimensional analysis by Ray & Bhattacharya [2007], neither of these assumptions are necessary if one uses the global mass conservation constraint $rU_{av}h = \text{constant}$. Note that any scaling relationship for the jump needs two more constraints other than the global mass in order to eliminate U_{av} and h from the relation.

50. [**Moncada *et al.*, 1999**]:
This is an analytical and experimental study. The authors define an imperfect jump and ascribe this nomenclature to the region of recirculation that is formed at the free-surface. In this particular kind of jump that the authors study, the jet is submerged under the fluid due to the presence of a weir at the outer edge of the plate, which causes a reverse flow to be generated. The experiment is characterised by various external parameters and the authors derive a relationship between these by applying inviscid, shallow-water conditions and mass and momentum conservation for a annulus-shaped control volume. Experiments are conducted to check the validity of these relations and good agreement is reported. Using the same control volume, a relation is also derived for the energy loss across the jump. Again a moderately good match is obtained with experiments.

Comments:
This is a study from a civil engineering perspective to the problem similar to earlier works like Khalifa & McCorquodale [1992]. Being of engineering interest, the range of parameters studied here mostly correspond to turbulent circular jumps.

51. [**Yokoi & Xiao, 1999**]:
One of the very few Navier-Stokes simulations of the circular hydraulic jump available in literature. The main results are:

- Capturing the transition from Type I to Type II jumps and the importance of non-hydrostatic pressure and the role of surface-tension in this transition. A heuristic physical reasoning is provided explaining the role of surface-tension and the observed pressure rise behind the jump, in causing the transition from Type-I to Type-II jumps.

- Partial validation of the Bohr scaling relationship [Bohr *et al.*, 1993] $Q^{\frac{5}{8}}\nu^{\frac{-3}{8}}g^{\frac{-1}{8}}$ for the radius of the jump. Power-law fits obtained from simulation data are presented only for the exponents of Q and ν, but not for g. The exponent of Q and ν are reported to be close to 5/8 and $-3/8$ respectively.
- Numerical evidence that the radius of the jump is independent of the density of the working fluid.

Comments:

An earlier attempt made in Bohr et al. *[1996] simulated Type-II jumps, although the simulations did not allow for the coupling between the interface and velocity-field,as the former was held fixed. This was the first axisymmetric Navier-Stokes simulation of Type-II jumps and the transition from Type-I to Type-II. The present simulation solves for both gas and liquid phases and surface-tension is implemented using the standard Continuum Surface Force model. The outer depth is controlled in these simulations. The importance of surface-tension effects for Type-II jumps was later reinforced by the discovery that surface-tension plays a crucial role in the formation of polygonal jumps which are found to arise only from Type-II jumps [Bush* et al.*, 2006].*

52. [**Yokoi & Xiao, 2000*a***]:
Axisymmetric Navier-Stokes simulations of the jump without the jet. Type I and Type II jumps were simulated and the transition between the two investigated. Dynamic pressure is proposed to be significant for the transition.

Comments:

The role of dynamic-pressure is usually not adequately highlighted in the standing hydraulic jump literaure (see [Bowles & Smith, 1992; Higuera, 1994]). Dynamic pressure is associated with streamline curvature and hence it is important even for Type-I jumps. We discuss this effect in detail in Chapter 2 and 3.

53. [**Yokoi & Xiao, 2000*b***]:
This is a numerical study performed using axisymmetric Navier-Stokes computations. The effect of dynamic pressure on the surface roller formation in case of a Type-II jump is studied. It is found that there are two regions

of high dynamic pressure straddling the surface-roller. The second region of high dynamic pressure is reported to be due to surface-tension. For a Type I jump, there is only one region of high dynamic pressure. The reverse transition from a Type-II to a Type-I jump is simulated and it is found that the secondary region of high-pressure gets progressively weaker in time as the jump moves towards its Type-I state.

Comments:
This is the first simulation of Type-II jumps using axisymmetric Navier-Stokes equations. No systematic mathematical models for Type-II jumps using simplified equations exist in the literature.

54. [**Hansen, 2001**]:
The first part of this thesis concerns sand ripples and is not directly relevant to the present discussion. The second part of this thesis studies polygonal hydraulic jumps experimentally and models the geometry of the observed polygons. A phase diagram obtained from experimental data is presented, which depicts the various stable non-axisymmetric shapes that jumps can deform into, for a given nozzle height and an externally imposed height at the edge of the plate. For the same value of these parameters multiple stable polygonal shapes are observed ranging from two-gons to a pentagon, thus showing time history-dependant behaviour. The geometry of the polygons is studied in detail and it is observed that the circumference and area of the polygons is independent of the number of corners of the polygons. Similarly shapes of the corners of the polygons is also reported to be independent of the number of corners. A nondimensional number P is defined and called the geometry number. It is found that P depends only on the externally imposed height but not on the nozzle height. A simple model is proposed which generates polygons by accepting as input the number of sides, the area and the circumference of the polygon. This model approximates the side of the polygons using a second order polynomial. The model shows good agreement with the experimentally observed structures. This model also sucessfully reproduces the experimentally observed feature that the shape of the corner of the polygon is independent of the number of sides.

Comments:

This was one of the early studies of polygonal jumps. This is a phenomological study of the polygons and attempts to model their geometrical features. Some important findings are the universal features of these polygons.

55. [**Chang *et al.*, 2001**]:
This is a theoretical and experimental study. The main results are:

- This study discusses experiments on jumps where the outer height is not controlled.
- Hydraulic jumps without separation are reported experimentally although the method used for detection of separation doesn't seems sophisticated enough to decide conclusively whether separation is indeed absent.
- Two different mechanisms of formation of jump are proposed - For jumps with separation, it is concluded that separation is the *cause* of the jump. For jumps without separation, it is concluded that capillary back-pressure is responsible for jump formation.
- A scaling relationship for the radius of the jump is proposed as $r_j' \sim Re^{1/3}\Lambda^{-1/8}$ where $Re \equiv Q/(a\nu)$ is the Reynolds number, $\Lambda \equiv (ga^3/\nu^2)Re^{-7/3}$ is referred to as the "modified Froude number" and $r_j' \equiv r_j/(aRe^{1/3})$ is the nondimensional radius of the jump.
- The axisymmetric BLSWE are numerically solved and the height profile is compared to the estimates of Azuma & Hoshino [1984] and good match is reported. The calculated wall-shear stress is compared with the measurements of Nakoryakov *et al.* [1978]. Note that the numerical solution does not provide a jump-like transition.
- An analysis is presented for estimating the jump radius. This is done by perturbing the flow about the self-similar solution of Watson [1964]. The jump radius in this case is estimated from the radius of separation and comparisons of this estimate with the jump radius with experiments show some deviations.

Comments:

This is one of the few studies which discusses the possibility of circular jumps

without separation at a radius where the boundary-layer has not yet reached the free-surface. However, the jumps reported without separation were described to be triggered by a capillary back-pressure mechanism. In our axisymmetric Navier-Stokes simulations discussed in Chapter 4, we show conclusive evidence that such jumps indeed exist. However the mechanism of formation of these jumps obtained by us does not depend on the presence of surface-tension.

56. [**Rao & Arakeri, 2001**]:
This is an experimental investigation of the wave structure in a radial film flow. This study is also relevant for transition to turbulence. Some of the observations are:

- The scaling relationship for the jump radius proposed by Bohr *et al.* [1993] shows good agreement for glass plates of various diameters, but plate edge conditions can cause deviations for Perspex and Aluminium plates with edges chamfered etc. The length of the separated bubble underneath the jump is reported to increase with increasing volume-flow rate.
- Photographs are used to study the evolution of waves upstream and downstream of the jump. At low flates (less than 4 litres per minute of filtered water) no waves are visible. At higher flow rates, transition to turbulence can occur upstream or downstream of the jump.
- For low flow rates, waves are not observed only downstream of the jump. The average wavelength of these waves decreases with increasing flow-rate. These waves are reported to be capillary-gravity waves and their origin is not clear.
- For flow-rates greater than 4 litres per minute, waves were observed upstream of the jump as well. It is proposed that the origin of these waves lie in the Rayleigh instability of the impinging jet.
- An alternative route to turbulence in thin film flows is proposed. This transition occurs due to breakdown of surface waves and is distinct and different from the transition due to T-S waves reported earlier by Azuma & Hoshino [1984]. The transition starts at some radius in the form of

radial streaks. Data is presented for variation of the radius of appearance of these streaks with flow-rate.

Comments:

Some of the experimental results presented here were also discussed earlier in Rao [1994]. Although the main focus of the study is on transtion to turbulence, there are many useful experimental results reported here e.g. measurements of the length of the separation bubble. The bubble shrinks in length as one raises the outer boundary (see Craik et al. *[1981]) and this was studied by Bowles & Smith [1992].*

57. [**Yokoi & Xiao, 2002**]:

This continues upon the preliminary results reported in [Yokoi & Xiao, 2000*b*]. Using axisymetric Navier-Stokes computations, the transition from Type I and Type II jumps was simulated. An attempt is made to provide a rough physical mechanism of appearance of two regions of high dynamic pressure near the free-surface for a Type-II jump. Surface-tension is thought to be a crucial ingredient for the rise of this secondary region of dynamic pressure.

Comments:

A 3D simulation of the circular hydraulic jump was also reported in Ferreira et al. *[2002] but those simulations did not contain surface-tension. It is interesting to see that it is possible to simulate Type-II jumps without surface-tension.*

58. [**Pelzer, 2002**]:

This is an experimental investigation. A jet impinges on a plate with a hole drilled in the center and the effect of the diameter of the hole on the jump radius is experimentally obtained. The height after the jump is reported to be independent of the diameter of the hole. A linear relationship between jump radius and flow rate is obtained.

Comments:

The author tries to argue/show in this work that the radius of the circular hydraulic jump is independent of the radius of the impinging jet. In Chapter 5 of this thesis, we will present experimental evidence to the contrary and provide physical arguments for the same. It is very interesting to note that

these experiments and the ones reported in [Silverstein, 2002] were carried out by two high-school students.

59. [**Silverstein, 2002**]:
An experimental work on hydraulic jumps formed from vertical jets impinging on inclined surfaces. Elliptic jumps were observed, but it is not completely clear as to whether the ellipse is complete, i.e., whether a well-defined jump exists in the region downstream. The angle of inclination is reported to linearly affect the major radius while the minor radius is relatively unaffected. Flow rates are reported not to affect the ratio of the two radii.

Comments:
Due to the presence of gravity, the effect of impingement of a vertical jet on an inclined surface is different from that of an inclined jet on a horizontal surface. The qualitative nature of the flow is dependent not only on the relative angle between the jet and plate but also the inclincation of the jet with respect to the gravity vector.

60. [**Ferreira *et al.*, 2002**]:
The first three-dimensional Navier-Stokes simulation of the circular hydraulic jump known to us. The simulations include the impinging jet and hence are the closest possible to the real problem. The simulations were carried out using a code named GENSMAC which is based on the marker-in-cell method. A comparison between the analytical solution by Watson [1964] and the Navier-Stokes solutions are made. The aim of this work was to benchmark the capabilities of the code by simulating Type I and Type II jumps. There are a lot of computational details in this study which focus on numerical algorithms and we do not discuss them here. There is no surface-tension in these simulations.

Comments:
Navier-Stokes simulations of laminar jumps in both circular and planar geometry are very sparse in literature. Bulk of the results available in literature are either experimental or obtained from modelling. From our own Navier-Stokes simulations, it becomes clear that there are two preliminary difficulties associated with such simulations viz. an accurate representation of the interface, especially near the jump, and the imposition of downstream boundary

conditions. Certain phenomena like Type-II jumps and polygon formation completely rely on the ability to model the outflow conditions accurately and we have found that a poor knowledge of these boundary conditions can be a major stumbling block in these simulations. It is perhaps not surprising that to date no study has successfully managed to simulate the formation of polygonal jumps using Navier-Stokes simulations. Also note this work reports simulations of Type-II jumps without any surface-tension.

61. [**Pacheco, 1999, 2003**]:
This is a numerical work where a new technique is proposed to solve the radial shallow-water equations alongwith an assumed wall shear stress. Three test problems are attempted, the last one being relevant for the current discussion. When the downstream height is imposed, a jump is obtained in the simulations. The numerical results obtained are compared with the experimental results of Ahmad [1967] and a good match is reported in the supercritical region while a moderate match is obtained in the subcritical region.The difference in the subcritical region is attributed to turbulence present in the subcritical region in experiments.

Comments:
The numerical technique developed in this work utilises the hyperbolicity of the shallow-water system with an assumed wall-shear, that is studied here. Thus, the direction of information propagation in the flow determines the boundary-conditions that are needed for different domains of the flow.

62. [**Bush & Aristoff, 2003**]:
An experimental and theoretical study of the effect of surface-tension on the Type-I circular hydraulic jump. The main results are:

- The effect of surface-tension force due to an azimuthal force is accounted for and used to improve the estimate of jump radius of [Watson, 1964].
- The new expression for the jump radius is seen to be in better agreement with experiments reported.
- The correction due to surface-tension is found to be overall not large but most siginificant for jumps of small radii.

Comments:

The effect of surface-tension on the circular hydraulic jump has been a subject of numerous studies. In chapter 6 we present a gravity free hydraulic jump from shallow-water theory. We also discuss this in Chapter 4 of this thesis where we present results from numerical simulations of axisymmetric Navier-Stokes equations. As expected, it is found that the "shape" of a circular hydraulic jump can strongly depend on surface-tension.

63. [**Mikielewicz, 2003**]:
This is a theoretical work and the author establishes an analogy between the averaged equations governing the evolution of an inclined jet impinging on a plate (the jet being normal to the plate) and those governing two phase downward flow in a vertical pipe. These equations have a critical point and the author describes the analogy through this.

Comments:

In Chapter 2, we present an analytical solution of the vertically averaged BLSWE in the neighbourhood of the critical point.

64. [**Ozar *et al.*, 2003**]:
An experimental study of thin film flows formed due to impinging jets on a rotating disk. This study is not directly connected to circular hydraulic jumps and we only discuss the results pertaining to the circular jump. For impingement on a stationary disk with a circular hydraulic jump present, the film thickness after the jump is reported to be an order of magnitude larger than that before the jump. The effect of rotation of the disk is to wash away the jump from the disk. Film thickness measurements are made using a laser light reflection technique and three regions are identified on the film formed on a rotating disk - a) An inertia dominated region b) A rotation dominated region where cetrifugal forces are important and c) a transition region where both effects are important.

Comments:

The effect of Coriolis force on the circular hydraulic jump needs to be studied carefully. It is not clear apriori how would the jump and its structure get affected when the time scale of rotation becomes of the same order as the convective time-scale. This is an interesting open problem for both experimental,

theoretical and numerical study. The physical relavance of this problem is in industrial situations where impingement cooling of rotating disks can be necessary.

65. [**Bohr *et al.*, 1997; Watanabe *et al.*, 2003**]:
This is a theoretical study which focusses on two problems viz. (a) The circular jump and (b) flow down an inclined plane. We discuss only the former and the main results are as follows:

- The authors use a vertical averaging approach in which they use the BLSWE alonwgwith a cubic profile having variable coefficients. The resultant system reduces to two coupled ordinary differential equations for the evolution of the film-thickness and the coefficients of the velocity-profile with streamwise distance. This system is solved as a two point boundary-value problem and jump-like transitions are obtained.
- An asymptotic analysis of the model is presented and analytical results are derived for the height-profile upstream and downstream of the jump. The solution downstream has a singularity which seem to be a generic feature of all shallow-water models. In the near jump region, using this model, a generalization of Rayleigh's shock relation is obtained.

Comments:

This work represents a significant progress amidst a large body of literature that use the vertical averaging technique for obtaining a height profile for hydraulic jumps. Until this study, all related works, where the vertical averaging method was used, failed to obtain realisitic solutions of the height-profile near the jump, obtaining instead of a jump a spiral or similar behaviour with a singularity in the derivative of height. This was the first study where the authors were able to obtain a jump including separation, without encountering singularities. This model however does not capture Type-II jumps. The cubic profile assumed by this model may provide a good aproximation to observations, but the BLSWE does not support a cubic term in the velocity profile, as we show in Chapter 2. The technique of using variable coefficients velocity-profiles was used earlier by Arakeri & Rao [1996] but no jump-like transition was obtained.

66. [**Aristoff *et al.*, 2004**]:
This is the experimental discovery that the symmetry breaking of hydraulic jumps can lead to not only polygonal shapes but also a new class of asymmetric shapes like cat's eyes, three- and four- clovers, sunflowers in viscous jumps etc. It was also experimentally demonstrated that surface-tension plays a crucial role in the symmetry breaking. Addition of a drop of surfactant led to resoration of the circular shape of the jump.

Comments:
It should be noted that such symmetry breaking has been observed in only viscous fluids like glycerol-water solution etc. Hydraulic jumps obtained using low viscosity fluids like water do not display any symmetry breaking.

67. [**Mikielewicz & Gumkowski, 2005**]:
This is an analytical and experimental study. The authors add a head-loss term to the Bernoulli's equation and extend the Rayliegh's shock criterion including energy loss. Relations are also obtained for the nondimensional jump-radius (scaled by nozzle diameter) expressed in terms of the nozzle Froude number and a Weber number. The validity of these expressions is checked against experiments and moderately good match is obtained.

Comments:
The model presented here is extended for jumps formed from an air-water spray in Gumkowski [2008]

68. [**Singha *et al.*, 2005**]:
This is an analytical and experimental study of planar hydraulic jumps. Although this survey excluded many planar jump studies, the work of Singha *et al.* [2005] is discussed because it is very relevant to this thesis. The authors extend the Rayleigh shock criterion by including viscosity in their equations. This is done by including a boundary-layer of constant thickness (less than the film-thickness) in the momentum balance written across the discontinuity. Inside the boundary layer a self-similar velocity profle is assumed and it is found that the height ratio downstream and upstream the jump (H_2/H_1) assumes a value greater than unity even when the upstream Froude number is unity. The authors view this as a shift from a second order transition to a first

order transition in the presence of viscosity. These authors also study the vertically averaged BLSWE using shock-fitting techniques and predict the jump location to scale as $(Q/L)^{5/3}\nu^{-1}g^{-1/3}$ where L is the channel width and all other parameters have their usual meaning. This scaling relation is obtained in two independent ways - firstly by shock fitting and secondly by arguing that at the jump, the diffusive times scale matches the convective time scale and the local Froude number is unity. Some experiments are also reported to validate the scaling relationship for the jump location/height-profile and a good match is reported.

Comments:

The analytical solution of the planar vertically averaged BLSWE shows a sigularity in the slope and an unrealistic turning around of the height profile, rather than a jump. This was the one of the first studies where time dependence in the viscous shallow-water equations are studied. The authors perturb the volume-flow rate and study the evolution of the resultant perturbation. The time scale of decay of a perturbation is estimated from this analysis and this time scale happens identical to the viscous diffusive time-scale. This procedure is also extended to a circular geometry where a more detailed analysis is carried out. We refer the reader to the discussion of reference Ray & Bhattacharya [2007] which follows later.

69. [**Gradeck *et al.*, 2006**]:

An experimental and computational study of the circular hydraulic jump formed from an impinging jet on a horizontally moving surface. A range of experimental results are reported with the velocity of the surface varying from 2.65m/s to 0.51m/s. Due to the motion of the surface, the shape of the jump resembles a parabola. A dimensional analysis is performed to express the non-dimensional radius of the jump as a function of other non-dimensional parameters. A power-law relationship is assumed and the exponents are determined. Computational results obtained from solving the Naveri-Stokes equations with a VOF model for resolving interfaces are reported. A non-linear $k-\epsilon$ model is used to resolve near-wall turbulence. Reasonably good agreement is reported for the position and the shape of the jump and the authors note that the choice of the near-wall turbulence model affects answers

significantly.

Comments:

Formation of a jump from a jet impinging on a moving surface causes an "open jump" and this is somewhat reminiscient of simlar "open" jumps which form on normal jets falling on inclined plates (see [Silverstein, 2002; Thiffeault & Belmonte, 2010]). However, the formation of an "open" jump is later debated by Kate et al. *[2009]. The present work is mostly of industrial relevance where cooling using a jet impinging on a moving surface is frequently used.*

70. [**Bush *et al.*, 2006**]:
An experimental investigation into the cause of symmetry breaking of the circular jump as reported earlier by Ellegaard *et al.* [1998]. The main results are:

- Numerous nonaxisymmetric stable shapes of the jump in addition to those reported by Ellegaard *et al.* [1998] are reported e.g., oval, cat's eye, bowtie, butterfly and clover-shaped jumps. These can be obtained by varying the nozzle size and using highly viscous working fluids like glycerol-water solution.
- As before, the symmetry breaking and the formation of stable polygonal jumps is shown to be related to a capillary instability of the circular jump by adding a surfactant which decreases the surface-tension and restores the circular symmetry. It was also found that reducing the surface-tension makes the jumps gentler.
- An extensive parametric study is conducted in the space of four nondimensional numbers - Reynolds number $Re \equiv Q/\nu a$, Bond number $Bo \equiv \rho g a^2/\sigma$, Weber number $We \equiv \rho Q^2/(\sigma H^3)$ and a/H where Q is the volume flow rate. ν is the kinematic viscosity, H is the outer depth, ρ is the density, a is the radius of the impinging jet at the nozzle outlet and g is the acceleration due to gravity. The different nonaxisymmetric shapes are classified in this parameter space.
- The expression for the jump radius that was proposed earlier in Bush & Aristoff [2003] is now tested for non-axisymmetric jumps as well. Here

the jump radius for a nonaxisymmetric shape is defined as the radius of a equivalent circle which has the same length of the circumference as the non axisymmetric shape. Some scatter is observed in the experimental data and this is ascribed to non-hydrostatic effects of pressure which is known to be important for Type-II jumps (which are the only ones that give rise to symmetry breaking) and neglected in the calculation of the present expressions.

- A rough physical reason is provided for the occurence of symmetry-breaking only in Type-II jumps. The jump is thought to be like the inner-portion of a torus, whose axisymmetry is broken by a capillary instability akin to the well-known Rayleigh-Plateau capillary pinch-off.

Comments:

This is one of the first attempts at understanding the physical mechanism governing the symmetry-breaking in the axisymmetric jumps leading to polygonal shapes. The present physical mechanism is related to a capillary instabiltiy. It is interesting to note that a different mechanism of polygon formation has also been reported in Dressaire et al. *[2009].*

71. [**Rolley *et al.*, 2007**]:
This is predominantly an experimental study of hydraulic jumps formed from liquid helium at temperatures above and below the critical temperature at which superfluid transition occurs.

    - Experiments are done above the critical temperature. The depth of the fluid before the jump, and the jump radius are measured. Capillary effects are siginificant and the surface-tension corrected model of [Bush & Aristoff, 2003] predicts the jump radius better than the model of [Watson, 1964]. The scaling relationship of [Bohr *et al.*, 1993] is found not to work well for jumps of small radii.

    - The radius of the jump hardly shows any change when the temperature is changed through the critical temperature. An explanation is provided for this by arguing that even below the critical temperature, superfluid helium has a viscosity when its speed being greater than a certain critical value (see comment below). Additionally the flow is reported to

develop many stationary ripples below the critical temperature. These ripples are modelled as planar capillary gravity waves and using their wavelength and the corresponding dispersion relation, the local fluid depth is estimated.

- The stability of these ripples is studied by considering the flow as locally being planar and doing a stability analysis on a parallel mean flow assumed to be a parabolic Poisseuille flow. Surface-tension appears through the boundary conditions on the Orr-Sommerfeld equations. At temperatures above the critical temperature, the spatial growth rates estimated from these calculations differ from the ones observed in experiment by about 20%. At temperatures below the critical temperature larger deviations are reported. Some heuristic explanation is provided for this by splitting up the fluid into its normal and superfluid component and imagining the oscillations to be those of the superfluid component.

Comments:

Liquid helium experiments below the critical temperature are interesting because they can be used as a check on phenomena which rely on viscosity for their formation. This is the second study of hydraulic jumps using liquid helium. The first one was in [Gribbon & Cope, 1963]. As the radius of the hydraulic jump is predicted to be strongly sensitive to viscosity [Bohr et al.*, 1993], it is very intriguing to note that the radius of the jump shows hardly any change across the temperature at which the viscosity of liquid helium is expected to sharply reduce. A partial explanation may be that even below the critical temperature, the fluid can have an effective viscosity if it flows above a certain critical speed. This reference explains that the mechanism of why this viscosity arises is a quantum effect and is not well-understood.*

72. [**Ray & Bhattacharya, 2007**]:
An analytical study of the circular hydraulic jump using unsteady boundary-layer shallow-water equations. This study builds upon the previous work reported in Singha *et al.* [2005] and applies it to a circular geometry. The main conclusions are:

- A linearised stability equation is derived starting from the boundary-layer shallow-water equations. The perturbation is in the volume-flow

rate. The stability of perturbations upstream and downstream of the jump is studied by treating a perturbation as a standing wave and assuming a Fourier mode in time. It is found that a standing wave downtream of the jump is damped by viscosity and the decay of the amplitude of the perturbation suggests a time scale. By matching this to the convective time scale and imposing the additional constraint that Froude number is unity, the scaling relationship of Bohr *et al.* [1993] is reproduced.

- The perturbation is also treated like a travelling wave and it is found that any upstream travelling wave is amplified in the subcritical region and gets damped in the supercritical region. This is used to conclude that no upstream propagation is possible from the subcritical to the supercritical region.

- The circular hydraulic jump becomes unstable as the flow rate is increased beyond a certain critical value [Hansen *et al.*, 1997]. The authors provide an estimate of the critical flow rate by equating the power dissipated in a mode at the jump location to the total energy input and obtaining the frequency of the mode from experiments of Hansen *et al.* [1997].

Comments:

This is one of the very few studies on the circular hydraulic jump which include explicit time dependence in their equations. Time dependence in a stability study was also earlier included in Cholemari [1998]. It is interesting to see that the scaling relationship obtained by Bohr et al. *[1993] by fitting a Rayleigh shock can also be obtained by intuitive dimensional arguments as done here. However some questions still remain unclear. For instance the authors obtain the radial location of the jump by equating the viscous time-scale obtained from a perturbative analysis to the convective time-scale. This viscous time scale is identical to the diffusion time-scale for vorticity. Thus one can also think of this time scale as an estimate of the time it takes for vorticity to diffuse throughout the entire fluid film. This is equivalent to assuming that the radial location of the jump coincides with the place where the growing wall boundary-layer reaches the free-surface. However, as shown by Watan-*

abe et al. *[2003] for typical experiments, the jump in fact occurs not where the boundary-layer reaches the free-surface, but much further downstream.*

73. **[Kate *et al.*, 2007*a*]**
This is an experimental study of hydraulic jumps formed from two impinging jets and their interactions. Visibly the most significant phenomenon that occurs when the flows from two impinging jets meet each other is what is known as the fountain formation. A sheet of water rises up in the air (shaped like a fan) formed out of the collision of two oppositely directed radial thin film flows. This interaction region can significantly alter the shape of the hydraulic jump that each jet produces. Experiments are reported for jets of equal and unequal strength i.e. depending on whether the jets are exactly identical or different in terms of diameter and average velocity. The main conclusions are:-

- **Equal jets** - The interaction between the flow formed from two impinging jets strongly depends on the distance between the two jets. The authors identify two length scales here. When the inter-jet distance is greater than a certain critical distance (S_c), there is no interaction and no fountain formation. S_c is found to be an increasing function of flow-rate and constitutes the first length-scale. The second length scale is R, defined as the average of the two hydraulic jump radii formed from the two impinging jets. When the inter-jet distance is less than S_c but greater than R, the authors report formation of a dome shaped fountain. When the interjet distance is less than both S_c and R, the shape of the fountain is more like a thin vertical sheet.
- **Unequal jets** - The main difference here is that the fountain formed here is not vertical but curved towards the weaker jet.

  Some experiments are also reported in this paper on interactions between a wall and a jet. The thin film is allowed to hit a wall and it rises up the wall and forms a fountain

Comments:

Apart from some fundamental appeal, this work has a certain amount of industry relevance where multiple impinging jets are frequently used for cooling.

A detailed understanding of the interaction between two impinging jets can be useful in cotrolling heat transfer rates. The flow generated by a Vertical Take-off and Landing (VTOL) aircraft involves upwash formation due to two impinging air jets striking the ground with ambient air all around. However as pointed out by the authors, the current flow is very different from this mainly due to the entrainment that occurs for the air jets and the lack of formation of a hydraulic jump there.

74. [**Kate *et al.*, 2007*b***]:
A experimental and analytical study of jumps with inclined jets. The main results are:

- Due to obliqueness of the jet, elliptic jumps are obtained upto a certain critical angle. For jet inclinations less than the critical angle, jumps with corners are reported.
- The boundary-layer shallow-water equations are vertically averaged and a self-similar profile is assumed for obtaining closure. This procedure leads to an ordinary differential equation for the average velocity. The solutions of this ordinary differential equation display a singularity at a critical radius. By identifying certain solutions as 'inner' solutions and others as 'outer' solutions, a discontinuity can be fitted using the Rayleigh shock criterion. This gives a scaling relation for the jump radius, which reduces to the predictions of [Bohr *et al.*, 1993] for a vertical jet. The ratio of the major to minor diameters of the elliptic jumps is predicted to be independent of the jet velocity at the nozzle.
- Comparisons with experiments of the scaling relationship show good agreement.
- Jump-jet interaction is proposed as a reason for the formation of jumps with corners, at low values of the jet inclination agle. These jumps with corners are further categorised as Type-I, II and III depending on their shapes. These shapes in turn depend on the jet velocity An analogy is drawn from shock-wave iteractions in compressible flow to give a phenomenological explanation of these varied shapes.

Comments:

The formation of elliptic jumps can be intuitively anticipated from the fact that the radius of the jump is known to depend on the volume-flow rate which in turn shows an azimuthal dependence for inclined jets. The formation of jumps with corners is however difficult to explain intuitively. This is explored more in [Kate et al.*, 2007*c*].*

75. [**Kate *et al.*, 2007*c***]:
The authors build upon their discovery of jumps with corners for inclined jets [Kate *et al.*, 2007*b*]. It was found earlier [Kate *et al.*, 2007*b*] that for inclined jets when the inclination angle becomes less than 25^0 the jump no longer remains elliptic/oblate but instead develops sharp corners, which the authors ascribe to jump-jet interaction. This is an experimental and analytical study of this phenomenon. The main results are:

- An analytical expression is derived for the critical angle using the expression for a Rayleigh shock and the flow geometry. This expression is checked against experiments and reasonable agreement is reported.
- A comparison is made between shock wave interactions and the jumps with corners studied here. A phase diagram is obtained from experiments to categorise the different kinds of shapes of jumps that are obtained.

Comments:

The generalisation of the scaling relationship by Bohr et al. *[1993] to hydraulic jumps formed from inclined jets needs calculation of the azimuthal variation of the mass flow-rate. The authors here use the expression derived by Hasson & Peck [1964]. There is an interesting study by Taylor [1966] on this topic.*

76. [**Rai *et al.*, 2008**]:
An analytical study of the circular hydraulic jump for generalised Newtonian fluids. The authors use a shear-stress model for a generalised Newtonian fluid and extend the anlysis of [Bush & Aristoff, 2003; Watson, 1964] for this model. Expression are derived for the evolution of film-thickness (extension of the zero-gravity solution of Watson [1964]). The surface-tension correction of Bush & Aristoff [2003] is extended for a generalised Newtonian fluid.

Comments:

Experiments on the circular hydraulic jump using non-Newtonian fluids have not been reported elsewhere in the literature. It is not clear if this aspect can bring qualitative changes for the circular jump. We have conducted some experiments using CMC (although no measurements were made) and we did not observe any qualitative changes due to the non-Newtonian property of the working fluid.

77. [**Kasimov, 2008**]:

This is an analytical work which builds on the earlier work of [Bohr *et al.*, 1993; Tani, 1949]. The vertically averaged equations derived by [Bohr *et al.*, 1993; Tani, 1949] have no asymptotic solutions downstream of the jump and additionally they display a negative singularity in the derivative of height at a certain location downstream. In this study an attempt is made to remove some of these issues. The main results are:

- The author models the bottom topography in order to improve the accuracy of the downstream solution of Bohr *et al.* [1993]. By modelling the plate using realistic profiles, it is shown that the resultant ordinary differential equation has a second critical point in addition to the original critical point in the equation of Bohr *et al.* [1993]. The radial location of this second critical point is used as a measure of the plate radius and the resultant radius of the circular jump is computed numerically using shock fitting by Rayleigh shock criterion supplemented by surface-tension. The resultant location of the jump is sensitive to the plate radius and is found to decrease with increasing plate radius.
- The role of surface-tension explored in the earlier work of [Bush & Aristoff, 2003; Bush *et al.*, 2006] is carried forward. It is found that a critical value of surface-tension exists above which Rayleigh's shock criterion has no solution. This is used to argue that for high enough surface-tension values an axisymmetric jump cannot exist and hence symmetry breaking is inevitable. It is also found that the critical value of surface-tension comes down with viscosity, a trend which is consistent with the experimental observation that symmetry breaking is observed for only highly viscous fluids.

Comments:

The author argues that for an infinite plate, no steady-state circular jump should be observable. However in high-speed photography of jump formation done by us, we were able to observe formation of a well-defined steady circular jump long before the fluid reached the edge of the plate. The effect of plate size on the jump radius was also studied experimentally in Rao [1994]. However, their experimental data shows some non-monotonic behaviour and hence no clear trend can be observed.

78. [**Thorpe & Kavcic, 2008**]:
This is the first experimental study of internal circular hydraulic jumps. Such jumps in planar geometries are well-known (see e.g. the theoretical and experimental work in Yih & Guha [1955] and more recently see Holland *et al.* [2002]) and the authors report the discovery of the same in a circular geometry. A theoretical foray is also made in this study.

- The occurence of circular jumps is reported for a jet submerged into a fluid of lower density. The jet has two orientations - upward and downward facing. Some undulations are reported downstream of the jump and the wavelength of these undulations decrease with increasing radius. The authors provide an explanation for this by equating the phase speed of surface-gravity waves to the local flow speed and assuming that the height downstream of the jump is practically a constant. This is also used to provide an estimate of the height immediately downstream of the jump.
- Far upstream of the jump the authors use Watson's gravity-free similarity solution [Watson, 1964].
- A modification of the Rayleigh shock criterion is proposed for jumps of finite width by assuming pressure to be hydrostatic.

Comments:

As correctly remarked by the authors, the fact that internal jumps should be possible in circular geometries is not surprising. Altering the density ratio of the two fluids is a way of varying the effective gravity that the hydraulic jump experiences. The theoretical model downstream of the jump makes one major

assumption i.e. the flow is irrotational and hence can be treated as inviscid. This is not a good assumption because the incoming flow just upstream of the jump is entirely vortical and it is not clear where this vorticity disappears while transitioning through the jump. The authors model the flow downstream of the jump as an uniform flow and provide a solution of the Laplace equation here. As we shall see in Chapter 4, in our simulations we too find a few undulations behind the jump in the absence of surface-tension and the wavelength of these decrease with streamwise distance.

79. [**Gumkowski, 2008**]:
The authors make a theoretical study and a limited comparison with experiments for jumps formed from an impinging jet of gas-liquid spray (aerosol). The theoretical part has been discussed earlier in Mikielewicz & Gumkowski [2005] in context of a single-phase jet and we discuss only the experimental part here. Experiments are conducted using a two-phase air-water jet. Data is reported for comparisons between the jump radius formed from a single phase jet and an aerosol jet. The jump formed by an aerosol jet is reported to be larger compared to the one formed by a single phase water jet for the same mass-flow rate of water in both the cases. Some other related results are also reported for aerosol jets.

Comments:
An experimental study of an impinging gas-liquid spray was earlier reported by Siwon [1993], although this work is not cited in the present reference. This work is more detailed and contains both experimental and analytical results and comparisons between the two.

80. [**Kate *et al.*, 2008**]:
An experimental study of jumps formed by inclined jets. The main results reported are:

- For large angles of jet inclinations, elliptic jumps are obtained. For perpendicular jets, circular jumps are obtained. For circular jumps, some comparisons are reported with previous height-profile measurements of [Rao & Arakeri, 1998; Rao, 1994] and the radius versus flow rate comparisons with the scaling of [Bohr *et al.*, 1993].

- Stagnation point pressure at the impingement point is measured. It is found that the ratio of the stagnation point pressures for a inclined jet to a circular jet depends on the inclination angle but is practically independent of the flow-rate.
- The ratio of the area of a circular jump to an elliptic jump is found to be dependent on the inclination of the jet but is observed to be almost independent of the mass flow rate.
- For inclined jets, the film thickness shows an azimuthal dependence.

Comments:

The variation of film-thickness with the azimuthal coordinate is to be expected. This is because for an inclined jet, the mass flow rate through a small azimuthal section depends on the azimuthal orientation of the section. Since mass flow-rate affects the film thickness, an azimuthal variation of the film thickness is thus expected. The problem of determining the azimuthal thickness of the film formed from an inclined impinging jet on a horizontal plate was attempted by [Taylor, 1966] where it was argued that the determination of the azimuthal dependence of the film thickness is not possible from mass and momentum considerations alone. Also see [Michell, 1890].

81. [**Kluwick *et al.*, 2009**]:
This is a study of planar jumps generated by an obstacle downstream. The authors study the case where the incoming Froude number is very close to unity and the asymptotic analysis presented corresponds to $Fr-1 << 1, Re \rightarrow \infty$. The flow structure in the near-jump region is found to have a triple-deck structure. For $\epsilon \equiv Re^{-1/9}$, the flow is divided into three parts - (a) A lower deck of thickness $O(\epsilon^4)$, a main deck of thickness $O(\epsilon^3)$ and an upper deck of $O(1)$ thickness. The response of the incoming undeveloped flow upstream of the obstacle takes a form in which viscous perturbations are confined to the lower-deck, the main-deck represents an inviscid displacement of the remaining part of the boundary-layer and the outer inviscid flow also undergoes a similar displacement. Due to the fact that $Fr-1$ is assumed to be a very small parameter, resonant conditions prevail and hence this necessitates a non-linear study. The authors restrict themselves to a study of the steady state for the nonlinear problem. For the corresponding linear problem, time

dependence is also included.

Comments:

This is essentially a study of nonlinear, viscous gravity waves propagating on a near critical flow ($Fr \sim 1$). This study builds upon earlier studies ([Gajjar & Smith, 1983], [Bowles & Smith, 1992], Higuera [1994]). In fact the assumption of $Fr - 1 << 1$ introduces a new pressure-diplacement law in the equations studied earlier by Bowles & Smith [1992] (who studied the case of large incoming Fr) and the authors study this.

82. [**Kate *et al.*, 2009**]:
This is a theoretical and experimental study of hydraulic jumps formed from normal and inclined jets on surfaces moving with a constant velocity. The main results are:-

- An inclined jet impinging on a surface moving with constant velocity can be treated as an equivalent jet impinging on a stationary surface with a different angle of inclination and a different jet velocity. The equivalent angle of inclination and jet velocity is calculated from the vector sum of the actual jet velocity and the velocity of the moving surface. The equivalent inclined jet is treated using the methods of Kate *et al.* [2007*b*] and a scaling relation for the radius of the elliptic jump is obtained. For normal jets impinging on a moving surface, "open" jumps were reported in Gradeck *et al.* [2006]. It is clarified here that these open jumps are actually part of ellipse shaped jumps. Some comparisons with experiments, the simulations of Gradeck *et al.* [2006] and the theoretical predictions are made.
- It is argued that it is possible to obtain a circular jump using an inclined jet on impinging on a moving plate, if the horizontal component of the jet velocity is cancelled by the horizontal velocity of the moving surface.

Comments:

This work builds upon the earlier work of Gradeck et al. *[2006] which studied jumps formed from normal impinging jets on a moving surface. Like the work of Gradeck* et al. *[2006] the present study is also very relevant for industrial applications where inclined impinging jets might be frequently encountered,*

83. [**Dressaire *et al.*, 2009**]:
This is an experimental and semi-analytical work on the formation of polygonal hydraulic jumps on micropatterned surfaces. The thin film thickness and roughness amplitude of the micropatterns are of the same order of magnitude. The main results are:

- By modifying the micron-scale surface topography, the symmetry of the circular hydraulic jump can be broken and stable polygonal jumps can be obtained. By further varying viscosity and surface-tension, the stability of these polygonal structures is not affected. This suggests that the polygonal jump formation may not always be due to a capillary or inertial instability but rather controlled by the geometry of the surface topography.
- The micropatterned surface is characterized by arrays cylindrical posts of height H, radius R and lattice distance D. Polygons are visible only for large flow-rates. The average radius of the polygons increases with flow-rate. For a given flow-rate, the average radius decreases with increasing H or decreasing D. the authors rationalise this by postulating that increasing H or decreasing D has the effect of decreasing the effective mass flow-rate through the thin film above the posts, due to "leakage" of some part of the flow through the micropatterned texture.
- A model is proposed for this by dividing the flow into two parts one though the microtexture and a thin-film flow above it. The presence of the microtexture introduces a slip boundary condition for the thin-film above it. Results obtained from this model are in good agreement with observations.

Comments:
The occurence of polygonal jumps for smooth surfaces has been traditionally thought to arise from a capillary instability Bush et al. *[2006]. This is an interesting demonstration that there might be alternative routes to symmetry-breaking too.*

84. [**Andersen *et al.*, 2009**]:
This study focusses on the importance of separation in pattern-formation

at moderate Reynolds numbers. The circular hydraulic jump is cited as an example where separation plays a strong role. In Type I jumps, the model of [Watanabe *et al.*, 2003] can be integrated through the point of separation. In case of Type-II jumps, no such simple model exists. There are other examples discussed in the paper which involve flow separation but those are not directly relevant to the circular hydraulic jump.

Comments:

Flow-separation can be a unifying theme for many flows and can be an important ingredient of pattern formation, as this work tries to illustrate and highlight. A relevant example here is the symmetry breaking of Type-II jumps resulting in formation of stable polygons. The existence of the surface roller seems to be a crucial element for this pattern formation as Type-I jumps have never been observed to break into polygons.

85. [**Mikielewicz & Mikielewicz, 2009**]:
An experimental and theoretical study. A model for calculating the radius of Type-I and Type-II jumps is worked out taking into account the existence of two separate eddies. The main results are:

- A head loss term is added to Bernoulli's equation and this term is split up into two parts. One loss is said to be because of the presence of eddies and another loss is due to sudden expansion at the jump. The first term is estimated by assuming a solid body rotation. A parameter P is introduced which takes the values of 4 or 8 depending on the number of eddies being modelled. A relation is derived which relates the heights before and after the jump to the upstream Froude number. However, this relation *does not* reduce to the Rayleigh shock criterion even when the eddy losses are not considered, although at high values of upstream Froude numbers both the relations start giving similar answers. An expression in derived to relate the non-dimensional radius of the jump (scaled by the nozzle diameter) to the upstream Froude number and this includes surface-tension contributions.
- Experiments are conducted to validate the relationships obtained. The predictions for the ratio of heights upstream and downstream of the jump, show reasonable agreement. The agreement for the prediction of

the location of the jump in terms of the upstream Froude number is moderate and the experimental data shows scatter.

Comments:

*Although very heuristic, this is the only published attempt in modelling Type-II jumps. A series of earlier numerical studies by Yokoi & Xiao [1999, 2000*a,b*, 2002] had focussed on the importance of surface-tension and nonhydrostatic pressure effects for the existence of the Type-II jump.*

86. [**Bonn *et al.*, 2009**]:
This is an experimental and theoretical study of jumps in a planar geometry. The experimental part studies planar jumps occuring from jets impinging in a thin channel of width varying from $0.4 - 1.2$cm and length 100cm. Film thickness measurements are made using a depth micrometre. Another set of experiments are performed using a sheet of water emerging from a slit and impinging upon a plate and where rhombus shaped jumps are obtained. Here too depth measurements are made. Some of the main results are:

- The height profile upstream of the jump is linear as is to be expected from Watson's gravity free similarity solution (Watson [1964]). However the slope obtained from experiments is an order of magnitude higher than that predicted by [Watson, 1964]. Additionally, the slope is found to be independent of the volume flow-rate Q unlike Watson's theory which predicts otherwise. The authors explain this by showing that the channel-flow is turbulent due to the presence of side-walls. An enhanced eddy viscosity model is proposed to explain the much higher slopes seen in experiments. The mixing length is taken to be proportional to the height of the liquid layer and the resultant eddy viscosity is directly proportional to the volume flow-rate. Using this model, good match with experimental data is reported. It is also pointed out that the experimental height-profile of Singha *et al.* [2005] is also an order of magnitude higher than the value predicted by laminar theory and a similar reasoning is offered for this deviation.
- The theoretical part uses a two dimensional vertically averaged model and a velocity profile whose shape is allowed to change only in the near jump region. The viscosity is replaced by the eddy viscosity obtained

earlier and different eddy viscosity models are used upstream and downstream of the jump. Fixing the shape of the velocity profile allows the solutions upstream and downstream of the jump to be determined which are then connected using a shock and good match is reported with experiments. In the near jump region, the authors use a cubic profile with streamwise evolving coefficients to obtain jump-like transition. However, the match of the near jump height profile to the experimental profile is reported to be not very good. Some measurements on rhombic jumps are also reported.

Comments:

The theoretical part of this study where the velocity profile is allowed to change shape, extends the methods presented in Watanabe et al. *[2003] to jumps occuring in a horizontal planar geometry.*

87. [**Khavari *et al.*, 2009**]:

This is a computational study of the circular hydraulic jump using the VOF method. The authors report simulations of Type-I jumps and simulations of jump formation. Computational results are compared with the approach of Bush & Aristoff [2003]; Watson [1964]. The computed radius of the jump agrees reasonably well with the experimental measurements of Errico [1986]. The effect of change of outer depth (controlled) is shown to cause a decrease in jump radius, consistent with well-known experimental results.

Comments:

The downstream boundary conditions which are very crucial in Navier-Stokes simulations are not discussed in adequate detail here. The authors report that they control the outer depth but the pressure boundary condition at the exit is not discussed. The Type-IIb jumps reported in Liu & Lienhard [1993] and also in Bush et al. *[2006] is simulated. Some 3D simulations and visualisation is reported but the details are not discussed.*

88. [**Rojas *et al.*, 2010**]:

This is a theoretical study and the authors derive equations which include inertia as a small parameter in a lubrication model. Although this is not a direct study of the circular jump, the authors report simulations of the jump

using their model and hence we discuss this reference here. In the limit of small Reynolds numbers, the lowest order equation for the evolution of the interface is derived, which contains the effects of inertia. The steady state version of this equation is then solved as a boundary-value problem and Type-I jumps are reported. The calculated radius of the jump is compared to the experimental results of Hansen *et al.* [1997] and a good match is reported, especially at high values of flow-rates.

Comments:

Hydraulic jumps have been traditionally studied under the boundary-layer or $Re \to \infty$ *approximation. This is only study we know of which looks at hydraulic jumps in the other limit of* $Re \to 0$.

89. [**Pirat *et al.*, 2010**]:

This is a study of the oscillations described by a levitating drop on a jump formed on an inclined plate. The pendulum-like motion of the levitating drop is studied analytically and experimentally and a gyroscopic instability mechanism is proposed for these oscillations. An approximate criterion is presented for the condition when the lowest point on the drop's trajectory ceases to be a stable equilibrium point.

Comments:

This study extends the observations of levitating drops reported earlier in Sreenivas et al. *[1999] and studies their dynamics in greater detail.*

90. [**Thiffeault & Belmonte, 2010**]:

This is an analytical and experimental study of jumps formed from impinging jets on inclined plates. In such situations open jumps are formed and the principal aim of this work is to obtain the dependence of the height of rise of the fluid on the inclination angle. The authors use the approach of Bohr *et al.* [1993] using vertical averaging of the BLSWE to obtain a prediction for the height of rise of the fluid up the incline. This expression is tested against experimental data and good agreement is reported for high flow-rates and small angles of inclination. The theory fails for low flow rates where poor agreement with experiments is reported and for large angles (close to $\pi/2$) where an unphysical non-monotonicity in the dependence of the height of rise, on the plate inclination angle is obtained.

Comments:

Jumps formed from inclined jets have been studied earlier by Silverstein [2002]. However, determining the dependence of height of rise of fluid on the volume flow-rate and the plate inclination angle have not been addressed earlier. The author is grateful to Mr. Anubhab Roy for bringing this reference to his attention.

91. [**Jannes *et al.*, 2010**]:
This is a theoretical study. The authors make some exotic analogies between a hydraulic jump and a white hole. We will not discuss this analogy but focus instead on some experimental results which are relevant for the present study. The main observations are:

- Measurement of the jump radius with volume flow-rate is presented and a linear relationship between the two quantities is reported although at low flow rates deviations are observed.
- The authors report the observation of a Mach cone when a disturbance is introduced upstream of a jump. Using the simple classical shock relation for a Mach cone, the cone angle is obtained experimentally at various radial positions. It is shown that this angle is less than $\pi/2$ in the supercritical region and becomes almost exactly $\pi/2$ at the jump and downstream of the jump, no Mach cones are obtained.

Comments:

A power-law relationship for the radius of the jump in terms of flow-rate is discussed in Chapter 5 although we shall also see in Chapter 4 that the jump radius really does not scale like a power-law. The author is grateful to Mr. Sumesh P. T. for bringing this reference to his attention.

1.3 List of references which could not be accessed

92. [**Kurihara, 1946**]:
The first attempt at including viscosity in the shallow-water equations. This reference is in Japanese.

93. [**Shen, 1961**]:
    This is a technical report on radial bores.

94. [**Larras, 1962**]:
    This is writen in French.

95. [**Saddler & Higgins, 1963**]:
    There are experimental results in this work.

96. [**Ahmad, 1967**]:
    A part of this work is available in [Koloseus & Ahmad, 1969] and has been reviewed earlier in this section.

97. [**Nirapathdongporn, 1968**]
    This work apparently contains a good literature survey of the circular hydraulic jump until 1968 (see [Avedesian & Zhao, 2000]).

98. [**Gachechiladze, 1970**]
    This is a study which approaches the problem from a civil engineering perspective.

99. [**Khalifa & McCorquodale, 1979**]

100. [**Bouhadef, 1978**]
     This reference is accessible and is written in French.

101. [**Nettleton, 1983**]
     This is a Master's thesis from University of Windsor.

102. [**Errico, 1986**]:
     This is a PhD thesis from Univsersity of Calfornia at San Diego on jet impingement.

103. [**Stevens, 1991**]:
     This is a PhD thesis of experimental work on jet impingement.

104. [**Hansen *et al.*, 2002**]:
     This is written in Danish and is freely available online.

105. [**Phillips, 2008**]:
This is an AIAA conference report. The circular hydraulic jump was experimentally simulated aboard a NASA microgravity research aircraft. The abstract is reproduced below:

- The behavior of the circular hydraulic jump has been studied, under conditions of reduced gravity aboard the NASA C-9 microgravity research aircraft, for Reynolds numbers based on jet diameter between 27000 and 58000 and Weber numbers between 1000 and 4600. The steady-state jump radius was observed to increase under conditions of reduced gravity, relative to its magnitude during hypergravity at the same flowrate. The measured jump radius achieved a steady-state value in approximately 3 to 5 s, which corresponded to the time for the establishment of steady reduced gravity conditions during each parabola. Jump radius in reduced gravity increased in a nearly linear fashion versus jet flowrate. Comparisons with available theories were incomplete due to unsuccessful attempts to measure the upstream and downstream jump depths.

1.4 Discussion

With the literature survey now complete, one can take a bird's eye view of how much understanding has been achieved in roughly one hundred years of studying laminar standing jumps, especially in circular geometries. We believe that theoretical attempts at understanding the jump can be broadly classified into two major categories viz. (a) The now classical vertical averaging approach (b) Asymptotic analysis in the form of higher-order boundary-layer theory.

Both the approaches have had their share of successes and deficiencies. The vertical averaging approach aims for a mathematically simpler description, provides useful scaling relationships which agree well with experiments and many times reveals the physics of the problem using equations which mostly are simple ordinary-differential equations. On the flip side this approach has not been very successful in providing a good understanding of the near-jump flow structure and/or the dominant physics there. Results obtained from these methods are frequently plagued

Approximate		Experiments	Navier-Stokes simulations	
Theory	**Numerical methods**		**Laminar**	**Turbulent**
Rayleigh, 1908	Tani, 1949	Tani, 1949	Dingwei, 1998	Rahman, 1991
Kurihara, 1946	Watson, 1964	Gribbon, 1963	Yokoi, 1999	Chippada, 1994
Tani, 1949	Koloseus, 1969	Watson, 1964	Yokoi, 2000a	
Benjamin, 1954	Arbhabhirama, 1975a	Olsson, 1964	Yokoi, 2000b	
Watson, 1964	Arbhabhirama, 1975b	Koloseus, 1969	Yokoi, 2002	
Hsieh, 1967	Labus, 1977	Arbhabhirama, 1975	Ferreira, 2002	
Nakoryakov, 1978	Nakoryakov, 1978	Labus, 1977	Gradeck, 2006	
Gajjar, 1983	Lawson, 1983	Ishigai, 1977	Khavari, 2009	
Lawson, 1983	Rahman, 1991a	Nakoryakov, 1978	Present work	
Varella, 1992	Rahman, 1991b	Lawson, 1983		
Bowles, 1992	Gharangik, 1991	Azuma, 1984		
Bohr, 1993	Khalifa, 1992	Vasista, 1989		
Godwin, 1993	Varella, 1992	Stevens, 1992		
Buyevich, 1993	Gajjar, 1984, Bowles, 1992	Liu, 1993		
Rao, 1993	Bohr1993	Bohr, 1993		
Higuera, 1993	Buyevich, 1993	Stevens, 1993		
Blackford, 1996	Rao, 1998	Siwon, 1993		
Murtuza, 1996	Higuera, 1994, 1997	Rao, 1994		
Bloom, 1997	Blackford, 1996	Murtuza, 1996		
Hansen, 1997	Bloom, 1997	Avedesian, 1996,2000		
Bohr, 1998	Bohr, 1998	Ellegaard, 1996		

Table 1.1: A compilation and classification of the literature on hydraulic jumps with strong bias towards the circular jump. Note that this is only a representative list and not an exhaustive classification. Many references have both experimental and numerical contributions and hence are listed more than once.

Approximate		Experiments	Navier-Stokes simulations	
Theory	**Numerical methods**		**Laminar**	**Turbulent**
Putkaradaze, 1997	Cholemari, 1998	Bloom, 1997		
Cholemari, 1998	Chang, 2001	Hansen, 1997		
Hansen, 2001	Pacheco, 2003	Bohr, 1998		
Chang, 2001	Bush, 2003	Ellegaard, 1998,1999		
Bush, 2003	Watanabe, 2003	Cholemari, 1998,2005		
Mikielewicz, 2003	Kluwick, 2009	Naraghi, 1999		
Bush, 2003	Rojas, 2010	Sreenivas, 1999		
Watanabe, 2003	Present work, 2010	Brechet, 1999		
Mikielewicz, 2005		Moncada, 1999		
Singha, 2005		Hansen, 2001		
Ray, 2007		Chang, 2001		
Kate, 2007b		Rao, 2001		
Kate, 2007c		Pelzer, 2002		
Rai, 2008		Silverstein, 2002		
Kasimov, 2008		Bush, 2003		
Thorpe, 2008		Ozar, 2003		
Gumkowski, 2008		Aristoff, 2004		
Kluwick, 2009		Mikielewicz, 2005		
Kate, 2009		Singha, 2005		
Dressaire, 2009		Gradeck, 2006		
Mikielewicz, 2009		Bush, 2006		
Bonn, 2009		Rolley, 2007		
Rojas, 2010		Kate, 2007a,b,c		
Pirat, 2010		Thorpe, 2008		
Thiffeault, 2010		Gumkowski,		
Present work, 2010		Kate, 2008,2009		
		Dressaire, Mikielewicz, Bonn, 2009		
		Pirat, Thiffeault, Shastry, 2010		

Table 1.2: continued from table 1.1

by singularities in the near-jump region and thus one has to be content with representing the jump as a mathematical discontinuity, which clearly it is not. The only successful attempt in curing this has been in Watanabe *et al.* [2003] albeit under the shallow-water approximation. A second disadvantage of the vertical averaged models is that they are frequently derived not from an asymptotic procedure, but from physical intuition. This procedure introduces an element of subjectivity and thus it is not always obvious how one could improve such models. The higher-order boundary layer analyses on the other hand suffer from the obvious disadvantage that they are only asymptotically correct. This can lead to discrepancies when results obtained from such analysis are compared to experiments. For instance in Kluwick *et al.* [2009], $Re^{-1/9}$ is a nominally small-parameter. If this quantity is taken to be actually small, let's say 0.1, this implies a Reynolds number of 10^9, a value astronomically high and never possibly realized in experiments. Nothwithstanding such drawbacks, higher-order boundary-layer methods have succeeded in making some progress in obtaining an understanding of the flow structure for the hydraulic jump. We classify the literature depending on the contribution it makes, in table 1.1 and 1.2.. The first thing to be noticed in this table is the paucity of Navier-Stokes simulations. In this thesis, we hope to take a first step towards bridging this gap.

In the opening paragraph of the previous section, we had asked a series of questions. In the light of the literature survey presented, it is useful to summarise to what extent and how many of these questions are answered. These are presented in the same order in which the questions were posed at the begining of this chapter.

- Separation is definitely not the cause of jump-formation. This is true for both circular and planar geometries. In a circular geometry, this was hinted at in the experiments of Chang *et al.* [2001]; Craik *et al.* [1981]. In simulations we show conclusive evidence of this in Chapter 4. For a planar geometry, while our simulations have not produced a jump without separation, we refer to studies in the literature survey which have reported such jumps either through simulations e.g. Chippada *et al.* [1994] or using approximate numerical methods e.g. Higuera [1994].

- The physical mechanism of jump formation from a waves perspective is still an open problem. There are only qualitative explanations and there is no

realistic quantitative model which shows how non-linear steepening of waves leads to the formation of a stationary jump. In this aspect, travelling jumps are much better understood compared to their stationary counterpart. The Froude number unity criterion works for circular jumps as well. In fact the inviscid Froude criterion seems to be a robust definition, even in the presence of viscosity as we find in our simulations. The impossibility of smooth transition from $Fr > 1$ to $Fr < 1$ is an experimental fact. Viscosity playes mutiple roles in this transition. Firstly, it is the agent which can cause a supercritical flow to become subcritical. Our near-jump analysis of Chapter 3 also shows the importance of the viscous terms in the neighbourhood of the jump.

- The scaling relationship obtained by Bohr *et al.* [1993] seems to be the most accurate till date. However, momentum flux provides a correction to it and we discuss this in Chapter 5.

- There are not many qualitative differences between the CHJ and a PHJ. However, there are plenty of quantitative differences and some of these are summarised in Chapter 4. There has been no comprehensive study on comparisons between travelling and stationary jumps and thus this is an answered question. The traditional explanation that the two are related by a Galilean transformation works only for an inviscid flow and it is well-known that for stationary jumps on thin-film flows viscosity is not negligible, at least in the near-jump region. Additionally, a stationary jump can arise only on a flow which is varying in the streamwise direction and this introduces difficulties in relating the travelling jump to the stationary jump.

- Obtaining stationary jumps from purely inviscid equations is unlikely. There is an extensive literature on dispersive shock waves (Hoefer & Ablowitz [2009]) which arise due to non-linear steepening being counterbalanced by dispersive effects. However even for such dispersive waves, a small amount of viscosity is needed in order to achieve stationary solutions (Genady *et al.* [2006]). There are many shock capturing numerical schemes which can simulate stationary jumps using purely inviscid equations. These however provide a very poor approximation to the near-jump region.

- This is a question that we take up in some level of detail in this thesis. Inclusion of dispersive effects has not been reported in the vertical averaging approach of studying hydraulic jumps. In Chapter 3, we derive the complete vertical averaged equation without any assumptions and this includes dispersive terms. It is found that these terms increase the order of the equation. We also show that at the lowest order, no term from the shallow-water equations is important in a neighbourhood of the jump. The inadequacy of the shallow-water assumption is discussed in detail in Chapter 2 and 3.

- This is an unanswered question. The role of wall-vorticity is not clear. However this is not a necessary condition for jump formation. The interactive boundary-layer analysis of Gajjar & Smith [1983] studies jumps occuring on an undeveloped flow.

- The idea of how separation arises in these viscous thin-film flows has been made clear in the works of Bowles & Smith [1992]; Kluwick *et al.* [2009]. The basic idea of self-induced separation is that a viscous layer near the wall generates its own adverse-pressure gradient by a mechanism which depends on the displacement of the layer itself, as a response to downstream conditions. Understanding the physics of how this separation occurs requires a detailed interactive boundary-layer analysis.

- The role of downstream boundary condition is something that we discuss in detail in this thesis. Here we argue that downstream boundary conditions are not an essential ingredient of jump formation. In fact on a horizontal plane, a supercritical flow has to invariably become subcritical at some location downstream due to viscous deceleration. We provide heuristic arguments that this transition cannot happen smoothly, thus hinting at formation of a jump. In this the downstream boundary condition has no role. However, the downstream boundary condition does have a influence on the jump location, its structure and the solution downstream of the jump.

- The role of the air-boundary layer and its influence on the jump is still largely an open area of research. Till date there have been only two studies which have looked at the air-boundary layer viz. Sreenivas *et al.* [1999] and Pirat *et al.* [2010]. These studies however did not focus on the effect of the air

boundary layer on the jump.

- It is understood now that the singularities in the vertical-averaged models mostly arise due to the self-similar assumption on the velocity profile (Watanabe *et al.* [2003]). An improvement over this method for the BLSWE is suggested. The drawbacks of vertical averaging are discussed further in Chapter 2 of this thesis. We also discuss the validity of the vertical averaged models in different regions of the jump.

- The role of surface-tension in gravity driven circular jumps is mostly well-understood. The same cannot be said with equal confidence in case of polygonal jumps and this continues to be an active and open area of research. In chapter 6, we discuss the possibility of surface-tension driven jumps in the absence of gravity. Understanding these jumps from a wave persepctive is still an open problem.

- The flow-structure of the hydraulic jump is not very well-understood. Numerical simulations of laminar standing jumps are also sparse in literature and this contributes to the gaps in understanding.

In the following chapters, we will make an attempt to elucidate on some of the above questions. This thesis is organised as follows - In Chapter 2, we study weak hydraulic jumps under the shallow-water and boundary-layer approximation. In Chapter 3, we study planar hydraulic jumps computationally and analytically. Chapter 4 is a computational study of circular jumps. In Chapter 5, we study the effect of momentum flux on the circular jump experimentally. Chapter 6 is an analytical study of surface-tension driven jumps at very small length scales. Chapter 7 explains an implementation of the Volume-Of-Fluid algorithm used to simulate free-surface flows.

CHAPTER 2

WEAK HYDRAULIC JUMPS: A SEMIANALYTICAL STUDY

Remarks:
A condensed version of this chapter has been published in Dasgupta & Govindarajan [2010].

2.1 Shallow-water assumption

Hydraulic jumps both standing and travelling have been traditionally studied under the assumption of hydrostatic pressure, also known more popularly as the shallow-water assumption. It is well known (see eg. [Stoker, 1992]) that assuming hydrostatic pressure in an unsteady gravity-driven free-surface flow is equivalent to assuming that the wavelength of any propagating surface wave is long compared to a corresponding vertical scale (say the undisturbed depth of the fluid over which the wave propagates). Correspondingly, in a steady free-surface flow, the hydrostatic pressure assumption is tantamount to assuming that the vertical acceleration experienced by a fluid parcel as it moves from once place to another is negligible. In other words, this is equivalent to neglecting the effects of streamline curvature. From physical reasoning, it is clear that such an assumption which neglects the effects of streamline curvature is going to be bad, at least in the near vicinity of the jump where streamlines abruptly curve upwards. The more abrupt the jump, the worse the assumption. Despite this obvious limitation, many recent studies [Bonn *et al.*, 2009; Kasimov, 2008] continue to use the hydrostatic assumption, even near the jump. There can be more than one reason attributed to this. As discussed in the first chapter, inviscid theory treats a hydraulic jump as being analogous to a gas-dynamic shock wave, the basis for this analogy being in the transformation of the inviscid unsteady shallow-water equations into their gas dynamic counterpart. This mathematical analogy holds good only under the shallow-water assumption, thus providing a reason for its continued its usage. An additional reason is the accompanying simplicity obtained by using the hydrostatic assumption. Without

the hydrostatic-assumption, the height of the free-surface h, which is an unknown, appears either in the boundary conditions or as a limit of integration in the integral version of the global mass conservation equation, and nowhere else in the governing system of equations. This can render the resulting system computationally very unwieldy. The hydrostatic assumption introduces this unknown into the governing equations, greatly simplifying the computational procedure. In this chapter we will study standing hydraulic jumps using the shallow-water assumption. This will thus restrict us to "weak-jumps" where the transition in height happens gradually rather than abruptly with streamwise distance. To make the idea of a weak jump more precise, we refer to figure 2.1.

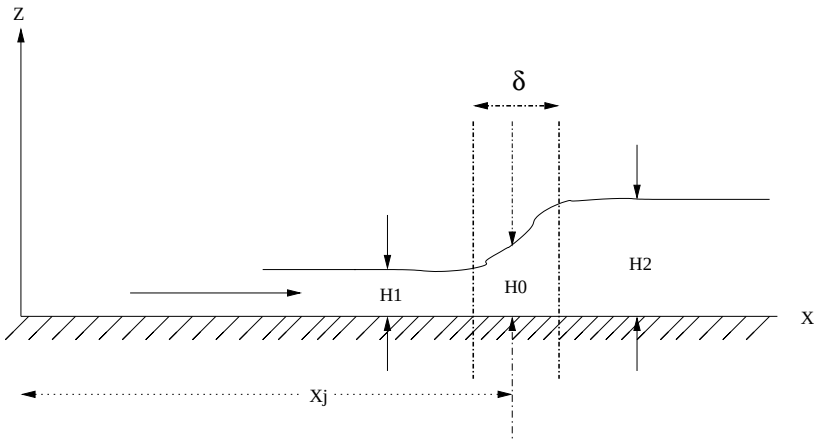

Figure 2.1: By definition, $H_0 \equiv (H_1 + H_2)/2$. δ is a measure of the "width" of the jump while H_0 is a measure of the jump height. Thus for a weak jump, $\epsilon \equiv \delta/H_0 \sim O(1)$.

This chapter is organised as follows - we start by reviewing the well-known inviscid, irrotational, shallow-water equations in planar and circular geometries and their solutions. The inadequacy of these solutions and the inability to obtain hydraulic-jump like solutions from them is used to motivate the inclusion of viscous terms in these equations. This leads us to viscous shallow-water equations of the boundary-layer type. We then discuss the traditional vertical averaging technique used for these equations and point out deficiencies in the technique. There is no immediate resemblance between the viscous and the inviscid solutions and we study the relation between them. We also find a new analytical solution to the vertically averaged viscous equation in a circular geometry. The main contribution of this chapter then follows, in a new transformation that we propose to the viscous

shallow-water equations. Analytical solutions to these transformed equations in the limit of high and low Froude number are obtained. These transformed equations are then numerically solved for both planar and circular geometries and hydraulic jump-like transitions are obtained when the local Froude number is of the order unity. Downstream of the jump, we report multiple solutions to the governing equations The chapter concludes with a comparison of our solutions with those obtained from vertically averaged models, experiments, other recent models and numerical solutions available in literature.

2.2 Inviscid shallow-water equations

2.2.1 Planar

The one dimensional, steady, inviscid, shallow-water equations in a planar geometry are integrated to obtain

$$\frac{u^2}{2} + gh = C, \tag{2.1}$$

$$uh = Q, \tag{2.2}$$

where Q and C are constants of integration and physically correspond to energy per unit mass and volume flow rate per unit transverse depth respectively. Elimating u from the two equations, we obtain the cubic equation for height

$$2gh^3 - 2Ch^2 + Q^2 = 0, \tag{2.3}$$

Note that Q and C are positive constants. We are interested in only real roots of the cubic and there are three distinct real roots if $C > \frac{2}{3}g^{\frac{2}{3}}Q^{\frac{2}{3}}$. It is easy to see from the form of the cubic that all three roots are not of the same sign. Additionally since $Q > 0$ two roots are always positive, corresponding to actual solutions for the heights, and one always negative. If we define Froude number as $Fr = \dfrac{Q}{gh^{\frac{3}{2}}}$, then the height at which Froude becomes unity is given by $h_c = Q^{\frac{2}{3}}g^{\frac{-2}{3}}$. One can easily show that one of the positive roots is subcritical ($Fr < 1$) and the other supercritical ($Fr > 1$), see figure (2.2). The condition $C < \frac{2}{3}g^{\frac{2}{3}}Q^{\frac{2}{3}}$ is of no interest since this corresponds to only one real root and that root is always negative. The

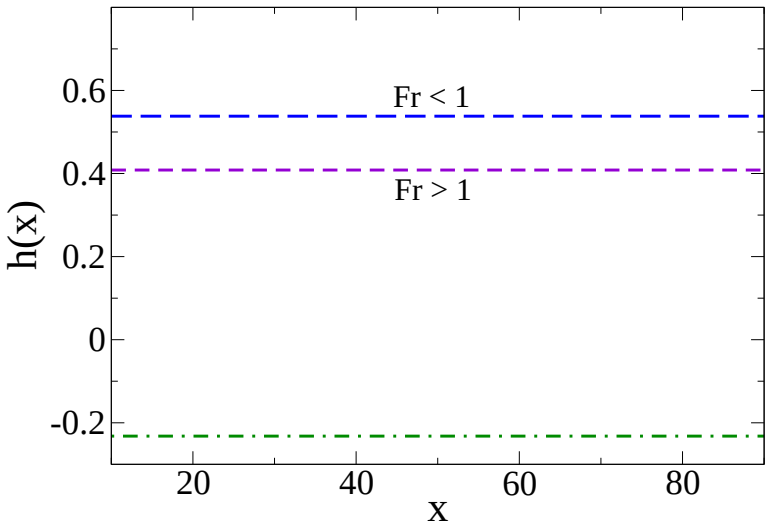

Figure 2.2: Roots of the cubic equation (2.3) for $Q = 1.0m^2/s, C = 7.0m^2/s^2, g = 9.8m/s^2$. There are two constant height solutions for the same value of C and Q. However, the equation predicts no transition between the two solutions. A supercritical flow ($Fr > 1$) remains supercritical and subcritical flow ($Fr < 1$) remains subcritical at all downstream distances. The dashed line in green is the negative unphysical solution.

particular value $C = \frac{2}{3}g^{\frac{2}{3}}Q^{\frac{2}{3}}$ corresponds to a repeated root and to $Fr = 1$.

2.2.2 Circular

In a circular geometry, the counterpart of equation 2.1 are,

$$\frac{u^2}{2} + gh = C, \tag{2.4}$$

$$uhr = Q, \tag{2.5}$$

where Q and C are constants of integration and physically correspond to energy per unit mass and volume flow rate respectively. Elimating u from the two equations, we obtain a cubic which can be solved to obtain

$$r = \frac{Q}{h\sqrt{2(C - gh)}}, \tag{2.6}$$

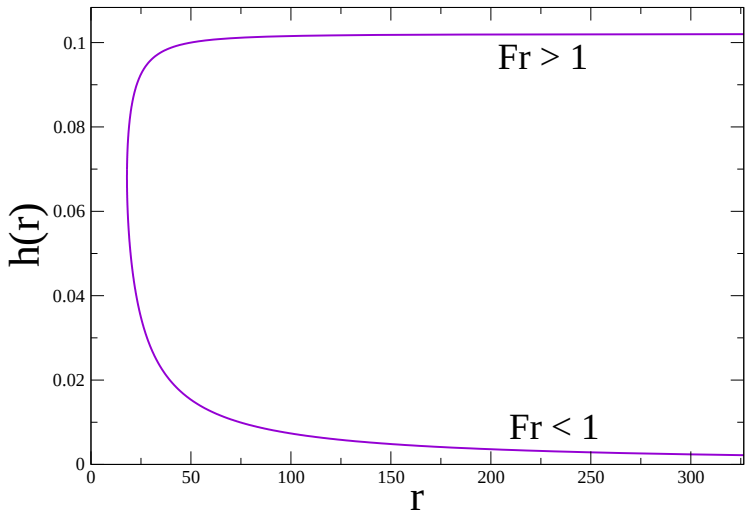

Figure 2.3: A plot of equation 2.6 for $Q = 1.0m^3/s$,$C = 1.0m^2/s^2$ and $g = 9.8m^2/s$. At large radii, two heights are possible in analogy with the planar case, one with $Fr > 1$ and another with $Fr < 1$. Note however that unlike the planar case, there are no real solutions below a certain radius for any value of Q and C [Bohr *et al.*, 1993]

Note that unlike the solution of equation (2.3), here h depends on the coordinate r. The solution of this equation [Bohr *et al.*, 1993] is plotted in figure 2.3.

Again there are two possible solutions for film thickness at a given spatial location, but no transition between the two is predicted. It is clear from figure 2.2 and 2.3 that while the inviscid shallow-water equations provide the basis for treating hydraulic jumps as shocks, they do not explain why a hydraulic jump should necessarily occur. Thus all that we may predict from inviscid shallow-water theory is that if a jump were to be assumed at a given location, the Froude number must go through unity there.

2.3 Viscous shallow-water equations

In order to explain a hydraulic jump, it has therefore traditionally been considered important to include the effects of viscosity. In the typical range of experimental parameters, it has been found [Watanabe *et al.*, 2003] that the near-wall vorticity diffuses across the entire film-thickness well upstream of the jump, so viscous effects

are likely to influence the jump dynamics substantially. The study of viscous effects dates back to Tani-Kurihara [Kurihara, 1946; Tani, 1949] who included a boundary-layer type term in the shallow-water equations. These equations are called the boundary-layer shallow-water equations referred to hereafter as BLSWE. They have been studied extensively in literature although mostly through the procedure of vertical-averaging [Bohr *et al.*, 1993; Kasimov, 2008; Rao & Arakeri, 1998; Rao, 1994; Singha *et al.*, 2005; Tani, 1949; Watanabe *et al.*, 2003]. This procedure while providing some useful predictions, gives a very unreal height profile near the jump: In a circular geometry, it turns around to form a spiral and in a planar geometry it just turns around. Before we delve into a discussion of the origin of this unrealisitic behaviour, we start with a discussion of the BLSWE in planar and circular geometries.

2.3.1 Planar

The BLSWE with the simplified boundary-conditions and the local and global continuity equations in a planar geometry are respectively

$$\begin{aligned} uu_x + wu_z &= -\frac{1}{\rho}gh' + \nu u_{zz}, \\ u_z|_{z=h(x)} = 0, u|_{z=0} = w|_{z=0} = 0, p|_{z=0} &= 0, \\ u_x + w_z &= 0, \\ Q &= \int_0^{h(x)} u dz, \end{aligned} \tag{2.7}$$

Here u and w are the respective velocity components in the coordinates x and z, $h' \equiv dh/dx$, ν is the kinematic viscosity, g is the acceleration due to gravity and Q is the volume flow-rate per unit transverse depth (m^2/s). The boundary conditions are of a stress-free interface and no-slip, no-penetration at the wall. Note that the boundary-condition of zero pressure at the interface has already been used to replace the pressure gradient term in the x momentum equation.

2.3.2 Circular

The BLSWE with the simplified boundary-conditions in a circular geometry is

$$\begin{aligned} uu_r + wu_z &= -\frac{1}{\rho}gh' + \nu u_{zz}, \\ u_z|_{z=h(r)} = 0, u|_{z=0} = w|_{z=0} &= 0, p|_{z=0}, \\ (ru)_r + (rw)_z &= 0, \\ Q &= 2\pi r \int_0^{h(r)} u dz, \end{aligned} \tag{2.8}$$

Here u and w are the respective velocity components in the coordinates r and z, $h' \equiv dh/dr$, Q is the volume flow-rate (m^3/s) while all other parameters and boundary-conditions remain the same as in the planar case.

It can be argued that equation (2.7) (and correspondingly equaton (2.8)) follows from Navier-Stokes equations from assuming that streamwise variations are small, i.e., $h' << 1$, and $\partial/\partial x << \partial/\partial z$. Consequently, the shear-stress boundary condition appears in its simplified form and non-hydrostatic contributions to pressure are neglected.

2.3.3 Derivation of the BLSWE from the Navier-Stokes equations

Equations (2.7) and (2.8) can also be derived from the corresponding Navier-Stokes equations and the exact boundary conditions using a rational asymptotic procedure. The scalings are not new and were first obtained in [Bowles & Smith, 1992]. We reproduce it here for completeness. It is sufficient to present it in a planar geometry. We introduce non-dimensional variables as $\tilde{u} = \frac{uH_1}{Q}$, $\tilde{w} = \frac{wH_1}{Q}$, $\tilde{h} = \frac{h}{H_1}$, $\tilde{p} = \frac{p}{\rho g H_1}$, $\tilde{x} = \frac{x}{H_1}$ and $\tilde{z} = \frac{z}{H_1}$ where $Re = \frac{Q}{\nu}$ and $Fr = \frac{Q}{gH_1^{1.5}}$. Here H_1 is the depth of the flow at some location upstream and L can considered the "width" of the jump (see figure 2.4). We drop the tilde over the nondimensional variables to obtain the non-dimensional Navier-stokes equations with the exact boundary conditions.

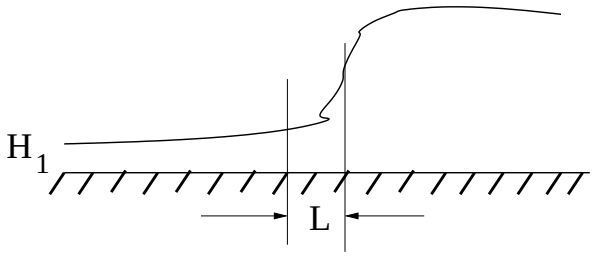

Figure 2.4: Schematic of a planar hydraulic jump where the flow is from left to right. The film thickness is H_1 at some upstream location. L can be thought of as the length-scale of interaction [Bowles & Smith, 1992]. The near-wall vorticity has diffused across the entire film in the location where the film-thickness is H_1

$$
\begin{aligned}
uu_x + wu_z &= -\frac{1}{Fr}p_x + \frac{1}{Re}\left[u_{xx} + u_{zz}\right] \\
uw_x + ww_z &= -\frac{1}{Fr}p_z - \frac{1}{Fr} + \frac{1}{Re}\left[w_{xx} + w_{zz}\right] \\
u_x + w_z &= 0 \\
\int_0^1 u dz &= 1 \\
p|_{z=1} &= \frac{2Fr}{Re}\left[\frac{h_x^2 - (u_z + w_x)h_x + w_z}{1 + h_x^2}\right]_{z=1} \\
\left[\frac{2(u_x - w_z)h_x + (u_z + w_x)(h_x^2 - 1)}{1 + h_x^2}\right]_{z=1} &= 0 \\
u = w &= 0|_{z=0}
\end{aligned}
\tag{2.9}
$$

We now assume that in the limit $Re \to \infty$ and $Fr \sim O(1)$, the length L is of $O(Re)$ (this automatically restricts us to weak jumps). Thus the x-scale is $O(Re)$ and since the flow is fully developed $z \sim O(1)$, $u \sim O(1)$. Local continuity implies $w \sim O(\frac{1}{Re})$. We thus introduce new rescaled variables defined as : $\bar{x} = \frac{x}{Re}$, $\bar{z} = z$, $\bar{u} = u$, $\bar{w} = \frac{w}{1/Re}$, $\bar{h} = h$, $\bar{p} = p$. It is now understood that as $Re \to \infty, Fr \sim O(1)$, all quantities with a bar are of $O(1)$. With this transformation, we obtain from

equation (2.9)

$$\begin{aligned}
\frac{1}{Re}\bar{u}\bar{u}_{\bar{x}} + \frac{1}{Re}\bar{w}\bar{u}_{\bar{z}} &= -\frac{1}{FrRe}\bar{p}_{\bar{x}} + \frac{1}{Re}\left[\frac{1}{Re^2}\bar{u}_{\bar{x}\bar{x}} + \bar{u}_{\bar{z}\bar{z}}\right] \\
\frac{1}{Re^2}\bar{u}\bar{w}_{\bar{x}} + \frac{1}{Re^2}\bar{w}\bar{w}_{\bar{z}} &= -\frac{1}{Fr}\bar{p}_{\bar{z}} - \frac{1}{Fr} + \frac{1}{Re}\left[\frac{1}{Re^3}\bar{w}_{\bar{x}\bar{x}} + \frac{1}{Re}\bar{w}_{\bar{z}\bar{z}}\right] \\
\bar{u}_{\bar{x}} + \bar{w}_{\bar{z}} &= 0 \\
\int_0^1 \bar{u} d\bar{z} &= 1 \\
\bar{p}|_{\bar{z}=1} = \frac{2Fr}{Re}\left[\frac{\frac{1}{Re^2}\bar{h}_{\bar{x}}^2 - (\bar{u}_{\bar{z}} + \frac{1}{Re^2}\bar{w}_{\bar{x}})\frac{1}{Re}\bar{h}_{\bar{x}} + \frac{1}{Re}\bar{w}_{\bar{z}}}{1 + \frac{1}{Re^2}\bar{h}_{\bar{x}}^2}\right]_{\bar{z}=1} & \\
\left[\frac{\frac{2}{Re^2}(\bar{u}_{\bar{x}} - \bar{w}_{\bar{z}})\bar{h}_{\bar{x}} + (\bar{u}_{\bar{z}} + \frac{1}{Re^2}\bar{w}_{\bar{x}})(\frac{1}{Re^2}\bar{h}_{\bar{x}}^2 - 1)}{1 + \frac{1}{Re^2}\bar{h}_{\bar{x}}^2}\right]_{\bar{z}=1} &= 0 \\
\bar{u} = \bar{v} = 0|_{\bar{z}=0} &
\end{aligned} \tag{2.10}$$

Retaining only terms of $O(1)$, we obtain the system

$$\begin{aligned}
\bar{u}\bar{u}_{\bar{x}} + \bar{w}\bar{u}_{\bar{z}} &= -\frac{1}{Fr}\bar{p}_{\bar{x}} + \bar{u}_{\bar{z}\bar{z}} \\
\bar{p}_{\bar{z}} &= -1 \\
\bar{u}_{\bar{x}} + \bar{w}_{\bar{z}} &= 0 \\
\int_0^1 \bar{u} d\bar{z} &= 1 \\
\bar{p}|_{\bar{z}=1} &= 0 \\
\bar{u}_z &= 0 \\
\bar{u} = \bar{w} &= 0|_{\bar{z}=0}
\end{aligned} \tag{2.11}$$

By integratintg the equation $\bar{p}_{\bar{z}} = -1$ and using the simplified boundary-condition on pressure, one can obtain the hydrostatic pressure assumption. Using this we thus recover the system of equation (2.7) from (2.11). A similar set of scalings can be followed to obtain the system of equation (2.8) from the corresponding axisymmetric version of Navier-Stokes equations and the exact boundary conditions.

2.3.4 Vertical averaging of the BLSWE

The BLSWE (2.7) and (2.8) constitute a closed set of equations in the unknowns u, w and h. There are three independent equations for three unknowns and hence this system can be solved numerically. However, the traditional technique used in literature [Bohr *et al.*, 1993; Kasimov, 2008; Rao, 1994; Singha *et al.*, 2005; Tani, 1949; Watanabe *et al.*, 2003] has been to vertically average these equations to obtain an evolution equation for the height-profile. The main contribution of this chapter is a new transformation of the equations (2.7) and (2.8) into a form more amenable to obtaining analytical and numerical solutions. Since we are going to compare our results to those obtained from vertical averaging, we roughly outline here the procedure used for deriving evolution equations using vertical averaging. In the process, it will also become clear to the reader as to what the problems are with the vertical averaging procedure. These problems are seldom if ever discussed in the literature.

Closure problem and other inconsistencies

We take the closed system of equations (2.7) and integrate them vertically. Integrating the local continuity equation from 0 to y and using the no-penetration boundary condition, we obtain

$$w|_{z=h(x)} = -\int_0^z u_x dz \tag{2.12}$$

Substituting the expression of w from (2.12) and integrating the momentum equation in (2.7) we obtain

$$\int_0^{h(x)} u u_x dz + \int_0^{h(x)} (-\int_0^z u_x dz) u_z dz = -g \int_0^{h(x)} h' dz + \nu \int_0^{h(x)} u_{zz} dz \tag{2.13}$$

$$\Rightarrow \int_0^{h(x)} (u^2)_x dz - U(x) \int_0^{h(x)} u_x dz = -ghh' - \nu u_z|_{z=0} \tag{2.14}$$

where $U(x)$ stands for $u(x, h(x))$ and the no-slip boundary-condition has been used. Using Leibniz rule for differentiation of an integral, this can be simplified to

$$\frac{d}{dx}\left(< u^2 >\right) = -ghh' - \nu u_z|_{z=0} \tag{2.15}$$

where $< u^2 > \equiv \int_0^{h(x)} u^2 dz$. The global continuity equation is

$$< u >= Q \tag{2.16}$$

We now have more unknowns than equations, unless we can relate $< u^2 >$ to h and $u_z|_{z=0}$. To do this, and thus close the system, we must resort to modelling, which can be done in different ways. The traditional approach to close the system is to make a self-similarity assumption on the velocity profile *i.e.* to express u as

$$u = V(x) f'(\eta)\,. \tag{2.17}$$

where $\eta = \frac{z}{h(x)}$, $f' \equiv df/d\eta$ where f is a non-dimensional streamfunction, and $V(x)$ has the dimensions of velocity. This assumption leads to the closure for the system when one assumes a form for $f[\eta]$. It is common to assume a polynomial form for $f[\eta]$, parabolic being the usual choice because the three coefficients of the parabolic form can be determined from the boundary-conditions and global mass-conservation without needing any more assumptions or fitting parameters. The qualitative nature of the solution of the evolution equation that is derived from the self-similar mode of obtaining closure, does not however depend on whether we choose a quadratic, a cubic or any higher-order polynomial [Watanabe *et al.*, 2003]. These evolution equations generically predict unphysical height-profiles near the jump irrespective of the order of the polynomial used to obtain closure. In a recent attempt at improving this deficiency [Bonn *et al.*, 2009; Watanabe *et al.*, 2003] have proposed a model which still uses vertical-averaging but does away with the assumption of self-similarity. Instead it allows the "shape" of the velocity-profile to evolve with streamwise distance. This model is an interesting one which gives useful answers which agree reasonably well [Watanabe *et al.*, 2003] with experiments. However, this model also has drawbacks and we will discuss them when we compare our results later in the chapter with those obtained from experiments and models.

We now show an inconsistency in the entire procedure of obtaining closure

using a self-similar velocity profile. For ease, we stick to planar geometry and equation (2.7). We remind the reader that a self-similarity assumption on the velocity profile is not sufficient in itself for achieving closure and we also need to assume a particlular form for $f'(\eta)$ in equation (2.17). If however instead of *assuming* a form for $f'(\eta)$, we *derive* an equation for it from the governing equation (2.7), we obtain

$$\left(\frac{1}{Re}\right)\frac{d^3f}{d\eta^3} + \left\{\left(\frac{df}{d\eta}\right)^2 - \frac{1}{Fr^2}\right\}h' = 0 \tag{2.18}$$

where Re is as defined earlier and $Fr^2 = Q^2/gh^3$. Here we have used a self-similar assumption of the form in equation (2.17) where $V(x) = \frac{Q}{h(x)}$. One can now easily see the discrepancy in equation 2.18. While we had assumed f to be only a function of η, equation 2.18 tells us that this assumption is inconsistent with the governing equation as equation 2.18 has coefficients *viz.* h' and $Fr^2 \equiv Q^2/gh^3$ which are functions of the streamwise coordinate x. This thus shows that the self-similar assumption is inconsistent except under certain limits. In the limit of $Fr \to 0$ and $Fr \to \infty$ however, equation 2.18 becomes variable-separable and thus admits a similarity solution. The high Froude number similarity solution was reported earlier by Watson [1964]. He set gravity to zero in the BLSWE (2.7) and obtained a closed form similarity solution, and the condition $h'Re = \pi/\sqrt{3} = 1.8137$. Further f' was expressed in terms of a Jacobian elliptic function. The above procedure also shows that such a self-similar solution is to be expected in the limit of high Fr. Thus the reader is reminded that although (2.17) is crucial for obtaining closure, its not necessarily a good option. The drawbacks of this closure model will further become apparent in the next chapter where we study strong jumps and examine the consequences of this assumption. Presently, we still follow the self-similar assumption on the velocity profile. Assuming a parabolic form for $f'[\eta]$, we obtain using the no-slip and zero-shear boundary conditions

$$u = U(x)\left[2\eta - \eta^2\right] \tag{2.19}$$

where $U(x)$ is as defined in equation (2.14). Using global continuity, we find

$$U(x) = \frac{3Q}{2h(x)} \tag{2.20}$$

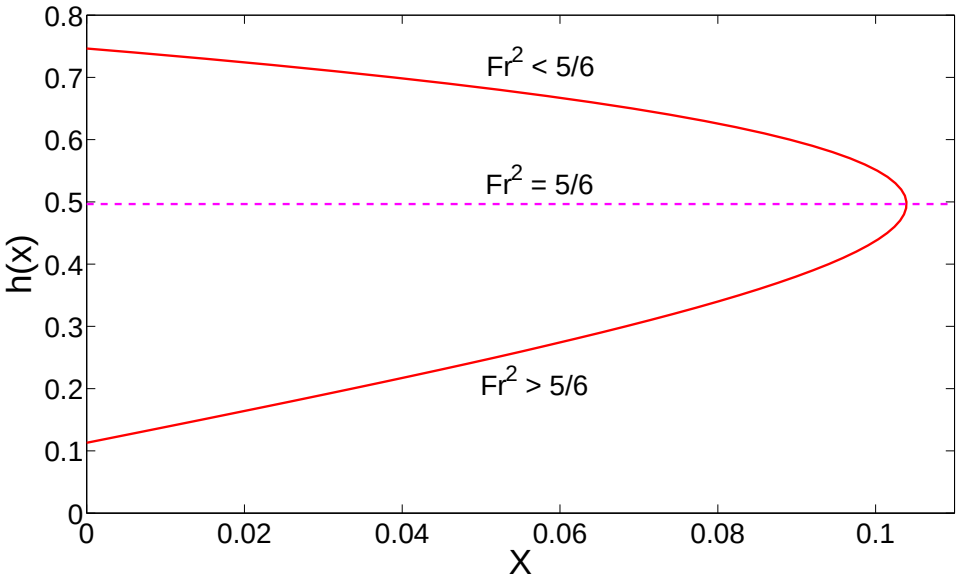

Figure 2.5: Solution of equation (2.21) for $Q = 1m^2/s$, $g = 9.8m/s^2$, $\nu = 1m^2/s$ and $C = 0.6757$. The curve 'turns around' when it reaches the critical height $h_c = (6Q^2/5g)^{\frac{1}{3}}$ where $Fr^2 \equiv Q^2/gh^3 = 5/6$

Substituting (2.19) in equation (2.15), we thus obtain our final evolution equation

$$\frac{dh}{dx} = \frac{15\nu Q}{6Q^2 - 5gh^3} \tag{2.21}$$

which can be integrated to obtain

$$x = \frac{6Q^2h - (5/4)gh^4 - 15Q\nu}{C} \tag{2.22}$$

where C is the constant of integration. This solution was earlier obtained by [Singha *et al.*, 2005]. A similar vertical averaging procedure with a self-similar parabolic velocity profile can be used to obtain an evolution equation in circular geometry.

$$\frac{dh}{dr} = \frac{\frac{5\pi\nu}{Q}r^2 - h}{r - \frac{10\pi^2 g}{3Q^2}r^3h^3} \tag{2.23}$$

This equation was obtained and analysed in Tani [1949], Bohr *et al.* [1993] although

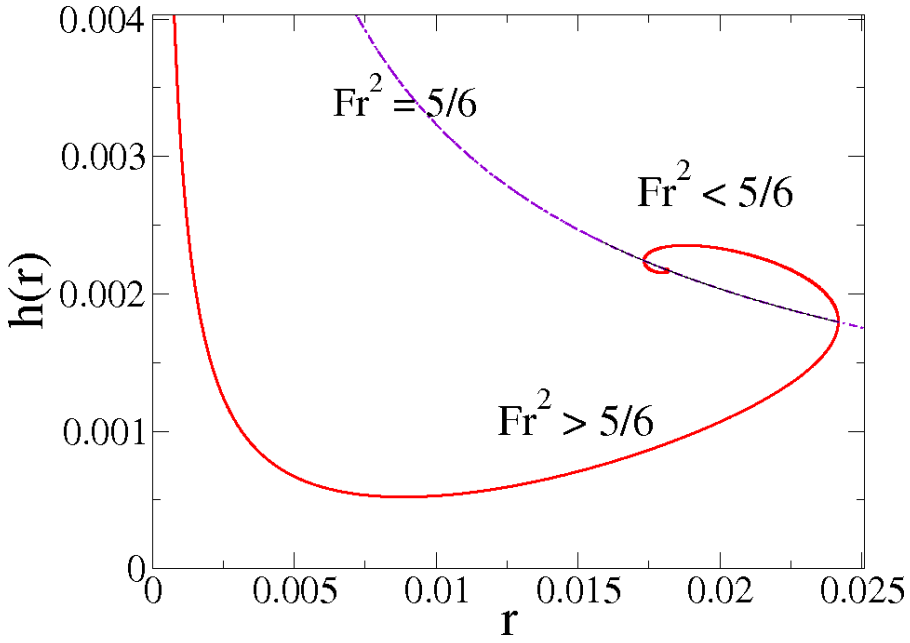

Figure 2.6: Solution of equation (2.23) for $Q = 33$ x $10^{-6} m^3/s$, $\nu = 14$ x $10^{-6} m^2/s$, $g = 9.8 m/s^2$. The curve 'turns around' when it intersects the critical height curve $h_c = (3Q^2/10\pi^2 g)^{\frac{1}{3}}\, r^{\frac{2}{3}}$. Unlike the planar case where h_c is a constant, in the circular case h_c varies with radius.

no analytical solutions to it have been reported in literature. The analytical solution (2.22) and a numerical solution of equation (2.23) are plotted in figure 2.5 and figure 2.6 respectively. In the planar case, the height is a mutivalued function of distance and there are no solutions beyond a certain distance as the curve 'turns around'. In the circular case, the height profile spirals around a point where $\frac{dh}{dr}$ is of the form $\frac{0}{0}$. We label this point as the *critical point* of the system (Incidentally notice that the origin is also a trivial critical point of the system). It is interesting that equation (2.23) is unchanged under the transformation $(r, h) \longrightarrow (-r, h)$ implying that the solution in the positive h and negative r plane is a mirror image of the solution in the positive h and positive r plane. Some care needs to be taken in the numerical solution of equation (2.23). Firstly, note from figure 2.6, that the spiral winds more and more tightly as we approach the critical point and we have a very frequent divergence of its slope. We work around this numerical difficulty by repeatedly exchanging the dependent and the independent variables. Thus where

dh/dr is large, dr/dh is small and there we treat r as the independent and h as the dependent variable and solve equation 2.23. The reverse procedure is followed where dr/dh is large. Secondly, since all initial conditions spiral onto the critical point, it is important to ensure accuracy by decreasing the step size as we approach the critical point.

2.3.5 Viscous to inviscid transition of the vertically averaged solution

While the solutions in figure 2.5 and figure 2.6 have been well-studied [Bohr *et al.*, 1993; Singha *et al.*, 2005; Tani, 1949], the relation of these solutions to their inviscid counterparts in figure 2.2 and 2.3, has never been discussed before to the best of our knowledge and we discuss it briefly here. For understanding the viscous to inviscid transition in the planar case, see figure 2.7. It is seen that every curve turns around when it reaches the critical height h_c (ie. the height where Froude becomes unity.) Every curve has two arms, the lower arm corresponding to $Fr^2 > \frac{5}{6}$ while the upper arm corresponds to $Fr^2 < \frac{5}{6}$. As the viscosity is decreased, the x-location at which the turning around occurs, goes to ∞ and thus we recover the two constant height solutions of (2.2). Note however, that here the constant height solution will correspond to $Fr^2 > \frac{5}{6}$ and $Fr^2 < \frac{5}{6}$ instead of $Fr > 1$ and $Fr > 1$ as in the inviscid case. This is due to the parabolic velocity-profile assumption compared to the inviscid case whereas the inviscid velocity profile is uniform.

Understanding of the viscous to inviscid transition in the circular case is more involved. The invscid solution in the shallow-water case is a horizontal U-shaped curve in figure 2.3 while the viscous solution is plotted in figure 2.6. To understand the relation between these two solutions which look very different, we rewrite equation (2.23) in nondimensional form as

$$\frac{dh}{dr} = \frac{(\frac{5\pi}{Re_0})r - \frac{h}{r}}{1 - (\frac{5}{6Fr_0^2})r^2h^3}, \tag{2.24}$$

where r and h are dimensionless having been nondimensionalized by r_0 and h_0 respectively, characteristic radial and vertical scales at some upstream location.

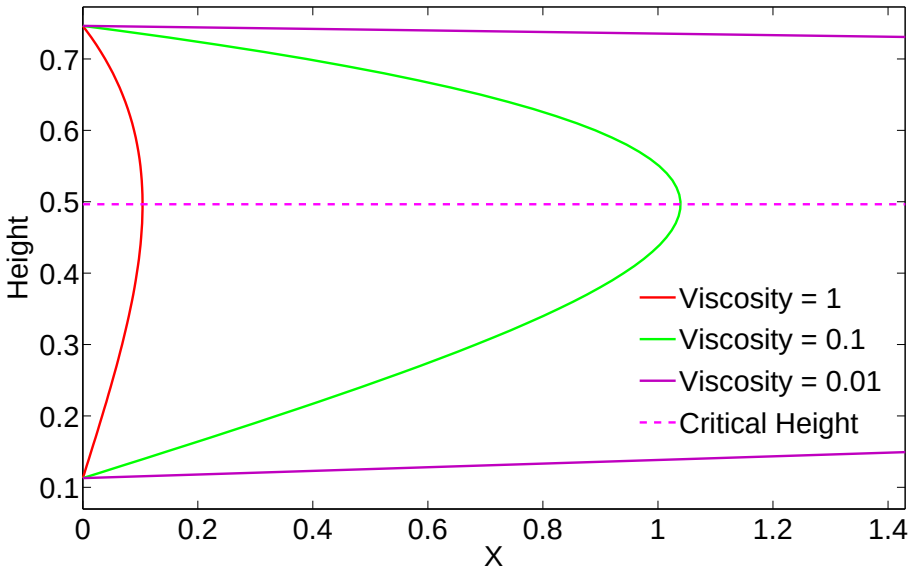

Figure 2.7: Plots of equation (2.22) for different values of viscosity ν. $Q = 1$, $g = 9.8$ and $C = 0.6757$. The curve for $\nu = 0.01$, turns around at a large value of x not shown in the figure.

The initial Reynolds and Froude numbers are defined as $Re_0 = \frac{Qh_0}{r_0^2\nu}$ and $Fr_0^2 = \frac{Q^2}{4\pi^2 r_0^2 g h_0^3}$. The critical point (as defined earlier) is located at

$$r_c = 0.364 Re_0^{\frac{3}{8}} Fr_0^{\frac{1}{4}}, \quad h_c = 2.083 Re_0^{-\frac{1}{4}} Fr_0^{\frac{1}{2}}, \tag{2.25}$$

Equation (2.24) is solved numerically for $Fr_0 = 2$ and different values of Re_0 and plotted in figure 2.8 and 2.9. With $Re_0 \to \infty$, the lower part of the spiral "unrolls" and goes to ∞ giving rise to the inviscid lower arm (see inset of figure 2.8). The upper arm of figure 2.9 looks like the inviscid upper-arm and at first sight it may seem from figure 2.9 that the upper-arm is qualitatively unaffected by viscosity and just like the inviscid upper arm, it also extends to arbitrary radius while asymptotically tending to a costant value. It was however argued by Bohr *et al.* [1993] that such an asymptotic behaviour is not possible. This was verfied numerically for different initial conditions and for every initial condition that we

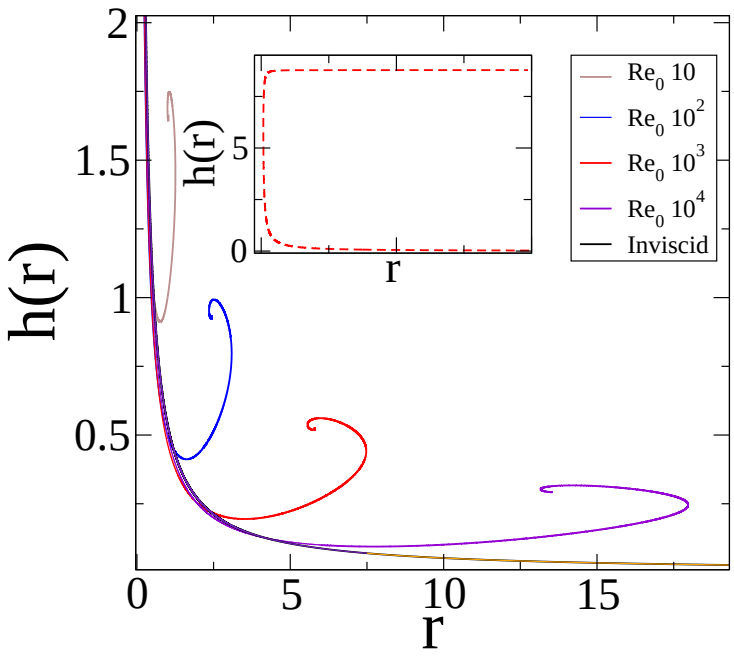

Figure 2.8: The rolling away of the critical point with $Fr_0 = 2$, as $Re_0 \to \infty$. As we approach the inviscid limit we recover the lower arm of the horizontal U-shaped curve of figure 2.3 also shown in the inset.

tried, it was found that the upper arm drops into the negative h plane at a certain radius as can be seen from the inset in figure 2.9. For many initial conditions, the upper arm can decay extremely slowly and in one case tried, the upper arm continues upto a radius of 10^{10} and then sudenly drops down. This is consistent with the argument of [Bohr *et al.*, 1993] that for any given initial condition, equation (2.24) has no solutions which extend upto infinite radius. As we increase the Reynolds the radius at which the upper arm drops into the negative h plane, tends to ∞ thus recovering the inviscid solution. Also note that for a given initial condition, no viscous spiral extends upto arbitrary small radius. This lack of solutions at small radius is not a viscous effect but a carry-over from the corresponding inviscid solution shown in figure 2.3 where too for a given initial condition there are no solutions at arbitrarily small radius. This completes our understanding of how does the inviscid U-shaped curve arise from the spirals as we increase the Reynolds number.

We conclude this section by presenting an analytical solution in the neighbour-

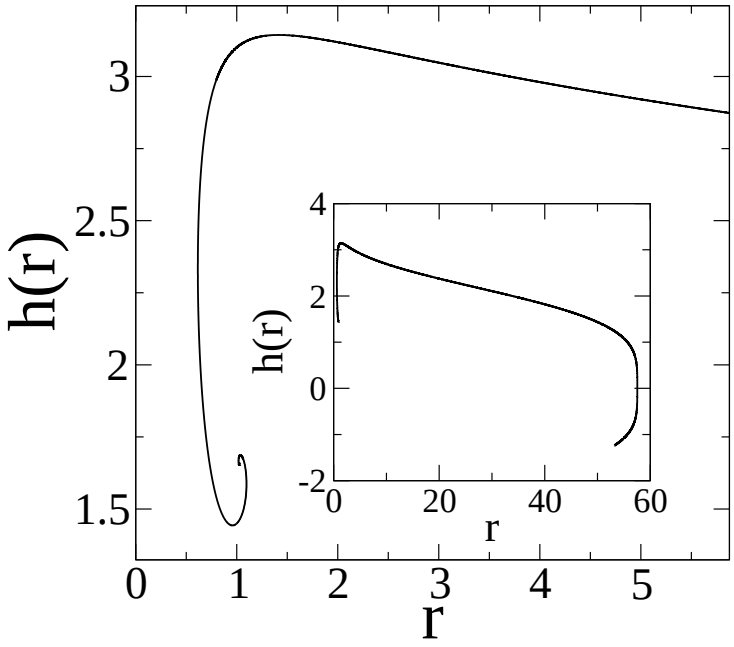

Figure 2.9: The upper arm of the viscous spiral resembles the upper arm of the inviscid solution, but unlike it cannot continue to infinity, as seen in the inset.

hood of the critical point. Scaling the height and radius by the coordinates of the critical point h_c and r_c, translating our origin to that location, and linearising equation (2.24) about the critical point values, we have

$$\frac{d\bar{h}}{d\bar{r}} = \frac{s-2}{3s+2}, \tag{2.26}$$

with $s \equiv \bar{h}/\bar{r}$, $\bar{r} = r/r_c - 1$ and $\bar{h} = h/h_c - 1$. This may be solved to give

$$\bar{r} = \frac{K}{\sqrt{3s^2+s+2}} \exp\left\{-\frac{3}{\sqrt{23}} \tan^{-1}\left[\frac{1+6s}{\sqrt{23}}\right]\right\} \tag{2.27}$$

where K is the constant of integration. This is a modified logarithmic spiral, which collapses very sharply into the critical point. The unphysical nature of the near-jump behaviour like the slope of the height-profile diverging, the profile 'turning-around', no solutions at arbitrary large streamwise distances etc. seems to be a generic feature of vertically averaged models using the self-similar assumption to obtain closure. This is partly due the fact that these equations have been derived

with the restriction $h' << 1$ and thus solutions where $h' \to \infty$ are in a domain where the underlying governing equation itself is invalid. The other reason is the self-similar assumption which leads to the dropping of higher-order derivatives in the streamwise direction, which are quite large in the near-jump region even for a weak-jump. Thus while vertical averaging itself is not an invalid mathematical procedure, we know of no easy, unique or consistent way of obtaining closure which does not suffer from the problems outlined above. To circumvent these problems, we propose a transformation of the $BLSWE$ in the next section. This transformation converts the BLSWE into a system which lends itself to analytical solutions in different limits and make it more amenable to numerical treatment. Further, without taking recourse to any modelling we are able to obtain jump-like transitions from our solution of the BLSWE.

2.4 Transformation of the BLSWE

2.4.1 In a planar geometry

The basic idea here is to use the streamfunction to reduce the number of independent variables in the equations (2.7) and (2.8). An additional benefit is that the global mass-conservation equation becomes a very simple equation. We use incompressibility to replace the velocity components with the streamfunction ψ and this is then non-dimensionalised as

$$\psi = Qf[\eta, \zeta], \quad \eta = \frac{z}{h(x)}, \quad d\zeta = \frac{dx}{h(x)Re}$$

so that $u = \frac{Q}{h} f_\eta$, $w = \frac{Q}{h}[\eta h' f_\eta - f_\zeta]$. Here $h' \equiv \frac{dh}{dx}$. For convenience the independent variable in the slope h' of the interface is retained as the dimensional x, while ζ is

used everywhere else. We then have the following

$$\begin{aligned} u &= \frac{Q}{h} f_\eta \\ w &= \frac{Q}{h}\left[\eta h' f_\eta - \frac{f_\zeta}{Re}\right] \\ u_x &= \frac{Q}{h^2}\left[\frac{f_{\eta\zeta}}{Re} - h' f_\eta - \eta h' f_{\eta\eta}\right] \\ u_z &= \frac{Q}{h^2} f_{\eta\eta} \\ u_{zz} &= \frac{Q}{h^3} f_{\eta\eta\eta} \\ u u_x + w u_z &= \frac{Q^2}{h^3}\left[\frac{f_\eta f_{\eta\zeta}}{Re} - h' f_\eta^2 - \frac{f_\zeta f_{\eta\eta}}{Re}\right] \end{aligned}$$

Substituting these in equation (2.7) we thus obtain

$$f_{\eta\eta\eta} - h' Re\left[\frac{1}{Fr^2} - f_\eta^2\right] = f_\eta f_{\eta\zeta} - f_{\eta\eta} f_\zeta \tag{2.28}$$

$$f(0,\zeta) = 0, \quad f_\eta(0,\zeta) = 0, f_{\eta\eta}(1,\zeta) = 0. \tag{2.29}$$

Here $Re \equiv Q/\nu$ and $Fr^2 \equiv Q^2/gh^3$. Equations 2.28 is going to be our central equation. At first glance equation (2.28) seems to have two unknowns viz. f and h'. However, it should be remembered that apart from respecting the boundary conditions (2.29), this equation must also satisfy the condition $f(1,\zeta) = 1$, which is the nondimensional form of global mass conservation. It will be seen that this provides a constraint using which we may determine $h'Re$. Hereafter, we will refer to these as the BLSWE and instead of the original equations 2.7 in primitive variables. Equation 2.28 is the BLSWE written down in coordinates which lend it to solution as successive ordinary differential equations in ζ and η and to simplification at various limits. Firstly, notice that the Reynolds number, which is constant for a given flow, merely causes a rescaling of x, and can be scaled out of equation 2.28. Secondly, since the additional constraint of global mass balance must be satisfied, $h'Re$ is not a free parameter. In fact, given a Froude number, this quantity is completely determined, since only select values of $h'Re$ will satisfy $f(1,\zeta) = 1$. Thus, given a starting Froude number, equation 2.28 may be solved not only to obtain the velocity profile at a given streamwise location, but to evolve the height profile of the film downstream. Since we obtain local velocity profiles and slopes,

we may march either downstream or upstream to get the height profile.

2.4.2 Analysis and numerical results - Planar Geometry

Let us now discuss the high and low Froude number limits of equation 2.28. For $Fr >> 1$, the first term within the square bracket in equation 2.28 may be dropped. We have seen that $h'Re$ depends on the Froude number alone. With the Froude number no longer present in the equation, $h'Re$ in this limit is a constant. Setting the right hand side of equation (2.28) to zero would reduce it to the similarity equation of [Watson, 1964]. Upon solving this and imposing the mass flux condition, it is found that $h'Re = 1.8138$ (see Figure 2.11), as in the gravity-free solution of Watson [1964]. Thus the height increases linearly at high Fr, qualitatively consistent with experimental findings [Bonn *et al.*, 2009; Singha *et al.*, 2005], and the Froude number $Fr = Q/(g^{1/2}h^{3/2})$ decreases as $x^{-3/2}$ with the downstream distance. The decrease of Froude number is also intutively seen if we remember that $Fr \equiv U_{av}/\sqrt{gh}$ and that viscous dissipation causes U_{av} to come down and due to global continuity h increases, thus causing Fr to come down monotonically. Thus the solution inevitably takes us towards $Fr = 1$, where a jump is seen. At very low Froude numbers on the other hand, the second term in the square bracket in equation 2.28 is negligible compared to the first. Since there is no x-dependant parameter in the problem in this limit, the right hand side can be set to zero. Thus we may obtain another self-similar solution in the form of a parabolic velocity profile, since the equation reduces to

$$f_{\eta\eta\eta} = \frac{h'Re}{Fr^2}, \quad h'Re = -3Fr^2 \qquad Fr \to 0. \tag{2.30}$$

The expression for $h'Re$ is obtained by integrating the first equation above in η and using the boundary conditions. Thus the height shows a slight downstream decrease at low Froude numbers.

The complete solution to equation (2.28) is now obtained at a given streamwise location. The approach is based on the fact that the BLSWE is derived by neglecting the non-hydrostatic pressure terms, which amounts to neglecting second and higher-order derivatives in ζ and retaining only the first derivative. This means we may treat the right hand side as a function of η alone, i.e., $f_\eta f_{\eta\zeta} - f_{\eta\eta} f_\zeta \equiv \phi(\eta)$, since for example, $f_{\zeta\zeta}$ being negligible implies that $f_\zeta = f_\zeta(\eta)$. If $\phi(\eta)$ were known,

then (2.28) would be just an inhomogeneous ordinary differential equation in η. Since we do not know it apriori we obtain $\phi(\eta)$ iteratively. The solution procedure uses three embedded iterative loops I_1 to I_3, and the outermost loop I_3 is designed to obtain $\phi(\eta)$, as discussed below. As a first approximation at the beginning of the computation, we set ϕ to 0 at every η. The middle loop I_2 is meant for arriving at the correct interface slope h'. We assume an $h'Re$ and begin at the innermost loop I_1. At $\zeta = 0$, we specify the starting Froude number Fr_0. We guess a slope for the velocity profile, $f_{\eta\eta}$ at the wall, and integrate the equation up to the film surface. By the Newton-Raphson technique, we iterate our guess for $f_{\eta\eta}(0, \zeta)$ until the stress-free boundary condition $f_{\eta\eta}(1, \zeta) = 0$ is satisfied at the film surface. We next enter loop I_2, where we obtain, again by Newton-Raphson technique, the correct $h'Re$ which ensures the satisfaction of global mass conservation. Loop I_3 is approached differently. We go to an incrementally downstream location $\zeta + \Delta\zeta$, use the same right hand side ϕ, and repeat loops I_1 and I_2. With the two neighbouring velocity profiles, we compute a new $\phi(\eta)$, which is usually a better approximation than the previous guess. Repeating this procedure until the right-hand side converges forms loop I_3. We now have a local solution, as well as a knowledge of the slope of the height, which enables us to proceed downstream or upstream as we wish by performing a quadrature in ζ. The entire height profile, as well as the velocity profiles at each location, may be obtained to excellent accuracy in a few seconds on a small computer.

At high Froude numbers only one solution is obtained, which is denoted here by P since it is of positive h', as seen in Figure 2.10. The slope of the height goes through a sudden increase in the neighborhood of $Fr = 1$, which is the critical value for a jump in the inviscid case. Further, the unphysical turning around of the height profile is absent. Downstream of the jump, in the regime of $Fr < 0.71$, equation (2.28) admits two solutions. In addition to the P solution, we have an N solution, labelled thus to denote that the slope of the height profile is negative in this case. These two are shown in figure 2.11 in terms of $h'Re$ versus the Froude number.

We now examine which of these solutions will be manifested. Up to $Fr = 0.71$, the P solution is the only possibility. It appears at first glance that the P solution would be sufficient at lower Froude as well. However, at low Froude numbers, the P solution constitutes a highly separated velocity profile. The separated region at

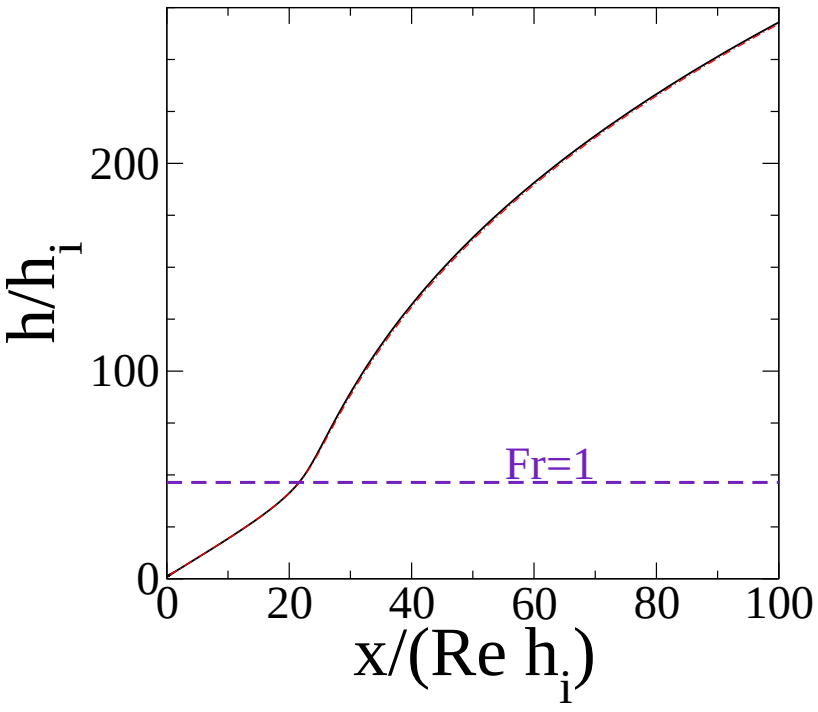

Figure 2.10: Variation of film height h with downstream distance of the P solution of equation 2.28. Notice the well-known [Bonn *et al.*, 2009] linear increase in height upstream of the jump. At $x < 22$, $Fr > 1$ and downstream, $Fr < 1$. h_i is the film height at the inlet.

a Froude number of 0.73 is seen in figure 2.12 to be quite large. As the Froude is further decreased, i.e., as one moves downstream, the separated region becomes larger and larger. The P solution is however not separated at Froude numbers above 0.8, i.e., at the jump and upstream of it, indicating a connection between the jump and flow separation. Profiles at various other Froude numbers are shown in the same figure. Figure 2.12 also underlines that the assumption of self-similar velocity profiles is only reasonable for Froude numbers above 1.5 or so. The N solution on the other hand is seen to be unseparated. It is better and better approximated by a parabolic profile as Fr decreases. Figure 2.13 shows the shear stress at the wall of the P and N solutions as functions of the Froude number. The rapidly increasing severity of separation in the P solution below $Fr = 0.8$ is evident. Given their inflexional nature, profiles with large separation are likely to be unstable. We therefore surmise that at some location downstream of the jump, the

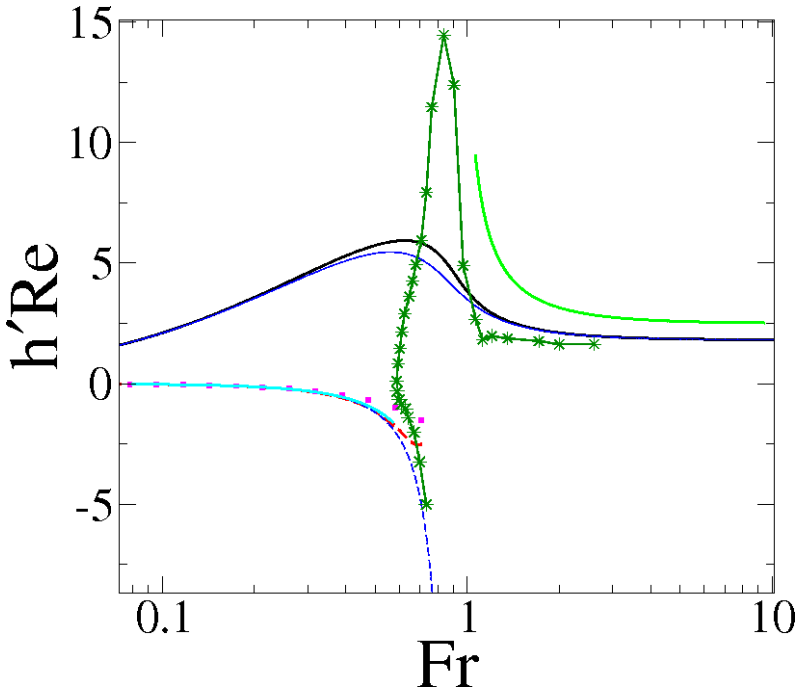

Figure 2.11: The slope of the film height as a function of the local Froude number. Thick black line: P solution of equation (2.28), thick red dashes: N solution for $Fr < 0.71$. The pink squares are the analytical solution (2.30) at low Fr. The line in green with symbols is obtained from Higuera's simulations, Figure 2 of [Higuera, 1994], for his case $S = 2$ where S is the inverse of Froude number. At high Fr, $h'Re \simeq 1.8138$ in agreement with [Higuera, 1994]. The thin blue lines are obtained by setting the right hand side of (2.28) to zero. The line in poison green and cyan are obtained from the self-similar solutions of 2.21

P solution becomes untenable, and the flow switches to the N. This is in analogy with the Falkner-Skan equations for adverse pressure-gradient boundary layers, which displays, for adverse pressure gradient, two such solutions, one separated and very unstable, and the other not, and much less unstable. For the present solutions, a stability study is underway, and initial results indicate that the P solution is extremely unstable at low Froude numbers. Given the highly non-parallel nature of the flow, that study is cumbersome and will be presented separately.

The predictions above are consistent with experimental observations, where the flow usually reattaches downstream [Higuera, 1994; Watanabe *et al.*, 2003]. Moreover, downstream of the reattachment point, the slope of the height profile is usually small and negative. The Froude number thus rises again downstream

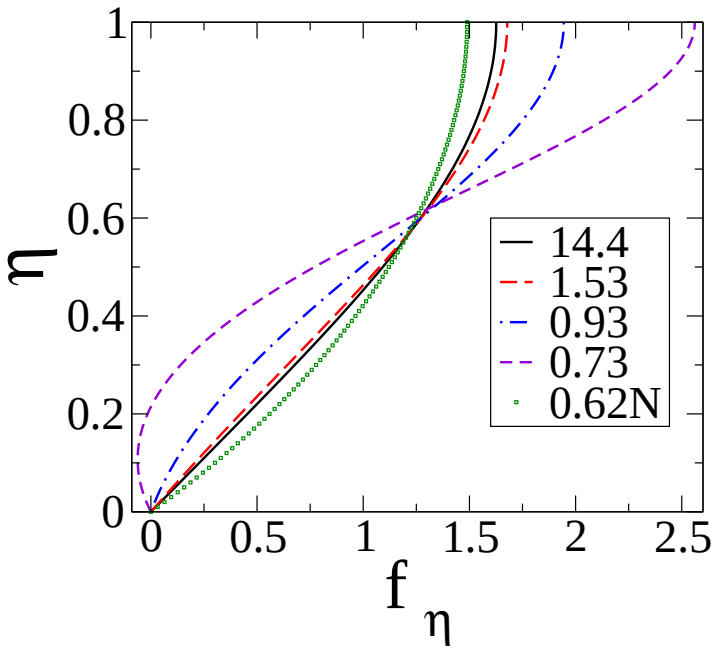

Figure 2.12: Velocity profiles for various Froude numbers, as listed. The curve for $Fr = 0.62$ is taken from the N solution, and is practically parabolic. Note the difference between the parabolic profile and the self-similar one at high Froude.

although slowly, as per the behaviour of solution N. We compare our results with those obtained in the numerical simulations of [Higuera, 1994]. Shown in green and blue respectively in Figure 2.11 and 2.13 are the slope of the height profile and the wall-shear stresses that we derive from [Higuera, 1994], as functions of Fr. The extreme right of the curve of Higuera corresponds to the most upstream location, and x increases monotonically as one moves along the green/blue line from this point. For the P solution, the height is a monotonically increasing function of x, and so $Fr = Q/(g^{1/2}h^{3/2})$ decreases monotonically. Higuera's curve with increasing x thus traces the P solution from right to left. For the N solution on the other hand, $h' < 0$, so the simulated curve turns around and traces it from left to right for increasing x.

Notice in Figure 2.11, that downstream of the jump i.e., at $Fr < 1$, the solution of [Higuera, 1994] transitions from the P solution to the N solution. The agreement with Higuera in the upstream and downstream regions is a check of our prediction that the slope for a given solution depends on the Froude number alone. It also

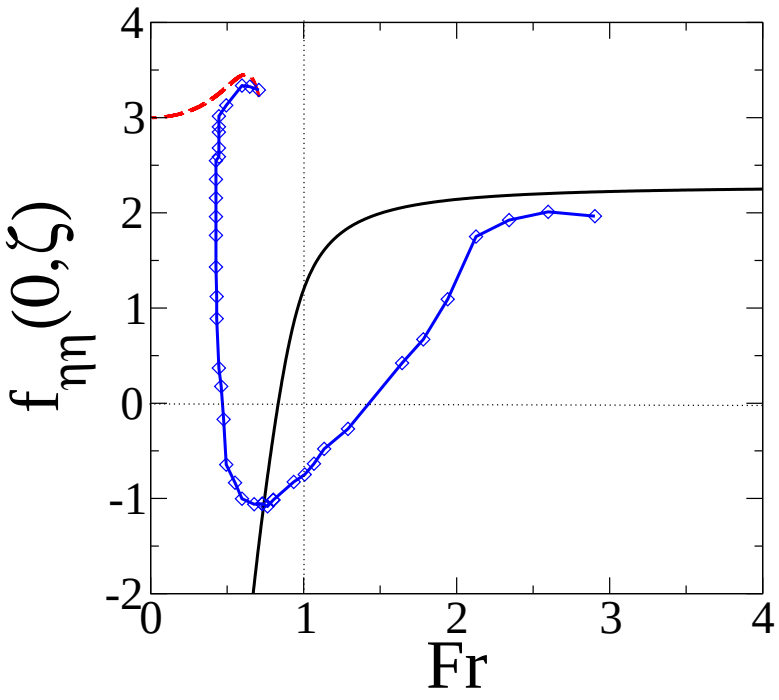

Figure 2.13: Wall-normal derivative of streamwise velocity at the wall, $f_{\eta\eta}(0,\zeta)$, as a function of local Froude number. Solid black line: P solution. Red dashes: N solution. The vertical line at $Fr = 1$ is provided to guide the eye. It is seen that the P solution flow separates downstream for $Fr < 1$. Fr is inversely related to x and hence the separated region is downstream. The line in blue with symbols is extracted from [Higuera, 1994], Figure 2, case $S = 2$.

supports our argument that away from the immediate neighborhood of the jump, the slope may be obtained locally. There is a sudden rise in the slope of the height profile near $Fr = 1$ in the numerical results too, but the quantitative behaviour is different. The switching from the N to the P solution, and the detailed behaviour in the region of this switching cannot be captured by the BLSWE. The local solution of the BLSWE thus fails in the immediate vicinity of the jump, whereas the numerical procedure of [Higuera, 1994] is able to go through, presumably because of numerically introduced effective higher-order derivatives which are barred in the BLSWE. The question now is whether the complete physics in the immediate vicinity of even a weak jump is contained in the shallow water theory. The present work indicates a negative answer, but does not constitute a proof, since it is possible that more solutions of the BLSWE exist. In the next chapter it is argued from the

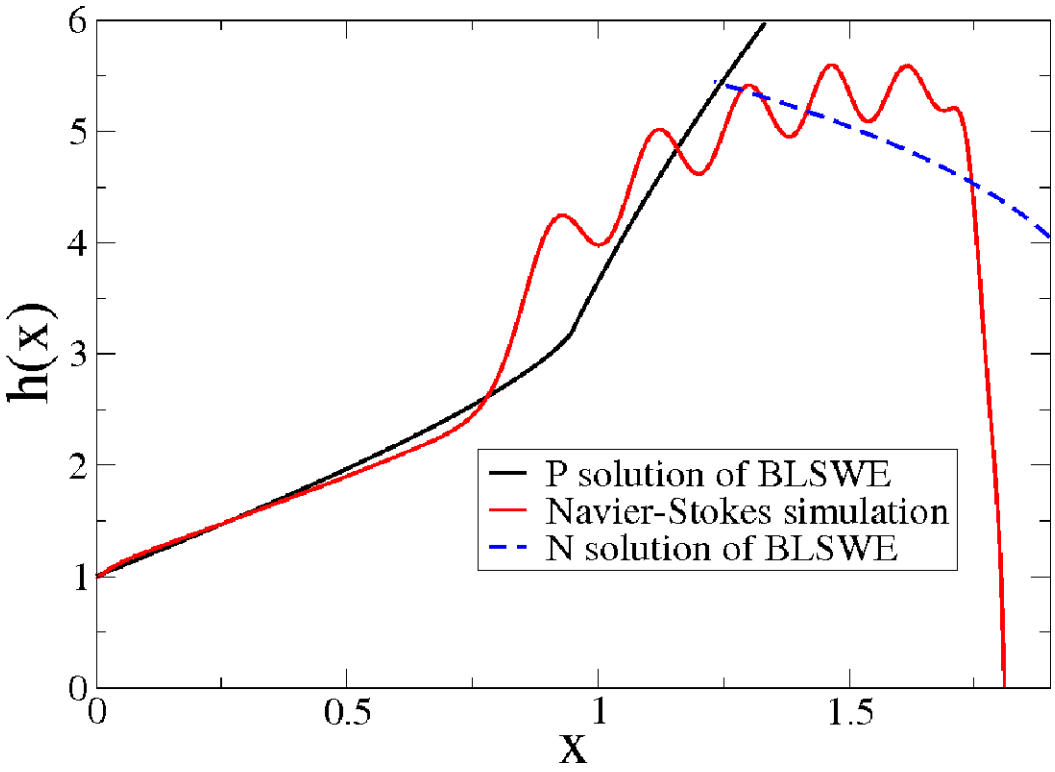

Figure 2.14: Comparison of the P and the N solution with the height profile obtained from Navier-Stokes simulations. Note that the waves occuring downstream of the jump *cannot* be predicted by a shallow-water theory [Benjamin & Lighthill, 1954]

complete equations that shallow-water theory is untenable in this region. In fact it turns out that in a narrrow vicinity of $Fr = 1$, gravity and inertia are unimportant and the dominant terms all arise from the vertical momentum equation. The divergence of the N solution as it reaches $Fr \sim 0.7$ in Figure 2.11 is consistent with the singularity in the downstream boundary condition of [Higuera, 1994; Watanabe *et al.*, 2003], where the local Froude number is around unity. Note that both the analytical and the numerical solution reach a Froude number between 0.7 and 0.8 at the most downstream location, where the height rapidly decreases, and its slope appears to diverge in the negative direction. To our knowledge, this is the first time the existence of multiple solutions downstream of the jump is reported, along with its consequences, including the finding that a self-similar parabolic profile is a good assumption at very low Froude numbers.

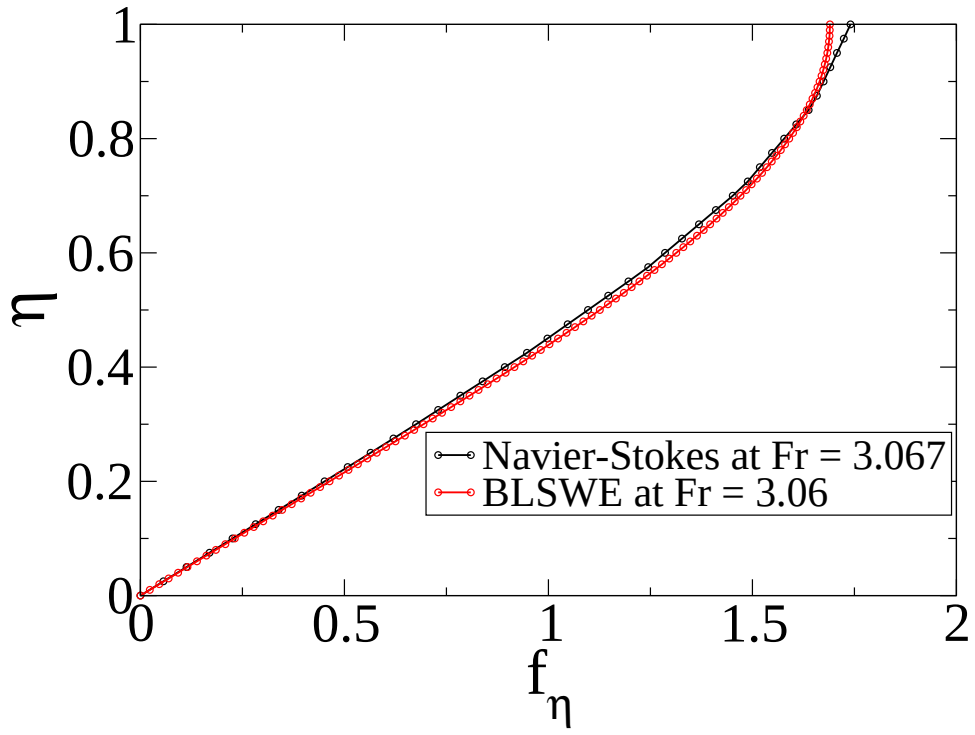

Figure 2.15: Comparison of velocity profiles obtained from the planar BLSWE with those obtained from Navier-Stokes simulations. The simulations are explained in greater detail in later chapters and are characterized by the inlet Reynolds Re_i and inlet Froude Fr_i numbers. The velocity profile is obtained from a simulation with $Re_i = 125$ and $Fr_i = 6$ and corresponds to a location where the local Froude $Fr^2 \equiv Q^2/gh^3 = 3.067$. The BLSWE velocity profile is obtained from a location where $Fr = 3.06$ and this corrresponds to the P solution. Note that the profiles almost lie on top of each other confirming that far upstream of the jump, the BLSWE is a good approximation to the full Navier-Stokes equations.

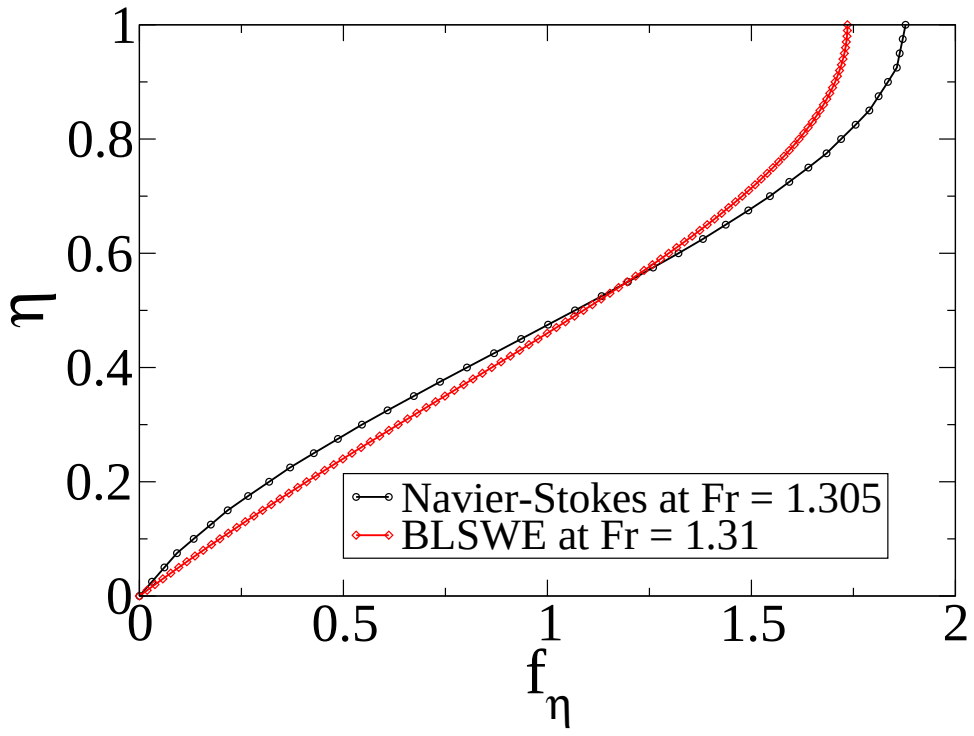

Figure 2.16: Simulation parameters, $Re_i = 125$ and $Fr_i = 6$. The streamwise location corresponds to a local Froude $Fr^2 \equiv Q^2/gh^3 = 1.305$. The BLSWE velocity profile corresponds to a location where $Fr = 3.06$. This profile corrresponds to the P solution. Notice that the difference between the simulation profile and the BLSWE profile grows larger as one approaches the jump. This highlights the inadequacy of the BLSWE as one approaches the jump.

To estimate how much the right hand side of equation 2.28 affects the answers, a solution with the right hand side set to zero is shown in the same figure. Except for minor differences in the vicinity of $Fr = 1$, we find good agreement. Note that since $h'Re$ and Fr vary with x, a neglect of the right hand side does not imply that the solution is self-similar. Thus, although we have no need to take recourse to it, the solution upstream and downstream of the jump may be obtained to good approximation by a homogeneous ordinary differential equation. In figure 2.14, the height profile of the P solution is compared to a profile obtained from Navier-Stokes simulations. These simulations are described in a later chapter in great detail and it is seen that upstream of the jump, the P solution is a good representation. Downstream of the jump, we often find undulations which incidentally cannot be

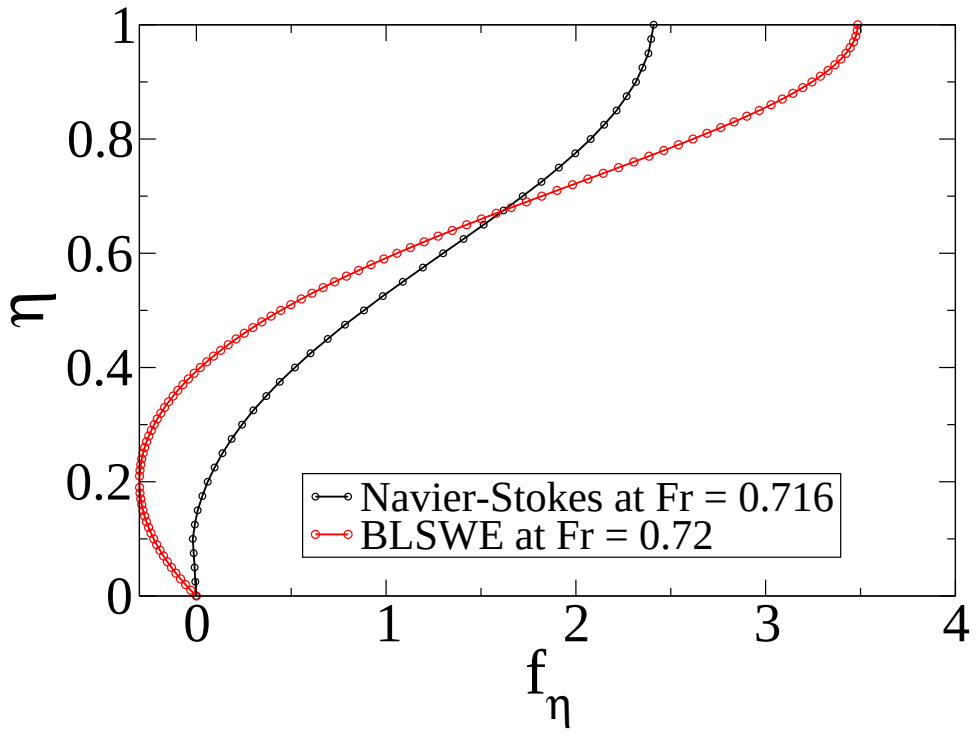

Figure 2.17: Simulation parameters, $Re_i = 125$ and $Fr_i = 6$. The streamwise location corresponds to a local Froude $Fr^2 \equiv Q^2/gh^3 = 0.716$ which is downstream of the jump. The BLSWE velocity profile corresponds to a location where $Fr = 0.72$. Notice that the P profile has a much larger reverse velocities when compared to simulations. In the simulations the profile would re-attach somewhere dowsntream whereas the P solution of the BLSWE does not smoothly transition to the N solution which has an attached profile.

described by the shallow-water equations (Benjamin & Lighthill [1954]). In figure 2.15, 2.16 and 2.17, we present comparisons of the velocity profiles obtained from the BLSWE to those obtained from Navier-Stokes simulations. One can notice from these figures that as the jump is approached the BLSWE solution becomes inadequate.

We saw that although the BLSWE is a partial differential equation, it is in effect a parametric ordinary differential equation, providing local solutions for a given Fr. Since the solution for a given Froude number is completely specified, this means in particular that we do not need boundary conditions in the streamwise direction. Now, it is well-known that downstream conditions can affect the location

of the jump and other behaviour upstream, so we must discuss how this may affect present predictions. In most experiments, an obstacle of a certain height H is placed at some downstream location L, which determines the maximum Froude number possible there as $Fr_m = Q/(g^{1/2}H^{3/2})$, since the height of the fluid interface there must be at least H. In simulations too, [Higuera, 1994] sees an effect of the prescribed downstream condition. If one could make the low Froude number assumption everywhere downstream of the jump, and we impose $Fr_j = 1$ at the jump location x_j, we would have, from equation (2.30)

$$L - x_j \simeq \frac{Q^{5/3}g^{-1/3}\nu^{-1}}{12}(Fr_L^{-8/3} - 1), \tag{2.31}$$

where $Fr_L \leq Fr_m$. Since the velocity profile is parabolic in the low Froude number limit, (2.31) is unsurprisingly just the scaling of [Bonn *et al.*, 2009; Singha *et al.*, 2005]. If the obstacle height H is large, (2.31) would demand a long distance between x_j and L, so the jump may be pushed upstream if L is inadequate. When L is long enough and H is not too intrusive, we expect the present predictions to hold, i.e., the downstream conditions not to have a significant effect. In this case, if the downstream solution involves a sharp turning around, the N solution predicts an $Fr_L \sim 0.7$.

2.4.3 In a circular geometry

In a circular geometry, following a similar transformation for equation (2.8) and non-dimensionalising the streamfunction as

$$\psi = \frac{Q}{2\pi}f[\eta, \zeta], \quad \eta = \frac{z}{h(r)}, \quad d\zeta = \frac{dr}{h(r)}$$

so that $u = \frac{Q}{2\pi rh}f_\eta$, $w = \frac{Q}{2\pi rh}[\eta h' f_\eta - f_\zeta]$. Here $h' \equiv \frac{dh}{dr}$. For convenience the independent variable in the slope h' of the interface is retained as the dimensional

r, while ζ is used everywhere else. We then have the following

$$\begin{aligned}
u &= \frac{Q}{2\pi r h} f_\eta \\
w &= \frac{Q}{2\pi r h} \left[\eta h' f_\eta - f_\zeta\right] \\
u_r &= \frac{Q}{2\pi r h} \left[-\frac{f_\eta}{r} - \frac{h' f_\eta}{h} + \frac{f_{\eta\zeta}}{h} - \frac{\eta h'}{h} f_{\eta\eta}\right] \\
u_z &= \frac{Q}{2\pi r h^2} f_{\eta\eta} \\
u_{zz} &= \frac{Q}{2\pi r h^3} f_{\eta\eta\eta} \\
u u_r + w u_z &= \frac{-Q^2}{4\pi^2 r^2 h^3} \left[\frac{h}{r} f_\eta^2 + h' f_\eta^2 + f_\zeta f_{\eta\eta} - f_\eta f_{\eta\zeta}\right]
\end{aligned}$$

Substituting these in equation (2.8) we thus obtain

$$f_{\eta\eta\eta} - h' Re \left[\frac{1}{Fr^2} - f_\eta^2\right] + \frac{hRe}{r} f_\eta^2 = Re(f_\eta f_{\eta\zeta} - f_{\eta\eta} f_\zeta) \tag{2.32}$$

$$f(0,\zeta) = 0, \quad f_\eta(0,\zeta) = 0, f_{\eta\eta}(1,\zeta) = 0. \tag{2.33}$$

Note that here $Re \equiv \frac{Q}{2\pi r \nu}$ and $Fr^2 \equiv \frac{Q^2}{4\pi^2 r^2 g h^3}$. Equation 2.32 also is constrained by the global mass condition $f(1,\zeta) = 1$

2.4.4 Analysis and numerical results - Circular geometry

There is an additional parameter now, namely the radial location for a given Froude number. We fix the upstream Froude number as 100 and examine the solution for different upstream radii, scaled by the height there. The solutions for the slope of the interface, and the wall shear stress are shown in figures 2.19 and 2.18 respectively. The N solution for the slope h' is not shown since, given that Fr is small and r is large, it looks very much like the planar N solution. The overall behaviour of the P solution too is qualitatively the same as the planar case. Some non-monotonic behaviour is possible for the P solution in the circular case when the starting radius is small. This is evident when the Froude number is large, where $Re(h' + h/r) = 1.8$, so at $r = h/(1.8Re)$ we must have $h' = 0$, i.e., a minimum in the height. Upstream of this radial location the height is a decreasing function of the radius. For small Froude numbers and large radii ie. downstream of the

jump, equation 2.32 also admits a similarity solution like its planar counterpart viz. $f_{\eta\eta\eta} = h'Re/Fr^2$. Using the boundary conditions 2.33 and the globas mass-conservation $f(1,\zeta) = 1$, this reduces to $h'Re = -3Fr^2$ analogous to the planar case. A crude prediction of the jump location can now be made by integrating this downstream solution. If the height at the location of the jump r_j is h_j, the height at a certain downstream location r_e is controlled and is h_e, then we obtain by the criterion that $Fr = 1$ at r_j that $h_j = \frac{Q^{\frac{2}{3}} g^{\frac{-1}{3}}}{4^{\frac{1}{3}} \pi^{\frac{2}{3}} r_j^{\frac{2}{3}}}$. Using this we have

$$\begin{aligned} h'Re &= -3Fr^2 \\ \Rightarrow \frac{dh}{dr} &= \frac{-3\nu Q}{2\pi r g h^3} \\ \Rightarrow \int_{h_j}^{h_e} h^3 dh &= \frac{-1.5\nu Q}{\pi g} \int_{r_j}^{r_e} \frac{dr}{r} \\ \Rightarrow \frac{6\nu Q}{\pi g} ln\left(\frac{r_j}{r_e}\right) + \left(\frac{Q^{\frac{8}{3}} g^{\frac{-4}{3}}}{4^{\frac{4}{3}} \pi^{\frac{8}{3}}}\right) r_j^{\frac{-8}{3}} &= h_e^4 \end{aligned} \tag{2.34}$$

Equation 2.34 can be used for obtaining crude estimate of the jump radius knowing the imposed downstream conditions. Figure 2.18 and 2.19 contains comparisons of the slopes and wall-shear for the circular and planar ($2D$) geometries. As seen from figure 2.18, separation occurs for a lower value of Fr in the circular case compared to the planar geometry. Also as seen from figure 2.19, the maximum value of $h'Re$ is greater in the planar case than in the circular case, so in general the planar case produces slightly steeper jumps.

2.5 Comparison with results from self-similar profiles, Pohlhausen profiles and Experiments

It is instructive to compare predictions obtained from the vertically averaged equations with the self-similar assumptions to the present, more realistic, ones. We return to equation 2.21 and rewrite it as

$$\frac{dh}{dx} = \frac{15/Re}{6 - 5/Fr^2} \tag{2.35}$$

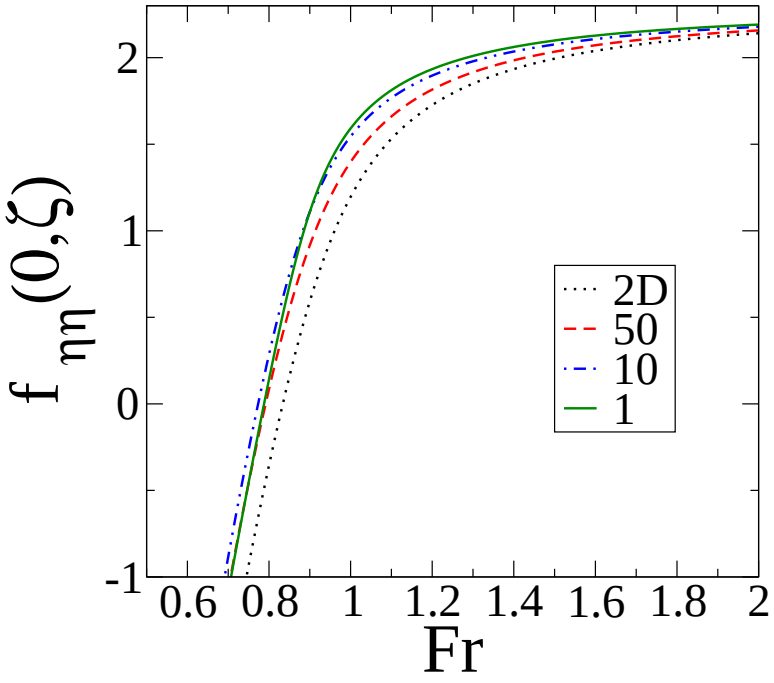

Figure 2.18: The shear stress at the wall in circular geometry. Flow separation is slightly delayed as compared to the planar case.The legend indicates the initial radial location at a Froude number of 100.

Comparing equation 2.35 with equation (2.28), in the limit of high Fr, we observe that equation 2.35 gives $h'Re = 5/2$ whereas the planar BLSWE (2.28) predicts a value of 1.813. Thus both approaches predict a linear height profile far upstream, with different slopes. This is of course due to the fact that equation 2.35 uses a parabolic velocity profile upstream whereas we have seen earlier that the self-similar solution upstream is not parabolic. Similarly equation (2.24) for the axisymmetric case is rewritten as

$$\frac{dh}{dr} = \frac{\frac{5}{2Re} - \frac{h}{r}}{1 - \frac{5}{6Fr^2}}, \tag{2.36}$$

which gives $Re(h' + h/r) = 5/2$ for high Fr. This quantity is again 1.813 in the circular BLSWE (2.32). In the other limit of low Froude number and large radius, both equations give $h'Re = -3Fr^2$, similar to the planar case of equation 2.30. In a region of low Froude number and large radius, moreover, a parabolic profile is a very good assumption. Note that the limiting case corresponds to the N solution

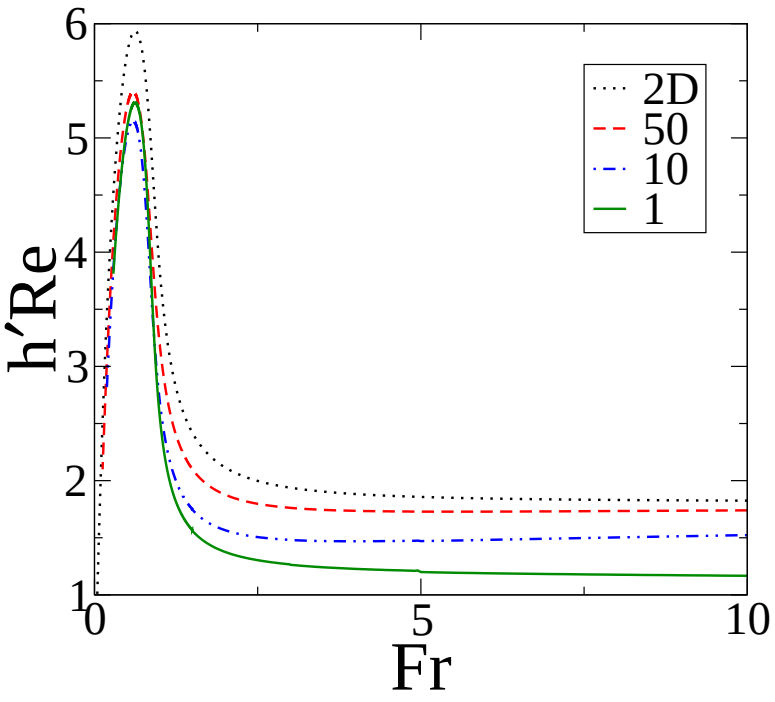

Figure 2.19: The slope of the film height as a function of the local Froude number in the circular case. The legend indicates the initial radial location at a Froude number of 100.

whereas in our numerical procedure we are able to obtain a P solution as well for quite small Froude numbers. However, in a real flow, the Froude number may never become too small, since as one proceeds well downstream of a jump, the Froude number increases again. Far downstream, we have seen that both the spiral solution and the present one will give qualitatively the same behaviour: of a sudden and sharp decrease in height at some radial location.

In figure (2.20) the solution of the circular BLSWE (2.32) is compared to the experimental observations of [Craik *et al.*, 1981]. The solution from the vertical averaging procedure is shown as well. The initial condition for both equations was obtained from the experimental data in the figure. The solid lines in black and red are our P and N solution respectively. The shape of the jump is reasonably close to the experimentally observed one, so the present solution does better than the spiral in this region. Downstream, our N solution does a good job of matching the experimental profile but unlike in the experimental profile, no smooth transition between the P and N solution is achieved. In addition, since we cannot predict

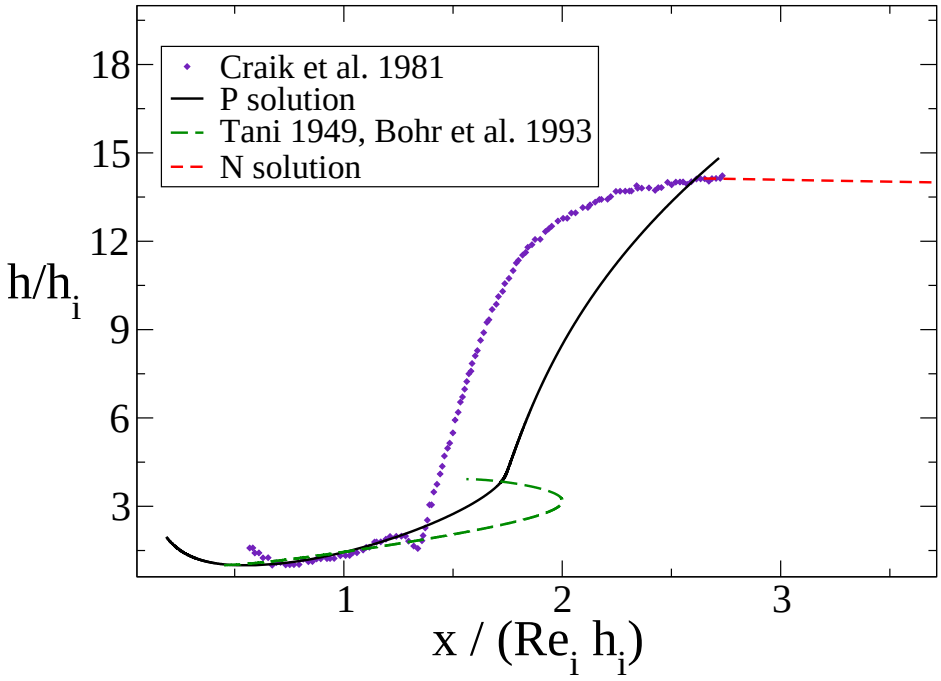

Figure 2.20: Comparison of the P and N solutions of equation (2.32) with the experiments of [Craik *et al.*, 1981] and the vertically averaged solution of [Bohr *et al.*, 1993; Tani, 1949]. The experimental data extracted from Craik is for the case $Q = 18$ ml/s obtained with dyed water as the working fluid. The line in green is the vertically averaged solution obtained from equation (2.36).

where the transition should occur, we have chosen a location which matches well with the experiment. Note that the N solution in figure 8 has a very small negative slope. We note that the same experimental data of [Craik *et al.*, 1981] was compared by [Bowles & Smith, 1992] to their theory. That comparison focussed on the precise shape of the jump itself with the jump height as input parameters. The present study on the other hand focusses on the regions away from the jump. In the next chapter, we will have the occasion to look at the near jump region.

We have mentioned that [Bonn *et al.*, 2009; Watanabe *et al.*, 2003] assume the velocity profiles to be cubic polynomials in η with streamwise varying coefficients. Due to this assumption, the solution obtained does not directly satisfy the governing equations, but only their moments [Watanabe *et al.*, 2003]. While the averaged equations, admit cubic profiles with variable coefficients, we will show below that

the governing equations themselves do not admit a cubic term in its solution. Writing the streamfunction in the BLSWE as a power series in η whose coefficients are functions of ζ, as

$$f[\eta,\zeta] = \sum_{j=0}^{\infty} a_j(\zeta)\eta^j,$$

substituting into the BLSWE (2.28), and equating coefficient of each power of η, we have:

$$\begin{aligned} a_0 &= a_1 = 0 \\ a_3 &= \frac{h'Re}{6Fr^2}, \qquad a_4 = 0 \end{aligned}$$

The remaining coefficients may be obtained from the recursion relation

$$n(n-1)(n-2)a_n = \sum_{p=2}^{n-3} p a_p[(n-p-1)\left(a'_{n-p-1} - a_{n-p-1}h'Re\right) - (p+1)a'_{n-p-2}]$$

All a_n for $n \geq 5$ may be written in terms of the hitherto undetermined coefficient a_2, and $h'Re/Fr^2$. The global mass balance may now be used to obtain a_2. Note that since $a_4 = 0$, the BLSWE does not admit a cubic-term in the velocity profile.

2.6 Conclusion

In this chapter, we have pointed out deficiencies in the technique of vertical averaging alongwith the origin of the unrealistic behaviour in the near-jump region. We have then cast the BLSWE as a parametric ordinary differential equation at a given streamwise location, and a novel solution method is used to obtain jump-like transitions. The only parameters are the local Froude number Fr and a product $h'Re$ of the interface slope and the Reynolds number. The second parameter is completely dependent on the first and may be obtained by imposing global continuity. This enables us to obtain the velocity profile at a given Froude number, and having the obtained the interface slope, march either downstream or upstream to obtain the height profile for a weak hydraulic jump. The jump is shown to occur at $Fr \sim 1$ even in the viscous case. Downstream of the jump, for $Fr < 0.71$ two solu-

tions are obtained and we show evidence from numerical simulations of [Higuera, 1994] to support our surmise that there is a switch from one solution to the other at a Froude number below 1. Instability of the separated profile is suggested as a reason for this switch. The exact nature of the switch, and the behaviour in its vicinity is beyond the reach of the BLSWE. We also compare our results with experiments and find reasonably good agreement. It is also seen that our solution improves over the vertically averaged model. By comparing the velocity profiles obtained from the BLSWE far upstream, near and far downstream of the jump, to those obtained from Navier-Stokes computations, we support out hypothesis that the BLSWE might be inadequate even for a weak-jump in the near jump region.

CHAPTER 3

COMPUTATIONAL AND ANALYTICAL RESULTS ON THE PHJ

3.1 Introduction

In the chapter 2, we discussed the regions upstream and downstream of the jump. It was also discussed that in the near jump region, the vertically averaged BLSWE gives unphysical results. A significant improvement of the solution in the near-jump region was obtained by Watanabe *et al.* [2003] and Bonn *et al.* [2009]. The main difference compared to previous studies was the relaxation of the self-similarity assumption, which led to realistic jump-like transitions. For practical purposes, this model is often sufficient, although it assumes pressure to be hydrostatic. The validity of this assumption in the near-jump region is one of the questions we examine later. It is thus seen that there is no simplified approach that can handle the near-jump region. One way to understand this region would be through direct numerical simulations. However, despite this being an active area of experimental and theoretical research, there is an acute paucity of full Navier-Stokes simulations of laminar standing hydraulic jumps, especially so in a planar geometry. The reason, as we believe and discuss below, is the treacherous nature of the downstream boundary conditions. In planar geometry, simulations of turbulent jumps exist which have relevance for civil engineering (see. e.g. [Rahman *et al.*, 1991*a*] and the RANS simulations of Chippada *et al.* [1994]). Yokoi & Xiao [1999] reported laminar simulations for circular jumps. Their main focus was to study the transition from the Type-I to Type-II jumps, and the role of surface-tension and non-hydrostatic effects in causing this transition. Simulations of the circular jump have also been reported by Ferreira *et al.* [2002] where the focus of the work was to validate the capabilities of a code using the hydraulic jump as a benchmark problem. The latter is the first 3D Navier-Stokes simulation of the circular hydraulic jump (also see Khavari *et al.* [2009]). The complete absence, to all appearances, of simulations of laminar planar standing jumps is a gap we aim to bridge in this chapter.

We show that the jump in a long enough domain is not very sensitive to the

length of the domain. If an obstacle is placed at the outer boundary, the jump is stronger and is pushed upstream. The viscous simulations agree with inviscid shallow water theory on two points. (i) It is found that a local Froude number $Fr = 1$ is a reliable criterion for locating the jump in a viscous flow too. (ii) The Rayleigh shock criterion provides a reasonable estimate of the post-jump height. We find that the strength of the jump, measured in terms of the slope of the height profile, varies inversely with the Reynolds number and inlet Froude number. The laminar planar hydraulic jump is found to be rather gentle. However, non-hydrostatic effects of pressure are large in the jump and undular regions.

We then derive a general depth-averaged equation for the evolution of the height profile. The process transforms the Navier-Stokes equations into a new equation which contains the film-thickness as an independent variable. This equation contains as subsets many well-known equations eg. the KdV equation, the KDB equation [Johnson, 1972] etc. Expectedly it also contains as subsets the vertically integrated BLSWE and also the previously derived vertically averaged equations of Singha *et al.* [2005]. A theoretical study of the near jump region is carried out using this equation. The validity of the assumption of hydrostatic pressure has been discussed in the circular hydraulic jump literature [Yokoi & Xiao, 1999]. Assuming pressure to be hydrostatic is equivalent to neglecting vertical accelerations experienced by a fluid parcel as it follows a streamline. Thus it is expected that the neglect of streamline curvature is not justified near the jump. This has often been remarked on for travelling jumps (see e.g. Genady *et al.* [2006]). In the standing jump literature, dispersive effects have been included in the interactive boundary-layer analysis e.g. Bowles & Smith [1992], Higuera [1994]. These studies focus on the structure of the flow in the neighbourhood of the jump and Higuera [1994] gives a description of the leading edge of the separated bubble, among other things etc. However, the dominant balance of terms which dictate the height-profile in the near jump region has not beeen studied earlier. Studies which focus on this region e.g. [Bonn *et al.*, 2009; Watanabe *et al.*, 2003], have done so under the shallow-water approximation. It is shown here that the shallow-water equations predict, with fair accuracy, the upstream region and the far downstream region of the flow, but are inadequate in the near-jump region of *even the weakest* of hydraulic jumps. Assuming that the jump occurs over a narrow width, we derive using our complete depth-averaged equation, the simplest equation which can describe the jump re-

gion at the lowest order. It is shown that none of the terms in the shallow water equation appears at the lower order in the neighborhood of the jump. We instead obtain a balance between dispersive and viscous terms both arising from the vertical momentum equation. In the limit of weak jumps no simplification is possible and one has to solve the full Navier-Stokes equations. Finally, a subset of this equation is used to model the undular region seen immediately behind the jump.

3.2 The geometrical model and the simulations

3.2.1 Numerical Method

Numerical simulations of planar hydraulic jumps are performed using an open source code, *GERRIS* [Popinet, 2010]. Gerris is a Navier-Stokes solver augmented with the Volume of Fluid algorithm for two phase flows [Popinet, 2003, 2009]. We describe briefly the algorithm it employs. A second-order accurate staggered time discretisation has been used for the velocity, volume-fraction/ density and pressure fields. Using a time-splitting projection method the discretized equations can be written as [Popinet, 2003]:

$$\rho_{n+\frac{1}{2}}\left[\frac{\mathbf{u}_\star-\mathbf{u}_n}{\Delta t}+\mathbf{u}_{n+\frac{1}{2}}\cdot\nabla\mathbf{u}_{n+\frac{1}{2}}\right]= \nabla\cdot\left[\mu_{n+\frac{1}{2}}\left(\mathbf{D}_n+\mathbf{D}_\star\right)\right]+\left(\sigma\kappa\delta_s\mathbf{n}\right)_{n+\frac{1}{2}}, \tag{3.1}$$

$$\frac{c_{n+\frac{1}{2}}-c_{n-\frac{1}{2}}}{\Delta t}+\nabla\cdot\left(c_n\mathbf{u}_n\right)=0, \tag{3.2}$$

$$\mathbf{u}_{n+1}=\mathbf{u}_\star-\frac{\Delta t}{\rho_{n+\frac{1}{2}}}\nabla p_{n+\frac{1}{2}}, \tag{3.3}$$

$$\nabla\cdot\mathbf{u}_{n+1}=0. \tag{3.4}$$

Here, $\mathbf{u}$ is the velocity field, p is the pressure field, D is the deformation rate tensor and c is the void-fraction field, being defined as the ratio of the volume of fluid in a computational cell to the volume of the cell itself. By definition, c is zero for the gas, unity for the liquid and takes a value between 0 and 1 at the interface. Equation 3.1 is the discretized Navier–Stokes equation with the terms on the left-hand side representing temporal and convective terms and the right hand terms are descretized viscous forces and surface tension. In the projection scheme used, the pressure terms are not included in the momentum equation but are used for

correcting the velocity field (see equation (3.3)) such that the resultant velocity field is solenoidal (Equation 3.4). Equation (3.2) is the advection equation for the void-fraction field. The subscripts indicate the time step at which the variables have been evaluated. The subscript $*$ indicates the auxillary time step. Convective terms are evaluated at the fractional time-step $(n + 1/2)$ using the Godunov procedure [Bell *et al.*, 1989]. Using equation (3.3) and the incompressibility condition (equation (3.4)), the Poisson equation governing the pressure field can be written as

$$\nabla \cdot \left(\frac{\Delta t}{\rho_{n+\frac{1}{2}}} \nabla p_{n+\frac{1}{2}} \right) = \nabla \cdot \mathbf{u}_{\star}. \tag{3.5}$$

The Poisson equation (3.5) for the pressure and the discretized momentum conservation equation (3.1) are solved efficiently using a quad/ octree-based multigrid solver with an underlying linear solver [Popinet, 2003]. The viscous terms are discretized using a second–order accurate unconditionally stable Crank–Nicholson scheme. The velocity, pressure and void-fraction are all collocated at the center of the computational finite-volume cell. The velocity and pressure fields are decoupled using an approximate projection method for the spatial discretization of the pressure correction equation and the associated divergence of the auxiliary velocity [Popinet, 2003]. The volume fraction field is advected using an operator-split algorithm and the velocity field obtained above [Li, 1995]. The volume flux for advection is computed geometrically to avoid numerical diffusion. The liquid-gas interface is reconstructed at each time step and the interface normal is computed using a mixed-Youngs-Centered (MYC) method [Aulisa *et al.*, 2007]. The surface tension force $(\sigma\kappa\delta_s\mathbf{n})_{n+\frac{1}{2}}$ is calculated using a balanced-force surface tension calculation [Francois *et al.*, 2006]. A second-order accurate estimate of the curvature is obtained using the Height-Function technique [Popinet, 2009]. Details of the implementation are available in Popinet [2003, 2009]. The quad/oct tree mesh in Gerris allows efficient mesh refinement and adaptation procedure. We use adaptive mesh refinement in our simulations by defining the vorticity and the gradient of the void-fraction variable as the cost function [Popinet, 2009].

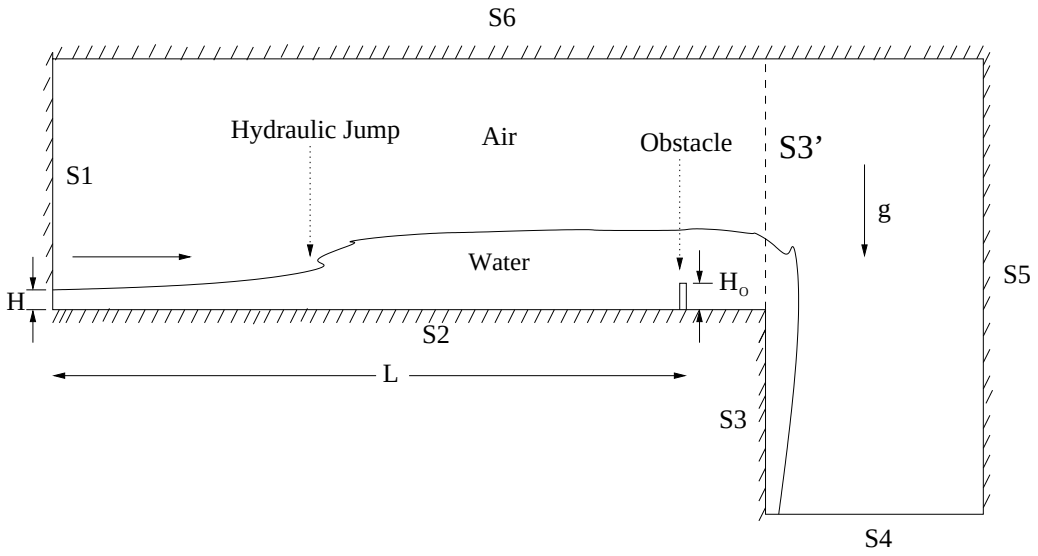

Figure 3.1: A pictorial representation of the computational domain. Fluid enters the domain through the a part of the domain labelled $S1$ and exits through $S4$. Note the obstacle of height H_o placed well downstream of the jump. The obstacle is useful for obtaining steeper jumps, but we can obtain jumps without obstacles too. The utility of the 'pit' downstream of the jump is discussed in the text.

Table 3.1: Boundary conditions for computational domain in figure 3.1

Side	on velocity	on pressure
S1	free-slip, no penetration except for inlet jet	Neumann condition
S2	No-slip, no penetration	Neumann condition
S3	Free-slip, no penetration	Neumann condition
S4	Neumann	Outlet condition, Dirichlet
S5	Free-slip, no penetration	Neumann condition
S6	Free-slip, no penetration	Neumann condition

3.2.2 Computational Domain and Boundary Conditions

Figure 3.1 shows the computational domain. The hashed sides represent walls where a no-penetration condition has been imposed. The boundary conditions are given in Table 1. In most of our simulations, we place a thin rectangular obstacle just ahead of the outflow boundary, although this is not strictly necessary. The effect of the obstacle on the free surface morphology is discussed later. Pressure is generally prescribed at the outflow boundary where for velocity a Neumann boundary condition is used. In cases involving gravitational acceleration and two-phase flow, the imposition of a constant pressure field at the exit or even a constant hy-

drostatic field leads to fictitious upstream flow of the liquid. For example, in this flow, it might have seemed natural to truncate the domain at $S3'$, and prescribe a classical outflow boundary condition there. Such a prescription, however, led to spurious reflections from the outer boundary. Thus to avoid imposing an artificial condition on $S3'$, we introduce a "pit" (see figure 3.1) and impose the classical outflow boundary condition (Dirichlet in pressure and Neumann for the velocity field) along the horizontal boundary $S4$. The introduction of this boundary condition makes the simulations much more reliable, eliminates many cases of severe wave-breaking and other convergence issues, and most important, is able to give grid independent results. The dependence on the outer boundary of the location of the jump and the shape of the height profile is also minimised if the outer boundary is placed far enough. A very long computational domain ending in a pit is thus advocated for such simulations.

The simulations reported here have been performed without surface-tension. For the simulations shown, the height H_o of the obstacle is fixed at twice that of the film thickness H at the inlet. The other dimensional parameters in the problem are the average velocity U_{av} at the inlet, the length L from the inlet to the obstacle, kinematic viscosities of the inlet fluid and the ambient fluid, ν_w and ν_a respectively, and their respectives densities ρ_w and ρ_a. The non-dimensional ratios that characterize the flow behavior are the Reynolds number Re, which is constant across the flow, the inlet Froude number Fr_i, the domain length $L^* = L/H$, H_o/H, ν_a/ν_w and ρ_a/ρ_w. The Reynolds and inlet Froude numbers are defined as $Re \equiv U_{av}H/\nu$ and $Fr_i = U_{av}/\sqrt{gH}$. In the simulations that are presented here, we fix $\nu_a/\nu_w = 10$ and $\rho_a/\rho_w = 0.001$, to be representative of a water-air system, while varying Re, Fr_i and the non-dimensional domain length L^*. The initial condition for all these simulations comprise of a layer of pre-wetting fluid upstream of the obstacle. As the simulation is started, the fluid layer, due to its initial velocity, flows over the obstacle and into the pit. An example of the very early stages of a simulation is shown in figure 3.2.

3.3 Results from simulations

Table 3.2 summarises the Navier-Stokes simulations that have been performed. These are unsteady simulations which have been allowed to proceed long enough

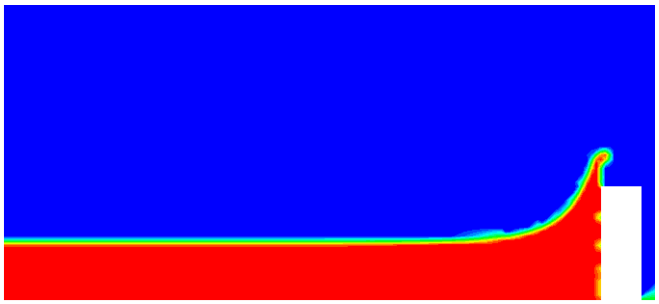

Figure 3.2: Very early stages of a simulation with $L^* = 290, Fr_i = 6, Re = 125$. The fluid due to its initial velocity topples over the obstacle and flows into the "pit".

$L^* = 90$		$L^* = 150$		$L^* = 215$		$L^* = 230$		$L^* = 290$		$L^* = 300$	
Fr_i	Re	Fr_i	Re	Fr_i	Re	Fr_i	Re	Fr_i	Re	Fr_i	Re
4	125	4	62.5	4	31.25	6	62.5	6	125	6	125
5	62.5	4	62.5	6	31.25	6	125	-	-	-	-
6	31.25	6	31.25	6	62.5	-	-	-	-	-	-
6	62.5	6	50	6	125	-	-	-	-	-	-
6	125	6	56.25	10	12.5	-	-	-	-	-	-
6	187.5	6	56.25	15	31.25	-	-	-	-	-	-
8	31.25	6	68.75	20	12.5	-	-	-	-	-	-
10	31.25	6	100	-	-	-	-	-	-	-	-
-	-	6	125	-	-	-	-	-	-	-	-
-	-	6	187.5	-	-	-	-	-	-	-	-
-	-	6	212.5	-	-	-	-	-	-	-	-
-	-	6	250	-	-	-	-	-	-	-	-
-	-	8	12.5	-	-	-	-	-	-	-	-
-	-	8	187.5	-	-	-	-	-	-	-	-
-	-	15	31.25	-	-	-	-	-	-	-	-
-	-	20	12.5	-	-	-	-	-	-	-	-

Table 3.2: Simulation parameters - for meanings of symbols refer to figure 3.1. All simulations have been performed fixing the height of the fluid film at the inlet at $H = 0.25$ and the height of the obstacle as $H_o = 0.5$.

to ensure that steady state is attained. The simulations have been conducted for at least $10L/U_{av}$, i.e., ten times the time it takes for an average fluid particle to traverse the entire domain. Given that we work with long domains, we see that the time scale for achieving steady state is thousands of times slower than the typical flow time scale $T = H/U_{av}$. At very low Reynolds numbers, less than 12.5, no steady state was attained anywhere, since wave-breaking occurred very close to the inlet and interfered with the downstream, so these cases are not listed in the table. We present only a few of the simulations. The main purpose in exploring a much larger parameter set was to ensure that the trends we report are general.

We begin by estimating how much of the flow is dictated by the outer boundary and the obstacle. It is well-known that the outer boundary can have a very strong effect on the jump, but it is not clear whether one can ever obtain jumps whose location and shape do not depend on the outer boundary conditions. In experiments, a downstream height is almost always imposed, and in circular jumps, an increase in the height of the obstacle can cause a dramatic loss of axisymmetry leading to polygon formation (see e.g. Ellegaard *et al.* [1998]). In planar geometries too, the traditional wisdom is that the solution depends on the downstream boundary conditions. To evaluate this effect, we examine separately, (i) the length of the domain, and (ii) the obstacle. We show in figure 3.3 the effect of domain size. Beyond a certain length of domain, the downstream boundary is seen to have only a small effect on the location of the jump. Note that the jump moves slightly upstream as the dowstream boundary is moved away. The reason for this is unclear at this time. The change in the detailed shape of the undular region is far more significant. In the rest of the computations presented, care has been taken to use a long enough domain, where we believe the flow, especially the jump location and strength, is not qualitatively dependent on the outer boundary. For shorter domains than those we show here, the outer boundary does have a much stronger effect, and in some cases determines whether a jump may be achieved or not. In fact in most planar jump experiments a tall enough obstacle is crucial for jump formation. A working definition of a jump Froude number would be useful to locate the jump. In inviscid shallow water theory, the flow speed being greater or less than the small-amplitude, long wave speed $\sqrt{gh}$, provides a natural distinction between super and subcritical flows. In the presence of viscosity however, it is not immediately obvious where this distinction may be made [Watanabe *et al.*, 2003].

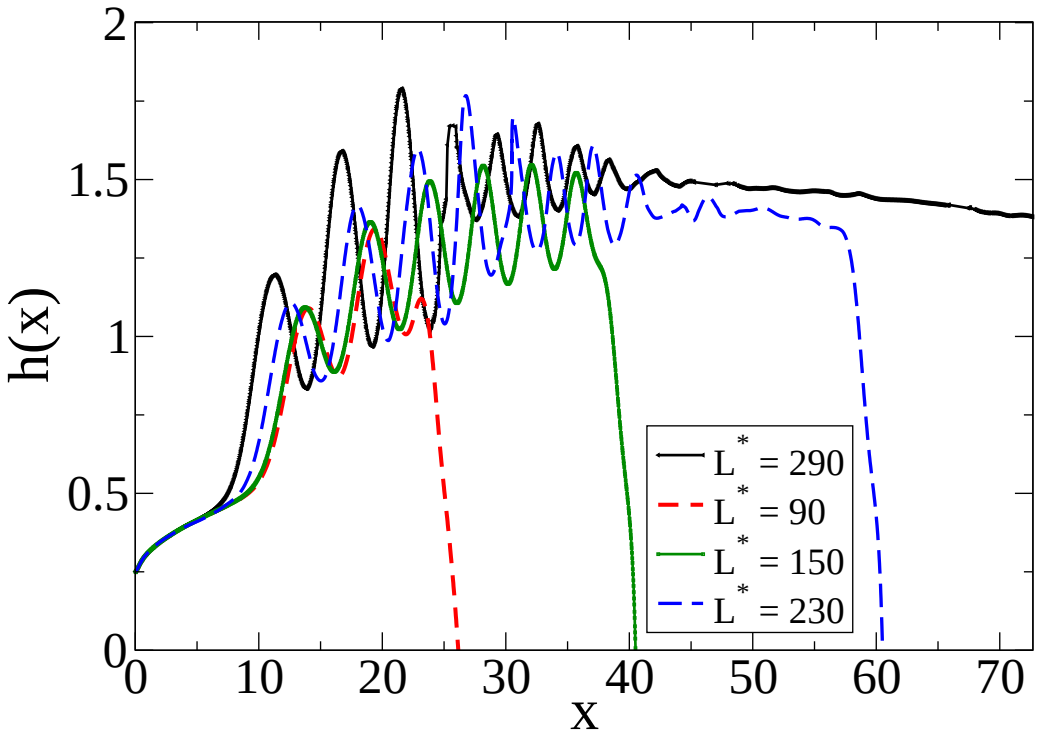

Figure 3.3: Effect of change of domain size - All simulations have $Fr_i = 6$ and $Re = 125$. The jump moves upstream because of the increase in domain size.

In figure 3.4, a typical height profile from our simulations is shown. The height where the Froude number, defined as $Fr = U_{av}/\sqrt{gh}$, is unity is shown by the dashed line. It is seen that $Fr = 1$ can be used as a reliable criterion for locating the jump. Moreover, the Froude number does not go through unity again anywhere downstream (except at the outlet, where the fluid falls into the pit). This is true of all our simulations. This working definition can be refined, if required, by a precise knowledge of the velocity profile.

The time evolution of formation of a jump is shown in figure 3.5. It is seen that the initially uniform height gradually develops a steep front which propagates upstream. The undulations too grow stronger with time. This is reminiscient of the process of nonlinear steepening of the fore of an upstream propagating wave leading to shock-formation. There is virtually no difference between the height profiles at $t/T = 1500$ and $t/T = 2000$, indicating that a steady state has been attained for

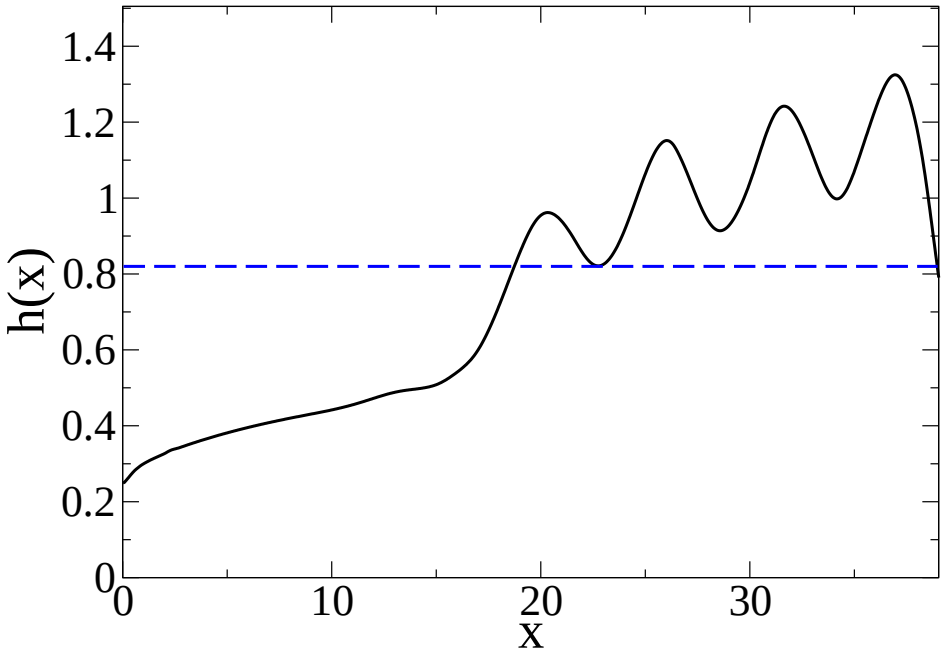

Figure 3.4: The Froude number reaches unity where the height profile intersects the dashed line. The parameters are $Re = 187.5, Fr_i = 6$ and $L^* = 150$.

this configuration in approximately ten times the time it takes for a typical fluid parcel to travel from inlet to exit. Figure 3.5 is thus a numerical solution of the initial-value problem of jump formation.

We would now like to examine the effect of the non-dimensional parameters Re and Fr on the jump. We will be making comparisons with the results of shallow water theory. It is useful therefore to first review what is expected from that theory. This will help in understanding where shallow water theory works, and where and why it fails.

3.3.1 Comparisons of the simulations with shallow water theory

The shallow water theory assumes that we may neglect dispersive effects, i.e., consider pressure to be hydrostatic. This is considered to be a good approximation in regions of small slope. In such regions, moreover, the viscous shallow-water equation may be reduced to its boundary layer form. In a transformed coordinate system defined by $\eta = y/h(x)$ and $d\zeta = dx/[h(x)Re]$, the boundary layer shallow

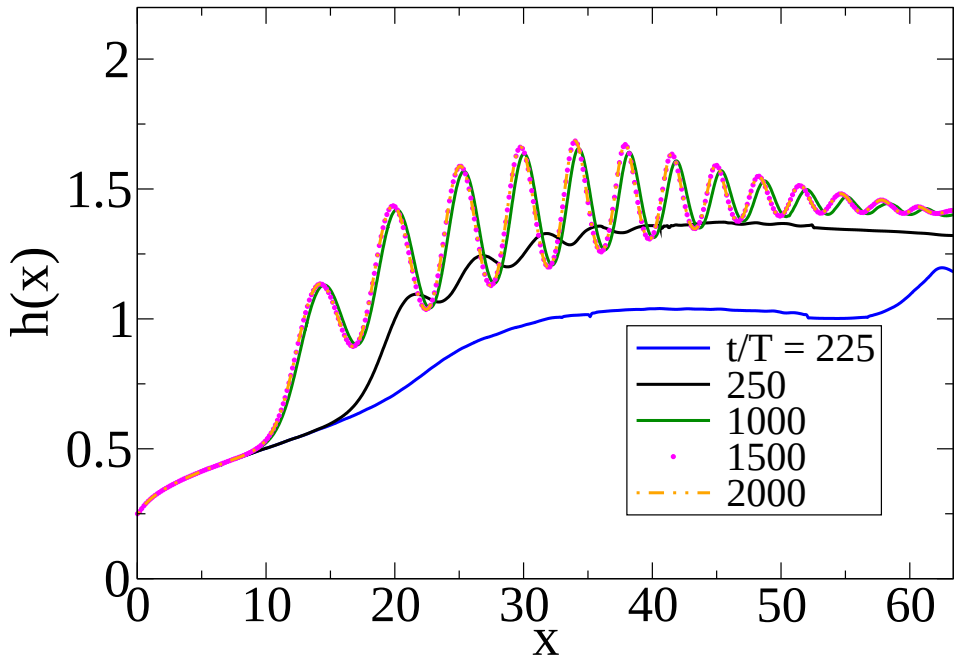

Figure 3.5: Time evolution of jump formation - The simulation is started with an uniform thin film and the downstream obstacle forces an upstream travelling wave-like structure whose front steepens as it moves upstream, as seen in the picture. The legend gives the value of t/T for each plot. The simulation parameters are: $Re = 125, Fr_i = 6, L^* = 290$.

water equation (BLSWE) is [Dasgupta & Govindarajan, 2010]

$$f_{\eta\eta\eta} - h' Re \left[\frac{1}{Fr^2} - f_\eta^2\right] = f_\eta f_{\eta\zeta} - f_{\eta\eta} f_\zeta \tag{3.6}$$

$$f(0,\zeta) = f_\eta(0,\zeta) = 0, \qquad f_{\eta\eta}(1,\zeta) = 0. \tag{3.7}$$

where the streamfunction is nondimensionalised as $\psi = Qf[\eta,\zeta]$. Note that the dimensional variable x is retained in the definition of the slope, i.e., $h' \equiv dh/dx$. Without resorting to vertical averaging or any further assumption, the above equation was solved as a parametric ordinary differential equation earlier in Chapter 2. Two observations about the BLSWE will prove useful for the present comparisons. (i) The Reynolds number merely rescales the streamwise coordinate x and otherwise plays no role. (ii) When combined with the global continuity equation, (3.6)

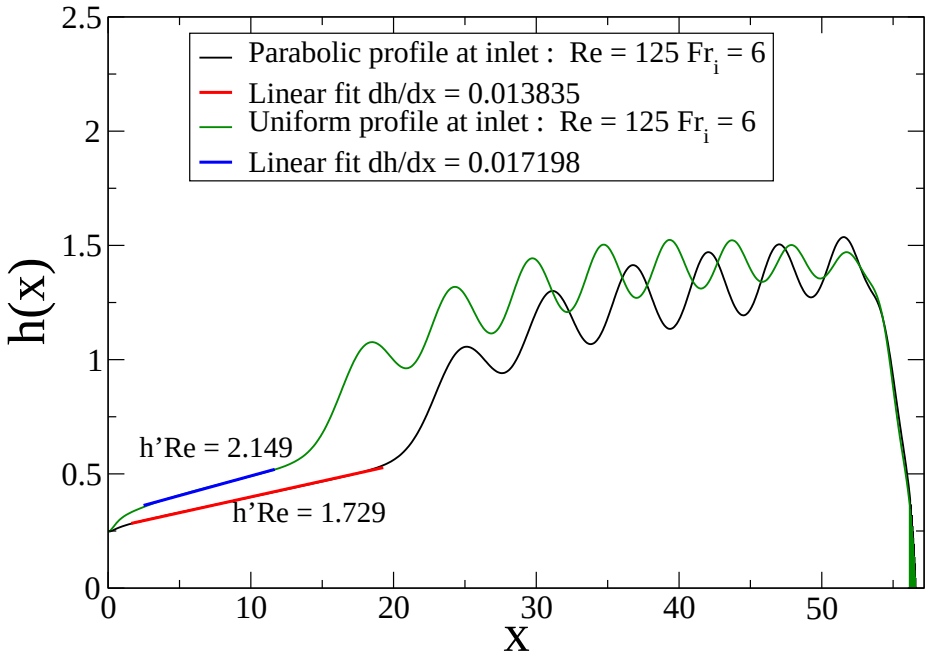

Figure 3.6: The effect of inlet profile on the upstream slope. The profile with $h'Re = 2.149$ has an uniform velocity at the inlet while the other profile has a parabolic profile at the inlet which gives the same mass flow-rate. $L^* = 215, Re = 125$ and $Fr_i = 6$.

provides a unique value of the slope h' for a given Froude and Reynolds number. Global continuity in fact appears as an additional boundary condition $f(1, \zeta) = 1$, to satisfy which, we must use the correct $h'Re$. For $Fr >> 1$ and $Fr << 1$, the BLSWE admits similarity solutions. Far upstream of the jump, i.e., at high Froude numbers, the first term in the square bracket in (3.6) may be neglected, so there is no x-dependence in the problem. The right hand side therefore vanishes, giving a similarity solution for the velocity profile. It follows then that far upstream of the jump, the slope must be a constant. We obtain $h' = 1.81838Re$ for $Fr >> 1$, which, as it should be, is the value of the slope in the gravity-free solution of Watson [1964]. A solution of the BLSWE shows that the slope remains close to this value for most of the upstream region, i.e., from $Fr = \infty$ to $Fr \sim 2$ [Dasgupta & Govindarajan, 2010]. This solution, which originates far upstream and proceeds downstream to very low Froude numbers, is denoted as the P solution, since it has a positive slope. In figure 3.6 we show the slope in the upstream region ob-

tained from numerical solutions. It is seen that the height increases practically linearly up to a height $h \sim 2h_i$, where $Fr \sim 2$. This value will depend on other flow conditions, as we shall see. Secondly, an effect of the inlet velocity profile is noticed. It is no surprise that viscosity has a greater effect on a uniform inlet velocity profile, giving a larger h'. A parabolic inlet profile on the other hand has an $h'Re$ closer to the BLSWE value of 1.8. This is to be expected, since a parabolic profile resembles the similarity velocity profile more closely than a uniform profile does. Incidentally, the similarity profile is not parabolic, as discussed in Dasgupta & Govindarajan [2010]. The downstream displacement of the jump is due to the higher inlet momentum-flux in the case of the parabolic profile. Since there is no qualitative difference between the two, unless otherwise specified, we have used a uniform inlet profile in the results presented.

It is appropriate at this point to return to the question of domain size, and ask how long a domain should be for a jump to occur spontaneously, i.e. without the help of an obstacle or other edge conditions. Both the BLSWE and the simulations show that upstream of the jump the height increases monotonically, so the Froude number decreases monotonically, with a slope of $1.8/Re$ or larger. In fact in turbulent flow, the slope is often an order of magnitude larger (see e.g. Bonn *et al.* [2009]). Thus a flow whose inlet Froude number is greater than 1 must, if the domain is long enough, inevitably reach a Froude number of unity. Most experimental planar channels are too short for this. For example, in figure 1 of Chanson [2009], both the flows would require channels hundreds of metres long for the Froude number to reach unity, even with a turbulent profile. The channels are however no longer than $20m$. An imposed downstream height, or an obstacle, thus serves to bring the jump forward, sometimes by a large amount.

A comparison of a typical simulation with the P solution of equation 3.6 is shown in figure 3.7. While there is a fair comparison ahead of the jump, the P solution is seen to always overpredict the location of the jump and always produce a jump that is much weaker than that obtained in the simulations. This might be explained by the fact that our simulated jumps are made steeper and brought upstream by the obstacle placed downstream. There is however another discrepancy in the near-jump region, in that the P solution consists of an unrealistically large separated region. Worse, the extent of this separated region in the wall-normal direction keeps increasing downstream (see figure 2.12 in Chapter 2). A stability

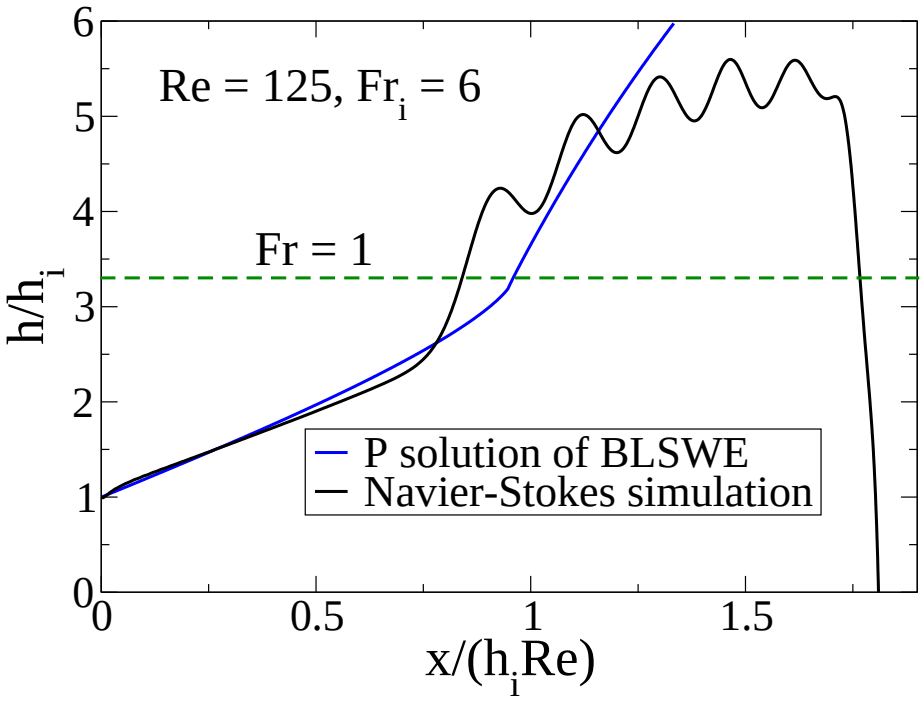

Figure 3.7: Comparison of the simulated height profile with the P solution from shallow water theory. The parameters for the Navier-Stokes solution are $Re = 125, Fr_i = 6, L^* = 215$. The inlet profile is specified as parabolic.

analysis of these velocity profiles is being conducted (Ramadurgam [2010]), and shows that such a profile is extremely unstable. Since the P solution is the only one we have found which satisfies the BLSWE in this region, we may conjecture that the shallow water theory is inadequate in describing this region. Note that the slope is in fact small everywhere in this flow including in the jump region. (The x-coordinate has been scaled by the Reynolds number in this plot). In spite of this, the shallow water theory does not work well. This argument may be put on a firmer footing, as seen in the next section.

Downstream, in addition to the P solution, we expect equation (3.6) to support another solution, which will reduce to the similarity solution mentioned earlier for $Fr << 1$. In that limit, we have, from equation (3.6), that $h'Re = -3Fr^2$ for similarity. In line with our expectations, for $Fr < 0.82$, we obtain another solution for the BLSWE, which is labelled as the N solution due to its negative slope. A simulation where we obtained a sizeable extent of a non-undular height profile

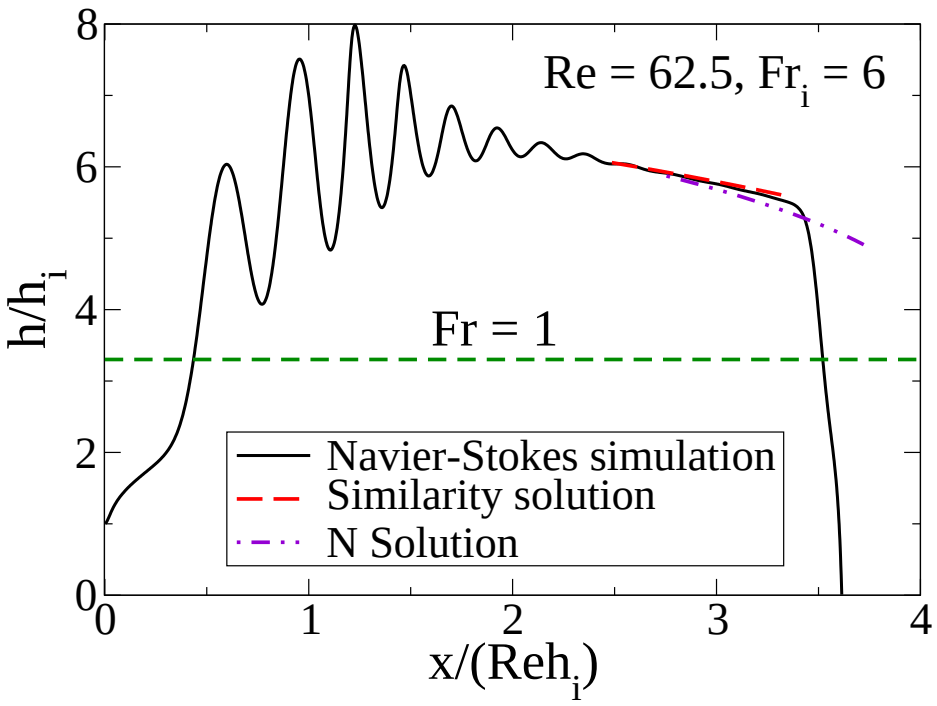

Figure 3.8: Comparison of the N solution, and the downstream similarity solution with the downstream profile obtained from simulations. The N solution has been obtained by using a starting Froude number of 0.421 at $x = 40.347$. The dashed line is obtained by integrating $h'Re = -3Fr^2$, choosing a constant of integration $h = 1.503$ to match the simulations at $x = 40.347$. For this simulation $L^* = 215$.

downstream is chosen in figure 3.8 for comparison with the N solution. It is clear that while the P and N solution work well upstream and downstream of the jump, the near-jump region is poorly described, and the undular region is not predicted at all. Also, there is no transition prescribed from the P to the N solution, which lends support to our contention that near the jump, equation 3.6 is a poor approximation to the full Navier-Stokes.

The BLSWE is able to provide a qualitative assessment of the effect of the Reynolds and the Froude numbers on the jump location. The Reynolds number in the BLSWE merely rescales the x-distance, i.e., a higher Reynolds number only means a proportionately smaller slope. Similar reasoning shows also that a higher initial Froude number results in a delayed jump. Since the constant slope solution is valid for most of the upstream region, we may write a scaling for the jump location x_j using $h' \sim 1.8/Re$, and prescribing the jump Froude number as unity,

as

$$\frac{x_j}{h_i} = \frac{Re}{1.8}\left[Fr_i^{2/3} - 1\right] \tag{3.8}$$

where the subscript i refers to the initial location $x = 0$. In figures 3.9 and 3.10, the effect of varying the Reynolds number and the inlet Froude number can be seen. Both Reynolds and Froude number, as they increase, have the effect of pushing the jump downstream. These effects could also have been anticipated on physical grounds as follows. Consider two flows with identical initial conditions but different viscosities. The higher viscosity flow would be decelerated more and hence produce a thicker film for the same mass flow rate. A thicker film implies a smaller Froude number, so this fluid would need less streamwise distance to reach Froude unity, and thence to jump, as seen in figure 3.9. The flows in figure 3.10 are prescribed to differ only in the numerical value of gravity, so they have the same initial film height and other conditions. Due to this, the flow with the smaller gravity, i.e., of higher initial Froude number, will take a greater streamwise distance to reach its critical height. Intuitively too, since the jump is fundamentally driven by gravity, it is to be expected that a smaller gravity will result in a delayed and weaker jump. The experiments of Avedesian & Zhao [2000] confirmed this for a circular jump.

It is also seen from figure 3.9 that decreasing the inlet Reynolds number makes the jump steeper. The BLSWE would predict a steeper jump as well, due to the rescaling of x, but the scaling in the full equations are different. Changing the Reynolds number also has an effect on the downstream undulations. Note that the BLSWE predicts that the inlet Froude number should have no effect on the steepness of the jump. This is contrary to what is observed in figure 3.10. We will return to these points later in the paper.

In a few of the low Re and low Fr_i simulations, we observed some local wave-breaking despite waiting for $3000T$. For example, in figure 3.9 the profile in the region of unsteadiness is shown in an average sense by a dashed line. In the small streamwise neighbourhood indicated, a wave would grow and break periodically, but the rest of the flow remains time-invariant.

Armed with these results, we are able to form a physical picture of this flow. We may divide the flow into four regions: (i) region P, well upstream of the jump, where the Froude number is greater than 1 and the slope of the height profile is positive. (ii) Region J in the immediate vicinity of the jump, where the Froude number goes through a value of unity. (iii) The undular region U, which could either comprise the

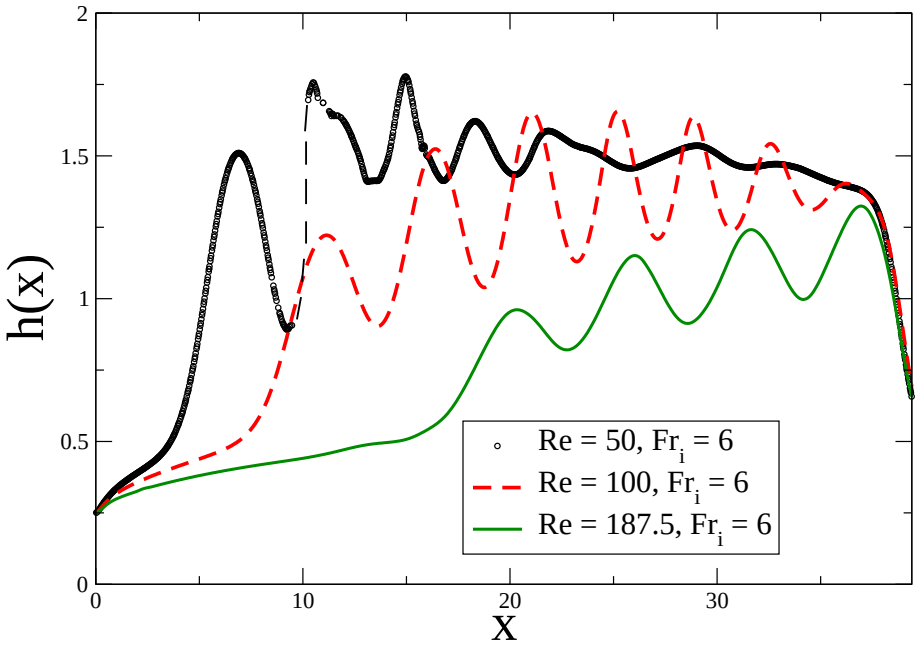

Figure 3.9: The effect of change of Reynolds number. Undulations appear downtream of the jump as the Reynolds number increases. The slope in the near-jump region becomes larger with decreasing Reynolds number. The broken line represents some local unsteadiness in the form of wave-breaking. The jump however has reached a steady state. $L^* = 150$ for these simulations.

entire post-jump flow or a portion of it. (iv) Region N of slowly decreasing height far downstream. The schematic shown in figure 3.11 represents the qualitative features observed in a simulation of a planar jump. Dividing this flow into various regions was attempted earlier, e.g., by Watson [1964], but the focus was on the upstream portion, and the regions different from those laid out here. A systematic attempt at providing equations governing the dominant physics of every region has not been made, to our knowledge. We attempt this in the next section. We have shown that the first and last regions, namely P and N respectively, where the slope of the height profile is small, are fairly accurately described by shallow water theory. To show the relative magnitudes of the non-hydrostatic and hydrostatic contributions to pressure in the J and U regions, we present figure 3.12. Though the jump is weak, the streamwise variation of dynamic pressure is larger than the streamwise variation of hydrostatic pressure, except in the region upstream of the jump. Since it is the gradient of streamwise pressure that appears in the

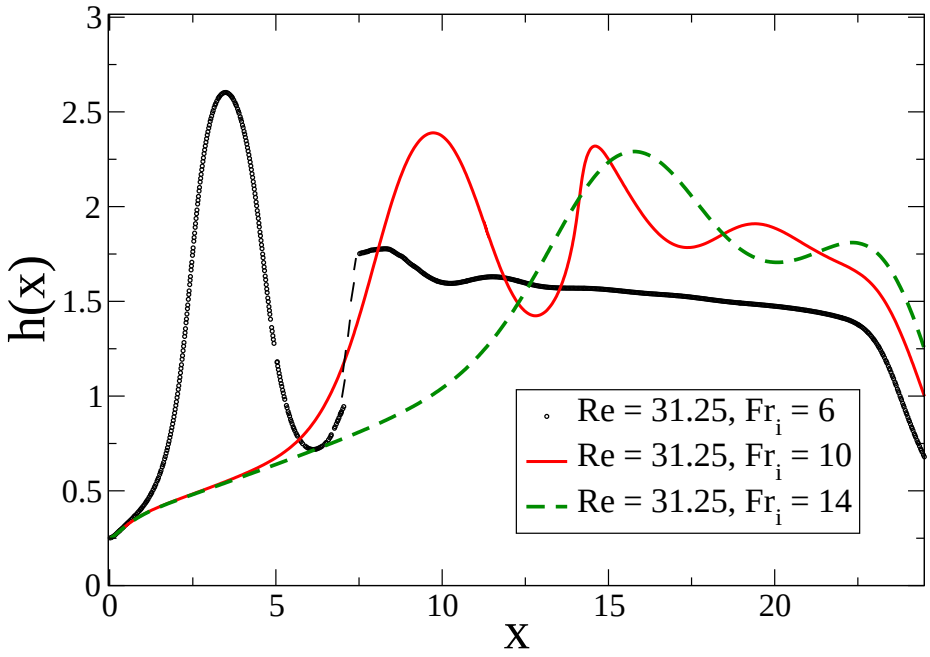

Figure 3.10: Effect of change of Froude number. Note that the jump becomes steeper as inlet Froude decreases. The dashed line indicates some wave-breaking and unsteadiness downstream of the jump but this was checked to have *no* influence on the location or structure of the jump upstream. For these simulations $L^* = 90$.

x-momentum equation, the static and dynamic contributions to this quantity are plotted in the figure rather than the pressure itself.

We have hitherto discussed on the slope h' of the height profile, but not the change in total height that is achievable across the jump. For this, it is simplest to consider the inviscid problem first.

3.3.2 The change in height and the Rayleigh shock criterion

In inviscid flow the jump may be treated as a discontinuity, and Rayleigh [1908, 1914] had shown using shallow-water theory that if mass and momentum flux are continuous across the jump, then energy flux cannot be continuous as well. The change in energy having to be negative due to dissipation, the height must increase. The ratio of the final to the initial height (refer to the discontinuity in figure 3.13),

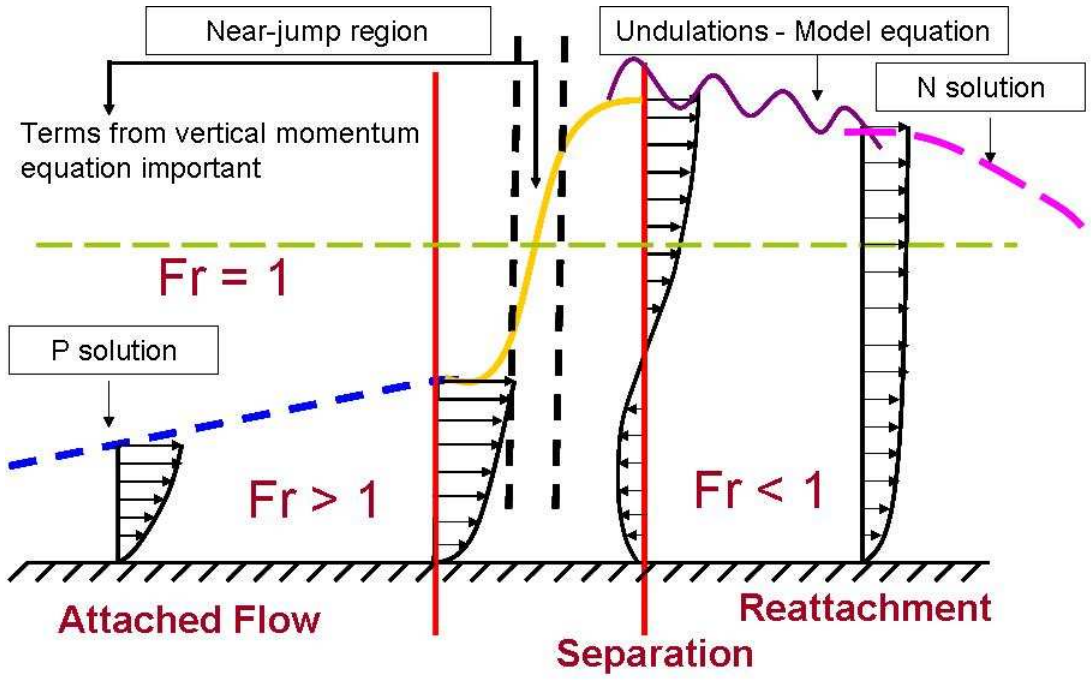

Figure 3.11: A schematic of the different regions of the jump. Far upstream and far downstream, we have two solutions labelled P and N. The depth-averaged equation 3.10, is used to study the near-jump region. The downstream undulations (when they are present) are modelled by a viscous KdV equation.

is predicted to be

$$\frac{H_2}{H_1} = \frac{-1 + \sqrt{1 + 8Fr_1^2}}{2}. \tag{3.9}$$

Given that the height at a given location is related to the Froude number by a power of $-2/3$, the above criterion may be used to express the downstream Froude number as just a function of that upstream, and this relationship is shown in figure 3.14. The presumption that both upstream and downstream heights are constant is not meaningful in a viscous case. In spite of this, equation (3.9) is still frequently used [Bohr *et al.*, 1993; Bonn *et al.*, 2009; Singha *et al.*, 2005] and hence it is worthwhile to examine whether it is representative of our full simulations. There is of course some subjectivity in what we define as Fr_1. From figure 3.15, where the downstream variation of Froude number for two different Reynolds numbers is shown, we see that the P solution is followed upto a certain Froude number, where the flow deviates from BLSWE, and near-jump behaviour sets in. We term

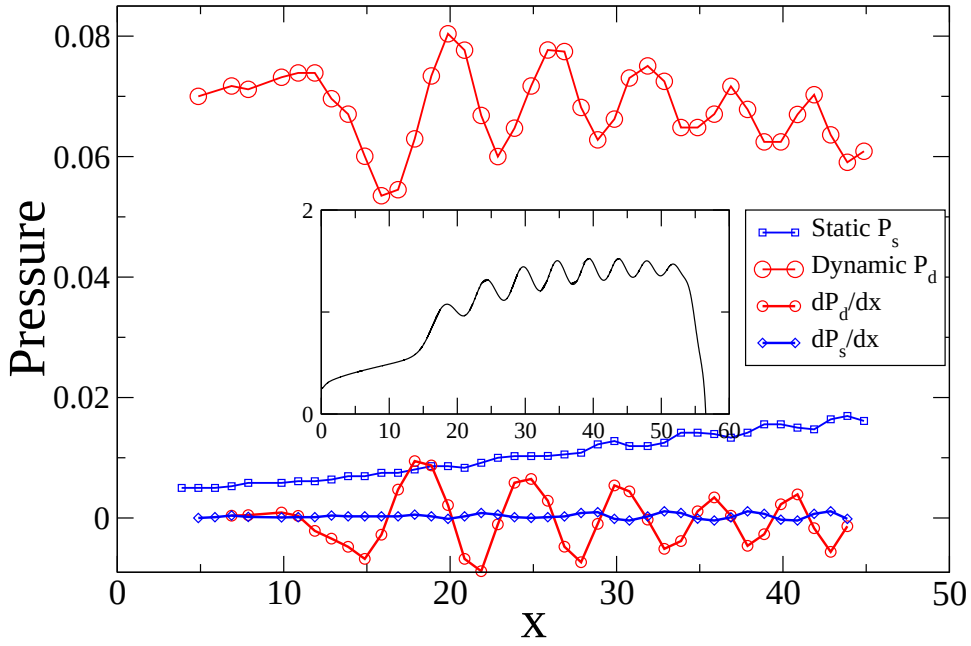

Figure 3.12: The gradients of dynamic pressure is larger than the gradient of static pressure in the vicinity of the jump. The inset shows the height profile from which the pressure data has been extracted. For this simulation $Re = 125, Fr_i = 6$ and $L^* = 215$.

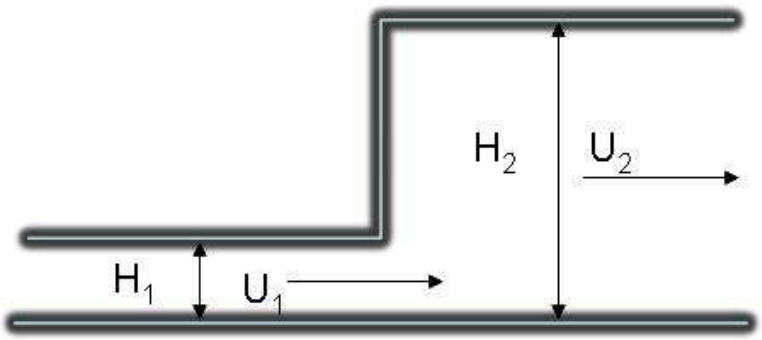

Figure 3.13: The jump was modelled as a discontinuity by Rayleigh [1914]. Using inviscid shallow-water theory he derived the relation (3.9) between the upstream and downstream conditions.

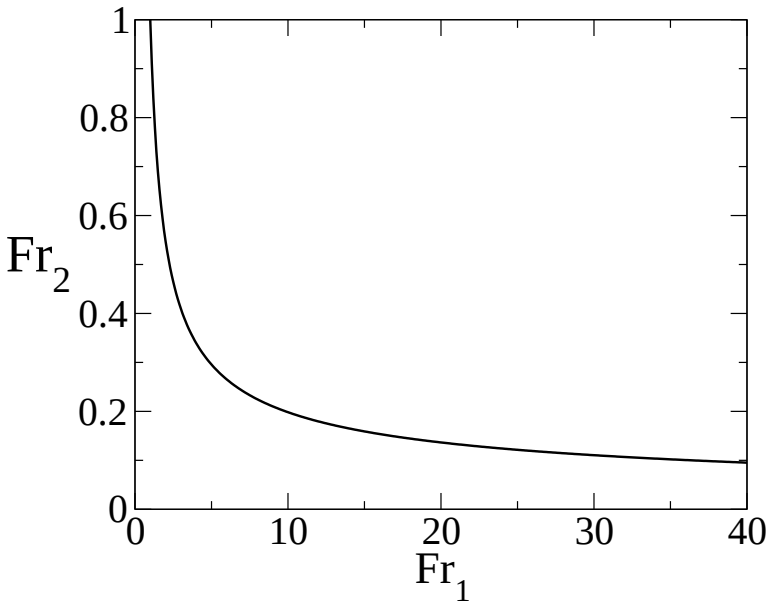

Figure 3.14: The relationship of downstream Froude number to that upstream according to this shock criterion.

this Froude number as Fr_1. We notice that Fr_1 is greater for a lower Reynolds number. A heuristic explanation for this may be given as follows: as the Froude number decreases towards unity, the combined intertial and gravity terms from the BLSWE become smaller. Viscous terms can match this small term at a larger Froude when the Reynolds number is smaller. Thus, it follows from Rayleigh's criterion that a smaller Reynolds number should produce a taller jump. Since the Rayleigh criterion assumes that momentum flux is constant between points 1 and 2, we must relate points which are as close to each other as possible on either side of the jump. Fr_2 is therefore chosen to be that of the location just downstream of the large change in height. Figure 3.16 shows the height profiles of the cases discussed in figure 3.15, along with the predictions by Rayleigh's criterion. In figure 3.17, we show the strongest jump we have been able to obtain, with the slope in the near jump region being approximately $h' \sim 1.1917$. The predictions may be said to be reasonable, given the grossness of the assumptions made, including the fact that for a wide jump, the constancy of momentum flux may be called into question. It can be checked that when a momentum reduction is permitted between points 1 and 2, the height ratio decreases.

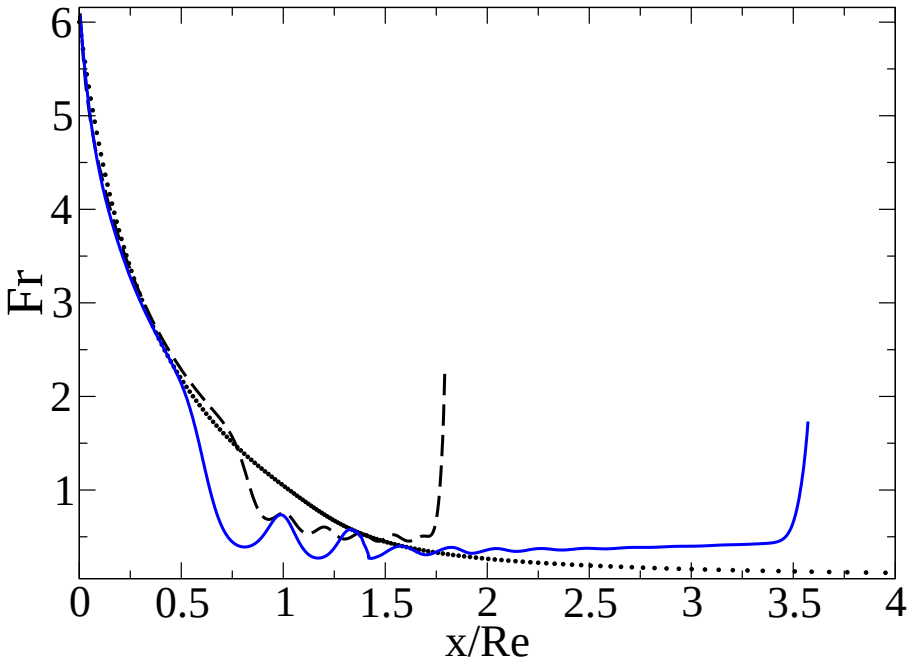

Figure 3.15: Variation of Froude number with streamwise location for $Re = 62.5$ (solid line) and $Re = 125$ (long dashes). The inlet Froude number is 6 in both cases and $L^* = 215$. Shown by the symbols for comparison is the result from the P solution, without any fitting parameters.

In effect thus, a very modest jump is predicted in a planar flow. In other studies of laminar jumps too, we have been able to find only modest jumps. For example, the experimentally obtained jumps of Binnie & Orkney [1955] do not exceed an H_2/H_1 of 2.02, and in the computations of Chippada *et al.* [1994], the highest value of this quantity is around 4.78.

We however define the strength of the jump in terms of the slope h'. By controlling downstream conditions, we may make this quantity large, even while H_2/H_1 is modest. We return to our discussion of this quantity in the near-jump region. Taking the pressure to be hydrostatic, as done in the BLSWE, and therefore in most hydraulic jump studies, was seen not to be reasonable in the jump neighbourhood, and most often in the post-jump flow as well. Although it has been known for a long time that streamline curvature should be important in the near-jump region, the failure of shallow water theory to predict even the weakest of jumps has not been discussed. Hitherto, we have thus considered a vastly simplified theory, and

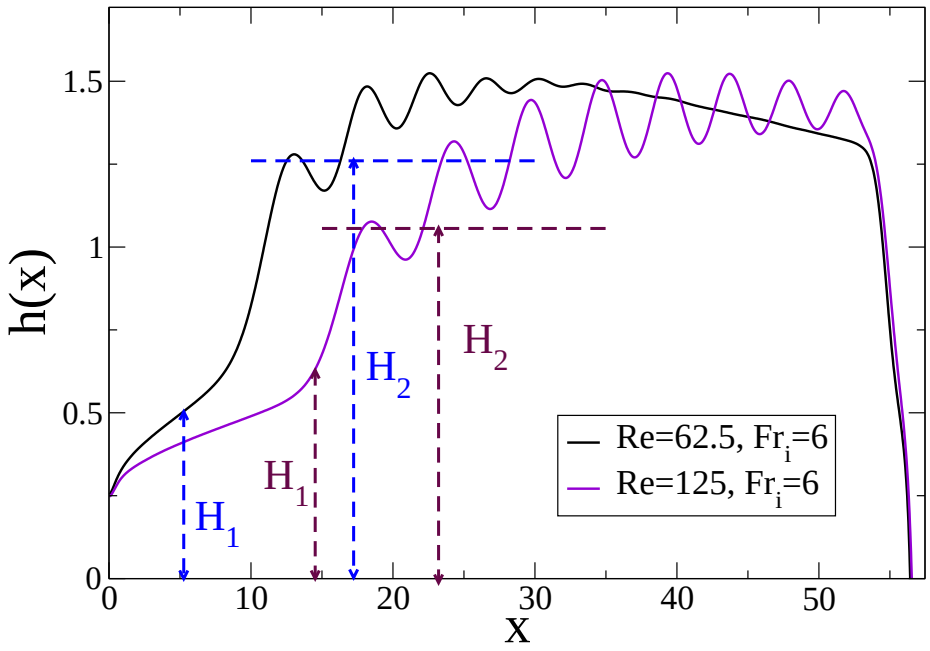

Figure 3.16: The height profiles for figure 3.15, with the corresponding Rayleigh shock predictions. H_1 in both the profiles is chosen to be that point in figure 3.15 where the curve local Froude number departs from the P solution. Note that the height-profile with $Re = 62.5$ has not yet reached steady state. However, this does not affect our qualitative conclusions here because as time progresses, the maximum height downstream will increase thus increasing the average height. For relatively steep jumps, Rayleigh's criterion underpredicts H_2. For these simulations $L^* = 215$.

we would like to generalise it to include the neglected effects. This is easiest done by depth-averaging.

3.4 The depth-averaged Navier-Stokes equation

To gain some insight into regions J and U, we derive the depth averaged Navier-Stokes equation. Such an equation describes the downstream evolution of height. The vertical averaging procedure has hitherto been employed [Bohr *et al.*, 1993; Kasimov, 2008; Singha *et al.*, 2005; Tani, 1949] on approximations of the Navier-Stokes equations, e.g., the BLSWE. The procedure for the complete Navier-Stokes equation is more involved. We first employ the transformation described in the

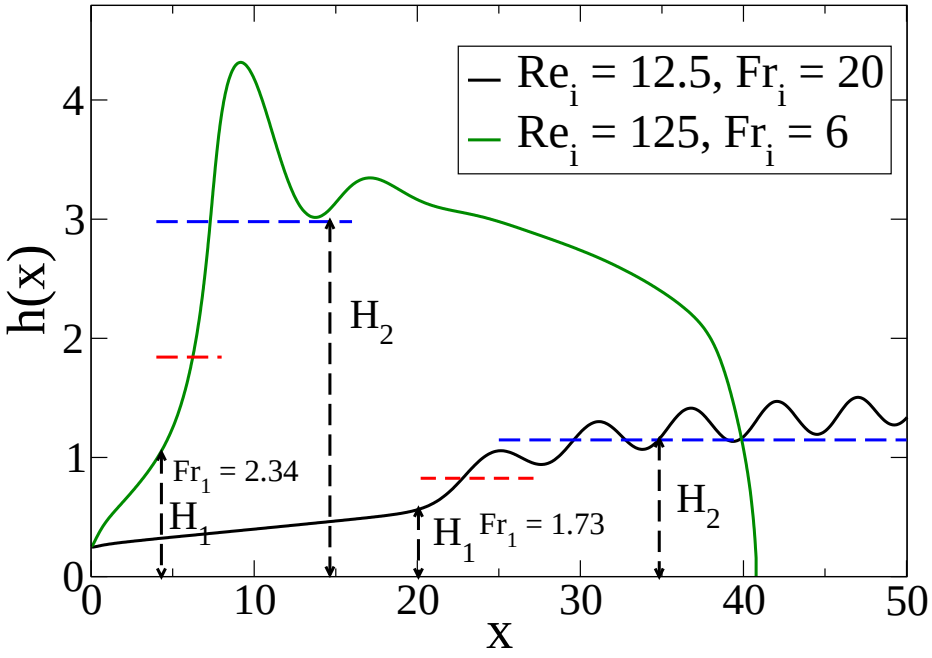

Figure 3.17: Rayleigh shock predictions for a weak jump and a moderately strong jump. The dashed lines in red are the places where the local Froude number goes through unity. For the simulation with $Re_i = 12.5$, $L^* = 150$ while for the second simulation $L^* = 215$. Note that the second simulation has a parabolic inlet profile.

context of equation 3.6, this time on the two-dimensional Navier-Stokes equations. We then follow the approach outlined by Hsieh [1967], who worked with a much simpler equation by making several approximations including the arbitrary neglect of several terms. We however make no assumptions. In particular we use the complete nonlinear free-surface boundary conditions whereas all earlier workers made a significant simplification by using linearised free surface conditions. We arrive at equation 3.10, which is the most general height evolution equation valid for any two-dimensional film flow. The derivation of equation 3.10 is lengthy and we provide it at the end of this chapter.

$$\underbrace{\mathcal{I} + \mathcal{G} + \mathcal{V}\mathcal{B}_{\mathrm{B}}}_{\mathrm{BLSWE}} + \mathcal{D} + \mathcal{D}_\zeta + \mathcal{B} + \mathcal{B}_\zeta + \mathcal{V} + \mathcal{V}_\zeta = 0 \tag{3.10}$$

The expressions for the operators are available at the end of the chapter. $\mathcal{I}$ stands for the inertial terms from the x-momentum equation, $\mathcal{G}$ is the gravity term, $\mathcal{VB}_B$ are the viscous boundary terms included in the BLSWE, $\mathcal{D}+\mathcal{D}_\zeta$ stands for dispersive terms from the vertical momentum equation, $\mathcal{B}+\mathcal{B}_\zeta$ are the terms evaluated at the boundaries and $\mathcal{V}+\mathcal{V}_\zeta$ represents viscous terms not included in the BLSWE. All terms with a subscript ζ, contain a ζ derivative in the velocity profile, i.e., where the departure from similarity appears explicitly whereas those without this subscript contain only η derivatives. The first three terms of the above equation are just the BLSWE integrated across the film thickness. The vertical momentum equation contributes many additional terms, including the dispersive effects $\mathcal{D}+\mathcal{D}_\zeta$ from the non-hydrostatic portion of the pressure. As discussed, these effects are usually neglected in equations of height evolution for the hydraulic jump [Bonn *et al.*, 2009; Watanabe *et al.*, 2003]. Expectedly, the well-known first order ordinary differential equations of Bohr *et al.* [1993]; Singha *et al.* [2005]; Tani [1949] are subsets of this equation. The equation also contains as its subset the Korteweig de Vreis (KdV) equation.

Transforming the momentum equations into a height evolution equation has the following advantages. First, vertical averaging brings the unknown independent variable h from the boundary-condition into the governing equation of motion. This is a considerable simplification in some situations. Additionally, pressure is eliminated from the equations, which is helpful in prescribing boundary conditions. Despite its apparent utility, verticaly averaging is not without pitfalls. The principal drawback is the closure problem that arises as a result. While the original Navier-Stokes equations are closed, equation (3.10) is not, and thus requires modelling of the velocity profiles so as to be solved.

A numerical solution of equation (3.10) is not attempted because it can be harder than solving the Navier-Stokes equations in their usual form, which anyway has already been done. Also it cannot yield any extra information. The objective here is to use the equation to extract the lowest order physics in the J and U regions.

3.4.1 The near-jump region J

We begin by noting that in the neighborhood of the jump, the sum of the inertial and gravity terms in the shallow water equation is small. A solution of the BLSWE shows that when $Fr = 0.78$ we in fact have $\mathcal{I} + \mathcal{G} = 0$. In the neighborhood where this sum is small, it is not reasonable to neglect other terms in comparison. In other words, to balance the viscous term in the BLSWE, there must be other effects that become $O(1)$ relative to this term in this vicinity. This brings us to the conclusion that even for the weakest of jumps, the BLSWE is not sufficient to describe the neighborhood of $Fr = 0.78$. In fact, for steep jumps, i.e., if $h' >> 1$, we can go further to say that *no* term from the BLSWE is important in a low order balance in the jump neighborhood. It is the dispersive and viscous effects coming from the y-momentum equation that form the dominant balance here. The following discussion demonstrates this.

We non-dimensionalise h and x in equation (3.10) by a characteristic height h_j of the jump, but for ease of writing, continue with the same symbols. We analyse it in the near-jump region using the WKB ansatz

$$h = e^{\mathcal{S}(x)} \equiv \exp\left[\sum_{l=0}^{\infty} S_l(x)\epsilon^{l-1}\right], \tag{3.11}$$

where ϵ is a small parameter related to the width of the jump. A similar expression may be written for the streamfunction, except that the variation in η must be included. To account for the difference in scales, and to allow f to change sign, we define

$$f = g(\eta)\exp\left[\sum_{l=0}^{\infty} R_l(\epsilon\eta, \zeta)\epsilon^{l-1}\right]. \tag{3.12}$$

Substituting the above ansatz into equation 3.10, we see that the largest terms on the left hand side of the equation are $O(\epsilon^{-3})$. The largest terms on the right hand side are of order $Re^{-1}\epsilon^{-4}$. These may or may not be of the same order as the largest effects on the left hand side. If they are, we have $\epsilon \sim Re^{-1}$, or in other words, an extremely strong jump. Since the planar jump is most often not strong at all, the more realistic limit is $\epsilon >> O(R^{-1})$. Upon collecting terms of order ϵ^{-3} and performing some algebra, we see that only terms containing ζ-derivatives of

the velocity profile from among the dispersive terms survive. We thus have

$$\frac{S_0'(x)}{h}\int_0^1 2\eta^2(g'^2 - gg'')R_{0\zeta}^2 \exp\left[2R_0(\epsilon\eta,0)\epsilon^{-1}\right]d\eta = 0. \tag{3.13}$$

The above equation contains only terms from the lowest order subset of $\mathcal{D}_\zeta$. Since the velocity profile must be modelled in this formulation, this equation merely gives us a condition which the profiles must obey, and is needs some kind of modelling to solve. At the next order in $1/\epsilon$, we must again make a choice, either $\epsilon \sim Re^{-1/2}$, or is much larger than this order. In the first case, we have a balance between a low-order subset of $\mathcal{D} + \mathcal{D}_\zeta$ and a low-oder subset of $\mathcal{V} + \mathcal{V}_\zeta$. The choice that viscous terms are even smaller would result in an even smaller subset. Our simulations suggest that the latter choice is better.

To establish our main point in this subsection, we do not need to solve equation (3.13) and its higher-order counterparts. We only need to observe that none of the terms appearing at the lowest orders in the J region of a steep jump appears in the shallow water equation. In fact the lowest order equations arise primarily from the vertical momentum equation, which is consistent with a region of high streamline curvature. This means that the shallow water equation is not relevant in the near-jump region, except at higher orders, and except in the form of boundary conditions at either end in x. The importance of the latter effect can be very large, however. The necessity to match the lowest order solutions to the P solution of the BLSWE at low x and to the N solution (often via a U region) at high x, means that gravity plays an important role in deciding not only where the jump begins, but also the total change in height. The next equation in this hierarchy too contains no shallow water term. As model equations in the near jump region, one may write down (not shown) and solve various reasonable subsets of the lowest order equations, and by patching with the P and the U or N solutions on either side, obtain jump-like profiles. In fact we are able to match any of the near-jump profiles obtained from the simulations. Given the freedom in both the model and the boundary conditions, this is not surprising, so we do not show them here.

The above analysis is for small jump widths. Laminar planar jumps, as predicted by our simulations, often too weak to fall under this category. Nevertheless, obstacle-assisted jumps may be made as steep as one would wish. Also circular jumps are rather strong, even when spontaneous.

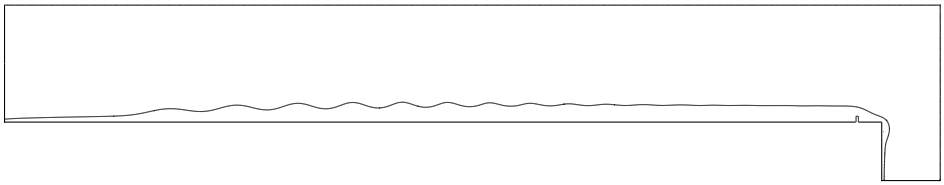

Figure 3.18: A viscous undular jump. The flow is from left to right. The simulation parameters are $Re = 125$, $Fr_i = 6$ and $L^* = 290$

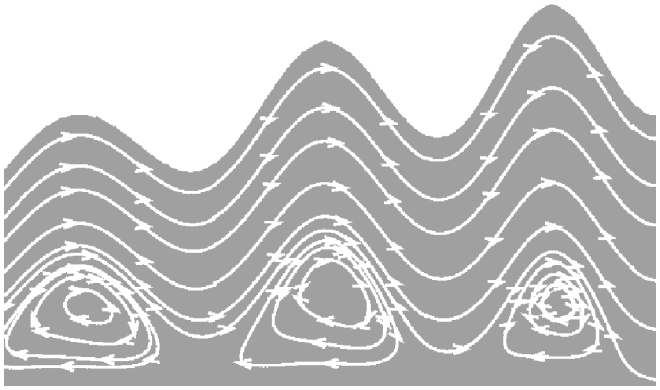

Figure 3.19: Streamlines of a viscous undular jump whose height profile is shown in figure 3.18 - Note the separation bubble underneath each undulation.

3.4.2 A model for the undular region U

The undular region U seen just behind the jump is prominent at the higher Reynolds numbers in our simulations. This region can be quite long, and often encompasses most of the post-jump domain. At low Reynolds numbers, these undulations are damped out at a downstream location. As seen from figure 3.19, each of these undulations is associated with a separation bubble undeneath. For a uniform velocity profile, there is no variation of f with x. Setting these terms, as well as viscosity to zero in equation (3.10), and scaling by some characteristic height h_i we have

$$\frac{h^3 h'}{Fr_i^2} - h' + \frac{1}{3}\left(h^2 h''' - 2hh'h'' + h'^3\right) = 0, \tag{3.14}$$

The coefficients C_1 and C_2 for a uniform velocity profile have been appropriately replaced by 1 and 1/3 respectively. The inviscid flow in this region may be described by a KdV equation, see e.g. Benjamin & Lighthill [1954]. The complete inviscid equation $\mathcal{I}+\mathcal{G}+\mathcal{D}=0$ can support periodic solutions which are descriptive of the undular region, this being a region of the flow where gravity, inertial and dispersive effects are all important. This may be integrated twice to yield

$$\underbrace{h'^2}_{K.E.}+\underbrace{\left(\frac{3}{Fr_i^2}\right)h^3+6a_1h^2+a_2h-3}_{P.E.}=0, \tag{3.15}$$

where a_1 and a_2 are the constants of integration. Equation (3.14) is equivalent to the steady-state KdV equation [Hsieh, 1967] and is known to have two kinds of solution - periodic solutions which are the cnoidal waves of Benjamin & Lighthill [1954], and their limiting case: the solitary wave. The former is descriptive of the undular region. Benjamin & Lighthill [1954] had interpreted equation (3.15) as the sum of kinetic ($K.E.$) and potential energy ($P.E.$) of a particle whose total energy is zero. Thus the oscillatory solutions to equation 3.14 are related to the real roots of the cubic potential, and become possible when the cubic admits three real roots. A solution of equation 3.14 is shown in figure 3.20.

In a region where the slope of the height profile is of $O(1)$, it is not possible to pare down the viscous terms in equation 3.10 by any formal means. Merely for the purpose of demonstration, however, we write down a model viscous KdV equation including only two viscous terms.

$$\frac{hh'}{Fr_i^2}-\frac{h'}{h^2}+\frac{1}{3}\left(h'''-\frac{2h'h''}{h}+\frac{h'^3}{h^2}\right)=\frac{1}{Re}\left(ah''^2-bh'^4/h^2\right), \tag{3.16}$$

This equation is only a slight modification of the equation of [Johnson, 1972], who had introduced a second derivative viscous term to obtain undular shapes which decay with downstream distance. Since fourth derivative term could become more important in regions of high slope, we choose two of these. A variety of undular profiles may be obtained depending on the model. One sees, from figure 3.20 how a height profile with decaying undulations appears in our simulations.

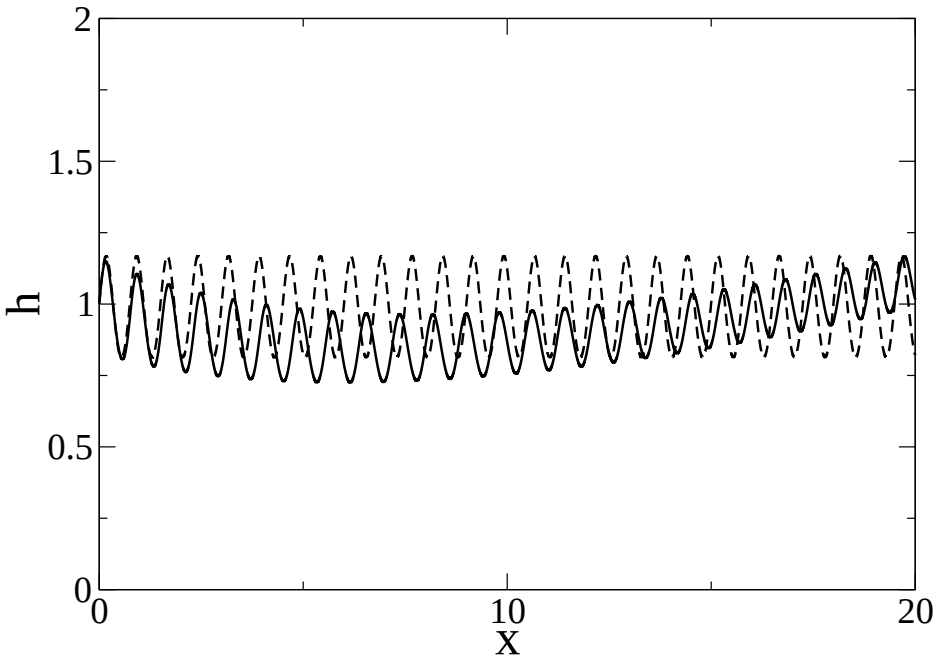

Figure 3.20: The inviscid flow in the undular region may be described by a KdV equation, which support periodic solutions, an example of which is shown by the dashed line. The solid line is the solution of the model viscous equation 3.16, which shows decaying oscillations.

3.5 Conclusion

In this chapter, we have looked at planar hydraulic jumps computationally and analytically. The main conclusions are summarised here. Planar jumps are usually weak, in the sense that h' is usually not much greater than 1. Even for the weakest jumps, the BLSWE is not a valid approximation in the near-jump region. Further, for a strong jump at the two lowest orders in an appropriate expansion, no term from the shallow-water equations enters the governing equation. In this case, the important near-jump effects arise out of dispersive terms, which are entirely neglected in the BLSWE, and viscous terms not included in the BLSWE either. A new depth-averaged equation is derived from the full Navier-Stokes along with the complete nonlinear boundary conditions at the free-surface. This equation has no assumptions and is the most general for a two-dimensional film flow. The near-jump region is studied using this depth-averaged equation. Far upstream, it is

shown that the BLSWE (P solution) is a good approximation to the Navier-Stokes. Far downstream of the jump, if a flat region occurs, a second (N) solution of the BLSWE works well again.

In the region immediately behind the jump, a long train of downstream undulations appear for high Reynolds numbers but were damped out at very low values. The BLSWE fails in this undular region as well. We justify this again by arguing that non-hydrostatic effects must be important near the undulations. We propose a model equation to describe the downstream undulations.

We study the effect of the downstream boundary condition and find that if the domain is sufficiently long, the location of the jump is not very sensitive to its length. The effect of increasing gravity or viscosity is to push the jump upstream while making it steeper. The Rayleigh's shock criterion is found to work well for weak jumps but under-predicts the post-jump height in the case of even slightly strong jumps.

3.6 Depth averaged Navier-Stokes equation

In this section we provide a derivation of equation 3.10. The approach we follow here was laid out in [Hsieh, 1967]. The two dimensional incompressible, steady Navier-Stokes equation in a planar geometry, local and global mass conservation equations alongwith the exact stress-free boundary conditions are:-

$$
\begin{aligned}
uu_x + wu_z &= -\frac{1}{\rho}p_x + \nu\left(u_{xx} + u_{zz}\right), \qquad (3.17)\\
uw_x + ww_z &= -\frac{1}{\rho}p_y + \nu\left(w_{xx} + w_{zz}\right),\\
u_x + w_z &= 0,\\
Q &= \int_0^{h(x)} u dz,\\
p|_{z=h(x)} &= \frac{2\mu}{1+h'^2}\left[w_z(1-h'^2) - h'(u_z + w_x)\right]|_{z=h(x)},\\
&\left[(u_z + w_x)\left(1-h'^2\right) - 4h'u_x\right]|_{z=h(x)} = 0,
\end{aligned}
$$

Here $h' \equiv dh/dx$. We use the incompressibility assumption to define $\psi = Qf\left[\eta, \zeta\right]$, $\eta \equiv z/h(x)$ and $d\zeta \equiv dx/h(x)$ and Q is the mass flow-rate per unit width. Integrating the z-momentum equation from z to $h(x)$ to obtain an expression for

pressure

$$\frac{p}{\rho} = \int_z^{h(x)} (uw_x + ww_z)\, dz + \frac{p}{\rho}|_{z=h(x)} + gh - gz - \nu \int_z^{h(x)} (w_{xx} + w_{zz})\, dz, \quad (3.18)$$

Substituting the expressions for ψ for the velocities in equations 3.18 we obtain,

$$\begin{aligned}
\frac{p}{\rho} &= \left(\frac{Q^2}{h^2}\right)\left[-\left(\int_\eta^1 f_\eta f_{\zeta\zeta} d\eta\right) + h'\left(\int_\eta^1 \eta f_\eta f_{\eta\zeta} d\eta\right) + \left(hh'' - h'^2\right)\left(\int_\eta^1 \eta f_\eta^2 d\eta\right)\right. \\
&\left. + \left(\int_\eta^1 f_\zeta f_{\eta\zeta} d\eta\right) - h'\left(\int_\eta^1 \eta f_\zeta f_{\eta\eta} d\eta\right)\right] + \left\{\frac{2\nu Q}{h^2(1+h'^2)}\right\}\left[-f_{\eta\zeta} - h'^2 f_{\eta\zeta} + h' f_\eta \right. \\
&\left. + h'^3 f_\eta - hh'h'' f_\eta - h'^2 f_\zeta + h' f_{\zeta\zeta}\right]_{\eta=1} + gh - gz \\
&+ \left(\frac{\nu Q}{h^2}\right)\left[-3h'\left(\int_\eta^1 f_{\zeta\zeta} d\eta\right) - \left(hh'' - 2h'^2\right)\left(\int_\eta^1 f_\zeta d\eta\right) + \left(\int_\eta^1 f_{\zeta\zeta\zeta} d\eta\right)\right. \\
&- 3h'\left(\int_\eta^1 \eta f_{\eta\zeta\zeta} d\eta\right) - 3\left(hh'' - 3h'^2\right)\left(\int_\eta^1 \eta f_{\eta\zeta} d\eta\right) + 3h'^2\left(\int_\eta^1 \eta^2 f_{\eta\eta\zeta} d\eta\right) \\
&+ 3h'\left(\int_\eta^1 \eta^2 f_{\eta\eta} d\eta\right) - h'^3\left(\int_\eta^1 \eta^3 f_{\eta\eta\eta} d\eta\right) + \left(6hh'h'' - 6h'^3 - h^2 h'''\right)\left(\int_\eta^1 \eta f_\eta d\eta\right) \\
&\left. + \left(\int_\eta^1 f_{\eta\eta\zeta} d\eta\right) - 2h'\left(\int_\eta^1 f_{\eta\eta} d\eta\right) - h'\left(\int_\eta^1 \eta f_{\eta\eta\eta} d\eta\right)\right] \qquad (3.19)
\end{aligned}$$

Integrating the x-momentum equation from $z = 0$ to $z = h(x)$, we obtain another expression for pressure

$$\frac{1}{\rho}\int_0^{h(x)} p_x dz = \nu \int_0^{h(x)} (u_{xx} + u_{zz})\, dz - \int_0^{h(x)} (uu_x + wu_z)\, dz \qquad (3.20)$$

We substitute into the left and right hand side of equation 3.20, the expressions obtained from equations 3.19 and the form of velocities respectively and using the following theorem (generalized from the one stated in [Hsieh, 1967])

$$\begin{aligned}
&\int_0^{h(x)} z^n \frac{\partial}{\partial x}\left\{ f(x)\left(\int_{z/h(x)}^1 g(t,\zeta)\, dt\right)\right\} dz = h^n\left[\left(fh' + \frac{hf'}{n+1}\right)\left(\int_0^1 g\eta^{n+1} d\eta\right)\right. \\
&\left. + \frac{f}{n+1}\left(\int_0^1 g_\zeta \eta^{n+1} d\eta\right)\right., \qquad (3.21)
\end{aligned}$$

we obtain the final equation (3.10)

$$\underbrace{\mathcal{I}+\mathcal{G}+\mathcal{V}\mathcal{B}_{\mathrm{B}}}_{\mathrm{BLSWE}}+\mathcal{D}+\mathcal{D}_{\zeta}+\mathcal{B}+\mathcal{B}_{\zeta}+\mathcal{V}+\mathcal{V}_{\zeta}=0$$

where the individual terms are

$$I=\left(\frac{1}{h^2}\right)\left[\int_0^1 f_\eta f_{\eta\zeta}d\eta-h'\left(\int_0^1 f_\eta^2 d\eta\right)-\int_0^1 f_\zeta f_{\eta\eta}d\eta\right] \tag{3.22}$$

$$G=\frac{ghh'}{Q^2} \tag{3.23}$$

$$\mathcal{V}\mathcal{B}_{\mathrm{B}}=\left(\frac{1}{h^2Re}\right)\left[f_{\eta\eta}(0)-f_{\eta\eta}(1)\right] \tag{3.24}$$

$$D=\frac{1}{h^2}\left(h^2h'''-2hh'h''+h'^3\right)\left(\int_0^1\eta^2 f_\eta^2 d\eta\right) \tag{3.25}$$

$$\begin{aligned}D_\zeta=&\frac{1}{h^2}\left[h'\left\{\int_0^1\left(\eta(f_\eta f_{\zeta\zeta}-f_\zeta f_{\eta\zeta})+\eta^2(f_{\eta\zeta}^2+f_\eta f_{\eta\zeta\zeta}-f_{\eta\eta\zeta}f_\zeta-f_{\eta\eta}f_{\zeta\zeta})\right)d\eta\right\}\right.\\&\left.+\left(hh''-h'^2\right)\left\{\int_0^1\eta^2(3f_\eta f_{\eta\zeta}-f_{\eta\eta}f_\zeta)d\eta\right\}+\left(\int_0^1\eta f_\zeta f_{\eta\zeta\zeta}d\eta\right)-\left(\int_0^1\eta f_\eta f_{\zeta\zeta\zeta}d\eta\right)\right]\end{aligned} \tag{3.26}$$

$$\begin{aligned}B=&\left(\frac{2}{Re}\right)\left[\frac{3h'^2h''}{h(1+h'^2)}-\frac{2h'^4}{h^2(1+h'^2)}-\frac{2h'^4h''}{h(1+h'^2)^2}+\frac{h'^3}{h^2(1+h'^2)}\right]f_\eta(1,\zeta)\\&-\left(\frac{2}{Re}\right)\left[\left\{\frac{h''^2}{1+h'^2}+\frac{h'h'''}{1+h'^2}-\frac{h'^2h''}{h(1+h'^2)}-\frac{2h'^2h''^2}{(1+h'^2)^2}\right\}f_\eta(1,\zeta)\right]\end{aligned} \tag{3.27}$$

$$\begin{aligned}B_\zeta=&-\left(\frac{2}{Re}\right)\left[\frac{-2h'}{h^2(1+h'^2)}-\frac{2h'h''}{h(1+h'^2)^2}+\frac{1}{h^2(1+h'^2)}\right]f_{\eta\zeta}(1,\zeta)\\&-\left(\frac{2}{Re}\right)\left[\frac{2h'h''}{h(1+h'^2)}-\frac{2h'^3}{h^2(1+h'^2)}-\frac{2h'^3h''}{h(1+h'^2)^2}+\frac{h'^2}{h^2(1+h'^2)}\right]f_{\eta\zeta}(1,\zeta)\\&+\left(\frac{2}{Re}\right)\left[\frac{h''}{h(1+h'^2)}-\frac{2h'^2}{h^2(1+h'^2)}-\frac{2h'^2h''}{h(1+h'^2)}+\frac{h'}{h^2(1+h'^2)}\right]f_{\eta\zeta}(1,\zeta)\\&-\left(\frac{2}{Re}\right)\left[\frac{h'h''}{h(1+h'^2)}f_{\eta\zeta}(1,\zeta)\right]\\&-\left(\frac{2}{Re}\right)\left[\left\{\frac{2h'h''}{h(1+h'^2)}-\frac{2h'^3}{h^2(1+h'^2)}-\frac{2h'^3h''}{h(1+h'^2)^2}\right\}f_\zeta(1,\zeta)+\frac{h'^2}{h^2(1+h'^2)}f_{\zeta\zeta}(1,\zeta)\right]\\&+\left(\frac{2}{Re}\right)\left[\left\{\frac{h''}{h(1+h'^2)}-\frac{2h'^2}{h^2(1+h'^2)}-\frac{2h'^2h''}{h(1+h'^2)^2}\right\}f_{\zeta\zeta}(1,\zeta)+\frac{h'}{h^2(1+h'^2)}f_{\zeta\zeta\zeta}(1,\zeta)\right]\end{aligned} \tag{3.28}$$

$$
\begin{aligned}
V = & \left(\frac{1}{h^2 Re}\right)\Bigg[\left(3\int_0^1 \eta^3 f_{\eta\eta}d\eta\right)\left(2h'^4 + h^2h''^2 + h^2h'h''' - 6hh'^2h''\right) \\
& -\left(\int_0^1 \eta^4 f_{\eta\eta\eta}d\eta\right)\left(3hh'^2h'' - h'^4\right) \\
& +\left(\int_0^1 \eta^2 f_{\eta}d\eta\right)\left(-18hh'^2h'' + 6h'^4 + 5h^2h'h''' + 6h^2h''^2 - h^3h''''\right) \\
& -\left(2\int_0^1 \eta f_{\eta\eta}d\eta + \int_0^1 \eta^2 f_{\eta\eta\eta}d\eta\right)\left(hh'' - h'^2\right) + \left(hh'' - 2h'^2\right) + \left(hh'' - 4h'^2\right)\left(f_\eta(1,\zeta) - 1\right) \\
& -h'^2\left\{f_{\eta\eta}(1,\zeta) - 2(f_\zeta(1,\zeta) - 1)\right\}\Bigg] \qquad (3.29)
\end{aligned}
$$

$$
\begin{aligned}
V_\zeta = & \frac{1}{h^2 Re}\Bigg[-3\left\{\left(hh'' - h'^2\right)\left(\int_0^1 \eta f_{\zeta\zeta}d\eta\right) + h'\left(\int_0^1 \eta f_{\zeta\zeta\zeta}d\eta\right)\right\} \\
& -\left\{\left(h^2h''' + h'^3 - 4hh'h''\right)\left(\int_0^1 \eta f_{\zeta}d\eta\right) + \left(hh'' - 2h'^2\right)\left(\int_0^1 \eta f_{\zeta\zeta}d\eta\right)\right\} \\
& -h'\left(\int_0^1 \eta f_{\zeta\zeta\zeta}d\eta\right) + \left(\int_0^1 \eta f_{\zeta\zeta\zeta\zeta}d\eta\right) \\
& -3\left\{\left(hh'' - h'^2\right)\left(\int_0^1 \eta^2 f_{\eta\zeta\zeta}d\eta\right) + h'\left(\int_0^1 \eta^2 f_{\eta\zeta\zeta\zeta}d\eta\right)\right\} \\
& -3\left\{\left(3h'^3 + h^2h''' - 6hh'h''\right)\left(\int_0^1 \eta^2 f_{\eta\zeta}d\eta\right) + \left(hh'' - 3h'^2\right)\left(\int_0^1 \eta^2 f_{\eta\zeta\zeta}d\eta\right)\right\} \\
& +3\left\{\left(2hh'h'' - h'^3\right)\left(\int_0^1 \eta^3 f_{\eta\eta\zeta}d\eta\right) + h'^2\left(\int_0^1 \eta^3 f_{\eta\eta\zeta\zeta}d\eta\right)\right\} \\
& +3\left(hh'h'' - 2h'^3\right)\left(\int_0^1 \eta^3 f_{\eta\eta\zeta}d\eta\right) \\
& -h'^3\left(\int_0^1 \eta^4 f_{\eta\eta\eta\zeta}d\eta\right) \\
& +\left(6hh'h'' - 6h'^3 - h^2h'''\right)\left(\int_0^1 \eta^2 f_{\eta\zeta}d\eta\right) \\
& -h'\left(\int_0^1 \eta f_{\eta\eta\zeta}d\eta\right) + \left(\int_0^1 \eta f_{\eta\eta\zeta\zeta}d\eta\right) \\
& -2h'\left(\int_0^1 \eta f_{\eta\eta\zeta}d\eta\right) \\
& -h'\left(\int_0^1 \eta^2 f_{\eta\eta\eta\zeta}d\eta\right) - \left(\int_0^1 f_{\eta\zeta\zeta}d\eta\right) + 3h'\left(\int_0^1 f_{\eta\zeta}d\eta\right) \\
& +2h'\left(\int_0^1 \eta f_{\eta\eta\zeta}\right)\Bigg] \qquad (3.30)
\end{aligned}
$$

CHAPTER 4

COMPUTATIONAL RESULTS ON THE CHJ

4.1 Introduction

In this chapter, we study circular hydraulic jumps computationally. The circular jump was probably first recognised by Rayleigh [1914]. The early approaches to the problem were mostly inviscid, using the radial shallow-water equations until it gradually became clear that the analysis needed viscosity to be included (Bohr *et al.* [1993]; Tani [1949]) without which very obvious quantities like the radius of the jump could not be predicted. The role of viscosity in the formation of a circular jump however, has been a source of debate and confusion in the literature. While it is recognised that estimating the radius of the jump from an inviscid theory is not possible (Bohr *et al.* [1993]), the main debate has been about the physical mechanism of jump formation. The analogy between the inviscid shallow-water equations and their gas-dynamic counterpart brought the original idea that the jump is a shock (see Dasgupta & Govindarajan [2010] and the references therein, for a discussion on the analogy). An alternative interpretation was offered by Tani [1949]. He included viscosity in his analysis of the shallow-water equations and hypothesized that the circular jump owes its existence to flow-separation happening underneath it. To quote his precise words *"Closer examination reveals, however that the thickening of layer is due to separation of flow, the separated flow getting*

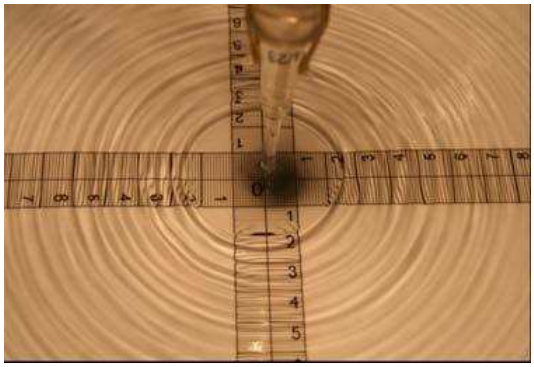

Figure 4.1: Experimental realization of a laminar circular hydraulic jump - Courtesy Vishwanath K. P.

over a standing vortex ring....". While Tani himself did not offer experimental evidence of the presence of a separated bubble, subsequent experiments [Craik *et al.*, 1981; Nakoryakov *et al.*, 1978] detected such a bubble and this lent much support to Tani's hypothesis. Although Tani's work has been an important starting point for the analysis of the boundary-layer shallow-water equation, his hypothesis has also been a cause of debate in the literature. e.g. subsequent workers like Craik *et al.* [1981]; Ishigai *et al.* [1977] have doubted this hypothesis and the possibility of a circular jump without separation has been hinted at in the mathematical model developed by Watanabe *et al.* [2003]. At the same time many studies treat the circular jump and separation as phenomena which are intimately tied to each other (Rao [1994]).

As discussed earlier, while the idea that separation is probably *not* the cause of jump formation is not new, concrete evidence for the same in form of circular jumps without separation obtained from direct numerical simulations does not exist to the best of our knowledge. Nevertheless, using mostly visual methods, circular jumps without separation have been very sporadically reported in the experimental literature (Chang *et al.* [2001]; Ellegaard *et al.* [1998]; Liu & Lienhard [1993]). Here it needs to be emphasized that while visual methods like dye-injection can be useful in showing the existence of a separated region, they are not always adequate for settling the inverse question viz. is separation indeed absent? This is because under typical experimental conditions, the film-thickness in a circular jump is so small that being absolutely sure that there is no separated bubble, no matter how small, requires experimental techniques more sophisticated than the usual visual methods. An example of one such method is the measurement of wall-shear done by Ishigai *et al.* [1977]. In this work, the authors studied jumps experimentally and categorised them into different kinds, but jumps without separation were not reported. Jumps without separation have been so rarely reported in the literature that the now standard classification of circular-jumps completely ignores their existence. The broad categorisation of circular jumps divides them into two types - Type-I and Type-II (Bush *et al.* [2006]; Ellegaard *et al.* [1996]). An illustration of these types is provided in figures 4.2 and 4.3. It is seen that both kinds are associated with a wall-eddy. A study by Chang *et al.* [2001] attempts to resolve the confusion by reporting two different and independent mechanisms for jump formation - one jump which is created due to boundary-layer separation and another

jump without separation which is triggered by capillary back pressure.

To resolve some of the above issues, it is clear that direct simulations of the Navier-Stokes equations would be useful and important, as would sophisticated experiments. The literature on the circular hydraulic jump, while being extensive, has surprisingly very few published studies of direct numerical simulations. Some simulations have been reported in Dingwei *et al.* [1998]; Ferreira *et al.* [2002]; Khavari *et al.* [2009]; Yokoi & Xiao [1999]. In the simulations by Dingwei *et al.* [1998], the effect of change of impingement height and nozzle radius on the radius of the jump was reported. The numerical simulations of Yokoi & Xiao [1999] were used to study the transition between a Type-I to a Type-II jump and it was reported that a region of high dynamic pressure was created for the Type-II jump which owed its origin to surface-tension. The numerical simulations of Ferreira *et al.* [2002] while being the first three-dimensional simulations of the circular jump, were focussed on using the circular hydraulic jump as a benchmark problem for comparing the capabilities of various codes. The study by Khavari *et al.* [2009] simulated the various types of jumps (Type-I, IIa, IIb etc.).

Thus it is seen that none of these studies addresses the issue of whether indeed jumps without separation can be obtained. The present study intends to make a first attempt towards bridging this gap as well as using these simulations to understand other related issues pertaining to circular jumps. This chapter is organised as follows - The first section describes the numerical details, computational domain and the initial and boundary conditions. We then show computational simulations of jumps with and without separation. The jumps without separation are obtained without any surface-tension and thus do not correspond to the capillary backpressure mechanism proposed by Chang *et al.* [2001]. This is followed by a discussion of the effect of downstream boundary conditions on the jump. We next discuss the effect of variation of viscosity, gravity and surface-tension on the structure of the jump. A discussion on the applicability of the Rayleigh shock criterion to circular jumps follows. We conclude with a discussion of the initial value problem of jump formation. The role of viscosity in preventing wave-breaking is pointed out by doing some inviscid simulations.

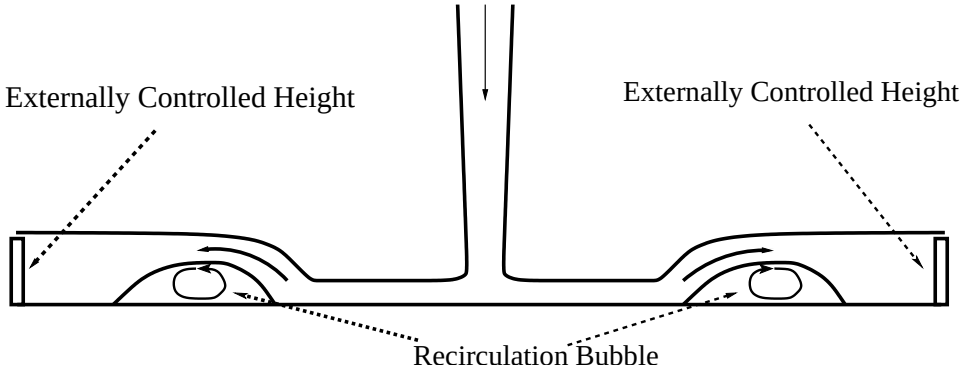

Figure 4.2: Type-I jumps (classification by Ellegaard *et al.* [1996])

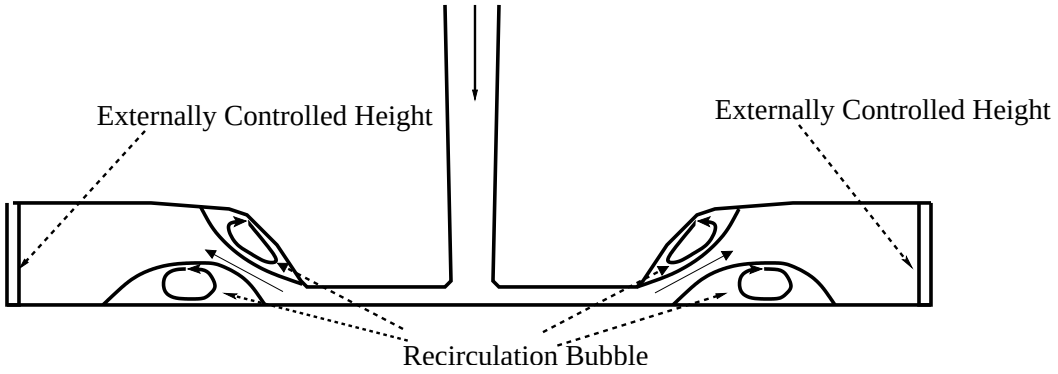

Figure 4.3: Type-II jumps (classification by Ellegaard *et al.* [1996]). Note that both Type-I and Type-II jumps are associated with a wall eddy.

4.2 Numerical Modelling

The axisymmetric Navier-Stokes equations are solved using the free-surface module of *GERRIS* [Popinet, 2010]. This has already been described in Chapter 2. Shown in figure 4.4 and 4.5 are the two kinds of computational domains used. The need for the Domain B in figure 4.5 arose because we wanted to control the outer depth close to the exit. Merely placing an obstacle near the exit and imposing a Dirichlet pressure boundary condition at the outlet caused the simulations to fail. This problem was circumvented by modifying Domain A to Domain B with the "pit". A similar device was also employed in our simulations of planar jumps reported in Chapter 3. The fluid flows into the pit where an outflow condition is imposed. The hashed sides represent impermeable walls. For the computational Domain A shown in figure 4.4, the variables in the problem are the velocity U_{av} at the inlet (taken to be a uniform profile), the height of impingement H, the nozzle radius

Table 4.1: Boundary conditions for figures 4.4 and 4.5

Side	on velocity	on pressure
S1	No-slip, no penetration	Neumann condition
S2 (Domain A)	Neumann condition	Dirichlet condition
S2 (Domain B)	Free-slip	Neumann condition
S3 (Domain A)	Neumann condition	Dirichlet condition
S3 (Domain B)	Free-slip, no penetration	Neumann condition
S4	Free-slip, no penetration	Neumann condition
S5	Free-slip, no penetration	Neumann condition
Axis of symmetry	Reflective condition	Neumann condition

r_n, the domain length D, kinematic viscosities of the inlet fluid and the ambient fluid, ν_w and ν_a respectively, and their respective densities ρ_w and ρ_a, acceleration due to gravity g and surface-tension coefficient σ. These lead to non-dimensional ratios nozzle Reynolds number $Re_n \equiv U_{av} r_n/\nu$, nozzle Froude $Fr_n \equiv U_{av}/\sqrt{gr_n}$, D/r_n, r_n/H, ν_a/ν_w, ρ_a/ρ_w and Bond number $Bo \equiv \rho g r_n^2/\sigma$. In all simulations we fix $\nu_a/\nu_w = 10$ and $\rho_a/\rho_w = 0.001$ which roughly corresponds to an air-water situation. For Domain B simulations, we have an additional non-dimensional ratio O/r_n. Simulations with Domain B were primarily conducted for obtaining qualitative answers and in this chapter we will mostly focus on simulations done with Domain A. Table 4.1 lists down the boundary conditions that were used for these simulations and table 4.2 lists all simulations carried out. Shown in figure 4.6 is the initial condition for all the simulations. Since GERRIS does not have a contact-line model, we were unable to simulate the more realistic case of a jet impinging on a dry plate. This problem was bypassed by pre-wetting the plate with a thin layer of fluid as an initial condition. The jet was given an initial velocity while the pre-wetting fluid on the plate was kept initially stagnant. It was verified that the final steady state obtained was independent of the latter initial conditions, by performing another simulation with exactly the same set of parameters but this time, with the pre-wetting film having an initial velocity. Both initial conditions were checked to produce the same eventual steady state solution.

$D/r_n = 48$		$D/r_n = 64$		$D/r_n = 80$	
Fr_N	Re_N	Fr_N	Re_N	Fr_N	Re_N
7.58	100	7.58	225	7.58	225
7.58	150	15.16	450	-	-
7.58	175	-	-	-	-
7.58	225	-	-	-	-
7.58	350	-	-	-	-
7.58	450	-	-	-	-
7.58	550	-	-	-	-
15.16	100	-	-	-	-
19.79	100	-	-	-	-
22.62	100	-	-	-	-
28.28	100	-	-	-	-
33.94	100	-	-	-	-
39.59	100	-	-	-	-

Table 4.2: Simulation parameters for Domain A - For meanings of symbols refer to figures 4.4 and 4.5. These simulations are all done for $r_n/H = 0.0625$. Although not listed here in the table, a few simulations with $D/r_n = 24, 32$ and 40 were also conducted during the early part of this study.

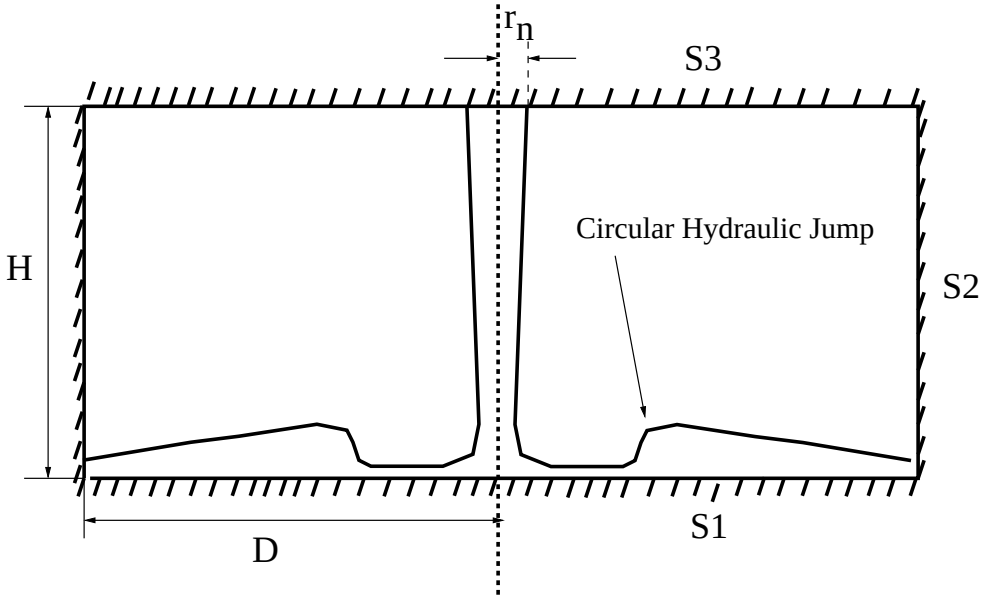

Figure 4.4: Schematic of computational Domain A - the outlet height is not controlled. These are axisymmetric computations and hence the equations are solved only for half of the domain and the complete solution is obtained by reflection about the axis of symmetry viz. the dotted line.

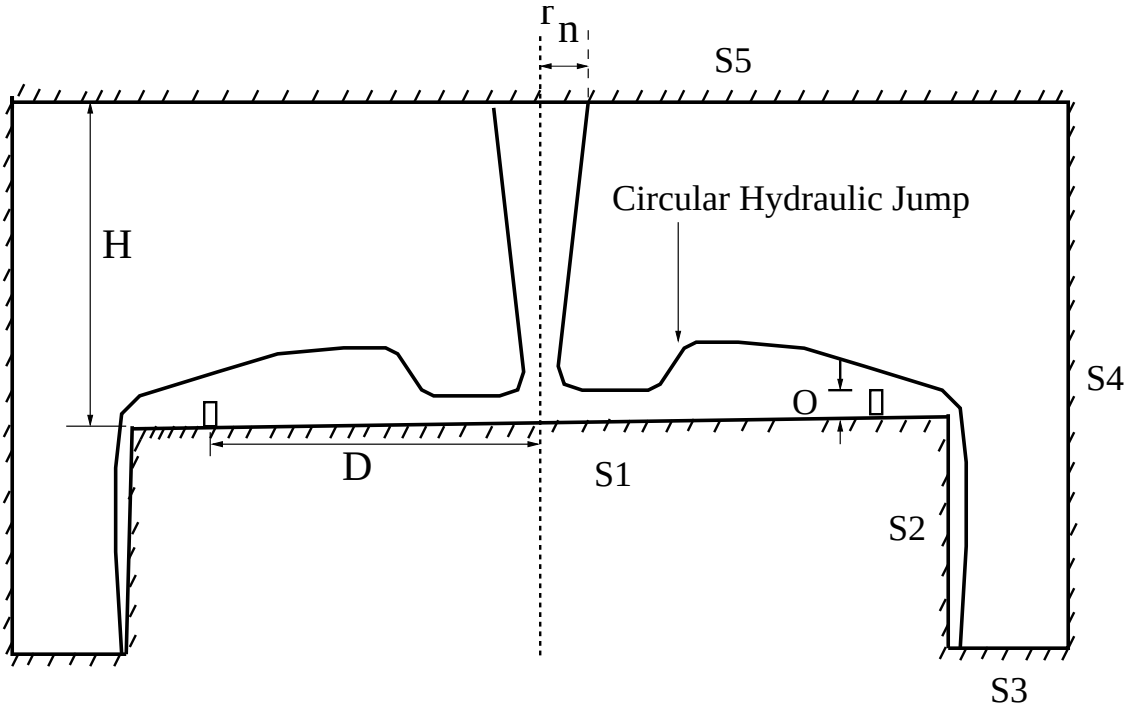

Figure 4.5: Schematic of computational Domain B - the outlet height is controlled using an obstacle O.

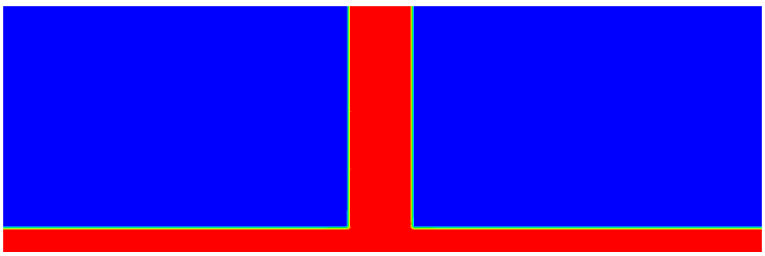

Figure 4.6: A typical initial condition used for simulating the circular jumps reported in the present study - A jet with some initial velocity impinging on a stagnant film. Similar initial conditions were used for both Domain A and B simulations.

4.3 Computational Results

We start this section with trying to answer the first question discussed in the introduction, viz. are jumps possible without any separation at the wall? In figures 4.7 and 4.9 we show two kinds of jumps - one with a separated bubble and another without any bubble. The corresponding streamlines are depicted in figures 4.8 and 4.10. It may appear from the streamline patterns in figure 4.10, that there could be a small separation bubble near the wall. The near-jump velocity profiles are hence plotted in figure 4.11 and it is seen that there is no region of reverse velocity near the jump. The height profile in figure 4.12 shows the near-jump region and the dashed lines indicate the radial locations from where the velocity-profiles are taken in figure 4.12. A valid objection to this result would be that we do not have sufficient grid resolution to capture the separated bubble. To be sure, we repeated some of these simulations with a finer grid and the results were found not to change. No separation bubble appeared with finer grids. The important point here is that we now have convincing evidence that Tani's hypothesis (Tani [1949]) was incorrect, since if it was true, our inability to resolve the separation bubble in our computations would have prevented the jump also from forming. The fact that we get one effect without the other, provides strong evidence that the physical mechanism of jump formation does not rely on separation. To the best of our knowledge, jumps without any separation at the wall in a circular geometry have not been reported in Navier-Stokes simulations before and we label these as "Type-0" jumps. Note that the jumps without separation reported by Chang *et al.* [2001] rely on a capillary back-pressure mechanism for their existence. The simulation in figure 4.9 is however done without any surface-tension and thus these jumps are not caused by capillary effects. We emphasize that separation is not the cause of the jump.

We have not attempted any study with the aim of determining those regions of the parameter space where Type-0 jumps might be expected. This is primarily due to the fact that a large number of non-dimensional parameters are involved in these simulations, due to which the parameter space is rather large. However some trends were observed. Keeping all other parameters fixed, larger nozzles gave Type-0 jumps while smaller nozzles would produce Type-I jumps. For low enough values of Re_n, if the fluid height at the exit was not controlled, it would produce

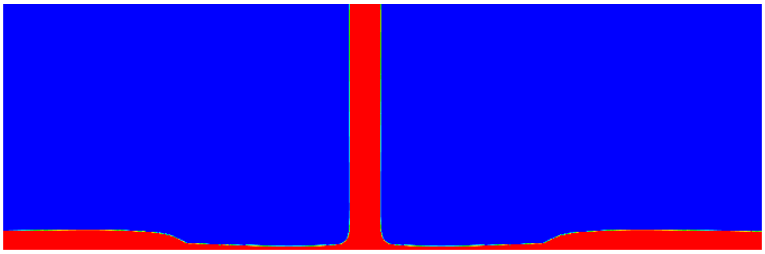

Figure 4.7: A simulation of a circular jump with separation. The simulation parameters are - Domain A, $Re_n = 450, Fr_n = 15.16, D/r_n = 64, r_n/H = 0.0625, Bo = 1.0877$.

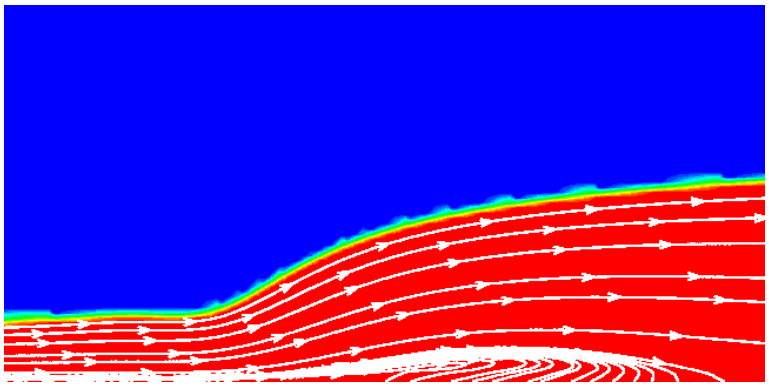

Figure 4.8: Streamlines of the jump in figure 4.7 indicate the presence of a separation bubble at the wall.

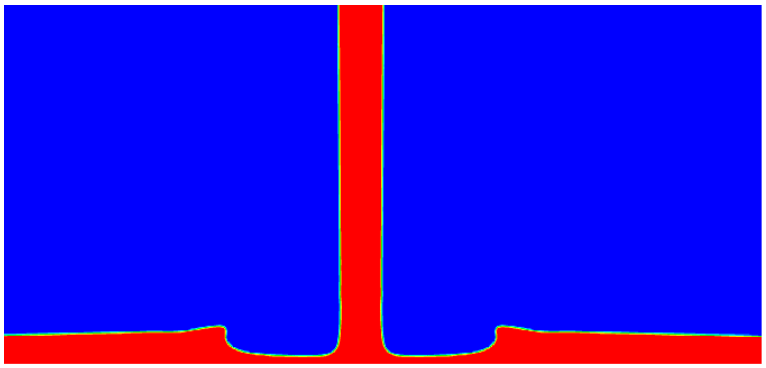

Figure 4.9: A simulation of a circular jump *without* separation. The simulation parameters are - Domain A, $Re_n = 100, Fr_n = 7.58, D/r_n = 48, r_n/H = 0.0625, Bo = \infty$.

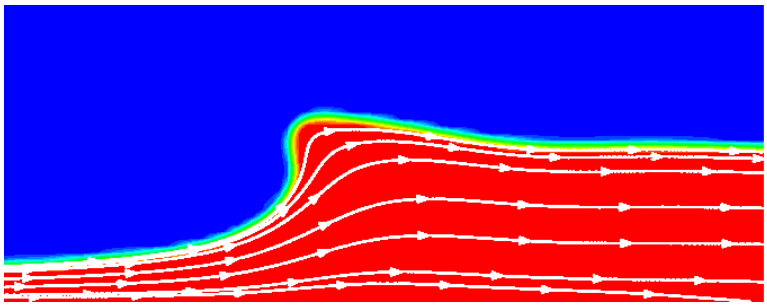

Figure 4.10: Streamlines of the jump in figure 4.7 *without* separation. We call these as Type 0 jumps.

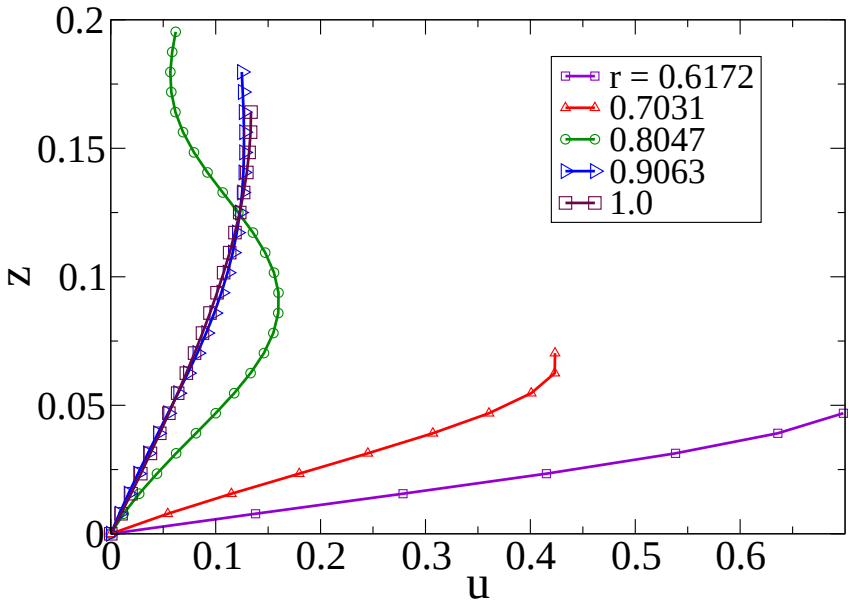

Figure 4.11: The velocity-profiles in the near jump region for the jump in figure 4.10. Note that there is no region of reversed flow in the near jump region.

Type-0 jumps. Seen in figure 4.13 is a Type-0 jump where the outer boundary is not controlled (Domain B simulation without an obstacle). An obstacle is then slowly raised at the outer boundary and this causes the jump to become steeper and develop a wall-vortex as seen in figure 4.14. Given the myriad states that these circular jumps display (Type-0, Type-I, Type-IIa, Type-IIb etc.), it should be an experimentally challenging task to classify the conditions under which each subtype is expected.

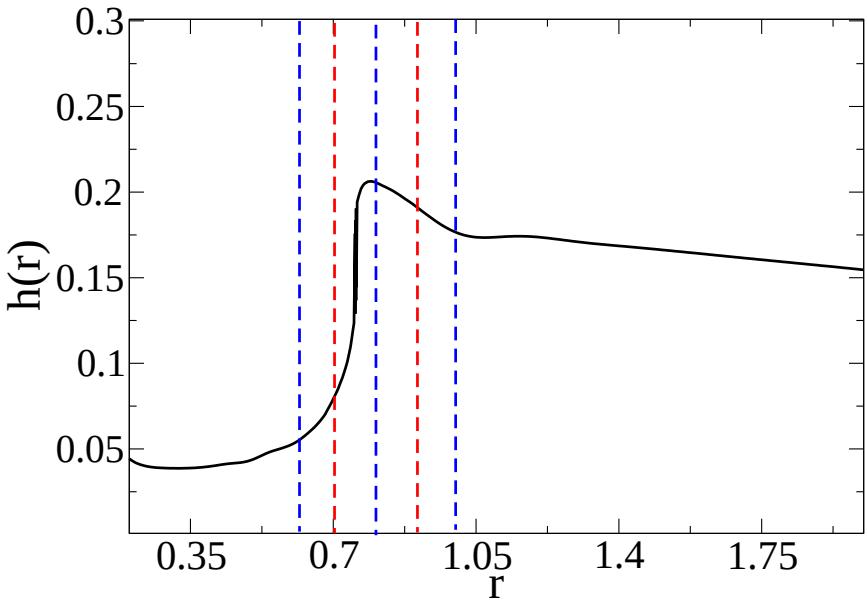

Figure 4.12: The height-profile for figure 4.11. The dashed lines represent the radial locations where the velocity-profiles have been extracted and correspond to the legend of figure 4.11.

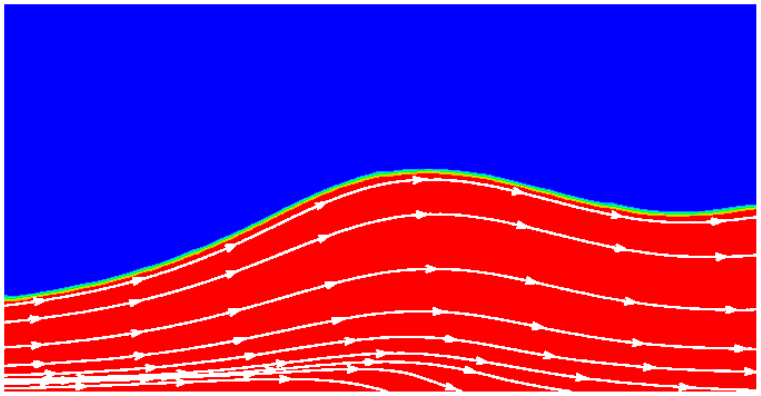

Figure 4.13: Domain B simulation. The parameters are $Re_n = 250, Fr_n = 5.36, D/r_n = 17.6, r_n/H = 0.125$ and $Bo = 4.35$. The simulation is initially conducted without placing any downstream obstacle and we obtain a Type-0 jump. Although the streamlines close to the wall seem to curve downwards, it can be checked from the velocity profiles that there is no separation bubble and no negative velocities.

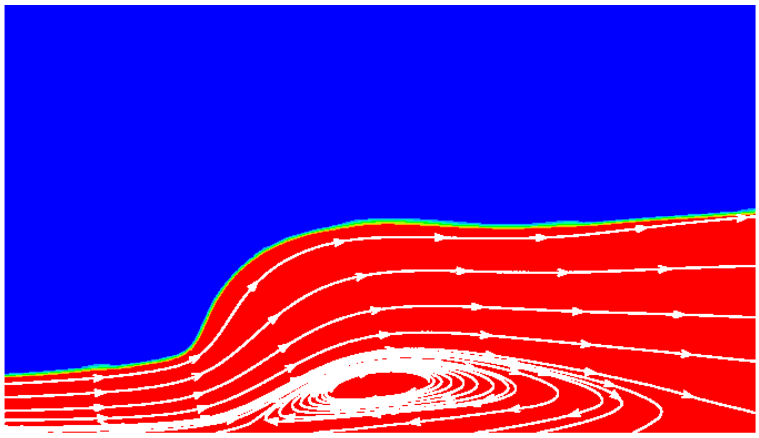

Figure 4.14: The simulation of figure 4.13 is carried forward by placing an obstacle at the outlet. The ratio $O/r_n = 0.6$. Note that the picture shown is not at steady-state. Raising the obstacle leads to a wave-breaking transition and in this particular simulation, led to the formation of a Type-II jump. Our numerical procedure of resolving the wave-breaking is not accurate and hence we do not show this here.

4.3.1 Effect of gravity, viscosity and surface-tension

In figure 4.15, the height profiles are obtained for various values of nozzle Reynolds number Re_n. It is seen that decreasing viscosity increases the steepness in the near jump region and produces stronger jumps. The same remains true for increasing gravity as seen in figure 4.16, this being consistent with the experimental observations and theoretical predictions of Avedesian & Zhao [2000] and Bush & Aristoff [2003]. Note that we define the strength of the jump in figures 4.15 and 4.16 based on the slope of the near-jump profile. This is in contrast to the usual inviscid definition of strength based on the ratio of upstream and downstream heights H_2/H_1. This description neglects the jump-width and treats it like a discontinuity. In figure 4.17, we see the effect of surface-tension on the radius and structure of the jump. It is seen that surface-tension has a negligible effect on the radius of the jump (Bush & Aristoff [2003]). Note however that it retains a significant influence on the jump structure, completely damping out the post-jump oscillations (see the height-profile in figure 4.15 corresponding. to $Re_n = 550$). These observed trends for the influence of gravity, viscosity and surface-tension are qualitatively the same for planar jumps as well.

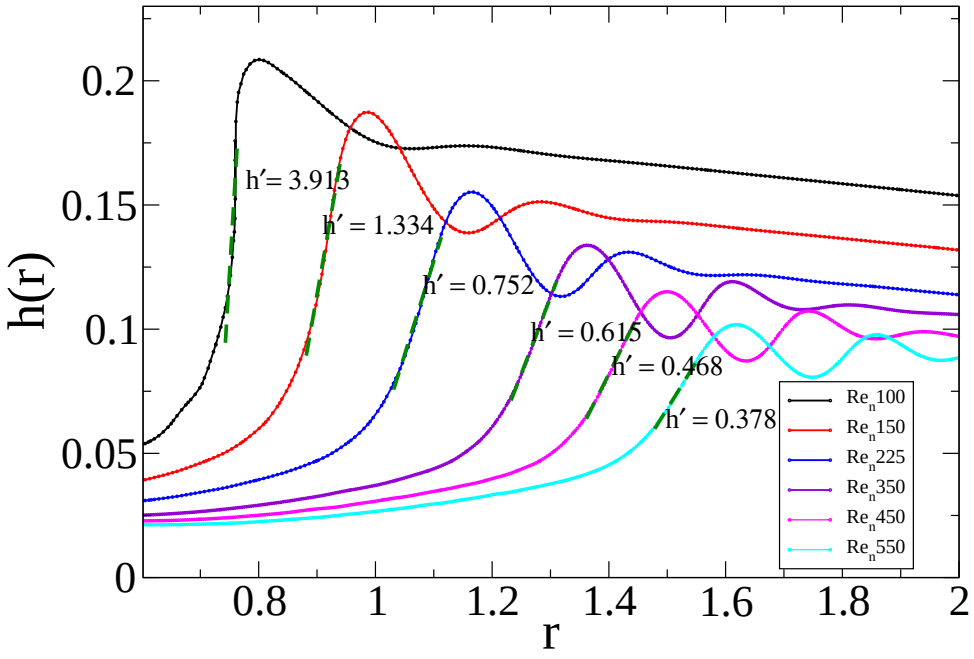

Figure 4.15: The effect of increase of nozzle Reynolds Re_n on the radius and the near-jump structure. The dashed lines in green are obtained from a linear fit to the near-jump profile and the value of the slope is denoted by h'. It is seen that as the Reynolds number decreases, the jumps become steeper with increasing values of h'. This observation is consistent with the experimental findings of Avedesian & Zhao [2000] and the predictions of Bush & Aristoff [2003]. The parameters are $Fr_n = 7.58, r_n/H = 0.0625, D/r_n = 48$ and $Bo = \infty$.

4.4 Comparisons

In this section we compare planar jumps to the circular ones. We also compare our Navier-Stokes results to those obtained from the solution of the radial BLSWE, discussed in Chapter 2.

4.4.1 Comparison between planar and circular geometries

In this section we make comparisons between planar and circular jumps. The most noticeable difference in our simulations was the occurrence of steep jumps in a circular geometry but rather gentle jumps in planar geometries. In figure 4.18 and 4.19, we compare the steepest jump obtained in our planar simulations to the

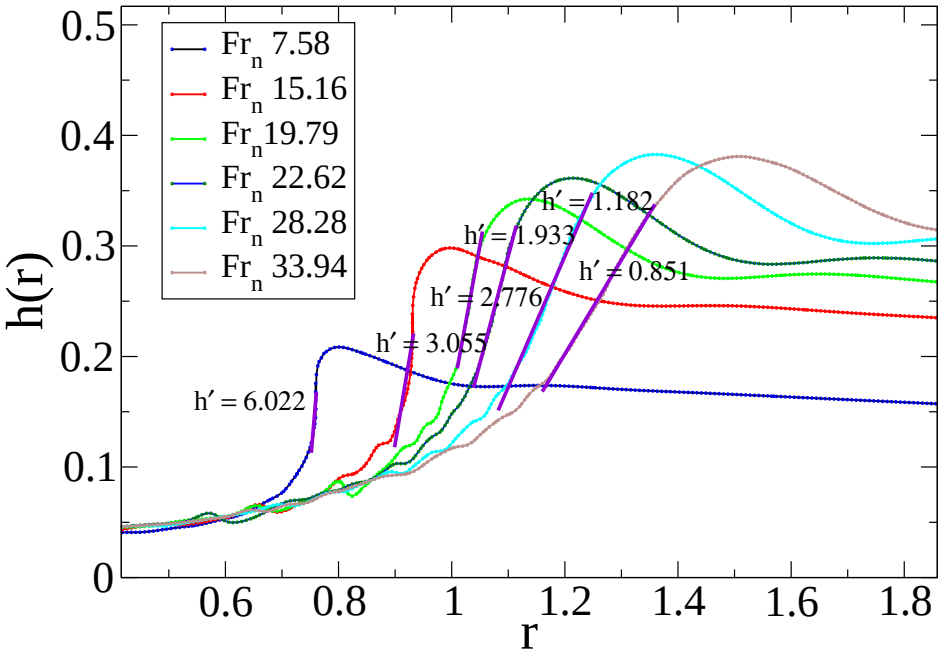

Figure 4.16: The effect of increase of nozzle Froude number Fr_n on the radius and the near-jump structure. The solid lines in purple are obtained from a linear fit to the near-jump profile and the value of the slope is denoted by h'. It is seen that as the Froude number increases, the jumps become steeper with increasing values of h'. The parameters are $Re_n = 100, r_n/H = 0.0625, D/r_n = 48$ and $Bo = \infty$.

steepest jump obtained in circular geometries. The reader is reminded that our definition of steepness is based on the slope of the near-jump region. It is seen from figures 4.18 and 4.19 that circular jumps are far steeper than their planar counterparts. The location at which Fr_1 is chosen is the place where the height-profile displays an abrupt change in slope. It is interesting to observe that although both have almost the same Froude number Fr_1, the circular jump is a much stronger jump. It is seen that Rayleigh shock criterion cannot predict anything about the slope h' of the near jump region.

Rayleigh shock criterion

Shown in figure 4.20 is an azimuthal section of a discontinuity in a circular geometry. Due to a circular geometry, a constant height is not a solution of the inviscid problem. We take the height to be varying, with the left-hand limit of the height

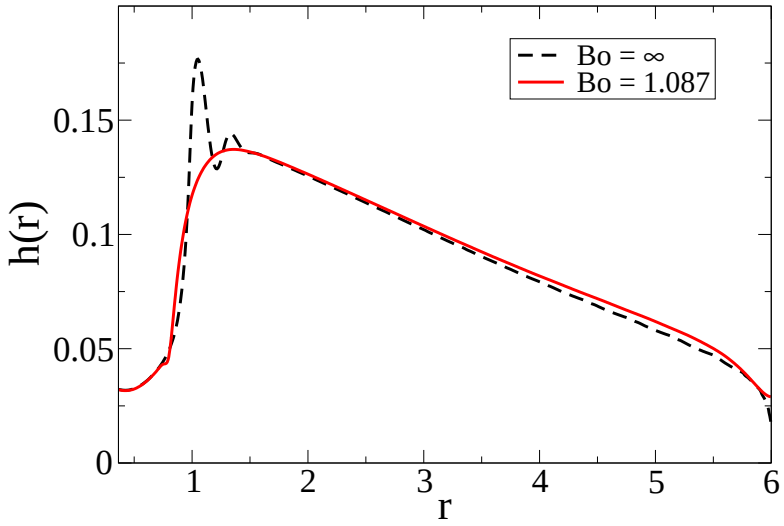

Figure 4.17: The effect of surface-tension on the jump radius and structure. The parameters are $Re_n = 175, Fr_n = 7.58, D/r_n = 48, r_n/H = 0.0625$. Note that surface-tension has practically no effect on the radius of the jump.

to be H_1 and that right hand limit to be H_2. Just like in a planar geometry, mass and momentum flux conservation relations are written across this discontinuity assuming uniform velocity U_1 and U_2 upstream and downstream of the discontinuity respectively. For a radius r_j of the discontinuity and assuming hydrostatic pressure,

$$\begin{aligned} H_1U_1 = H_2U_2 \equiv \frac{Q}{2\pi r_j}, \\ \pi r_j g\left(H_1^2 - H_2^2\right) = Q(U_2 - U_1). \end{aligned} \tag{4.1}$$

Combining the two equations in 4.1, one can obtain equation (4.2), where $Fr_1 \equiv Q/2\pi r_j\sqrt{gH_1}$.

$$\frac{H_2}{H_1} = \frac{-1 + \sqrt{1 + 8Fr_1^2}}{2}. \tag{4.2}$$

Equation (4.2) is identical to its planar counterpart studied earlier in Chapter 3. This equation has been derived in Bohr *et al.* [1993]; Liu & Lienhard [1993] and in many other studies discussed in Chapter 1.

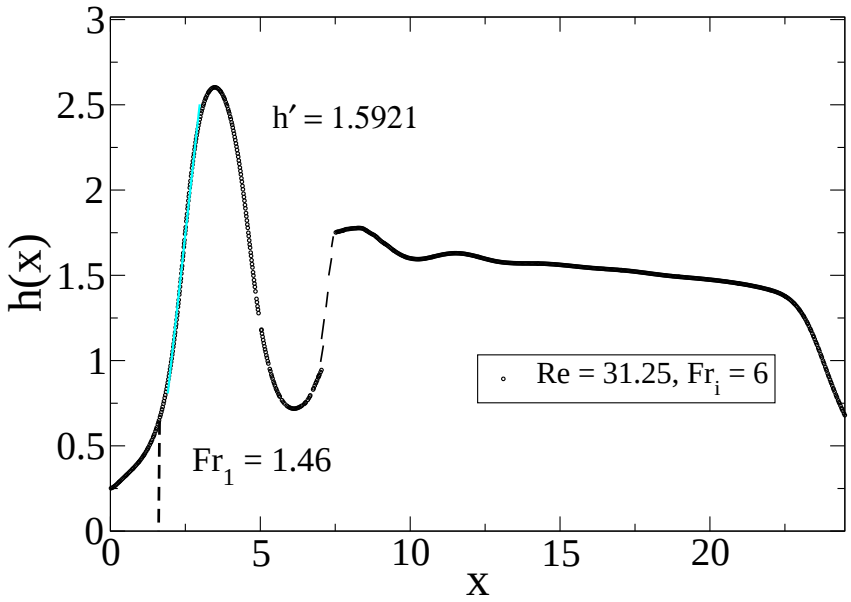

Figure 4.18: The steepest steady planar jump that was obtained in our simulations. We define Fr_1 to be at that point where the height-profile shows an abrupt change in slope. this is determined by visual inspection. The line in cyan is a linear fit to the near-jump region with the slope $h' = 1.592$. The broken line represents some local wave-breaking.

A paradox in circular geometry

It is interesting to discuss an apparent paradox related to the Rayleigh shock criterion of equation (4.2) which arises only in a circular geometry. Equation (4.2) was derived by insisting that the net momentum-flux should be counterbalanced by hydrostatic pressure forces on either sides of a height discontinuity in a circular geometry shown in figure 4.20. Indeed this procedure is nothing more than applying Newton's second law of motion to a control volume containing the discontinuity, and then taking the limit of the control volume shrinking to zero in such a way that the discontinuity is always contained inside the control-volume. This leads to the following quantities being conserved on either side of the jump

$$\begin{aligned} U_i H_i &= C_1, \\ Q U_i + \pi r_j g H_i^2 &= C_2', \\ \Rightarrow 2U_i^2 H_i + g H_i^2 &= C_2, \end{aligned} \tag{4.3}$$

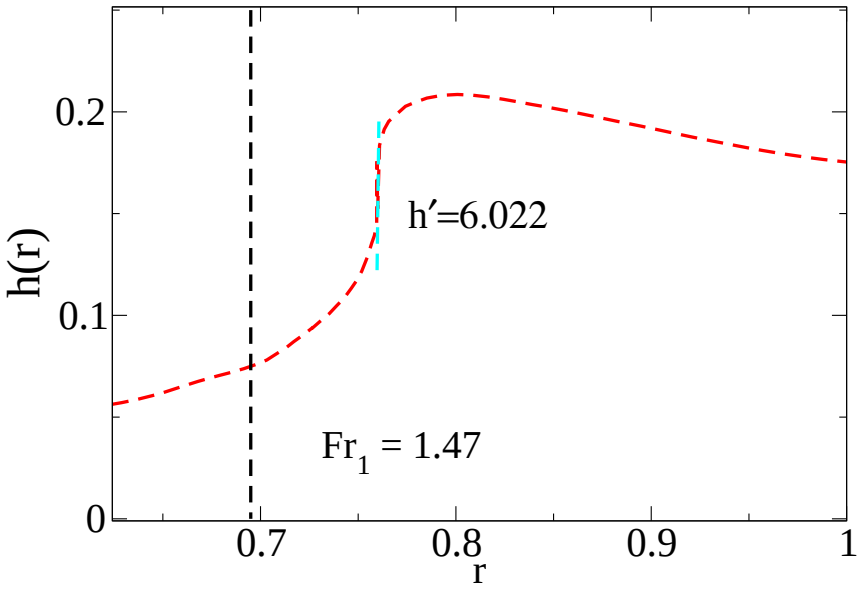

Figure 4.19: The steepest circular jump obtained from simulations. The near jump slope here is much larger than the steepest planar jump in figure 4.18. The line in cyan is a linear fit to the near-jump region. The parameters are $Fr_n = 7.58, Re_n = 100, r_n/H = 0.0625, D/r_n = 48$ and $Bo = \infty$.

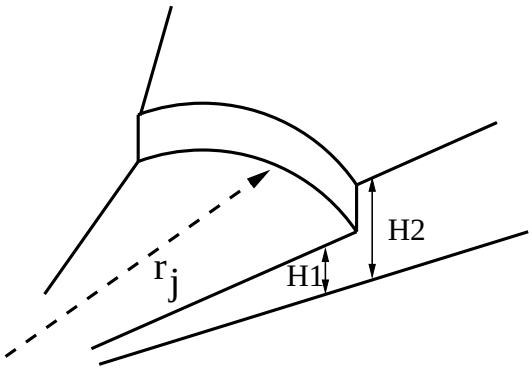

Figure 4.20: An inviscid circular jump represented as a shock discontinuity. Mass and momentum flux relations written across the axisymmetric discontinuity constitute the extension of Rayleigh shock criterion to a circular geometry.

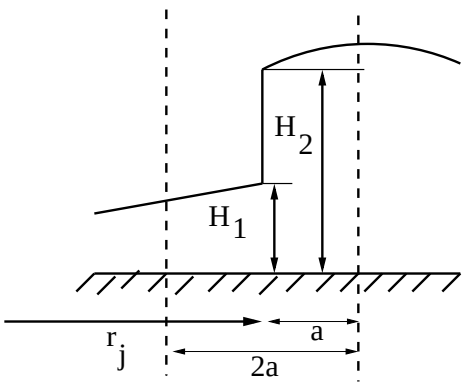

Figure 4.21: A control volume centered on the discontinuity.

where C', C are constants, $C \equiv C'/r_j\pi$ and the subscript $i = 1, 2$. Until now, everything discussed has been exactly identical to a planar geometry with no qualitative changes. However, if we now write down the inviscid shallow-water equations for a circular geometry, a discrepancy becomes apparent. These equations are:

$$\begin{aligned} UrH &= \frac{Q}{2\pi}, \\ \frac{U^2}{2} + gH &= M, \end{aligned} \tag{4.4}$$

where Q is as before and M is a constant having dimensions energy per unit mass. Combining the two equations 4.4 one can obtain a conservative form (Bohr *et al.* [1993]),

$$\frac{d}{dr}\left[rH\left(U^2 + \frac{gH}{2}\right)\right] = \frac{gH^2}{2} \tag{4.5}$$

Refer to figure 4.21, we integrate equation (4.5) from $r = r_j - a$ to $r = r_j + a$ and then take the limit $a \to 0$. This thus gives

$$\begin{aligned} \lim_{a\to 0}\left[rH\left(U^2 + \frac{gH}{2}\right)\right]_{r_j-a}^{r_j+a} &= \frac{gH_2^2}{2} - \frac{gH_1^2}{2} \\ \Rightarrow H_2\left(U_2^2 + \frac{gH_2}{2}\right) - H_1\left(U_1^2 + \frac{gH_1}{2}\right) &= \left(\frac{1}{r_j}\right)\left[\frac{gH_2^2}{2} - \frac{gH_1^2}{2}\right] \\ \Rightarrow H_i\left(U_i^2 + \frac{gH_i}{2}\right) &\neq \text{Constant} \end{aligned} \tag{4.6}$$

It is evident that left hand side of both equations 4.3 and 4.5 contain the quantity $2U_i^2H_i+gH_i^2$. However, while equation (4.3) predicts that this is a conserved quantity across the discontinuity, equation (4.5) tells us that it is not. This paradox was first noticed by Bohr *et al.* [1993] although these authors did not comment elaborately on it while choosing to use equation (4.2) for fitting a shock and estimating the jump radius. This is an important point of departure of the applicability of Rayleigh's shock criterion for a circular geometry. In a planar geometry, Rayleigh's criterion predicts that flow through a mathematical discontinuity can conserve mass and momentum flux but not energy. In case of a circular geometry, even momentum-flux is not conserved across a discontinuity, as the governing equations show above. Despite this apparently paradoxical result, equation (4.2) has been extensively used in the circular hydraulic jump literature. In an experimental study by Liu & Lienhard [1993], the validity of equation (4.2) for circular jumps was examined, and it is reported that poor agreement was obtained. These authors attributed the poor much to surface-tension rather than a radial geometry. Shown in figure 4.22 are the predictions obtained from equation (4.2). It is seen that equation (4.2) overpredicts the outer height H_2. Notice however that the simulation reported in figure 4.22 has no surface-tension and hence it becomes clear that the inadequacy of equation (4.2) is not just due to surface-tension effects. We take the view that the not so good prediction by 4.2 is due to the fact that in an axisymmetric geometry, the inviscid shallow-water equations do not support a discontinuity. This is readily understood if we observe that both equations (4.3) and (4.5) are two different ways of writing Newton's second law of motion and hence should give the same answer if a discontinuity were supported, as it does in a planar geometry. The fact that it leads to different answers when applied at a discontinuity shows that inviscid, shallow-water theory does not support discontinuities. The inadequacy of the estimate of H_2 in figure 4.22 is further evidence to this argument.

4.4.2 Comparison with BLSWE

In Chapter 2, we had seen that the boundary-layer shallow-water equations admit a similarity solution at large values of local Froude (see equation (2.32) in Chapter 2). This solution is $Re(h' + h/r) = 1.8$ which can be integrated from an initial

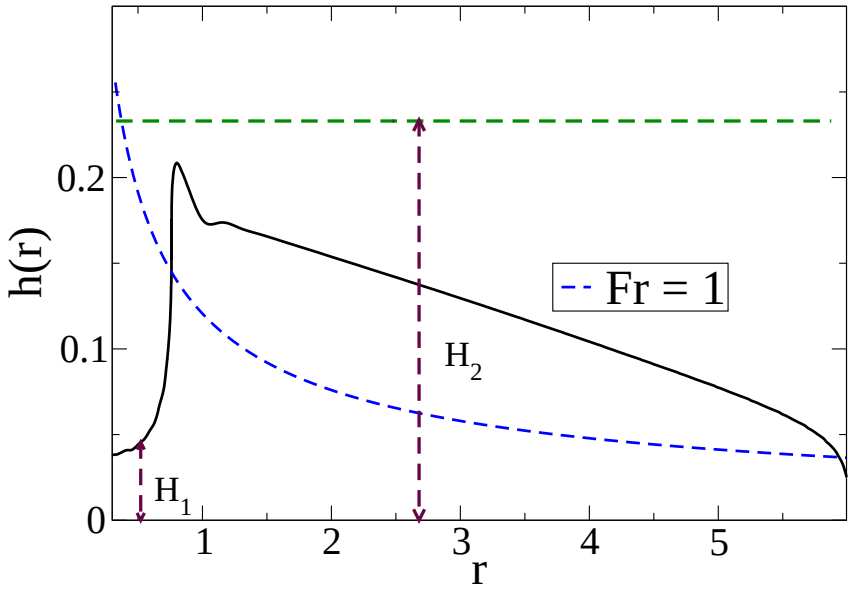

Figure 4.22: Comparison of predictions of equation 4.2 with Navier-Stokes simulations. The simulation parameters are Domain A, $Re_n = 100, Bo = \infty, Fr_n = 7.58, r_n/H = 0.0625, D/r_n = 48$. The choice of H_1 is somewhat arbitrary and made by visual inspection. The Froude numbers Fr_1 at the height indicated as H_1 is 4.1. Note the H_2 is overpredicted by the relation 4.2. One should compare this to planar geometry in figure 4.23 where comparatively much better predictions for H_2 are obtained by using the same relation.

location r_1, where h_1 is known, to the radius of the jump r_j, to obtain r_j.

$$\begin{aligned} Re(h' + \frac{h}{r}) &= 1.8 \\ \Rightarrow \frac{Q}{2\pi\nu}\left(h' + \frac{h}{r}\right) &= 1.8r \\ \Rightarrow \frac{d}{dr}(rh) &= \frac{3.6\pi\nu}{Q}r^2 \\ \Rightarrow r_j h_j - r_1 h_1 &= \frac{1.2\pi\nu}{Q}(r_j^3 - r_1^3) \end{aligned} \tag{4.7}$$

(4.8)

where h_j and h_1 are the film thicknesses at r_j and r_i respectively. Imposing the constraint that $Fr_j = 1$, we further obtain $h_j = Q^{2/3}/\left(16\pi^2 g r_j^2\right)^{1/3}$. Thus equation (4.7) can be used to obtain an algebraic relation for r_j knowing r_1, h_1 and in terms

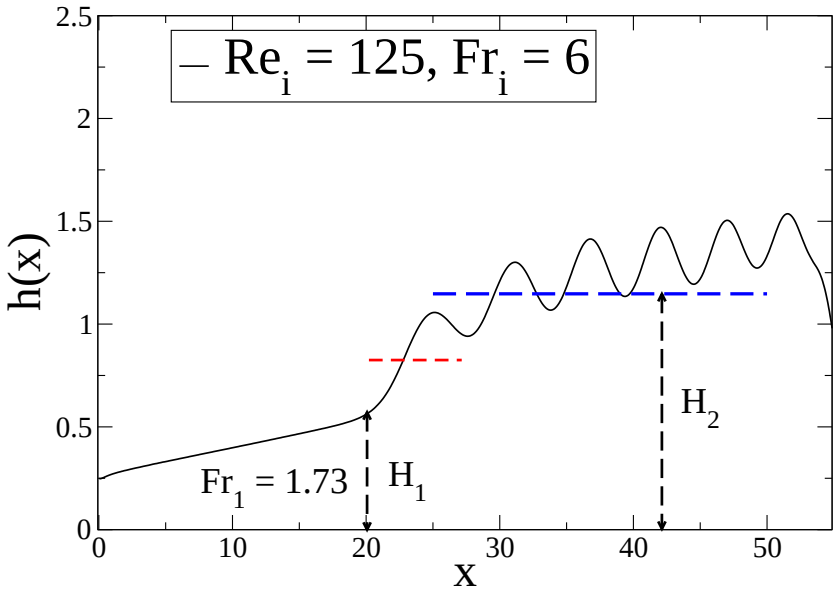

Figure 4.23: Prediction of equation 4.2 for a planar jump. The predictions are H_2 are much better than those for in a circular geometry shown in figure 4.22. The dashed red line is the location where the local Froude is unity.

of Q, ν and g, which is

$$\left(\frac{Q^2}{16\pi^2 g}\right)^{1/3} r_j^{1/3} - \frac{1.2\pi\nu}{Q} r_j^3 + \frac{1.2\pi\nu}{Q} r_1^2 - r_1 h_1 = 0 \tag{4.9}$$

In a circular geometry, the variable r is not a quantity that may be translated at will like the x in a planar geometry, and so we need a reference radius. It is convenient to choose this as the radius r_m where the height h_m is at a minimum. If this point is at a high Froude number, then we have from the similarity solution

$$\frac{h_m}{r_m} = 1.8Re \tag{4.10}$$

Choosing $r_1 = r_m, h_1 = h_m$, writing $\tilde{r_j} \equiv r_j/r_m$ and dropping the tilde for convenience, we may re-write equation (4.9) in non-dimensional form as

$$4^{-1/3} F r_m^{2/3} r_j^{1/3} - \frac{1}{3}\left(r_j^3 - 1\right) = 1 \tag{4.11}$$

where $Re_m \equiv Q/(2\pi r_m \nu)$ and $Fr_m^2 \equiv Q^2/(4\pi^2 g h_m^3 r_m^2)$. Notice that due to choosing of r_m as our origin, the Reynolds number has been scaled out of equation (4.11). In figure 4.24, we plot the radius calculated from equation (4.11). It is seen that equation (4.11) gives a good estimate of the jump radius. Also note that equation this is an algebraic equation and its general solution will not give a power-law scaling relation for r_j. This is in contrast to the frequent power-law assumptions that are made in literature about the scaling relation for the radius of the jump. We discuss this more in Chapter 5. The counterpart of equation 4.9 for planar flows can also be easily obtained using the high Froude number limit of equation 3.6 in Chapter 2. This is $h'Re = 1.8$ and thus obtains integrating from x_1 to x_j, and using the $Fr = 1$ criterion which gives $h_j = (Q^2/g)^{1/3}$

$$\frac{x_j}{h_1} = \frac{Re}{1.8}\left[Fr_1^{2/3} - 1\right] + 1 \tag{4.12}$$

where $Re \equiv Q/\nu$. In figure 4.25 we provide comparisons between the solution of the BLSWE and a Navier-Stokes simulation. It is seen from the figure that upstream of the jump, the P solution agrees very well with the simulations. Downstream, we see that the comparison with the N solution estimates the slopes well but overpredicts the height. The radius of the jump is also somewhat overpredicted by the P solution.

4.4.3 Effect of downstream boundary conditions

As remarked earlier, the downstream boundary conditions are crucial in these simulations. It has been reported in experiments by Rao [1994] for example that the radius of the jump is sensitive to the radius of the plate, as well as conditions at the edge (e.g. whether the edges are sharp or rounded). It is very difficult to mathematically formulate the pressure boundary condition for a rounded edge compared to a sharp edge and hence validation of this was not possible. However, we find computationally that the radius of the jump can be made fairly insensitive to the location of downstream boundary, provided one chooses a boundary which is much larger than the jump radius. In figure 4.26, we show this insensitivity to the location of the downstream boundary. All the three simulations have the same exit boundary condition and it is only the place where this boundary condition

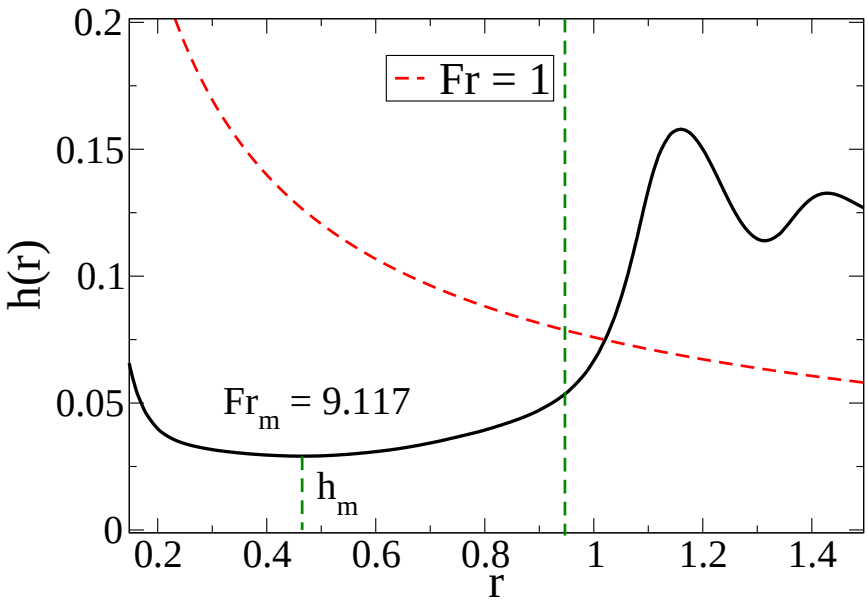

Figure 4.24: The simulation parameters are Domain A, $Re_n = 225, Bo = \infty, Fr_n = 7.58, r_n/H = 0.0625, D/r_n = 48$. The initial conditions chosen are $r_m = 0.465, h_m = 0.029$. The dashed line in green indicates the calculated radius from equation (4.11) and the dashed line in red indicates the curve of $Fr = 1$. The radius where the red curve intersects the height profile is the $Fr = 1$ location.

is applied which is varied between the three simulations. Figure 4.27 shows that similar to a planar geometry, moving the end of the domain downstream moves the jump location upstream although the extent of change is much less than in a planar geometry.

4.5 Undular jumps - Radial KdV like equation

In Chapter 3, we had used the process of vertical averaging to derive an ordinary differential equation which contained the KdV equation as a subset. Here we repeat the exercise for a radial geometry, but only for the inviscid equations. We have the

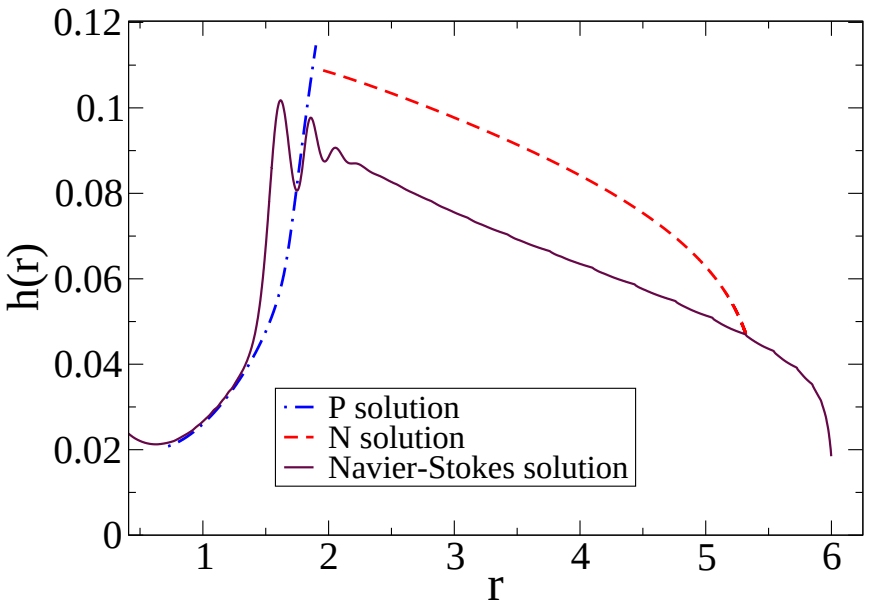

Figure 4.25: A comparison of the P and N solutions of the BLSWE with Navier-Stokes simulation. The simulation parameters are Domain A, $Re_n = 550, Bo = \infty, Fr_n = 7.58, r_n/H = 0.0625, D/r_n = 48$.

following governing equations

$$(ru)_r + (rw)_z = 0, \tag{4.13}$$

$$Q = 2\pi r \int_0^{h(r)} u dz, \tag{4.14}$$

$$uu_r + wu_z = \frac{-1}{\rho} p_r + \nu \left[u_{rr} + \frac{1}{r} u_r + u_{zz} - \frac{u}{r^2} \right], \tag{4.15}$$

$$uw_r + ww_z = \frac{-1}{\rho} p_z + \nu \left[v_{rr} + \frac{1}{r} v_r + v_{zz} \right], \tag{4.16}$$

with the boundary conditions

$$\begin{aligned} p|_{z=h(r)} &= 0, \\ u_z|_{z=h(r)} &= 0, \\ u|_{z=0} = w|_{z=0} &= 0. \end{aligned} \tag{4.17}$$

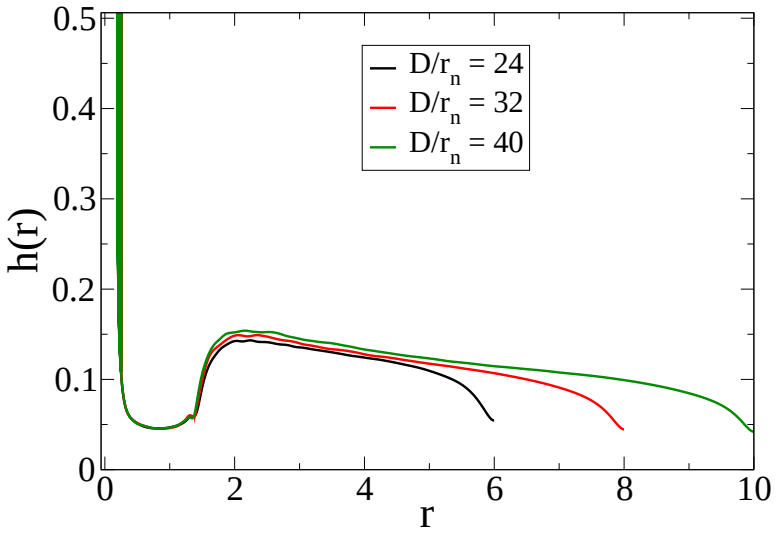

Figure 4.26: Effect of domain size on the radius and structure of the jump. All three simulation have the parameters - Domain A, $Re_n = 225, Fr_n = 2.68, r_n/H = 0.125, Bo = 4.3509$. Note that the upstream height profile and the radius of the jump is practically unaffected by the location of the downstream boundary. However, the height profile downstream of the jump is affected although far less than in the planar case. For improved readability, the figure does not show the entire length of the jet used in the simulation.

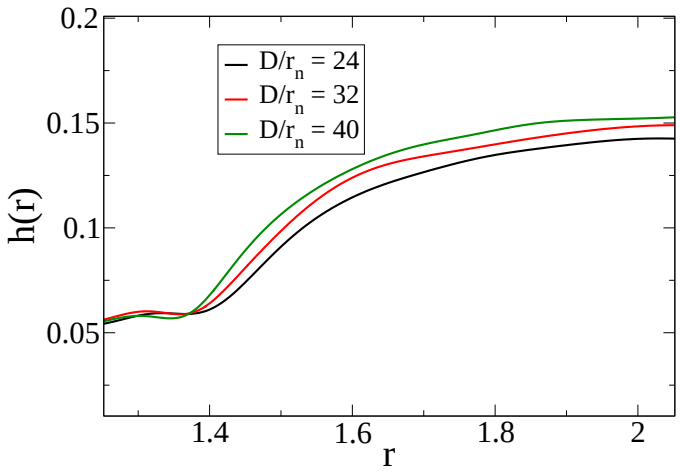

Figure 4.27: The near-jump region of figure 4.26. Note that the jump moves slightly upstream as the domain length is increased qualitatively similar to what was observed for planar jumps, albeit to a much smaller extent.

As we had done in Chapter 3, we also assume here

$$\psi = \frac{Q}{2\pi} f\left[\frac{z}{h(r)}\right] = \frac{Q}{2\pi} f\left[\eta\right], \tag{4.18}$$

which thus gives

$$\begin{aligned} u &= \frac{Qf'}{2\pi rh}, \\ w &= \frac{Q\eta f'h'}{2\pi rh}, \\ uw_r + ww_z &= \frac{-Q^2\eta f'^2}{4\pi^2 r^3 h^3}, \end{aligned} \tag{4.19}$$

where $f' \equiv df/d\eta$. Integrating the vertical momentum equation from z to $h(r)$, and using the simplified boundary-conditions we obtain

$$\begin{aligned} \frac{p}{\rho} &= gh - gz + \int_z^{h(r)} \left[uw_r + ww_z\right] dz, \\ \Rightarrow \frac{p}{\rho} &= gh - gz - \frac{Q^2}{4\pi^2 r^3 h^2}\left(rh'^2 + hh' - rhh''\right)\left(\int_\eta^1 \eta f'^2 d\eta\right), \end{aligned} \tag{4.20}$$

Similar to Chapter 3, we differentiate this expression and integrate it from 0 to h and use the identity 3.21 in Chapter 3, to obtain

$$\frac{h'}{Fr^2} - C_1\left[\frac{h}{r} + h'\right] + C_2\left(h'^3 + 2\frac{hh'^2}{r} - 2hh'h'' + \frac{3h^2h'}{r^2} - \frac{3h^2h''}{r} + h^2h'''\right) = 0, \tag{4.21}$$

where $Fr^2 \equiv Q^2/4\pi^2 r^2 g h^3, C_1 \equiv \int_0^1 f'^2 d\eta$ and $C_2 \equiv \int_0^1 \eta^2 f'^2 d\eta$. We term equation 4.21 as the radial KdV or the r-KdV equation. Shown in figure 4.28 is a sample result of the r-KdV equation, compared to the result of the KdV for the same initial conditions. A slight reduction in the amplitude of the oscillations is noticed. More significant however is the reduction in wave-length that is evident downstream. Viscous effects would be much larger at lower wavelengths, and we would expect a viscous quenching of the oscillations downstream. Thus the undular region behind a planar jump may be expected to be longer than in a circular jump, which is indeed evident on comparing figures 4.29(a) and 4.29(b).

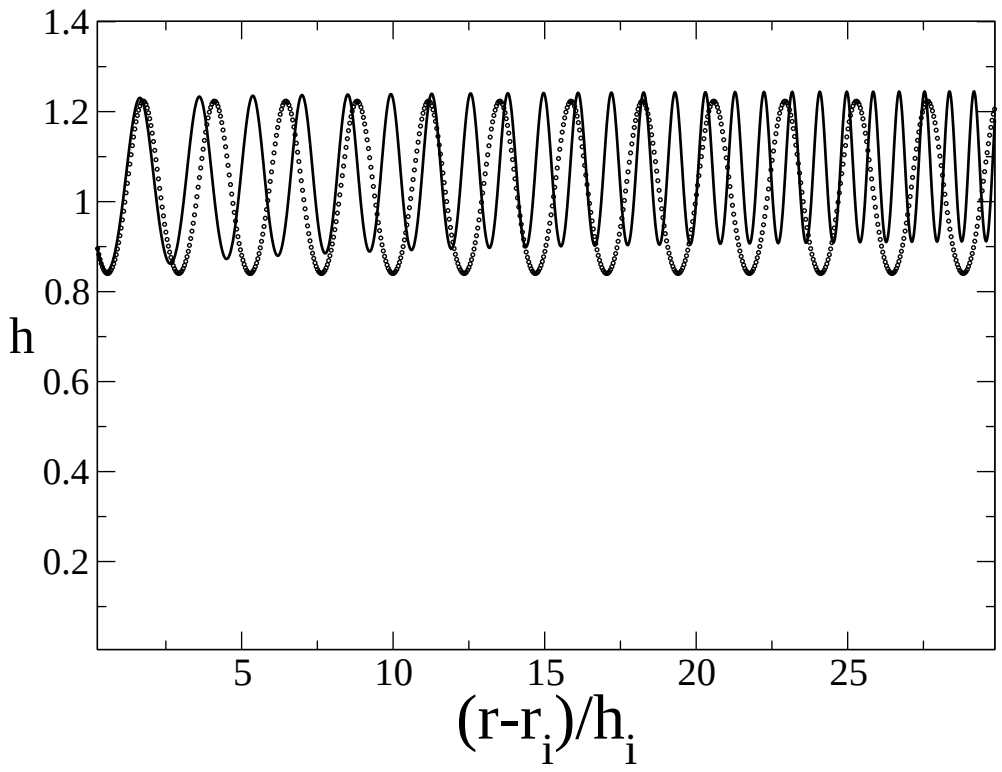

Figure 4.28: Sample solution of the r-KdV equation (solid line) compared to the periodic solution of the KdV (symbols) for the same initial conditions.

4.6 Some other qualitative studies

4.6.1 Initial-value problem of circular jump formation

In this section we show an interesting process through which a Type-0 jump is eventually formed. We study the transients of jump formation and find a rich variety of states during the transients. Shown in figures 4.30(a), 4.30(b), 4.31(a) and 4.32 is the time evolution of formation of a Type-0 jump. The instantaneous streamline patterns reveal that the jump undergoes different kinds of transitions before reaching a steady-state. The repeated appearance and disappearance of the wall-eddy is particularly interesting and the physics of these transients are not clear at the moment. The non-dimensional time-step T^* is defined as $tU_{av}/(H+D)$, where t is the dimensional time. Note that $(H + D)/U$ is the time-scale on which a fluid particle introduced at the nozzle inlet reaches the domain outlet.

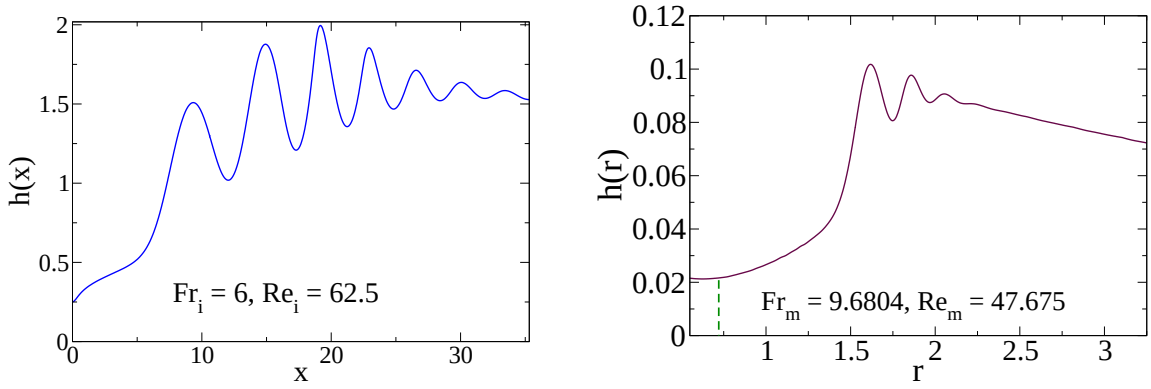

(a) (b)

Figure 4.29: (a) Downstream undulations in a planar jump. The simulations parameters are $Re = 62.5, Fr_i = 6, L^* = 220$. (b) Downstream undulations of a circular jump. The local Reynolds and Froude numbers are calculated at the minimum radius r_m. In the circular case, the undulations rapidly decay downstream, compared to the planar case. The simulation parameters are $Re_n = 550, Bo = \infty, Fr_n = 7.58, r_n/H = 0.0625, D/r_n = 48$.

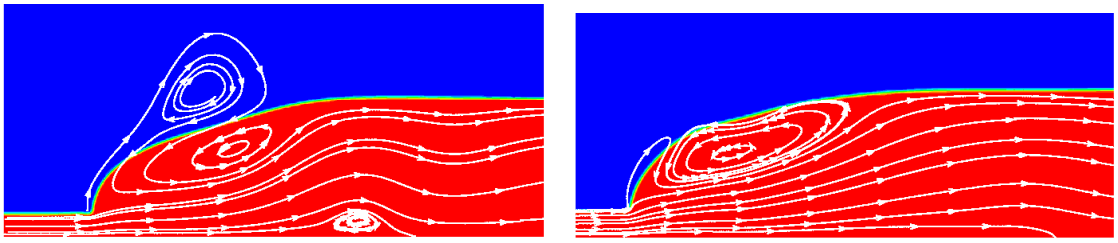

(a) (b)

Figure 4.30: (a) Instantaneous streamlines during the formation of a circular hydraulic jump. The parameters are - Domain A simulation, $Re_n = 225, Fr_n = 2.68, Bo = 4.35$ and $D/r_n = 24$ and $r_n/H = 0.125$. Note that since this is in the transient stage, the interface is still changing shape and hence streamlines need not be tangential to the interface. The fluid in blue is the ambient fluid and eddies are created in this too. This picture is is at $T^* = 7/8$ and looks like a typical Type-II jump. (b) At $T^* = 1.25$. Note that the wall-eddy has vanished and now this is a jump without separation. These kinds of jumps have been observed earlier by Ellegaard *et al.* [1998].

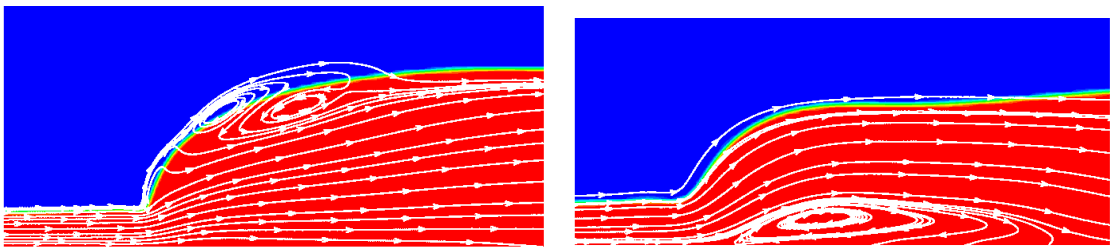

(a) (b)

Figure 4.31: (a) $T^* = 1.875$ - The surface-eddy shortens in radial extent and the jump has also steepened (b) $T^* = 2.5$ - Surface eddy has vanished and now the wall-eddy has re-appeared. At this stage this looks like a simple Type-1 jump.

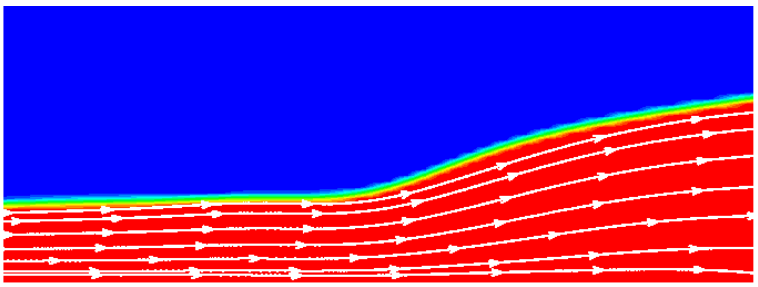

Figure 4.32: Domain A simulation: $T^* = 3.75$ - Final steady state and a Type-0 jump. Note that there is no surface roller and no wall-eddy. Although this simulation has surface-tension, we have seen also earlier in figure 4.10 that jumps without separation can happen without surface-tension.

4.6.2 Inviscid wave-breaking

In figures 4.33(a), 4.33(b) and 4.33(c) we show the effect of viscosity in forming stationary structures. These simulations were done by setting viscosity to zero and making the walls free-slip. A numerical solution to the initial-value problem which otherwise would have produced a stationary jump, now instead led to wave-breaking, beyond which the simulations failed. Although very heuristic, this gives us an idea about the role of viscosity and wall-vorticity in formation of the jump.

4.7 Conclusion

In this Chapter, we have studied the circular hydraulic jump using numerical simulations and we have compared the results with the analytical results obtained. It is shown clearly from simulations that separation is not the cause of jump formation

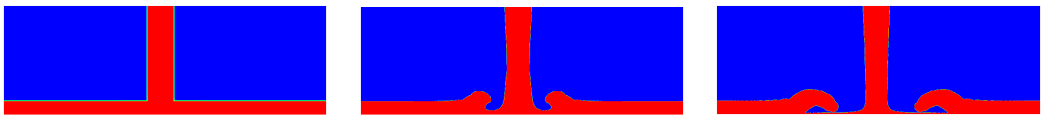

(a) (b) (c)

Figure 4.33: (a) Initial condition and wave breaking at later stages. The progress of time is from left to right. As the simulation progresses, a "blob" of fluid progresses downstream unless the fore part of this fluid parcels, displays something akin to wave-breaking. The same simulation run with viscosity and the no-slip condition led a Type-0 jump without any wave-breaking.

and jumps without separation can indeed occur. It is seen that increasing viscosity and/or gravity pushes the jump upstream and makes it steeper. The effect of change of domain size is found to be very minor. Surface-tension has a strong effect on the shape of the jump but not on its radial location. We have compared our results with those obtained from the BLSWE and found good agreement upstream and downstream of the jump. It is seen that in a circular geometry, Rayleigh's criterion does not work very well unlike in the planar case. The reason for this has been explored and a possible explanation offered. We also study the initial-value problem of jump formation numerically and find that during the transient stage, the streamline pattern goes through a complex series of steps. The undulations behind the jump are modelled using a radial KdV equation and this shows a decay in wavelength downstream. Finally, the effect of viscosity in inhibiting wave-breaking is pointed out.

CHAPTER 5

EFFECT OF MOMENTUM FLUX ON THE CHJ

Acknowledgements:
The work reported in this chapter was carried out in collaboration with Dr. Vishwanath K. P. and Prof. K. R. Sreenivas, Engg. Mech. Unit, JNCASR.

5.1 Scaling laws for the radius of the CHJ

There have been numerous attempts in the literature to obtain a scaling relationship for the radial location of the circular hydraulic jump. Many of these attempts were based on simplified models with adhoc assumptions. In table 5.1 we reproduce the different scaling relations for the circular hydraulic jump that have been proposed. We have omitted the radius predictions of Watson [1964] and Bush & Aristoff [2003] from this table, because these are not scaling laws. Among the scaling relationships in 5.1, the most reliable and accepted is that of Bohr *et al.* [1993]. The radius of the jump is predicted to scale as $Q^{5/8}\nu^{-3/8}g^{-1/8}$ where the mass flow rate is Q, ν is the the kinematic viscosity and g is the acceleration due to gravity. This work builds upon the analysis of Tani [1949] and the approach of Rayleigh [1914]. Equation (2.23) is used for this analysis and reproduced below for convenience.

$$\frac{dh}{dr} = \frac{(5\pi\nu/Q)\, r^2 - h}{r - (10\pi^2 g/3Q^2)\, r^3 h^3} \tag{5.1}$$

A rough outline of the method for obtaining the scaling relationship is given in figure 5.1. For any initial h and r, we obtain a solution of equation (5.1) which spirals into the critical point (defined as the point where dh/dr is of the form $0/0$) as shown. The solutions at small values of the radius are labelled as inner solutions and the ones at large radius are termed as outer solutions. For each pair, one notices an overlap region. A discontinuity is fitted in this region using the Rayleigh shock criterion [Rayleigh, 1914]. The location of the critical point in equation (5.1) scales as $Q^{5/8}\nu^{-3/8}g^{-1/8}$ [Bohr *et al.*, 1993]. The location of the fitted shock lies very close to the location of the critical point of equation (5.1) thus providing the required scaling relation. Additionally, the scales for the horizontal

Scaling laws for r_j	
Bohr *et al.* [1993]	$Q^{5/8}\nu^{-3/8}g^{-1/8}$
Godwin [1993]	$a^{4/3}V^{1/3}\nu^{-1/3}$
Brechet & Neda [1999]	$Q^{2/3}h^{-1/6}\nu^{-1/3}$
Chang *et al.* [2001]	$r_j' \sim Re^{1/3}\Lambda^{-1/8}$
Hansen *et al.* [1997]; Ray & Bhattacharya [2007]	Exponent of $Q = 0.5$ for large Q
Kate *et al.* [2007*b*]	$\left[\frac{a^2}{2}\frac{sin^3\phi}{(1+cos\phi cos\theta)^2}V\right]^{5/8}\nu^{-3/8}g^{-1/8}$

Table 5.1: Various scaling relationships for the radius r_j of the circular hydraulic jump. Here Q is the volume flow rate, ν is the kinematic viscosity, g is the acceleration due to gravity, a is the nozzle radius, V is the average velocity of the jet at the nozzle outlet, h is the nozzle height, ϕ is the inclination angle for an inclined jet, θ is the azimuthal angle, $Re \equiv Q/(a\nu)$ is the Reynolds number, $\Lambda \equiv (ga^3/\nu^2)Re^{-7/3}$ is referred to as the "modified Froude number" but is more like a Grashof number scaled by $Re^{-7/3}$ and $r_j' \equiv r_j/(aRe^{1/3})$ is the nondimensional radius of the jump, r_j being the corresponding dimensional jump radius.

and vertical coordinates of the critical point have the property that scaling r and h by them, makes equation (5.1) independent of Q, ν and g. This scaling relation $Q^{5/8}\nu^{-3/8}g^{-1/8}$ was also obtained by a scaling and dimensional analysis in Ray & Bhattacharya [2007]. The validity of this scaling relationship has been the subject of many experimental studies see e.g. [Bohr *et al.*, 1993; Hansen *et al.*, 1997; Rao, 1994]. This formula displays agreement with experiments which can vary from moderate to good depending on the range of flow parameters.

An intriguing aspect of the scaling relationship of [Bohr *et al.*, 1993] is the absence of any effect of the nozzle-diameter / nozzle height on the radius of the jump. Experiments conducted by [Hansen *et al.*, 1997] to validate this relationship did find a dependence of the jump radius on the nozzle radius but the dependence was reported to be weak and not investigated further. Effect of nozzle diameter and nozzle impingement height was also studied brielfy in Naraghi *et al.* [1999] although the physical reason for why these parameters should influence the jump radius was not pointed out. In the next section, we make physical arguments and use experimental and numerical evidence to show that these two parameters can significantly affect the jump radius. We relate these two parameters to the momentum-flux of the thin film upstream of the jump and provide a physical reason as to why the momentum-flux can significantly influence the jump radius. A brief study of

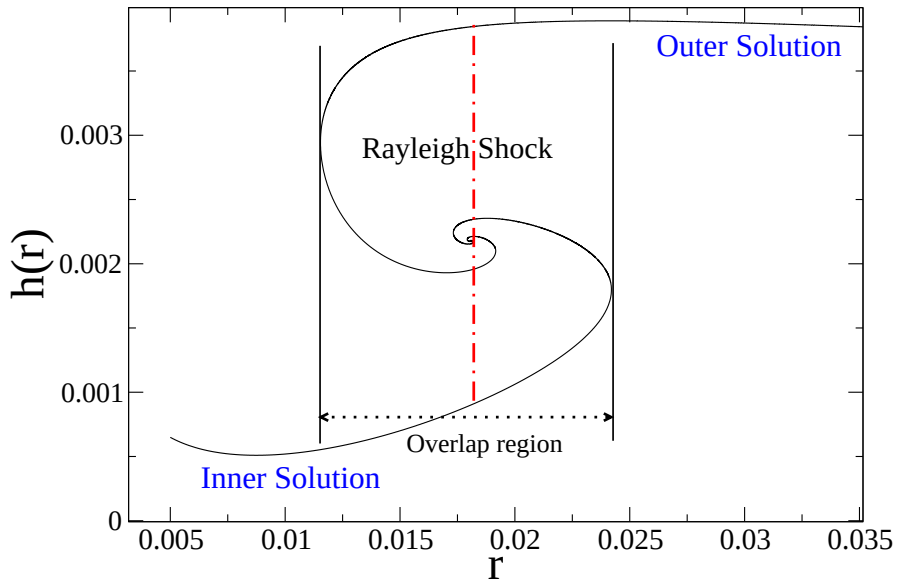

Figure 5.1: Solutions of equation (5.1) for $Q = 33\text{x}10^{-6}\ m^3/s$, $\nu = 14\text{x}10^{-6}\ m^2/s$ and $g = 9.8m/s^2$.

the effect of nozzle diameter and nozzle impingment height was also conducted in Naraghi *et al.* [1999]. These authors reported that increasing the impingement height lead to an increase in the jump radius. A numerical study by Dingwei *et al.* [1998] concluded that increasing impingment height leads to an increase in the radius of the jump while a change of nozzle diameter has no effect.

5.2 Momentum-flux

An intuitive understanding of the effect of momentum-flux can be obtained from figure 5.2. It is a common experience that keeping the volume flow rate constant if we squeeze the tip of a garden-hose, the jet shoots farther. This is due to the fact that squeezing the tip increases the momentum of the fluid. In the context of hydraulic jumps, increasing the nozzle height or decreasing the nozzle diameter has a similar effect: an increase in the momentum-flux of the liquid in the thin film. It is intuitively evident that for a given mass flux, a fluid film with a larger momentum will have a smaller thickness. We have seen computational results earlier that the Froude number (defined as $U_{av}/\sqrt{gh}$) goes through unity at the jump and can

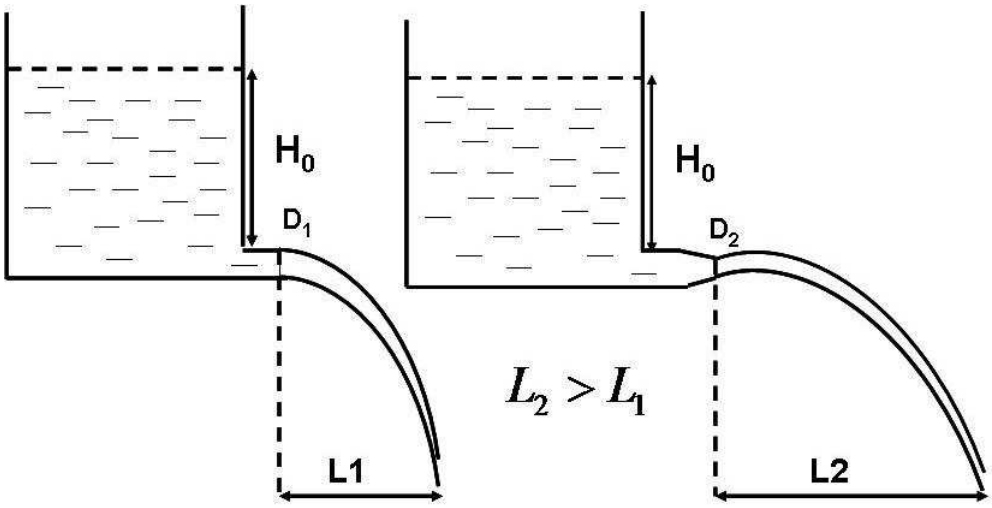

Figure 5.2: Effect of squeezing the tip of a jet. Note that both the tanks have the same head and the same orifice diameter. However, in the tank to the right, the pipe coming out from the orifice has a constriction at the end. Assuming that this constriction does not create a large back-pressure, mass flow rate in both the tanks is the same. However, the jet emanating from the right tank shoots further because of increased momentum-flux due to the constriction.

be used as a reliable measure of the jump location. Morever, the upstream slope is only a function of the Froude number Fr for a given Reynolds Re and for a sufficiently high Froude this slope is practically constant. So a film which has a higher momentum-flux has a higher initial Froude, so it takes much more distance to reach Fr unity compared to a film with a lower momentum-flux. In the case of circular hydraulic jumps, the dependence of the radius on momentum-flux brings in an additional length-scale into the problem.

5.2.1 Dimensional analysis

We begin with a simple dimensional analysis for a circular jet impinging on a horizontal flat plate and spreading radially outwards in an axisymmetric fashion. Neglecting surface tension, there are four quantities which should completely determine the jump radius, viz. the average jet velocity U_i just before impingement, the jet radius r_i just before impingement, the kinematic viscosity ν and the acceleration due to gravity g. We have here made the assumption that the precise shape of the velocity profile within the jet at the point of impingement does not influence the

jump radius. We also assume that the surface at impingement is smooth and the losses at the turning are a function only of the impinging jet parameters and independent of the surface properties. These assumptions may require re-examination. Since all the quantities are in terms of length and time, from the Buckingham-Pi theorem, we arrive at three non-dimensional groups, which are the jump to impingement radius ratio, the impingment Reynolds number and the impingement Froude number, defined respectively as

$$r_j^* = \frac{r_j}{r_i}, \quad Re_i = \frac{U_i r_i}{\nu}, \quad \text{and} \quad Fr_i = \frac{U_i}{(g r_i)^{0.5}}. \tag{5.2}$$

The solution of the Navier-Stokes equation will provide a functional relationship between the three non-dimensional groups. We assume that a power law relationship holds,

$$\frac{r_j}{r_i} = a Re_i^b Fr_i^c \tag{5.3}$$

Note that the continuity equation gives $Q = \pi r_i^2 U_i$ which connects U_i to r_i. It follows from equation (5.3) that the quantity $Q^{b+c}\nu^{-b}g^{-c/2}r_i^{1-b-2.5c}$ has the dimensions of length for any real value of b and c. For $b = 3/8$ and $c = 1/4$, we recover the scaling relation of [Bohr *et al.*, 1993]. It is also clear that if $b + 2.5c = 1$, then the length-scale r_i drops out of the scaling relation and does not influence the jump radius. The values $b = 3/8$ and $c = 1/4$ are one such pair which satisfy this equation. We treat this length-scale r_i as a measure of momentum-flux. For a given mass flow-rate, the influence of both nozzle radius and nozzle height are contained in r_i (also see Naraghi *et al.* [1999]).

If the velocity at the nozzle outlet is U, volume flow rate Q, the velocity at impingment is U_i, nozzle radius is r_n and the nozzle height is H, then we obtain the following from mass conservation and Bernoulli's equations

$$\frac{U^2}{2} + gH = \frac{U_i^2}{2}, \tag{5.4}$$

$$\pi U r_n^2 = \pi U_i r_i^2 = Q, \tag{5.5}$$

$$r_i = \frac{Q^{0.5}}{\pi^{0.5}\left(\frac{Q}{\pi r_n^2} + 2gH\right)^{0.25}}, \tag{5.6}$$

We thus obtain a single length scale r_i which contains the effect of both nozzle impingement height H and nozzle radius r_n, being directly proportional to the former and inversely proportional to the latter. This length scale can be related to the momentum-flux at impingement as $M_i \equiv QU_i = Q^2/\pi r_i^2$, so momentum-flux at impingement M_i is inversely related to the impingement radius r_i. We have argued earlier that keeping everything else fixed, if M_i is increased, it should increase the jump radius. Hence we anticipate that the exponent of this length scale r_i should come out negative in the scaling for the jump radius. In order to demonstrate that the exponent of r_i has a non-zero negative value.one has to take recourse to either experiments or data obtained from simulations. We perform both to obtain these exponents. In the experiments r_i is obtained knowing r_n and H and assuming an inviscid relationship between the two quantities (see equation 5.6). In simulations the radius at impingement is known, as the jet is a part of the simulation.

5.2.2 Experiments

Two sets of experiments are performed - a) radius measurements b) film thickness measurements. In both sets of experiments, the initial momentum flux is varied in two ways viz. by changing the nozzle diameter and by varying the nozzle height.

Description of the setup

A schematic of the experimental set up is shown in figure 5.3. It consists of a reservoir, constant head setup, nozzles of various diameters, circular glass plate, flow meter and an overhead tank. The glass plate of diameter 497 mm and 10 mm thickness is placed on the adjustable stand which enables height adjustment [Vishwanath, 2010]. Horizontal levelling of the glass plate is ensured by adjusting the leveling screws in the stand using a spirit level. A glass plate is placed on a height-adjustable stand. A nozzle is mounted on a specially fabricated stand and oriented vertically. The water from the nozzle impinges on the glass plate, spreads out radially and then falls into a tank. the nozzle is attached to a constant head setup using rubber tubes, a flow control valve, a stop valve and a flow meter. The flow control valve is used to vary the flow rate from the constant head setup. The constant head setup consists of two coaxially placed cylindrical tanks. The diameter and height of the inner tank is 127 mm and 210 mm respectively. The height

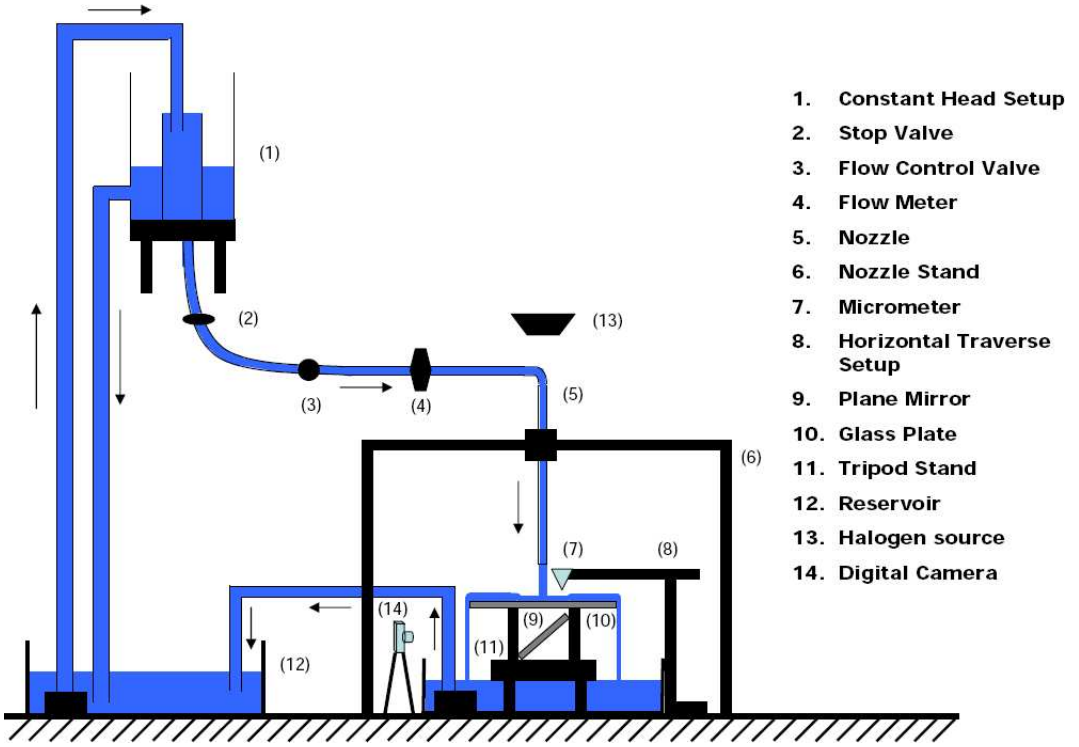

Figure 5.3: Schematic of the experimental setup for radius and film-thickness measurements

of the outer tank is 350 mm with a diameter larger than that of the inner tank. Water is pumped from a reservoir of 100 liters to the constant head setup. The stop valve is opened and the flow control valve is adjusted to a particular position so that the water flows out of the nozzle and impinges on the glass plate forming a circular hydraulic jump. Radius measurements are made using the shadowgraph technique and film-thickness measurements are made using the contact method.

For radius measurements, two length scales with least count one millimeter are attached to the glass plate at right angles to each other. Light from a circular fluorescent source around the nozzle casts a shadow of the jump on the scale. This shadow is deflected by a plane mirror, placed under the glass plate at 45 degrees inclination, onto a camera. The photographs of the shadow of the jump formed on the translucent screen are captured and these raw images are then transformed into binary images using the image processing toolbox in *Matlab*. In some cases the center of the jet might not coincide with the center of the glass plate which in turn

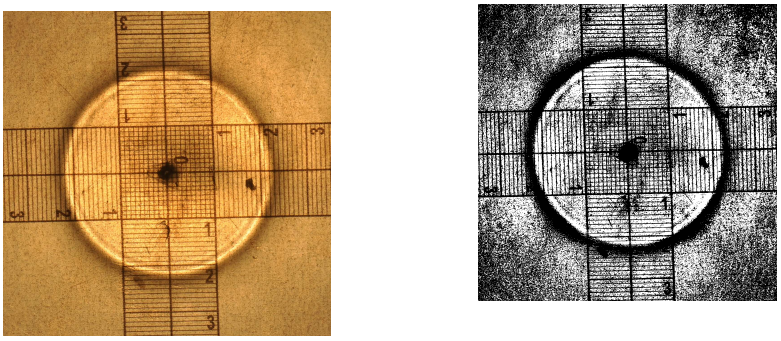

(a) (b)

Figure 5.4: a) Raw image of the jump b) Binary image of the jump

might cause an error in measurement of radius. To minimize this error, four values of the shadow of the jump, $\pi/2$ apart in phase, are obtained. These are used to fit a circle, which depicts the jump, by the method of least squares [Kasa, 1976]. A typical photograph of the shadow of the jump and its corresponding binary image are shown in figure 5.4.

To measure the height of the fluid film a horizontal traverse stand is used. This traverse stand consists of a digital micrometer of measurement range $0-25mm$, and least count 1 *micron* that can be moved horizontally and vertically. A scale on the traverse with a least count of $1mm$ measures the distance covered along the radius. The height measurement is based on the method of contact. An electrical circuit that consists of the micrometer, a special probe in order to maintain the electrical continuity during the rotation of the shaft of the micrometer, and a multimeter is rigged up. The micrometer and the multimeter, whose battery is the power source, are connected in series. The open end of the wire connected to the multimeter is brought in contact with the water close to the edge of the glass plate. Salt is added to the reservoir in order to increase the conductivity of water. The micrometer is lowered at a very slow pace towards the surface of the glass plate. When the probe attached to the micrometer comes in contact with the water, the circuit is closed and a reading on the multimeter is obtained. The height 'h_1' displayed by the micrometer is noted and the micrometer is further moved until the probe touches the surface of the glass plate. The height 'h_2' displayed by the micrometer is again noted. The difference between the two heights "$h_2 - h_1$" gives the thickness of the

fluid film at the particular radius. The above procedure is repeated for various radial locations by using the horizontal traverse. The net height for various values of the radius is tabulated for different flow rates and nozzle diameters.

5.3 Simulations

Axisymmetric Navier-Stokes simulations are also carried out. The simulations are performed using GERRIS (see [Popinet, 2010]) as described in detail for a circular geometry in Chapter 4. For simplicity we have set surface-tension to zero in these simulations. We believe that this does not influence our conclusions as surface-tension has a very small effect on the radial-location of the jump (although it can strongly influence its shape)[Bush & Aristoff, 2003].

5.4 Results and Discussion

In this section, we present results obtained from experiments and numerical simulations. Figure 5.5 shows the radius of the jump for different nozzle impingment heights and while figure 5.6 shows the same for different nozzle diameters. The increase in jump radius with increasing momentum flux at the point of impingement is evident from figures 5.5 and 5.6. For a constant volume flow-rate, the radius of the jump can be increased by almost a factor of 2 by varying the momentum-flux, provided one chooses the flow regime carefully.

The effect of momentum flux can also be observed on the radial film thickness as shown in figures 5.7, 5.8 and 5.9. It is seen that increasing the momentum-flux decreases the local film thickness at a particular radial location causing the local Froude number at that location to increase. Thus for a film with a higher momentum-flux, it takes more radial distance to reach $Fr = 1$ and consequently increasing momentum-flux causes the jump to move downstream.

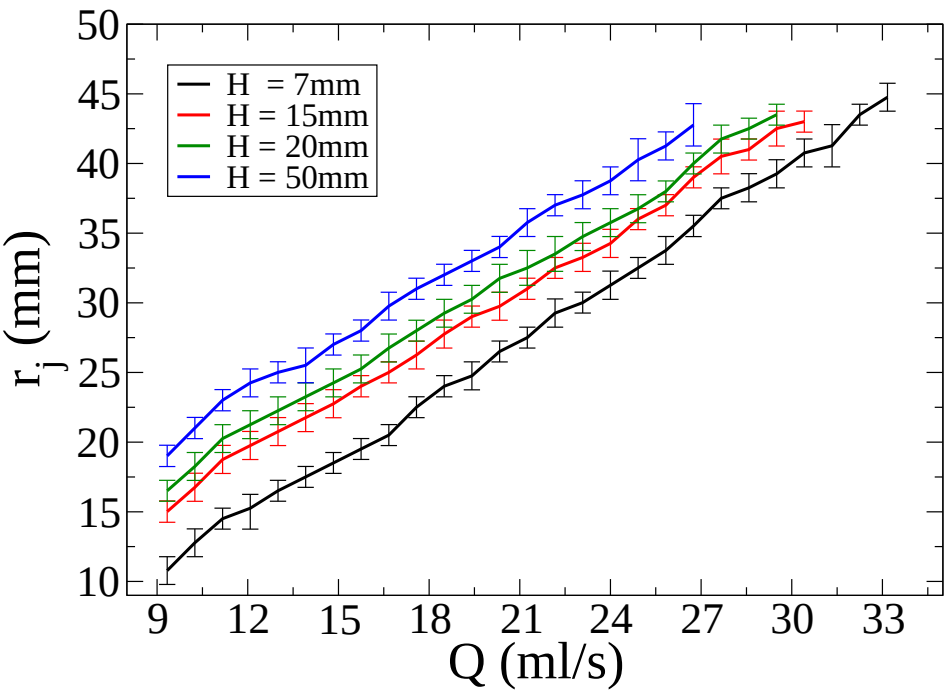

Figure 5.5: Jump radius r_j versus volume flow rate Q for different nozzle heights H and a nozzle radius $r_n = 4.6\ mm$. For a given value of Q, the jump radius increases with increasing nozzle height displaying the effect of momentum-flux.

5.4.1 Determining the exponents

We use data obtained from numerical simulations and experiments to obtain the exponents a, b and c in equation (5.3). Shown in figures 5.10 and 5.11 are the height-profiles obtained from numerical simulations and the symbols indicate the location where Fr is unity. Data obtained from these simulations and experiments are used to obtain exponents of the power law 5.3, using $Mathematica's$ in-built function named $FindFit$. This function uses the least-squares criterion to generate the best fit. In the space of r_j/r_i, Re_i and Fr_i, equation (5.3) represents a surface, and the exponents generated by $Mathematica$ give the best power-law fit to it. As seen in figure 5.12(b) and 5.12(a), the data shows little scatter and hence the exponents may be considered reasonably good fits. The values of a,b and c are shown in Table 5.2. As we had predicted from physical arguments, the exponent of r_i viz. $1-b-2.5c$, indeed comes out to be a non-zero quantity. It is also satisfying to note that both experiments and simulations predict the same sign (negative) for

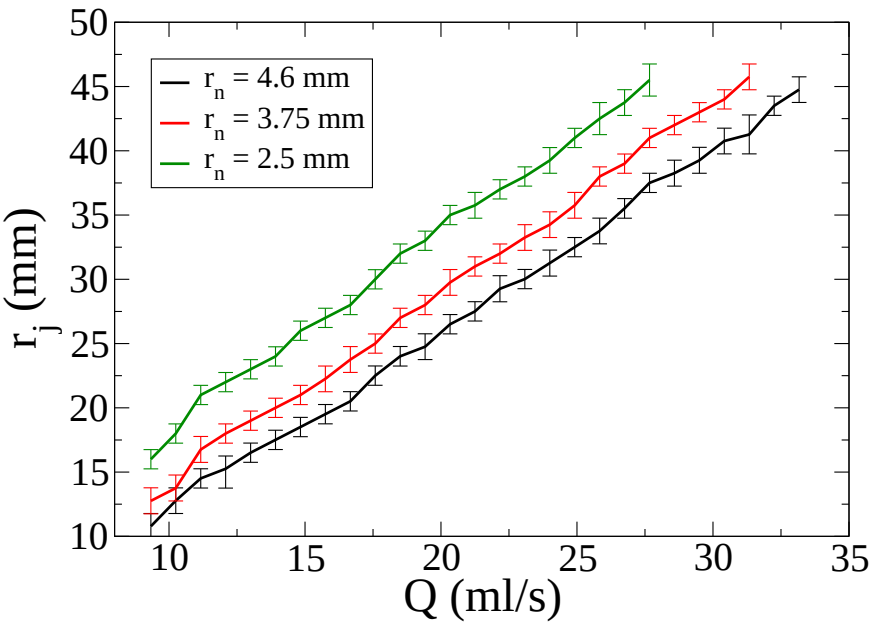

Figure 5.6: Jump radius r_j versus volume flow rate Q for different nozzle radii r_n and a nozzle height $H = 7\ mm$. For a given value of Q, the jump radius increases with decreasing nozzle diameter thus showing the effect of momentum-flux.

this quantity as is physically expected. However, there is considerable difference in the values of these quantities obtained from experiments and those obtained from simulations. In figure 5.13(a) and 5.13(b), we plot the simulation data using the exponent obtained from experiments and vice-versa respectively. The slopes do not seem to be very different but the intercepts are. Although we have tried to analyse the reasons for these differences (like analysing the effects of surface-tension present in experiment but absent in simulations, the downstream boundary condition at the edge of the plate whose precise form is difficult to impose numerically), we have not been able to find a specific reason for this. There are of course many differences between the experiment and the simulations e.g. The velocity profile at the nozzle outlet would be a full-developed profile whereas we use an uniform profile. The losses at the impingement region could be very different between the experiments and the simulations because whereas the later is axisymmetric the former will surely have azimuthal effects in the impingement region. It should also be remembered that we have very few data points from numerical simulations due to computational limitations and hence this could be an important source of error

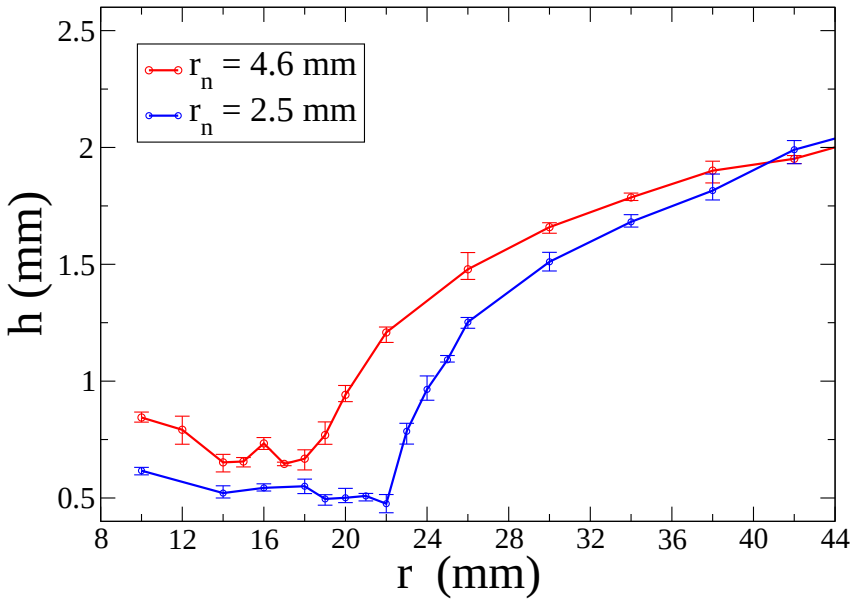

Figure 5.7: Effect of variation of nozzle radii on film thickness with $Q = 13$ ml/s. The nozzle height $H = 7mm$ is held constant for both the profiles. Note the decrease in film thickness with increased momentum-flux. For a given mass-flow rate, the film-thickness can be thought of as being determined by a competition between convective effects, an increase of which makes the film thinner, and viscous dissipation, an increase of which makes the film thicker, so that global mass Q is preserved. Momentum-flux is one of the quantities which can influence the convective effects, there being other parameters like gravity which too can do this. This is analogous to the boundary-layer thickness over a zero-pressure gradient flat plate where too the boundary layer thickness is estimated by equating the convective time-scale to the diffusive time-scale.

in determining the exponent of the power law in equation (5.3).

5.5 Comparisons with previous experiments

In this section we try to compare our results with those obtained by earlier workers (Bohr *et al.* [1993]; Hansen *et al.* [1997]; Tani [1949]). The exponent of Q is a quantity for which data is most easily available and we show in figure 5.14, the exponents obtained from the experimental data of Bohr *et al.* [1993]. Similar plots

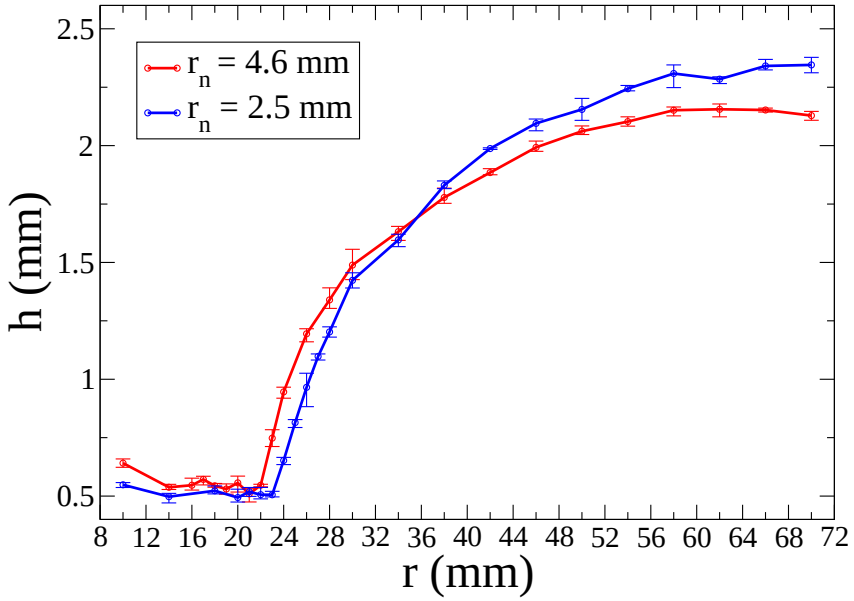

Figure 5.8: Effect of variation of nozzle radius r_n on the shape of the jump with $Q =$.

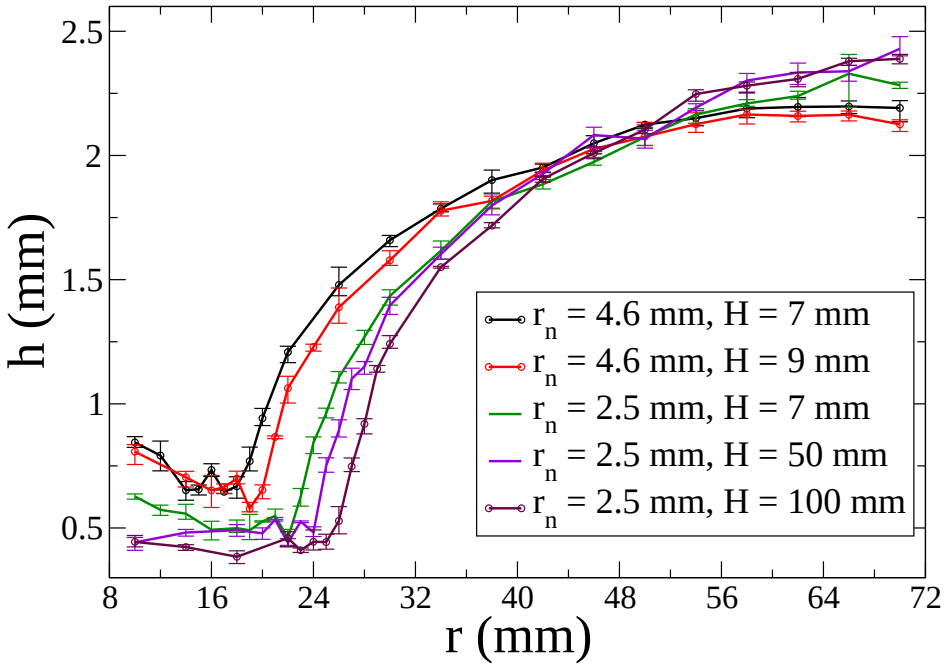

Figure 5.9: Radial film thickness for nozzles of various radii r_n and heights H at $Q = 13$ ml/s

Table 5.2: The constants a, b and c determined from experiments and numerical simulations. Also shown are the exponents of [Bohr *et al.*, 1993]

	Simulations	Experiments	Bohr *et al.* [1993]
Power law fit $aRe_i^b Fr_i^c$	$a = 0.440$	$a = 0.035$	$a = 0.47046$
	$b = 0.414$	$b = 0.682$	$b = 0.375$
	$c = 0.322$	$c = 0.302$	$c = 0.25$
Exponent of r_i $1 - b - 2.5c$	-0.219	-0.437	0

.

are also obtained from the data of Hansen *et al.* [1997] in figures 5.15 and 5.16. For comparison, we also provide plots obtained from our experiments in figure 5.17 and 5.18. It is seen from these figures that the range predicted for the exponent of exponent of Q is 0.429 to around 1.079. Also it is seen that a linear-fit works well in many cases, see e.g. figures 5.15 and 5.16. This implies that a fit almost as good can be obtained by changing the exponent somewhat. This ambiguity is general for any data set where we try to fit a power law with a decade or less of data. Therefore without having access to a wider range of experimental data, it is a difficult task to make this range any narrower. However, the main task that we had set for ourselves in this chapter was not to achieve a more accurate scaling relationship for the jump, but to demonstrate that the exponent of r_i cannot be zero i.e. that momentum-flux is an additional parameter which can strongly influence the jump radius. Figure 5.16 is another independent evidence for the same obtained from the data of Hansen *et al.* [1997]. The power-law relationship depicted in figures, 5.17 and 5.18 also shows a similar momentum-flux dependence. The fact that the exponents show a wide range can also be attributed to the assumption that there exists a power-law relationship of the form in equation 5.3. As we saw earlier in Chapter 4, this may not be true. Irrespective of whether a power-law is a good assumption or not, this analysis is expected to convince the reader of the strong effect that momentum-flux can have on the radius of the jump.

5.6 Conclusion

In this chapter, we have established using experiments, numerical data and dimensional analysis that inlet momentum-flux is a quantity which can have a strong effect on the radius of the circular hydraulic jump . The physical reason for why it

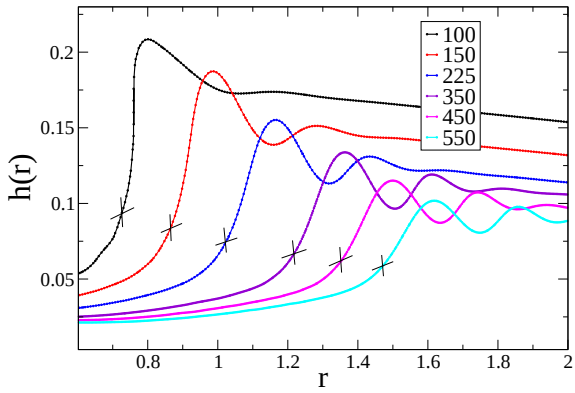

Figure 5.10: The effect of varying nozzle Reynolds number $Re_n \equiv Ur_n/\nu$ on the height profiles obtained from axisymmetric Navier-Stokes simulations for a nozzle Froude number $Fr_n \equiv U/\sqrt{gr_n} = 7.58$. Here U is the uniform velocity-profile at the jet, r_n is the nozzle radius and ν is the kinematic viscosity. These axisymmetric simulations and the accompanying boundary and initial conditions are described in greater detail in Chapter 4 (Domain A simulations). Note that increasing Re_n pushes the jump downstream. The cross symbols indicate the location where the local Froude Fr is unity. Although not shown here, the simulations include the jet and we use the impingement radius r_i from the simulations to define Re_i, Fr_i and to non-dimensionalise the jump radius. The legend indicates the value of Re_n.

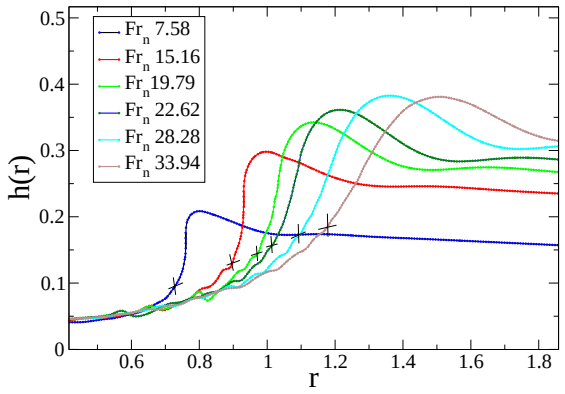

Figure 5.11: The effect of varying nozzle Froude number $Fr_n \equiv U/\sqrt{gr_n}$ on the simulation height profiles for a nozzle Reynolds number $Re_n \equiv Ur_n/\nu = 400$. For meanings of the cross symbols, see figure 5.10. Note that some small wavelength, undulations arise upstream of the jump as the nozzle Froude number is increased. We have taken these simulations for adequate number of time-steps such that a steady state is reached. There is no surface-tension in these simulations.

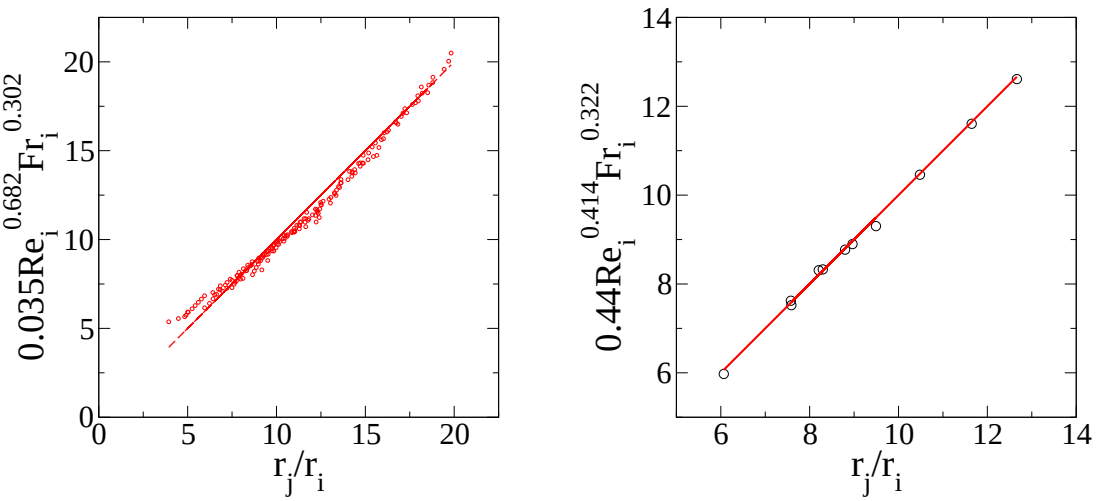

(a) (b)

Figure 5.12: a) Scatter for experimental data. b) Scatter for simulation data. Note that due to computational limitations, we have very few data points available.

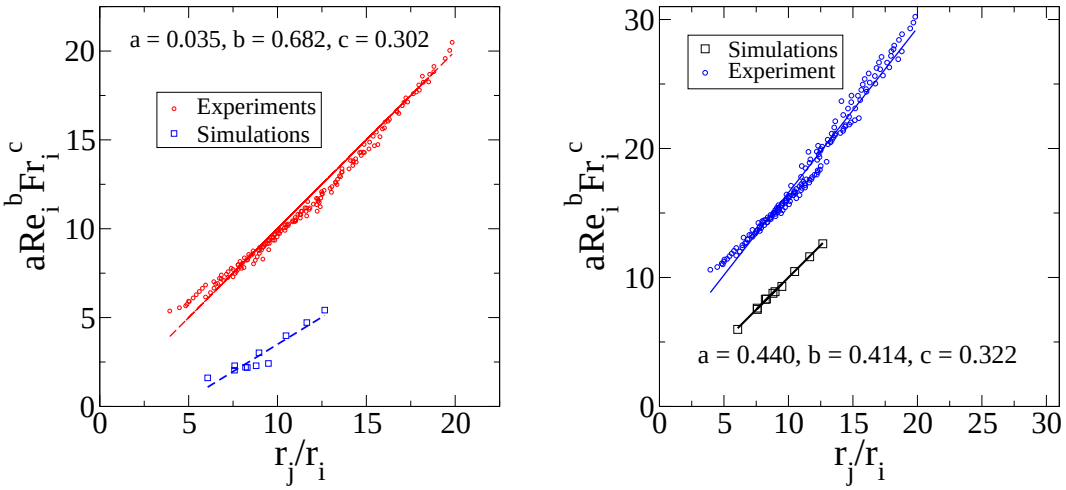

(a) (b)

Figure 5.13: a) The exponents obtained from experiments are used to plot the data obtained from simulations b) Vice-versa.

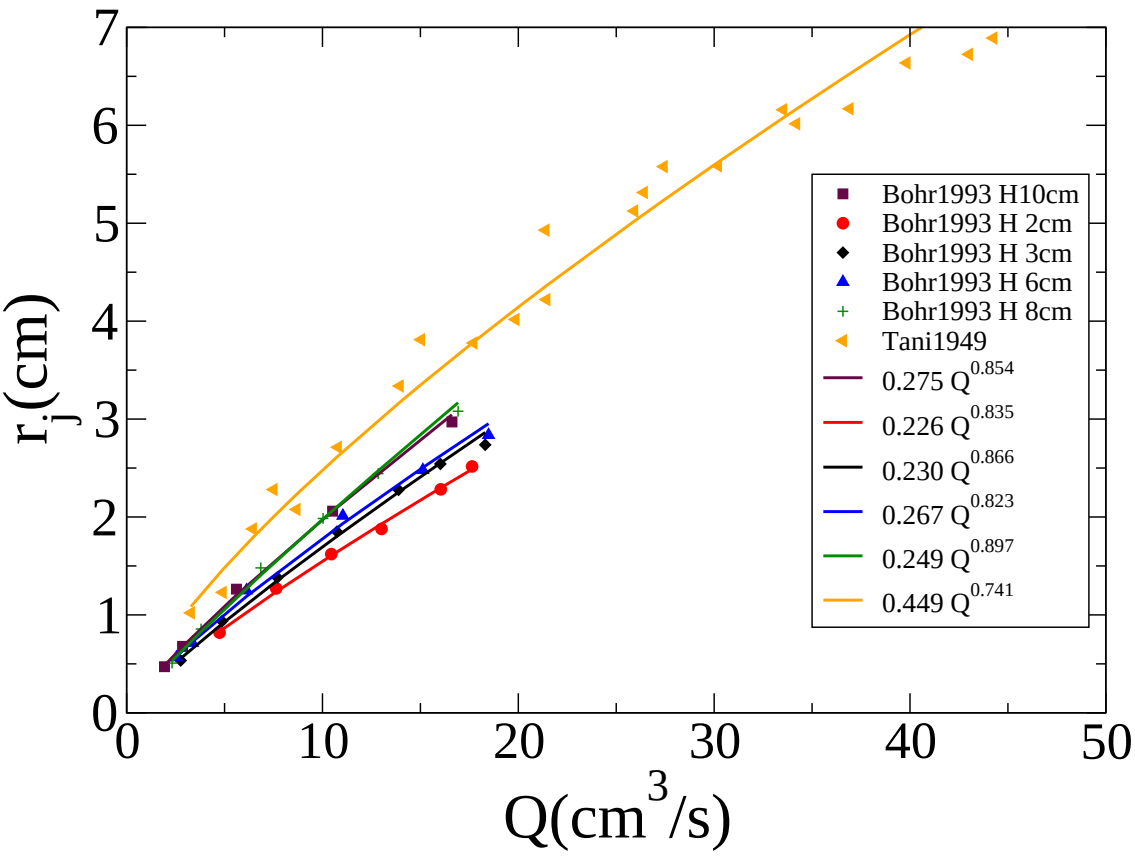

Figure 5.14: Data extracted from experiments reported in [Bohr *et al.*, 1993] and Tani [1949]. The symbols are the experimental data points and the solid lines are power law fits obtained by us.

should be so is also given from a consideration of the effect of momentum-flux on the local film thickness and the corresponding local Froude number. Momentum-flux enters the scaling relation as an additional length-scale whose effect on the jump radius has not been systematically taken into account in earlier works.

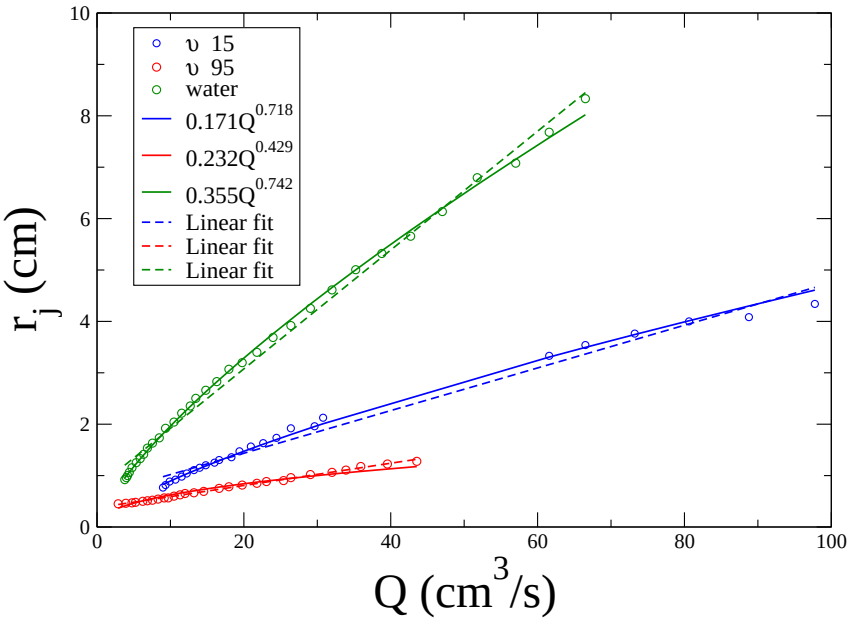

Figure 5.15: Power Law for [Hansen *et al.*, 1997] from their paper. The symbols are the experimental data points and the lines are power law fits obtained by us. The viscosities reported in the legend are normalised by the viscosity of water.

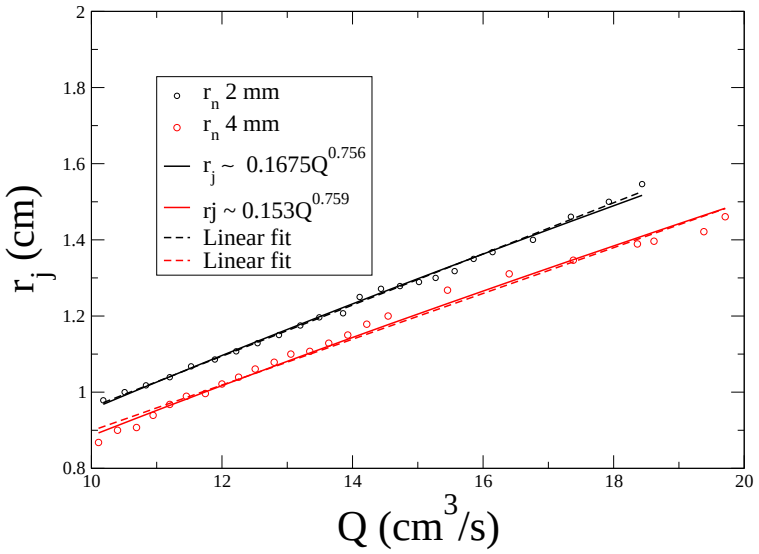

Figure 5.16: Power Law for [Hansen *et al.*, 1997] from their paper. This work observes an effect of momentum-flux but concludes that the effect is weak. The symbols are the experimental data points and the lines are power law fits obtained by us.

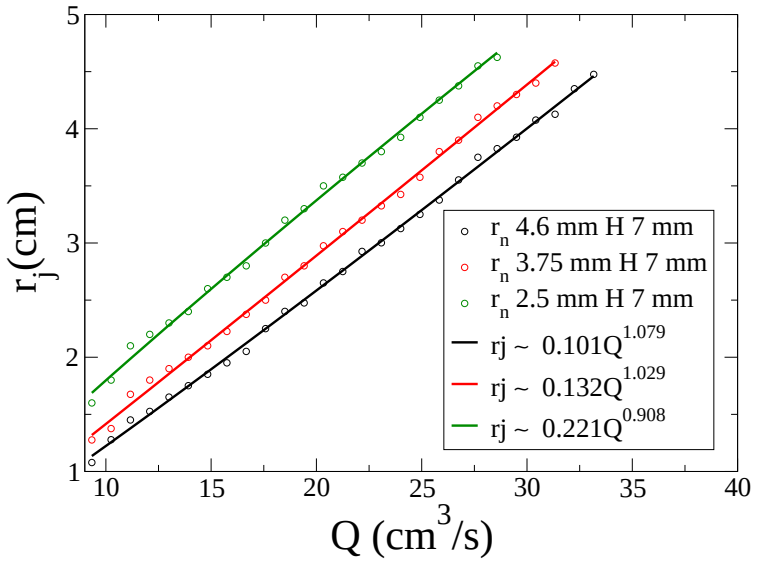

Figure 5.17: Power Law for experimental data - Nozzle Diameter variation. The symbols are the experimental data points whereas the lines represent power law fits.

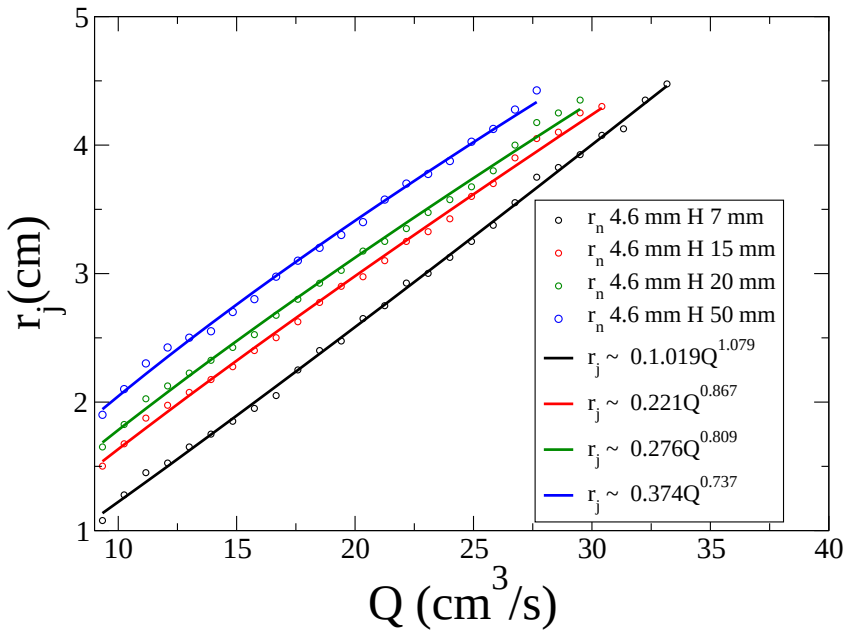

Figure 5.18: Power Law for experimental data - Nozzle impingement height variation. The symbols are the experimental data points whereas the lines represent power law fits.

CHAPTER 6

SURFACE TENSION DRIVEN JUMPS

Remarks:
A condensed version of this chapter has been published in Mathur *et al.* [2007]. The experiments reported here were carried out by N. R. Selvi, Dr. N. S. John in collaboration with Prof. G. U. Kulkarni, CPMU, JNCASR, Bangalore.

6.1 Introduction

Until now we have concerned ourselves with gravity driven jumps at macroscopic length scales. In this chapter we go on to small length scales to study the possibility of surface-tension driven jumps. The driver here is surface tension at the liquid-air (or liquid-vacuum) interface, and jumps may be expected to occur when relevant length scales are submicron for impinging molten metals. This theoretical study was prompted by experiments showing that molten metal droplets impinging on a solid substrate display such a jump, solidifying into cup-shaped containers of femtolitre capacity. The droplets are created by laser-ablation of a solid metal target. Femtocups of different metals on various substrates are formed under optimized conditions of laser energy and substrate temperature. Outside this narrow range of parameters, the droplets solidify to form lumps on the substrate, as one would normally expect. The ability to make, and subsequently leach out, these metallic femtocups at will has potential applications ranging from nanoscale synthetic chemistry to single cell biology. We first discuss what causes a gravity-free hydraulic jump from an impinging sub-micron scale axisymmetric jet. The unsteady case of an impinging droplet (more relevant to the reported experiments) is discussed briefly later.

6.1.1 Analysis for a jet

Consider a steady axisymmetric jet of fluid of radius a impinging on a solid plate placed normal to it. The fluid then spreads radially outwards within a relatively

thin film, the dynamics within which is described by the axisymmetric shallow-water equations including the effect of surface-tension and supplemented by the local and global continuity equation.

$$uu_r + wu_z = \nu u_{zz} - gh' + \frac{\sigma}{\rho}\frac{d}{dr}\left[\frac{\nabla^2 h + h'^3/r}{(1+h'^2)^{3/2}}\right], \tag{6.1}$$

$$u_r + \frac{u}{r} + w_z = 0, \tag{6.2}$$

$$Q = 2\pi r \int_0^{h(r)} u dz \tag{6.3}$$

where $\nabla^2 \equiv d^2/dr^2 + (1/r)d/dr$, r and z are the radial coordinate and the coordinate perpendicular to the solid wall respectively, with origin on the solid surface at the centre of the impinging jet. The respective velocity components are u and w, and $h(r)$ is the height of the film. A prime denotes a total derivative with respect to r, while the subscripts denote partial derivatives. The density of the surrounding medium is neglected. The parameters in the problem are the acceleration due to gravity, g, the surface tension coefficient, σ for the liquid-air or liquid vacuum interface, and the density ρ and the kinematic viscosity ν of the impinging fluid. Note that equation (6.1) assumes pressure to be hydrostatic plus a surface-tension contribution due to the curvature of the interface thus implying $p = p_a + \rho g(h(z) - z) + c$, where p_a is the atmospheric pressure assumed to be constant (zero) at the interface and the term c arises due to the curvature of the interface and surface-tension. In the parameter range of our interest in this chapter, gravity is unimportant as we shall see.

Similar equations were studied earlier in Chapter 2. However the main difference here is the inclusion of surface-tension, which causes the pressure on the fluid side of the interface to be different from that on the gaseous side. This is the last term in equation (6.1). As in chapter 2, we follow the procedure of vertical averaging of equations 6.1, 6.2 and 6.3 to derive an ordinary differential equation for the evolution of film-thickness h. To resove the closure problem, we assume a parabolic radial velocity profile, satisfying the no-slip condition at the wall ($z = 0$) and the zero shear stress condition at the free surface ($z = h$).

$$u(r, z) = \zeta(r)(z^2 - 2h(r)z), \tag{6.4}$$

but any reasonable profile will give qualitatively similar results. Using continuity in its global and local form and the kinematic condition $w = Dh/Dt = uh'$ at $z = h$, equation (6.1) integrated over z from 0 to h becomes

$$b\left[\frac{h}{r} + h'\right] = \frac{2r}{Re} + \frac{r^2h^3h'}{Fr} - \frac{r^2h^3}{We}\frac{d}{dr}\left[\frac{\nabla^2 h + h'^3/r}{(1+h'^2)^{3/2}}\right] \tag{6.5}$$

where all lengths are scaled by the inlet jet radius a, and the $O(1)$ positive constant b is $2/5$ for a parabolic profile. The left-hand side of (6.5) represents inertia, and the terms on the right hand side appear due to viscosity, gravity and surface tension respectively. The relative importance of the inertial term to each of these is quantified respectively by the Reynolds number $Re \equiv u_j a/\nu$, the Froude number $Fr \equiv u_j^2/(ga)$, and the Weber number

$$We \equiv \rho u_j^2 a/\sigma \tag{6.6}$$

u_j is a characteristic inlet jet velocity. In large-scale flows surface tension has been shown [Bush & Aristoff, 2003] only to make a small correction to the jump location, so the last term is unimportant. This is as expected, since Fr in the kitchen sink is of order unity, while $We \sim 10 - 100$. In contrast, consider $u_j \sim 10m/s$ and $a \sim 10^{-7}m$, so $Fr \sim 10^8$ and $We \sim 10^{-2}$. Here surface tension determines whether and where a jump will occur, whereas it is the *gravity* term that may be dropped entirely.

In general in a jump, the pressure gradient becomes increasingly adverse as the flow proceeds downstream, and attains a magnitude large enough to counter the relevant inertial effects. Such an adverse pressure gradient may be created by gravity, or surface tension, or both. With gravity alone, equation (6.5) reduces to

$$h' = (2r/Re - bh/r) \;/\; (b - h^3r^2/Fr). \tag{6.7}$$

Equation (6.7) was analysed ealier in Chapter 2 and it was seen that the denominator goes to zero at some r where the slope of the local film-thickness diverges. In the neighbourhood of this divergence point, shock fitting techniques have been used to obtain a scaling for the jump-radius which is $Q^{5/8}\nu^{-3/8}g^{-1/8}$ (Bohr *et al.* [1993]). A similar qualitative behaviour can also be observed with surface-tension terms alone. A crude prediction of a similar singularity in height can be made by

assuming the height upstream to be slowly varying in r, i.e., $|h'| << 1$, and thus setting $h'' = h''' = 0$. We may then rewrite equation (6.5) as

$$h' \simeq (2r/Re - bh/r) \ / \ (b - h^3/We). \tag{6.8}$$

A divergence of slope in equation (6.8) occurs when the denominator goes through a zero. Also note that the second term in the denominator appears due to *radial* spreading, i.e., surface tension alone cannot give rise to a one-dimensional jump like a tidal bore, under the small slope approximation. It is thus seen that equations (6.7) and (6.8) are qualitatively similar. The inviscid limit of equation (6.8) admits an analytical solution similar to equation (2.6) in Chapter 2. As $Re \to \infty$, equation (6.8) can be integrated as follows

$$\begin{aligned} \frac{dh}{dr} &= \frac{\frac{-bh}{r}}{b - \frac{h^3}{We}} \\ \Rightarrow \frac{dr}{dh} + \frac{r}{h} &= \frac{-rh^2}{bWe} \\ \Rightarrow r &= \frac{K}{h} e^{\frac{h^3}{3bWe}} \end{aligned} \tag{6.9}$$

A solution of equation (6.9) is plotted in figure 6.1. We compare this with the U-shaped curve (studied earlier in Chapter 2) inviscid solution of equation (6.7). It is seen that unlike the inviscid gravity solution, the "upper-arm" in figure 6.1 does not asymptote to a constant value but instead keeps growing monotonically. The inviscid "lower-arm" retains the same qualitative behaviour and goes asymptotically to zero as radius increases. Similar to the gravity solution, there is a minimum radius below which there are no inviscid solutions and this radius can be estimated by setting $dr/dh = 0$, which gives $r_{min} = Ke^{1/3}/(bWe)^{1/3}$. Also note the presence of multiple solutions at a given radius. Numerical solutions to equation (6.7) which are spirals which converge to a critical point in the $h - r$ plane where $dh/dr = 0/0$, have been discussed earlier in Chapter 2. Shown in figure 6.2 is a numerical solution to equation (6.8) for different initial conditions. It is seen that these are also spirals all of which converge onto a single point in the $h - r$ plane where dh/dr is of the form $0/0$. The viscous to inviscid transition is shown in figure 6.3. We can also obtain an analytical solution to equation (6.8) in the neighbourhood of the critical point, similar to what we had done in Chapter 2 for

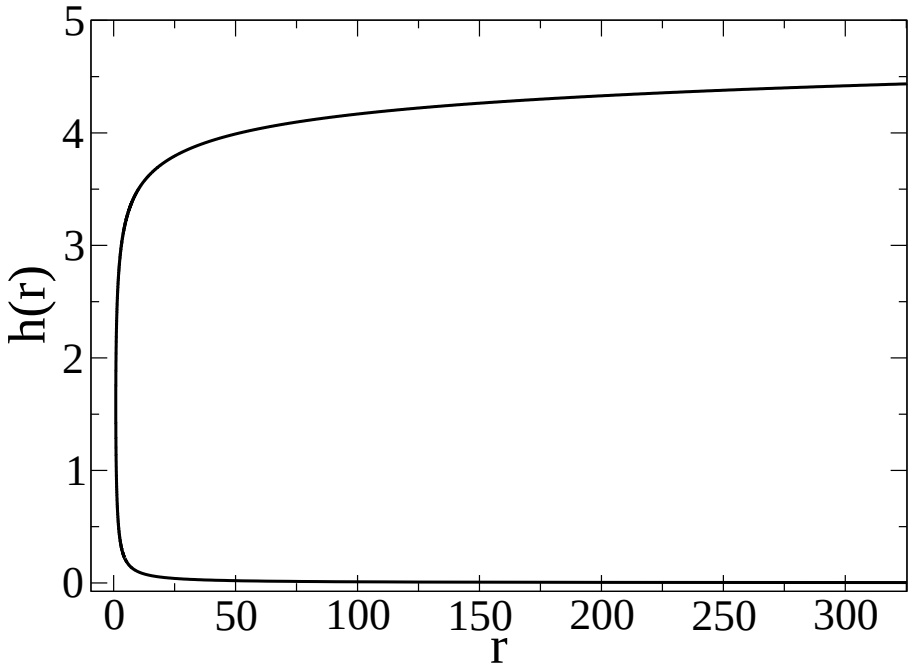

Figure 6.1: The inviscid solution of equation (6.9) - $K = 1, We = 10$. The "upper-arm" increases monotonically without any bound.

equation (6.7). For this it is useful to scale out Re and We from equation (6.8) by using the following re-scalings

$$\begin{aligned} \bar{r} &= \frac{r}{r_0} \\ \bar{h} &= \frac{h}{r_0} \\ h_0 &= We^{1/3} b^{1/3} \qquad (6.10) \\ r_0 &= 0.5^{0.5} b^{2/3} Re^{0.5} We^{1/6} \qquad (6.11) \end{aligned}$$

thus obtaining

$$\frac{d\bar{h}}{d\bar{r}} = \frac{\bar{r} - \frac{\bar{h}}{\bar{r}}}{1 - \bar{h}^3} \qquad (6.12)$$

Note that the scales used in equation (6.10) and 6.11 are the coordinates of the critical point of equation (6.8) and thus in equation (6.12), the critical point has the coordinates $(1, 1)$. Using shock-fitting techniques, Bohr *et al.* [1993] had esti-

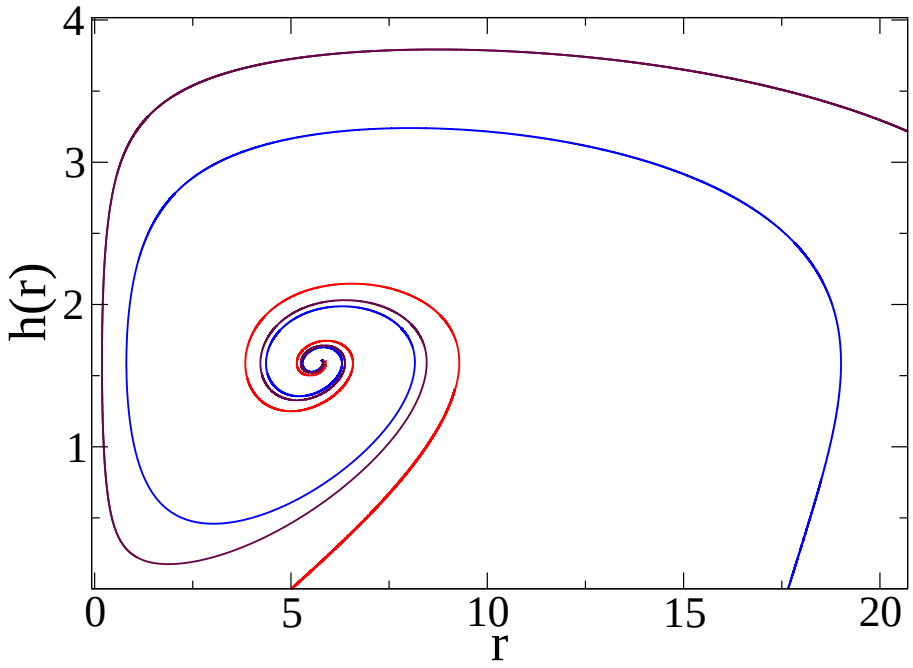

Figure 6.2: A solution of equation (6.8) with $Re = 100$ and $We = 10$ and with different intial conditions. The spiralling around to the critical point is reminiscient of the behaviour of the solution of equation (6.7). The "upper-arms" of the spirals do not continue to ∞ but instead drop down at a finite radius and go into the negative h plane.

mated the radius of the circular jump to be identical to the radial location of the critical point of equation (6.7) leading to a scaling relation which in dimensional terms is $Q^{5/8}\nu^{-3/8}g^{1/8}$ where Q is the volume flow rate and $Q = \pi a^2 u_j$. A similar length-scale is given by equation (6.11) which in dimensional terms gives us $u_j^{5/6}a^{2/3}(\sigma/\rho)^{1/6}\nu^{-1/2}$.

We translate our orgin to the critical point $r' \equiv \bar{r} - 1, h' \equiv \bar{h} - 1$ and linearise about the critical point to obtain

$$\frac{dh'}{dr'} = \frac{h' - 2r'}{3h'(1 + r')} \tag{6.13}$$

which admits an analytical solution. By moving over to polar coordinates $h' = L\sin\theta, r' = L\cos\theta$, we can show that the solution of equation (6.13) is a modified logarithmic spiral (analogous to what we had seen for equation (6.7) in Chapter

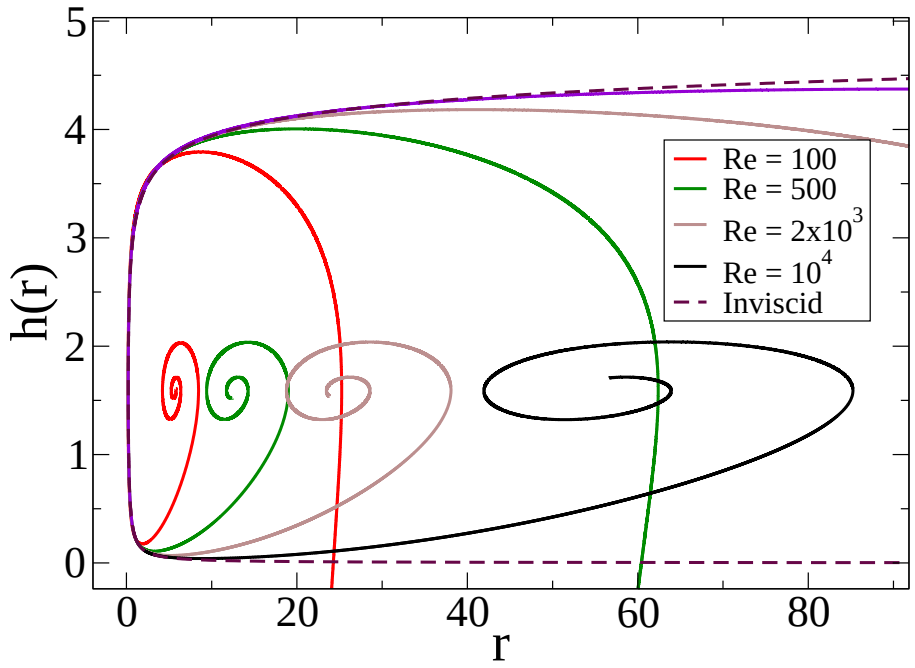

Figure 6.3: The viscous to inviscid transition of the solution of equation (6.8). All solutions have $We = 10$ and intial condition $r = 1.1, h = 0.22$ The dashed line is the corresponding inviscid solution 6.9 where the constant K has been calculated with the same intial-condition. Note that unlike the gravity solution, the y coordinate of the critical point of equation (6.8) is not affected by viscosity. As the Reynolds number is increased, the lower arms of the spirals unrolls and the radial coordinate of the critical point goes to ∞ thus approaching the inviscid solution.

2). This spiral in the neighbourhood of the critical point has the form

$$L = L_0 \sqrt{\frac{1+\tan^2\theta}{3\tan^2\theta - \tan\theta + 2}} e^{\frac{-3\tan^{-1}\left[\frac{6\tan\theta - 1}{\sqrt{23}}\right]}{\sqrt{23}}} \tag{6.14}$$

where L_0 is the constant of integration.

We now return to equation (6.5) and solve it as an initial value problem beginning at some location r_i and marching downstream. A fourth-order Runge-Kutta algorithm is used. An initial radius r_i somewhat larger than a is chosen, where it is assumed that a parabolic profile has been attained. The initial conditions in h and its derivatives are not known exactly for this complicated problem, and numerical studies are being done to understand the flow in this vicinity. We have repeated

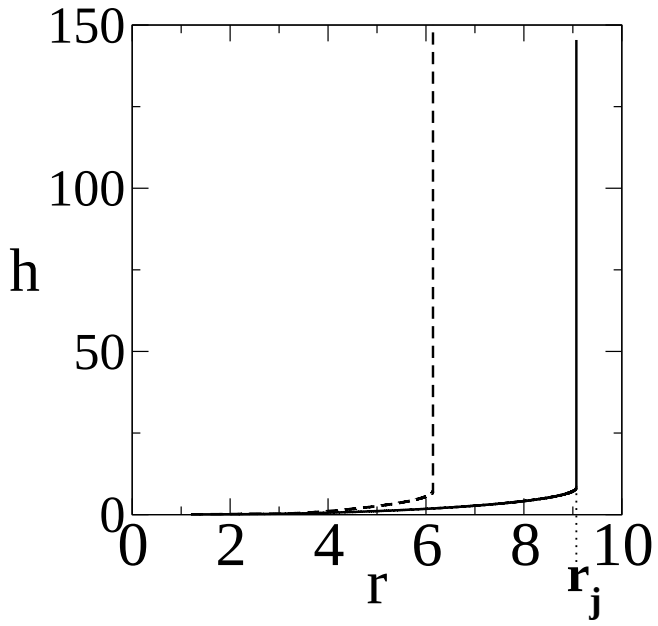

Figure 6.4: Typical solutions of equation (6.5), with $Fr = \infty$, containing a singularity at $r = r_j$. For demonstration, properties of molten silver ($\rho = 5000$ kg m^{-3}, viscosity $\mu = 0.005$ Nsm^{-2} and $\sigma = 0.9$ Nm^{-1}) are used, and $a = 5\mu m$, Solid line: $u_j = 5$ cm/sec; dashed line: $u_j = 80$ m/sec. The axes are nondimensionalised by a.Values typical of tin show similar behaviour.

the computations with varied initial height profiles, and a range $1.2 < r_i < 5$ and $0.2 < h < 1$, and the results did not change qualitatively. A typical solution is shown in figure 6.4. At a particular radial location $r = r_j$, there is a singularity in the height of the fluid layer. Note that as we approach r_j the shallow water equations are no longer valid, even approximately, so the present analysis cannot tell us anything about the actual shape close to or after the jump. The dependence of the jump location on the Reynolds number is not monotonic, as seen from figure 6.5. The Reynolds number Re is varied by changing the inlet velocity, so the Weber number increases as Re^2, from 3×10^{-9} to 90. For very low Re or very high We, jumps are unlikely to form within the available radius, i.e., inertia and surface tension must be in the right balance. The Reynolds and Weber numbers are now varied independent of each other (figure 6.6). In the regions shown in red and blue, $r_j > 50a$ and $r_j \sim a$ respectively, so jumps are not predicted. Gravity-free hydraulic jumps may be expected in the relatively narrow patch of intermediate

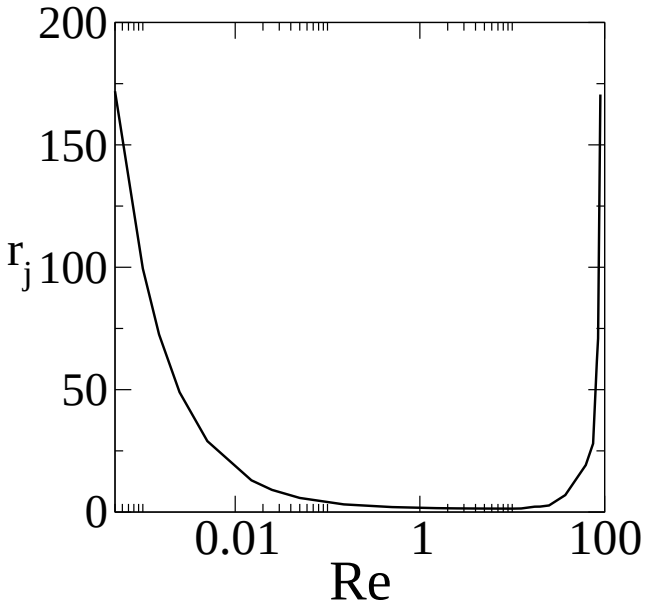

Figure 6.5: The location r_j (nondimensionalised by a) of the singularity as a function of the Reynolds number. For Re between 0.01 and 90 ($u_j = 0.02 - 180m/s$), the jump radius in the demonstration computations is $O(10^{-6})$ m. Here $We/Re^2 = 0.01$.

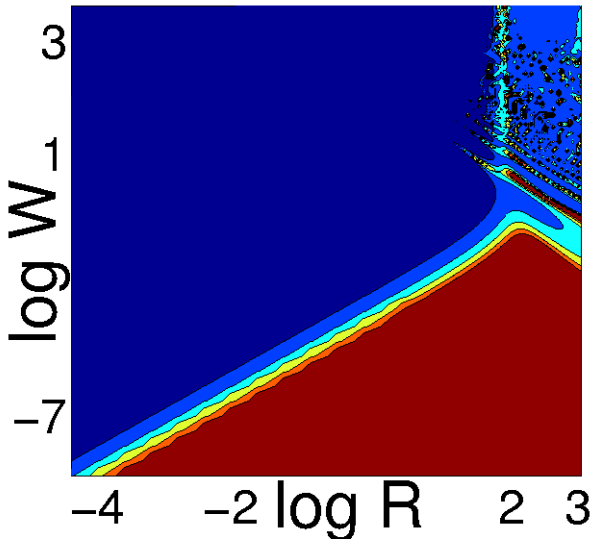

Figure 6.6: Contour plot of jump location in the $Re - We$ plane. In the dark blue regions $r_j < 1$, while in the red regions $r_j > 50$. Jumps are expected in the region of intermediate color.

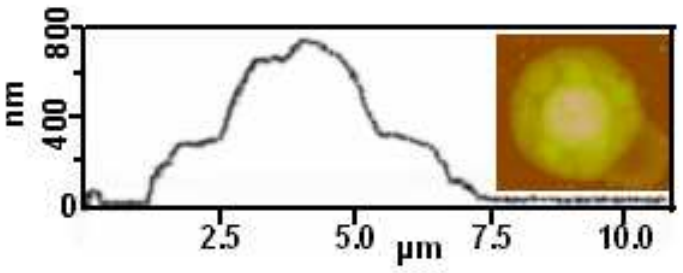

Figure 6.7: AFM image (right) and height profile (left) of a silver blob on silicon substrate kept at room temperature.

color when $Re < 100$, which is seen to lie in a linear fashion. The boundaries of this patch are given by $0.3 < We/Re^2 < 300$. Using this criterion, given all other parameters we can estimate the jet-radius a. For typical values corresponding to silver or water, the order of magnitude estimate of a ranges from $10^{-8}m$ to $10^{-11}m$. Since, the ratio We/Re^2 is independent of the inlet velocity u_j, this implies that (a) the existence of a jump does not depend on the inlet jet velocity, and (b) that both for molten silver and for water, gravity-free hydraulic jumps can occur when the inlet jet radius is in the range of a few nanometers (although in this limit other physics will enter) to a few microns.

6.1.2 Analysis for a drop

Although we have discussed the theoretical possibility of a steady jump formed from an impinging jet, our experimental flow displaying height discontinuities in spreading droplets of molten metal is transient in nature. Though we do not aim to solve the full transient problem here, we argue that a similar jump could occur in low We and high Re flows early in the droplet spreading process. In the early stage of droplet spreading [Fedorchenko & Wang, 2004; Fedorchenko *et al.*, 2005], i.e., when the time after impact $\tau << D/U$, where D and U are the diameter and velocity of the approching droplet respectively, a thin film of fluid emanates from the droplet. Scaling analysis reveals that surface tension effects are significant at early times for $We << 1$, downstream of a location $r_0(t)$ to be specified below. The sheet flow equations of [Fedorchenko *et al.*, 2005] may be rewritten, assuming

$|h_r| << 1$ as

$$u_t + uu_r = (\sigma/\rho)(\nabla^2 h)_r + \mathcal{V} \tag{6.15}$$
$$(hr)_t + (uhr)_r = 0.$$

The viscous effects are represented by a very small term $\mathcal{V}$, neglecting which we obtain

$$u = r/3t \tag{6.16}$$
$$h = At^{-2/3} - \sigma r^4/(144\rho t^2) + Cr^2 t^{-4/3}. \tag{6.17}$$

where A, C are constants. The form of u is as in [Fedorchenko *et al.*, 2005] while the expression for h is a new result. Matching with the solution of [Fedorchenko *et al.*, 2005] at $r = r_0(t)$, where convective and capillary time scales become comparable, $r_0^3\rho \equiv \sigma t^2$, setting $A = 0$, and since the second term on the right hand side of the equation for h in (6.16) is negligible compared to $h(r_0)$ for our parameters, we have $C = \frac{3}{2}U^4 D^3(\rho/\sigma)^{8/3}$. For small viscosity μ and a parabolic velocity profile [Fedorchenko *et al.*, 2005], the viscous term in (6.15) may be written in terms of the inviscid solution for u and h as $\mathcal{V} = -3\mu u/\rho h^2$. A viscous solution constructed as a linear perturbation on the inviscid one becomes singular at $h = 0$, i.e., at the radius $r_j = (144\sigma C/\rho)^{1/2} t^{1/3}$. We thus obtain a jump condition at $\tau << D/U$ for droplet impact analogous to the steady case, but the jump here moves downstream with time. A tiny non-zero viscosity is necessary. While the jump is close to the contact line here, we found that in a steady jet a surface-tension driven jump occurs in the bulk. The present predictions thus need to be checked numerically, with emphasis on the dynamics near the contact line, which will also determine features like the shape of the blob downstream of the jump [Fedorchenko & Wang, 2004]. Numerical studies are also required because as in the steady case, in the vicinity of the jump, the sheet-flow equations fail. Thus the above criterion only indicates the likelihood of a jump when flow parameters are in the right range. Incidentally jumps in droplet flow at larger scale are known [Chandra & Avedisian, 1991].

In the experiment, a Q-switched frequency tripled Nd:YAG laser ($\lambda = 355$ nm, repetitive frequency, 10 Hz) is focused with pulse energy E_p on a rotating metal disc in a vacuum chamber (10^{-7} torr) and the resultant plume received at a distance

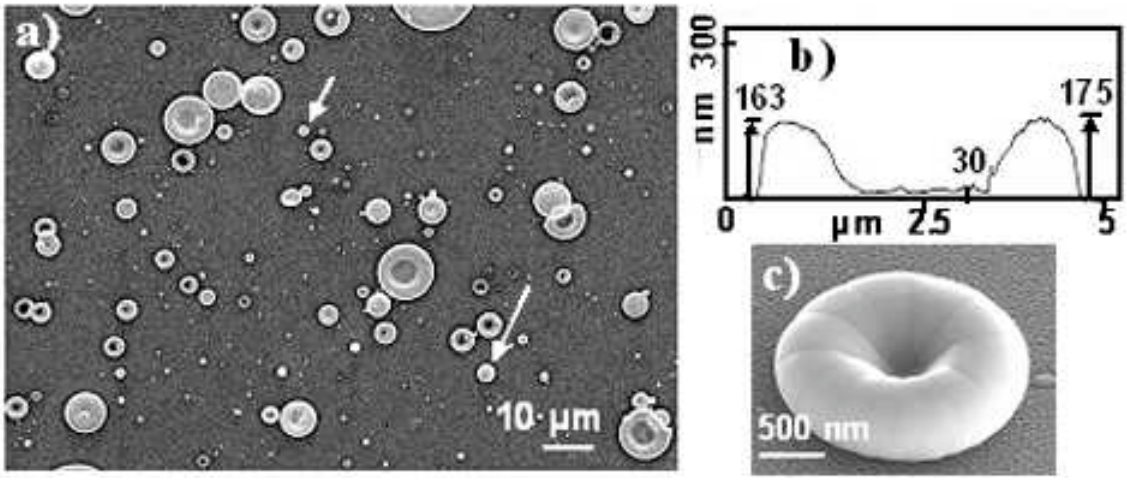

Figure 6.8: Microscopy analysis of metal cups (a) SEM image of femtocups of silver on a silicon substrate obtained at $E_p = 100$ mJ/pulse and $T_s = 1173K$. A few blobs exist, see arrows.(b) Typical height profile of a cup from AFM analysis. (c) Tilted field emission SEM image of a tin cup on silicon.

of 4 cm on a clean vertical substrate held at a temperature T_s, for a duration of 20 min [John *et al.*, 2006]. The resulting metallic structures on the substrate are studied by scanning electron microscopy (SEM), atomic force microscopy (AFM) and energy dispersive X-ray analysis (EDAX). Over most of the range of E_p and T_s, we expect, and obtain, ill-shaped blobs of solidified metals, see figure 6.1.1. However, for a small range of these parameters, there is a strong preference to form cup-like structures of outer diameters $\sim 300nm$ to $10\mu m$, with side walls $\sim 100nm$ high, and capacity $\sim 1fL$ (fig. 6.8). The jump diameter is around half the total diameter. Height profiles associated with atomic force micrographs (figure 6.8b) as well as EDAX spectra [John, 2007] confirm that the central region is raised from the substrate and contains metal. Interestingly, pulsed-laser ablation has been used extensively to produce a variety of structures [Terrones *et al.*, 1997], but femtocups have not been reported, although we notice stray instances of similar structures in other studies [Henley *et al.*, 2003]. Cups have however been obtained by lithography, electrospinning or layer-by-layer assembly [Rondelezl *et al.*, 2005]. This surprising structure is consistent with the proposed dynamics.

To confirm that these cups are formed purely due to fluid dynamics and not due to chemistry, we repeat the experiment with a variety of materials. By optimising

the laser energy in each case, and by maintaining the substrate a few degrees below the melting point of the metal ebing used, we obtain femtocups of gold, silver, copper, tin and niobium of repeatable statistics on glass, silicon and graphite (HOPG), see examples in figure 6.12 and in [John, 2007]. The solid surface being vertical and the length scales small mean that the effect of gravity is negligible. Inertia however is considerable, since velocities are high. We estimate u_j from earlier measurements [Chrisey & Hubler, 1994] to be in the range 1-100 m/s. The laser fluence determines scales and speeds in the incoming jet, and therefore the range of Re and We.The number of well-defined cups drops sharply with E_p lowered below 100 mJ/pulse (compare figures 6.8a and 6.9a). At higher E_p, cups do form (fig. 6.9b), but the throughput is lower, consistent with similar experiments at very high laser fluence [de Riet *et al.*, 1993]. When the substrate is hotter than the metal's melting point T_m, the cup may form initially but cannot solidify and liquid flows back into it, so the final object is ill-formed (fig. 6.9d) With T_s far below T_m, the tendency to form cups is much reduced (figure 6.9c), probably because rapid solidification at the contact line intervenes. Optimal conditions are thus E_p ($\sim$ 100 mJ/pulse for silver) and T_s close to but below T_m. Outside this range, blobs form rather than cups. That the jump is directly related to droplet dynamics is confirmed by varying the substrate orientation with respect to the incoming jet (Fig. 6.10). With increasing inclination, the structures become increasingly elliptical, in accordance with the azimuthal variation of Re and We. Since the experiment includes additional complexity in the form of solidification, we estimate relative time-scales of jump formation t_j and solidification of a droplet t_c. For the experimental values of substrate thickness, t_c ranges from $\sim 3 \times 10^{-4}$ sec on silicon to $\sim 10^{-2}$ sec on glass (taking into consideration conduction, radiation and latent heat), while $t_j << r_j/u_j \sim 10^{-6}$ sec. Despite this disparity, local freezing at the contact line can be very rapid [Schiaffino & Sonin, 1997], and even dictate dynamics in the late stages of droplet spreading. We do notice a dependence on the substrate of the size distribution of cups (figure 6.12) and also some visual differences in shape. An ongoing numerical study, including a non-uniform temperature profile and its effects, is therefore aimed at a better representation of the experiments. Also being addressed are the experimental finding of radial striations, and the theoretical finding of undular jumps (see figure 6.11), under certain conditions.

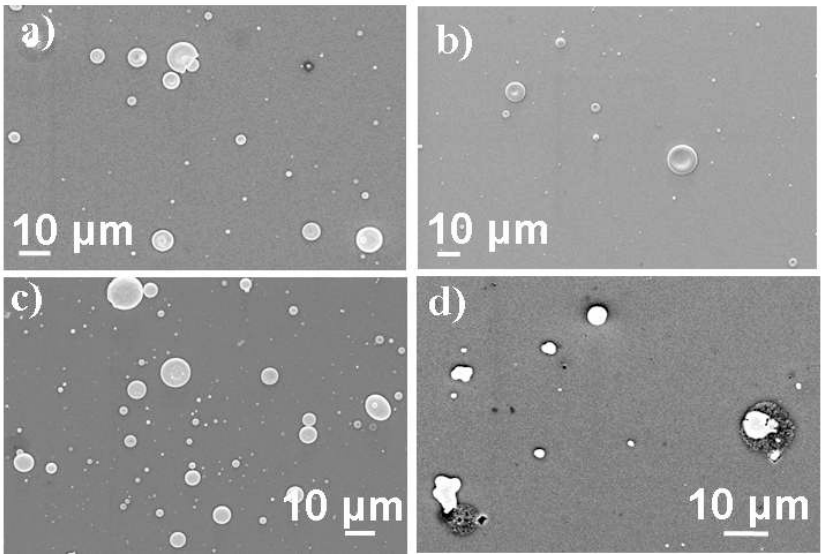

Figure 6.9: SEM images of Ag on Si. (a) $E_p = 60$ mJ/pulse. The number-density of well-formed cups is small. (b) $E_p = 200$ mJ/pulse. (c)$E_p = 100$ mJ/pulse, $T_s = 773K$ much less than $T_m = 1234K$. The cups are not well-formed. (d) $T_s = 1273$ K $> T_m$. Only patches are observed.

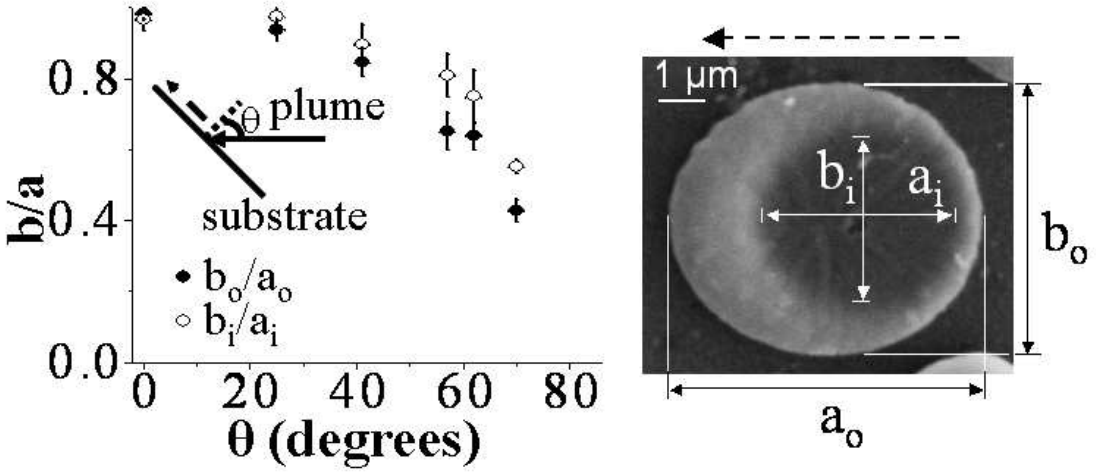

Figure 6.10: Elliptical cups with inclined jets. Inset: Sample SEM image of tin at $\theta = 40 \pm 1.5°$, defining a and b. The major axis is parallel to the maximum flow (dashed arrows).

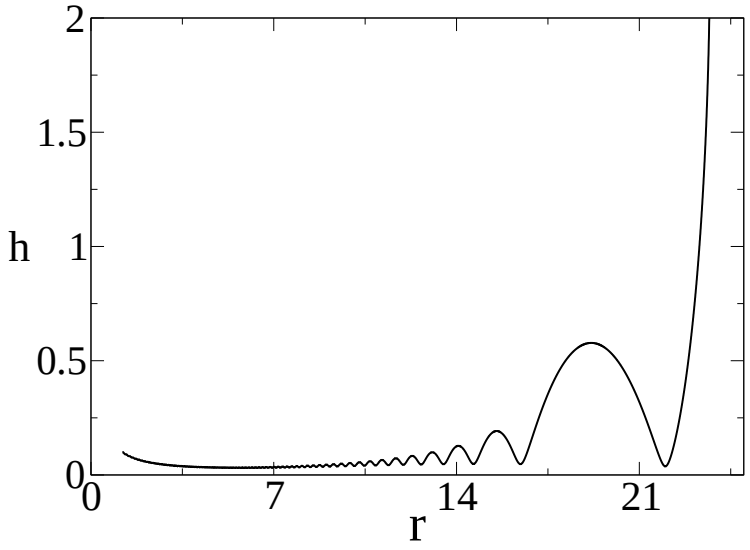

Figure 6.11: An undular jump.

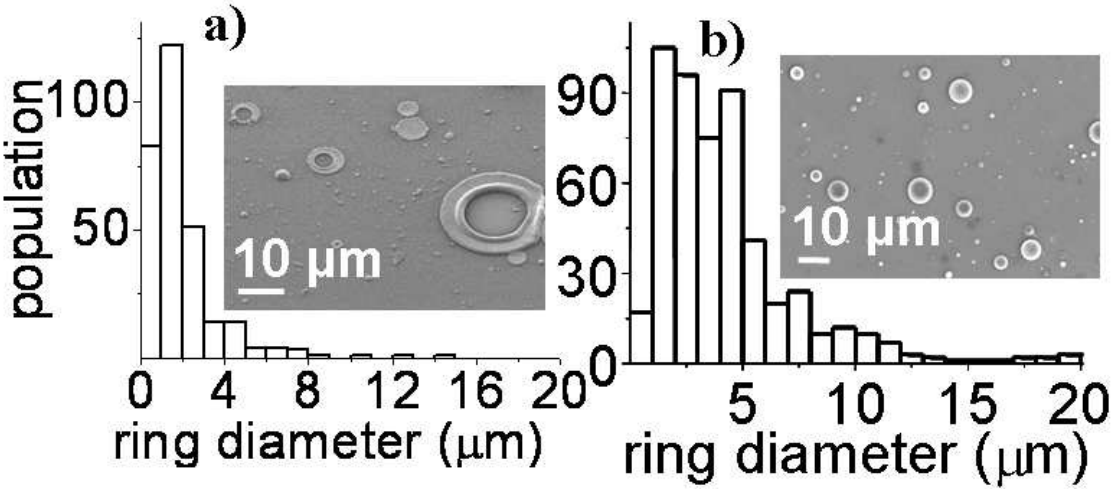

Figure 6.12: Histograms and SEM images of tin femtocups on (a) glass and (b) silicon, deposited simultaneously.

6.2 Conclusion

To the best of our knowledge, this is the first demonstration that in the absence of gravity, shallow-water equations driven solely by surface tension can display a singularity. Just as the gravity driven shallow-water equations behave unphysically near the jump, our equations too display an unphysical singularity instead of a well-resolved jump. It is again expected that these singularities will be cured by addition of neglected terms in the full Navier-Stokes equations. Experimentally we find structures consistent with such jumps in submicron high inertia droplets of molten metals spreading radially outwards on a substrate. The detailed shape close to the jump and the transient problem including solidification and the full transient problem of drop impingement, are a very good subject for future study.

CHAPTER 7

THE VOLUME-OF-FLUID METHOD

Remarks:
The simulations in this thesis have been conducted using GERRIS (Popinet [2010]). In addition an in-house code by the volume-of-fluid method was developed during this doctoral tenure, and is in a mature stage of development. It is described in this chapter. The author is grateful to Dr. Murray Rudman, CSIRO, Australia for assisting with queries and for sending some useful references.

7.1 The Volume-Of-Fluid(VOF) method

Many daily-life fluid flows are "free-surface" flows. In such flows and other similar moving boundary problems, the location of the interface/boundary changes with time and has to be determined at every time-step. Apart from the desire to see the evolution of the interface in time, a knowledge of the location of the interface at every time-step is also necessary in many cases so as to be able to apply boundary conditions. In these situations, we end up with the following - The motion of the interface causes the velocity field to change in time and the changing velocity field in turn causes motion of the interface. The Volume-of-fluid (VOF) method originally proposed by Hirt & Nichols [1981], is an algorithm for finding the interface location at every instant of time and to move it with the underlying velocity field. There are different algorithms for implementing the VOF technique and in this chapter, we describe the implementation of one of these, viz. the one proposed by Pilliod & Puckett [2004]. A computer code implementation of the VOF technique is a coding intensive activity that involves many algorithmic details. This chapter is designed to assist the reader who wishes the implement the VOF method for tracking free-surface flows.

7.2 The Basic Steps in VOF

We start by defining a quantity called volume-fraction denoted by the symbol F for every cell in the computational domain. F is defined as the ratio of the fluid in

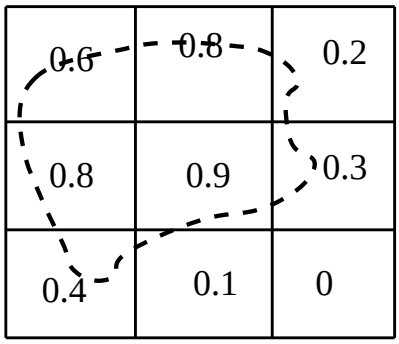

Figure 7.1: An illustration of the $F-$field on a 3x3 block of cells. The dotted line encloses a blob of fluid and is surrounded by vacuum. Note that the values of F are for illustration and are not obtained from actual calculations.

the cell to the volume of the cell itself. Thus cells with $F = 0$ would be empty cells, $F = 1$ would indicate completely filled cells and $0 < F < 1$ would indicate cells which contain the interface. For incompressible flows the volume of a fixed mass of fluid does not change as it travels from one place to another. Thus moving with a parcel of fluid in an uniform grid, the value of F does not change. This leads to an evolution equation (7.1) for F

$$F_t + (\vec{u}.\vec{\nabla})F = 0. \tag{7.1}$$

where $\vec{\nabla} = (\frac{\partial}{\partial x}, \frac{\partial}{\partial z})$ and $\vec{u} = (u, w)$. Given an F-field at time $t = 0$ and an underlying velocity-field, equation (7.1) governs the evolution of F in time with the underlying velocity field. One could now attempt at tracking the time evolution of the interface by a numerical solution of equation 7.1 using e.g. finite differencing to evolve the F-field in time and then using an algorithm to reconstruct the interface knowing the F-field. However, this scheme runs into problems as the accuracy is compromised due to the "smearing" of the F-field near the interface (Hirt & Nichols [1981]). An alternative way of resolving the problem is to use the VOF method which, simply stated, is a graphical way of solving equation 7.1. As mentioned earlier, in a real fluid flow problem, there exists a coupling between the interface evolution and the temporal evolution of the velocity field. In what follows, we decouple the two and describe the technique used for moving an interface with a prescribed velocity-field. As it will be seen, this in itself is a computationally difficult task. The VOF method consists of two basic steps:

- Take the initial distribution of F. This "F field" would contain the value of F for every cell in the grid. Using this as an input, re-construct the interface in those cells where $0 < F < 1$. This step is known as Interface Reconstruction.

- Use the underlying velocity field to evolve the F-field in time and calculate the new F-field at the next time-step. This step is called advection. Go back to the previous step and re-construct the interface for the latest F-field.

7.3 LVIRA - An interface reconstruction algorithm [Pilliod & Puckett, 2004]

As mentioned in the previous section, reconstruction involves drawing the interface in every cell for which 0 <F< 1. The basic difficulty with reconstruction arises due to the fact that given an F-field there is no unique way to reconstruct the interface and mutiple representations are possible. Hence there are many algorithms availabe in the literature for reconstruction e.g. SLIC, PLIC etc.. Each of these algorithms introduce additional constraints to make the reconstruction unique. LVIRA or **L**east-Squares-**V**olume-Of-FLuid-**I**nterface-**R**econstruction-**A**lgorithm is one such algorithm which was proposed by Pilliod & Puckett [2004]. LVIRA is a piecewise-linear approach (PLIC) which represents the interface using a straight line (in 2D) and a plane (in 3D) using the F distribution information of a 3x3 block of cells centered at the interfacial cell. The constraint that it uses is that if the original interface happens to be straight-line/plane, LVIRA is able to reproduce it exactly. We implement LVIRA in two dimensions and the basic steps are listed below:

- Locate a cell with 0 <F< 1. Such a cell is called an interfacial cell.

- Take the 3x3 block of cells centered on the interfacial cell and calculate an initial guess of slope, from the given distribution of F in the 3x3 block.

- With this guessed slope, draw a straight line in the interfacial cell.

- Move this straight line parallel to itself inside the cell in such a way that it subscribes an area numerically equal to the area of the fluid occupying the cell.

- Calculate the perpendicular distance of this straight line from the cell corner. The cell-corner chosen for drawing the perpendicular depends on the orientation of the normal and this will be explained later in detail.

- Extrapolate this line to a 3x3 block of cells, centered on the interfacial cell.

- Calculate the F-field using the area subscribed by this line for each cell in the 3x3 block.

- For each cell, in the 3x3 block, calculate the square of the difference between the F-field thus calculated using the area subscribed by the line and the F-field supplied initially. By construction, this difference will be zero for the central cell with coordinates (r, c) .

- Sum the above squares of differences, for each cell in the 3x3 block.

- Rotate the straight line by a small amount to obtain a new value of slope. Repeat all the steps above to obtain a new value of sum of squares. Keep doing this till a minimum value of sum of squares is found. Ensure that the minimum is a global one.

- The slope and the perpendicular distance of the fitted line corresponding to the global minimum are the desired values and the fitted line is the desired aproximation to the interface for cell (i, j).

In what follows, each of the steps mentioned above are described in detail. Before this, it is useful to choose a few conventions.

- The unit vector $\widehat{\mathbf{n}}$, normal to the line, always points in a direction away from the fluid.

- The components of $\widehat{\mathbf{n}}$ in the x and y directions are n_x and n_y respectively.

- The angle θ is always measured with the positive or negative direction of the x-axis.

- P is the perpendicular distance of the straight line from one of the cell corners, as described in figure 7.2.

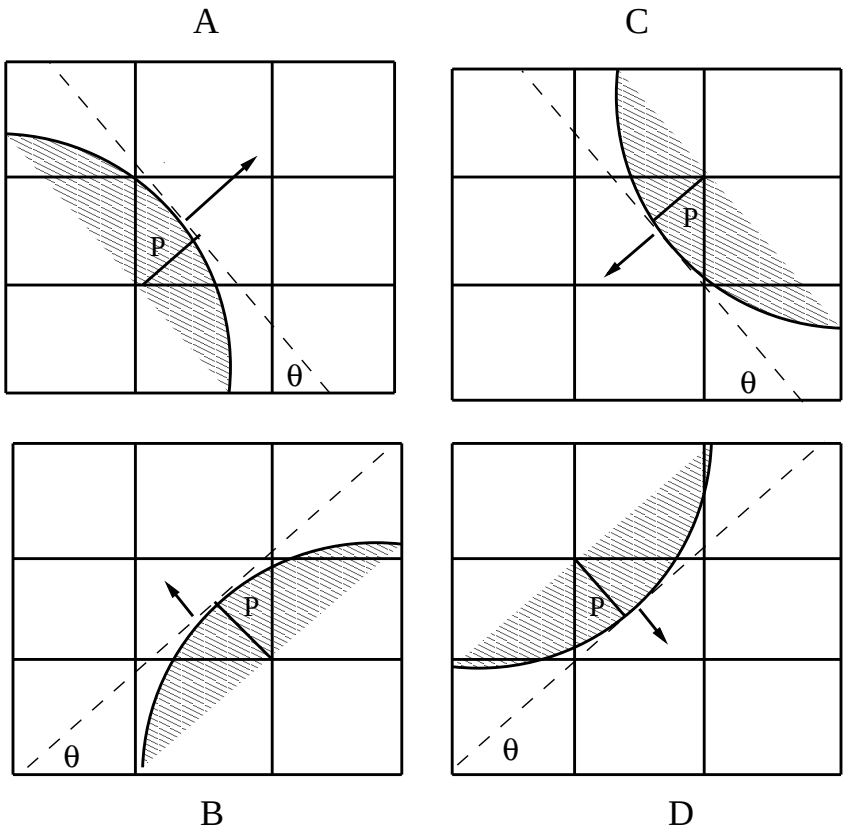

Figure 7.2: The four possible orientation of the normal to the interface. The normal is drawn at the cell-center and the hashed region indicates the region filled with fluid. Note that the cell-corner that is chosen for drawing the perpendicular line of length P, depends on the quadrant into which the normal $\widehat{\mathbf{n}}$ points to.

It is seen from figure 7.2 that the normal to the interface can point towards any one of the four quadrants depending on the orientation of the fluid. For the remainder of this chapter, we will present formulae, only for a normal oriented towards the first quadrant. The results for the other three quadrants can be recovered by rotation by $\pi/2$ at a time.

7.3.1 Step A - Intial guess of slope

The initial guess of the slope for the line to be drawn in an interfacial cell is calculated fom the Green-Gauss gradient by the following formula obtained from Gerlach *et al.* [2006]. For meaning of symbols in equations (7.2) and (7.3), refer to

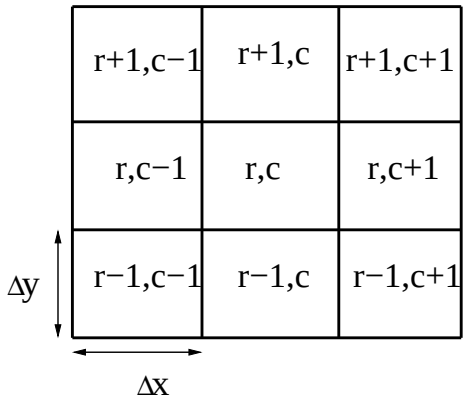

Figure 7.3: A 3x3 block of cells centered on the interfacial cell with coordinates (r, c). Here r stands for row and c for column. The task is to draw a straight line in the interfacial cell (r, c) using the F-field information from its 8 neighbours shown here.

figure 7.3.

$$n_x = -\frac{1}{\triangle x}\left(F_{r+1,c+1} + 2F_{r,c+1} + F_{r-1,c+1} - F_{r+1,c-1} - 2F_{r,c-1} - F_{r-1,c-1}\right) \quad (7.2)$$

$$n_y = -\frac{1}{\triangle y}\left(F_{r+1,c+1} + 2F_{r+1,c} + F_{r+1,c-1} - F_{r-1,c+1} + 2F_{r-1,c} + F_{r-1,c-1}\right) \quad (7.3)$$

The signs of n_x and n_y determine the quadrant into which $\widehat{\mathbf{n}}$ points. We use n_x and n_y to calculate θ, refer to figure 7.2 for the definition of θ. Equation (7.4) gives the formula for calculating θ,

$$\theta = \frac{\pi}{2} - \tan^{-1}\left(\frac{n_y}{n_x}\right) \quad (7.4)$$

7.3.2 Step B - Fit a Straight line

Knowing the orientation of the line (from knowing θ), we need to draw a line at this angle inside the cell and for this we need to calculate P. There are an infinite number of straight lines inside the cell which have the same value of θ having different values of P. To fix P uniquely, we determine the "shape" of the region filled with fluid. Figure 7.4 shows the three different shapes possible. Note that

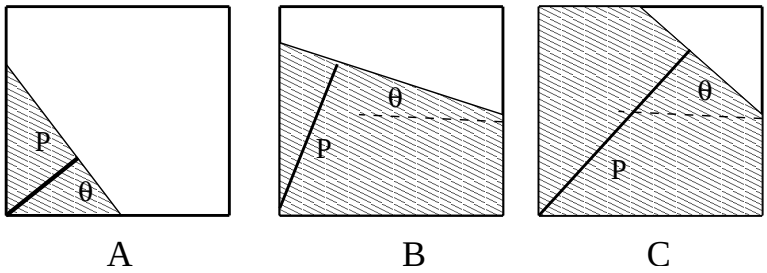

Figure 7.4: The various shapes possible for a piecewise linear re-construction. The shaded region contains fluid. The various shapes are (A) Triangle (B) Trapezium (C) Complement of a triangle. The multiple criteria for each shape in equation 7.5, is for the case $\theta < \pi/4$ and $\theta > \pi/4$.

this classification is possible knowing only $F_{(r,c)}$, the volume-fraction for the cell.

$$F_{(r,c)} \leq \frac{\tan\theta}{2} \quad \text{or} \quad F_{(r,c)} \leq \frac{1}{2\tan\theta} \rightarrow \text{Triangle} \tag{7.5}$$

$$\frac{\tan\theta}{2} \leq F_{(r,c)} \leq 1 - \frac{\tan\theta}{2} \rightarrow \text{Trapezium} \tag{7.6}$$

$$\frac{1}{2\tan\theta} \leq F_{(r,c)} \leq 1 - \frac{1}{2\tan\theta} \rightarrow \text{Trapezium} \tag{7.7}$$

$$\text{Else} \rightarrow \text{Complement of a triangle} \tag{7.8}$$

7.3.3 Step C - Calculate the perpendicular distance

Once the shapes are identified, geometrical formulas can be used to calculate P, the perpendicular distance. These relations are easy to calculate from elementary geometry. Note from figure 7.2 that that the cell corner used for defining P depends on the orientation of the normal $\widehat{\mathbf{n}}$.

7.3.4 Step D - Extrapolate line and calculate sum of squares

The constructed line is extrapolated into the 3x3 block as shown in subfigure A of figure 7.2. The area subscribed by this line can be used to define a volume-fraction for each of the 8 other cells in this block, denoted by F_{new} while the old volume fraction fields are denoted by F_{old}. For obtaining the best linear fit

for an interfacial cell (r, c), we minimise the quantity $\sum_{r,c}(F_{old} - F_{new})^2$ where the summation is performed over the 8 cells in the 3x3 block centered on the interfacial cell. In order to minimise the aforementioned quantity, we need to rotate the line.

7.3.5 Step D - Rotate line

To rotate the line, we add incremental amounts to the components n_x and n_y of the unit vector $\widehat{\mathbf{n}}$. This causes the unit vector $\widehat{\mathbf{n}}$ to rotate by a small amount $d\theta$ clockwise or anticlockwise, depending on the signs chosen for the increments. In this new configuration, we repeat all the above mentioned steps to calculate the quantity $\sum_{r,c}(F_{old} - F_{new})^2$. This process of rotation of the line is continued until the minimum of $\sum_{r,c}(F_{old} - F_{new})^2$ is found. Note that this should be a global minimum. The slope and perpendicular distance corresponding to the angle where the global minimum occurs, completely determine the line. This line represents the interface for the chosen interfacial cell.

The process described above generates a straight line for every interfacial cell. These lines are expected to represent the interface with sufficiently high degree of accuracy on a sufficently fine grid. In figure 7.5, we reconstruct a circle from exact volume-fraction data calculated analytically. It is found that the reconstructed circle represents the actual circle very well for a 30x30 grid resolution.

7.4 Advection

Having reconstructed the interface, we now have to move the interface using equation (7.1). This is once again done using a geometrical technique (see details from Puckett *et al.* [1997]). This step involves geometrical flux calculations for each cell wall as shown in figure 7.6. From this figure, it is seen that knowing θ and P, one can calculate that the amount of fluid A leaving through the left hand wall of the

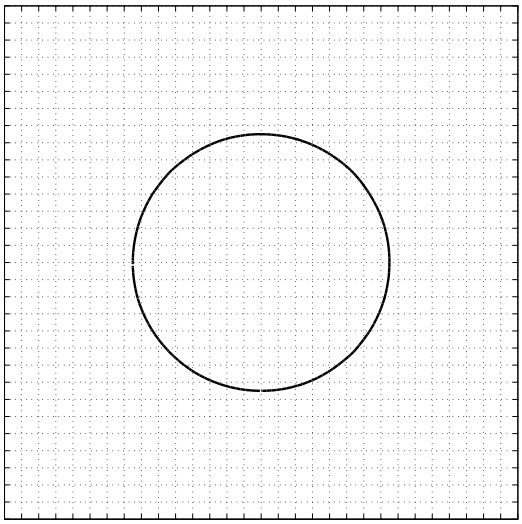

Figure 7.5: Re-construction of a circle. The $F-$ field is obtained by drawing a grid on the circle and calculating the values of F for each cell. The resultant $F-$field is given as an input to the re-construction code and the reconstructed circle is shown here.

cell is:

$$A = \left(\frac{2P}{\cos\theta} - u \triangle t \tan\theta \right) u \triangle t \quad \text{for} \quad u \triangle t \leq \frac{P}{\sin\theta}$$
$$A = \frac{P^2}{\sin 2\theta} \quad \text{for} \quad u \triangle t \leq \frac{P}{\sin\theta} \tag{7.9}$$

The two criterion in equation 7.9 are the ones which decide whether a partial or the entire amount of fluid present in the cell in figure 7.6 goes into the neighbouring cell. Once the fluxes are known, a numerical solution of equation 7.1 helps in calculating the new values of $F_{r,c}$ for every interfacial cell.

7.5 Benchmark tests

We report here results from some standard benchmark tests which have been performed. Apart from this, the code was thoroughly tested for many cases of interface orientation. The three standard benchmark tests well-known in the literature (see

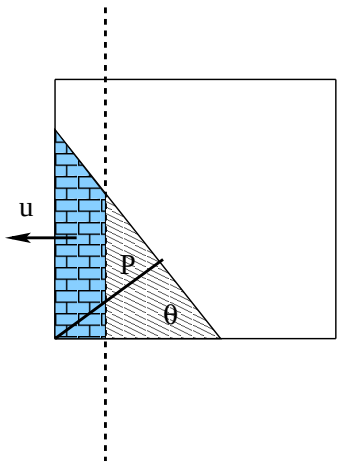

Figure 7.6: An illustration of the method for flux calculation for an interfacial cell. The interfacial cell is effluxing into its left neighbour with the wall-velcocity U. Here the "shape" of the fluid parcel is a triangle and only a part of the fluid present in the cell is effluxed to the neighbouring cell on the right. This region is represented in blue. The amount of efflux depends on the velocity at the cell-wall, the size of the time-step $\triangle t$ and the "shape" of the fluid-parcel present in the cell.

Gerlach *et al.* [2006]) are: (a) Translation test ($u_x = w_z = 0$) (b) Solid-body rotation test ($u_x \neq 0, w_z \neq 0$) (c) Shear test.

7.5.1 Translation test

Figures 7.7 and 7.8 show the results of translation of a circle using the following underlying velocity field

$$u = w = \frac{1}{30} \tag{7.10}$$

In this test, the circle is expected to translate without deforming. It is seen from figure 7.8 that this condition is satisfied.

7.5.2 Solid body rotation test

The solid body rotation test is designed to check the ability of the interface to handle a constant vorticity. Figures 7.9, 7.10 and 7.11 show the results of solid body rotation of a square by an angle of 2π. The underlying velocity field is

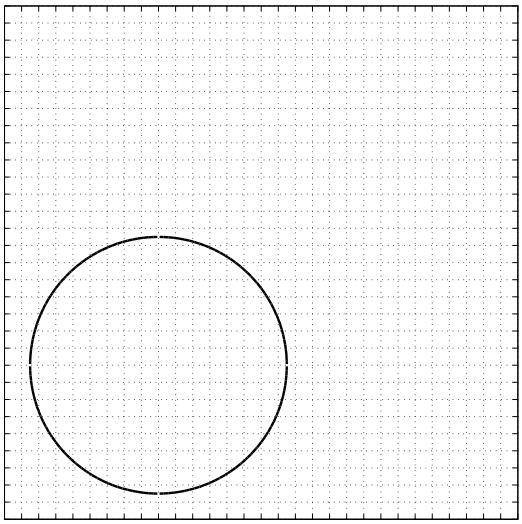

Figure 7.7: A circle being advected by a uniform velocity field $u = w = 1/30$ at $T = 0$. The motion of the circle should be parallel to the diagonal of the square domain.

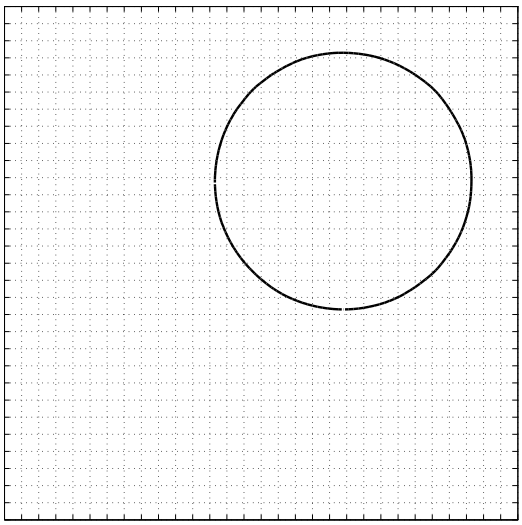

Figure 7.8: The circle gets advected like a rigid body along the diagonal of the square domain.

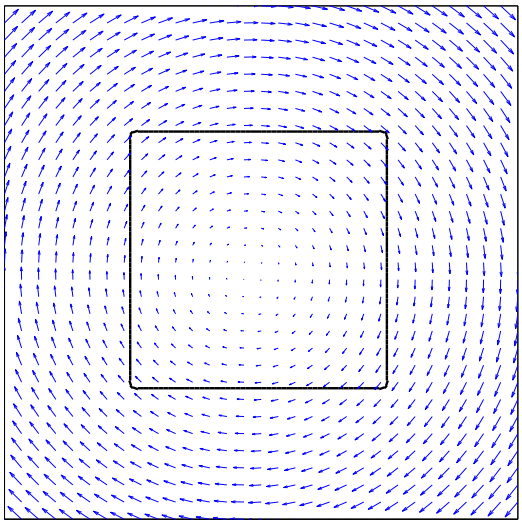

Figure 7.9: Solid body rotation at $t = 0$.

specified as the following:

$$\begin{aligned} u &= \frac{y\pi}{30} - 1.5 \\ w &= \frac{-x\pi}{30} + 1.5 \end{aligned} \tag{7.11}$$

Note that the quantities 30 and 1.5 appear in equation 7.11 due to domain size. It is seen from figure 7.10 that shape of the square is approximately preserved although the corners appear to become rounded in contrast to the sharp right angle at $T = 0$. The latter is to be expected because of the discontinuity in the derivative at the four corners.

7.5.3 Shear test

The vortex test is designed to test the ability of the interface to get deformed and is the most demanding of the three bechmark tests produced here. The underlying

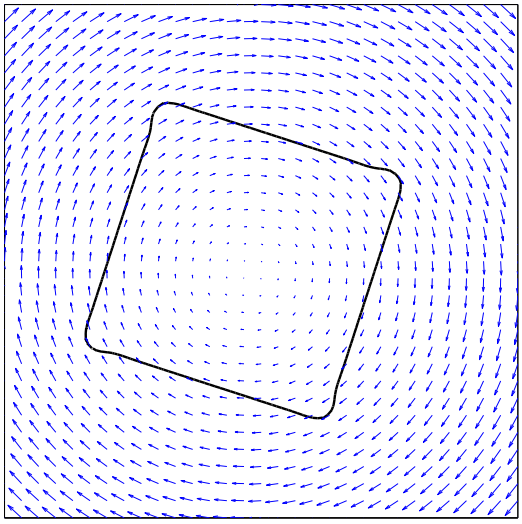

Figure 7.10: Solid body rotation at $t = T/5$ where T is the amount of time taken to rotate by an angle of 2π. Note the smoothening and slight deformation of the corners.

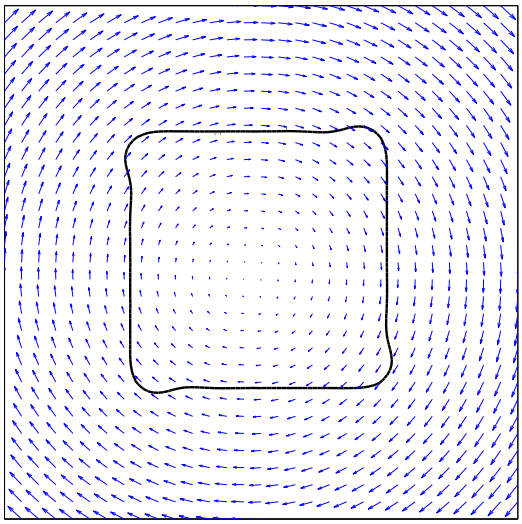

Figure 7.11: Solid body rotation at $t = T$.

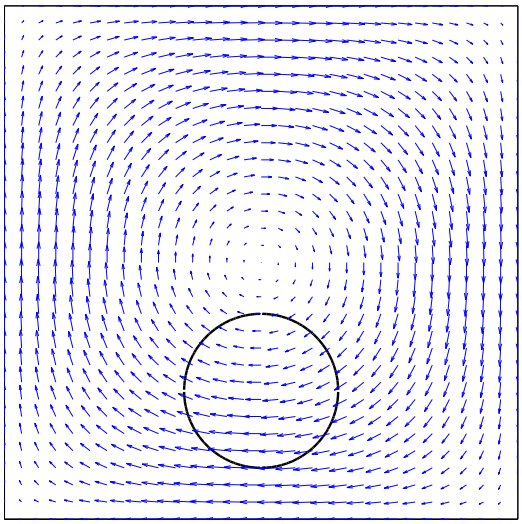

Figure 7.12: Shear test - t = 0. The underlying velocity field is given by equation (7.12).

velocity field is:

$$\begin{aligned} u &= -\sin\left(\frac{\pi x}{30}\right)\cos\left(\frac{\pi y}{30}\right) \\ w &= \cos\left(\frac{\pi x}{30}\right)\sin\left(\frac{\pi y}{30}\right) \end{aligned} \tag{7.12}$$

Note that the factor 30 appears in equation (7.12) due to the domain size of figure 7.12.

7.6 Coupling the interface with Navier-Stokes

Until now, we have only discussed how the interface responds to advection while the effect of the interfacial motion on the fluid velocity-field has been suppressed. This however does not correspond to a real situation where the flow-field is coupled to the motion of the interface and vice-versa. There are two ways in which this coupling can be achieved numerically. We can either solve for a single fluid in which case the effect of the "outer" ambient fluid enters through the boundary

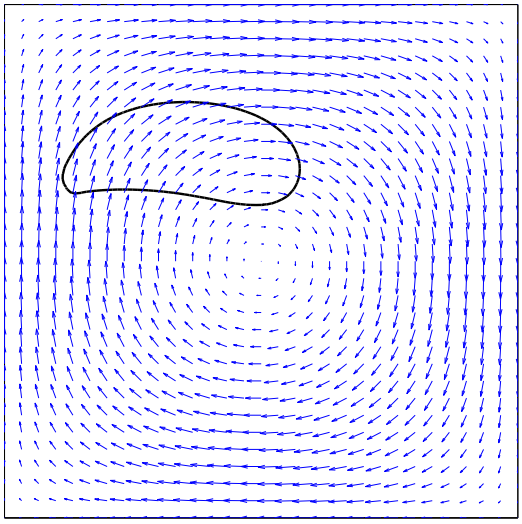

Figure 7.13: Shear test - t = $T/2$ whetre T is the time taken for a 360 degree turn around the center of the domain.

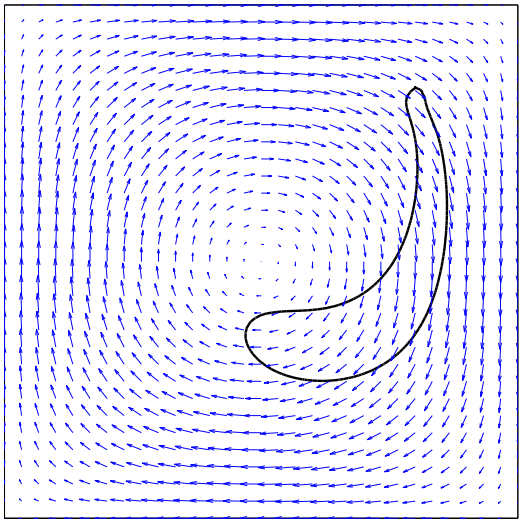

Figure 7.14: Shear test - t = T. Note that the circle becomes tear-drop shaped as it gets advected along.

conditions at the interface. Alternatively, we could also solve for both the fluids simultaneously. Both methods have their advantages and disadvantages. In case of the former, the main difficulty lies in applying the boundary-condition at the interface. This is because at every time step, we have to apply the boundary-condition on a surface whose shape is evolving with time. This is especially difficult when simulating problems like the hydraulic jump, due to the large deformation of the interface at the jump. The exact non-linear boundary conditions at the interface for the continuity of tangential and normal stresses are substantially complicated in themselves and applying these on a curve/surface whose shape changes with time is a difficult task. Many recent VOF models bypass this difficulty by solving for both the fluids simultaneously. This has the advantage that one does not need to prescribe boundary conditions at the interface but only at the domain boundaries, which can always be chosen as per convenience. However, the primary difficulty here lies in dealing with the density discontinuity at the interface. This severely restricts the range of density-ratios which can be solved for numerically. This difficulty is not there in the one-fluid model. Despite its limitations, the two-fluid VOF model has gained popularity in recent times. The interested reader is referred to Flow-3D [2010] for a discussion on this. GERRIS, the code that was used for the simulations reported in this thesis, is based on the two-fluid VOF model.

7.7 Conclusion

In this chapter, we have reviewed in some detail, the Volume-Of-Fluid (VOF) method. An implementation of the $LVIRA$ algorithm for interface reconstruction was discussed in detail. The details for the advection algorithm were also presented. Standard benchmark tests have been performed to validate the code and these results are reported here. In future, we plan to couple this code to a Navier-Stokes solver in order to be able to simulate interfacial flows.

References

Ahmad, D. 1967 Circular hydraulic jump. Master's thesis, Colorado University.

Andersen, A., Bohr, T. & Schnipper, T. 2009 Separation vortices and pattern formation. *Theor. Comput. Fluid Dyn.* **24**, 329–334.

Arakeri, J. H. & Rao, A. 1996 On radial film flow on a horizontal surface and the circular hydraulic jump. *J. Indian Inst. Sci.* **76**, 73–91.

Arbhabhirama, A. & Wan, W.-C. 1975 Characteristics of a circular jump in a radial wall jet. *Journal of Hydraulic Research* **13**, 239–262.

Aristoff, J. 2010 Surface tension and the hydraulic jump. Website, `http://www.princeton.edu/~aristoff/www/jump.htm`.

Aristoff, J. M., Leblanc, J. D., Hosoi, A. & Bush, J. W. M. 2004 Viscous hydraulic jumps. *Phys. Fluids* **16**.

Aulisa, E., Manservisi, S., Scardovelli, R. & Zaleski, S. 2007 Interface reconstruction with least-squares fit and split advection in three-dimensional cartesian geometry. *J. Comput. Phys.* **225**, 2301–2319.

Avedesian, C. T. 1996 The circular hydraulic jump in microgravity. *Tech. Rep.* NASA Grant NAG 3-1627. NASA.

Avedesian, C. T. & Zhao, Z. 2000 The circular hydraulic jump in low gravity. *Proc. R. Soc. Lond. A* **456**, 2127–2151.

Azuma, T. & Hoshino, T. 1984 The radial flow of a thin liquid film. *Bull. of JSME* **27**, 2739–2770.

Bell, J., Colella, P. & Glaz, H. 1989 A second-order projection method for the incompressible Navier-Stokes equations. *J. Comput. Phys.* **85**, 257–283.

Benjamin, T. B. & Lighthill, M. J. 1954 On cnoidal waves and bores. *Proc. Roy. Soc., Ser. A* **224**, 448–460.

Bidone, G. 1819 Report to academie royale des sciences de turin **XXV**, 21–112.

Binnie, A. M. & Orkney, J. C. 1955 Experiments on the flow of water from a reservior through an open horizontal channel ii - the formation of hydraulic jumps. *Proc. Roy. Soc. Lond. Ser. A* **230**, 237–246.

Blackford, B. L. 1996 The hydraulic jump in radial spreading flow: A new model and new experimental data. *American Journal of Physics* **64**, 164–169.

Bloom, C. 1997 The circular hydraulic jump. Website, `http://cbloom.com/hydraulic/index.html`.

Bohr, T., Dimon, P. & Putkaradze, V. 1993 Shallow-water approach to the circular hydraulic jump. *J. Fluid Mech.* **254**, 635–648.

Bohr, T., Ellegaard, C., Hansen, A. E. & Haaning, A. 1996 Hydraulic jumps, flow separation and wave breaking: An experimental study. *Physica B* **228**, 1–10.

Bohr, T., Ellegaard, C., Hansen, A. E., Hansen, K., Haaning, A., Putkaradze, V. & Watanabe, S. 1998 Separation and pattern formation in hydraulic jumps. *Physica A* **249**, 111–117.

Bohr, T., Putkaradaze, V. & Watanabe, S. 1997 Averaging theory for the structure of hydraulic jumps and separation in laminar free-surface flows. *Physical Review Letters* **79**, 1038–1041.

Bonn, D., Andersen, A. & Bohr, T. 2009 Hydraulic jumps in a channel. *J. Fluid Mech.* **618**, 71–87.

Bouhadef, M. 1978 Etalement en couche mince dun jet liquide cylindrique vertical sur un plan horizontal. *Z. angew. Math. Phys.* **29**, 157–167.

Bowles, R. I. & Smith, F. T. 1992 The standing hydraulic jump: theory, computations and comparisons with experiments. *J. Fluid Mech.* **242**, 145–168.

Brechet, Y. & Neda, Z. 1999 On the circular hydraulic jump. *American Journal of Physics* **67**, 723–731.

Bush, J. W. M. & Aristoff, J. 2003 The influence of surface tension on the circular hydraulic jump. *J. Fluid Mech.* **489**, 229–238.

Bush, J. W. M., Aristoff, J. & Hosoi, A. E. 2006 An experimental investigation of the stability of the circular hydraulic jump. *J. Fluid Mech.* **558**, 33–52.

Buyevich, Y. A., Mankevich, V. A. & Ustinov, V. A. 1993 Spreading flow of an axisymmetric laminar jet over a horizontal obstacle. *J. Engg. Phys.* **64**, 31–37.

Buyevich, Y. A. & Ustinov, V. A. 1994 Hydrodynamic conditions of transfer processes through a radial jet spreading over a flat surface. *Int. J. Heat and Mass Transfer* **37**, 165–173.

Chandra, S. & Avedisian, C. 1991 Effect of capillary and viscous forces on spreading of a liquid drop impinging on a solid surface. *Proc. R. Soc. Lond. A* .

Chang, H. C., Demekhin, E. A. & Takhistov, P. V. 2001 Circular hydraulic jumps trigerred by boundary layer separation. *J. Colloid and Interface Science* **233**, 329–338.

Chanson, H. 2009 Hydraulic jumps and related phenomenon - a survey of experimental results. *European J. Mechanics B/Fluids* **28**, 191–201.

Chippada, S., Ramaswamy, B. & Wheeler, M. F. 1994 Numerical simulation of the hydraulic jump. *International Journal For Numerical Methods In Engineering* **37**, 1381–1397.

Cholemari, M. 1998 Evolution of axisymmetric waves on radial film flow. Master's thesis, Indian Institue Of Science.

Cholemari, M. R. & Arakeri, J. H. 2005 Waves on radial film flows. *Physics of Fluids* **17**, 084108:1–7.

Chrisey, D. B. & Hubler, G. K. 1994 *Pulsed laser deposition of thin films*. Wiley, New York.

Craik, A. D. D., Latham, R. C., Fawkes, M. J. & Gribbon, P. W. F. 1981 The circular hydraulic jump. *J. Fluid Mech.* **112**, 347–362.

Dasgupta, R. & Govindarajan, R. 2010 Non-similar solutions of the viscous shallow-water solutions governing weak hydraulic jumps. Phys. Fluids (In Press).

Debnath, L. 1994 *Nonlinear water waves*. Academic Press.

Dingwei, Z., Chongfang, M. & Yutao, R. 1998 Theoretical analysis of hydraulic jump on extremely small size liquid jet impingement. *Journal of Thermal Science* **7**, 176–180.

Dressaire, E., Courbin, L., Crest, J. & Stone, H. 2009 Thin-film fluid flows over microdecorated surfaces: Observation of polygonal hydraulic jumps. *Phys. Rev. Lett* **102**, 194503.

Ellegaard, C., Hansen, A. E., Haaning, A. & Bohr, T. 1996 Experimental results on flow separation and transitions in the circular hydraulic jump. *Physica Scripta.* **T67**, 105–110.

Ellegaard, C., Hansen, A. E., Haaning, A., Hansen, K., Marcussen, A., Bohr, T., Hansen, J. L. & Watanabe, S. 1998 Creating corners in kitchen sinks. *Nature* **392**, 767–768.

Ellegaard, C., Hansen, A. E., Haaning, A., Hansen, K., Marcussen, A., Bohr, T., Hansen, J. L. & Watanabe, S. 1999 Cover illustration: Polygonal hydraulic jumps. *Nonlinearity* **12**, 1–7.

Errico, M. 1986 A study of the interaction of liquid jets with solid surfaces. PhD thesis, University of California, San Diego.

Fedorchenko, A. & Wang, A. B. 2004 On some common features of drop impact on liquid surfaces. *Physics of Fluids* .

Fedorchenko, A., Wang, A. B. & Wang, Y.-H. 2005 Effect of capillary and viscous forces on spreading of a liquid drop impinging on a solid surface. *Physics of Fluids* .

Ferreira, V. G., Tome, M. F., Mangiavacchi, N., Castelo, A., Cuminato, J. A., Fortuna, A. O. & McKee, S. 2002 High-order upwinding and the hydraulic jump. *Int. J. Numerical Methods in Fluids* **39**, 549–583.

Flow-3D 2010 Vof - what's in a name ? `http://www.flow3d.com/cfd-101/cfd-101-VOF.html`.

Francois, M. M., Cummins, S. J., Dendy, E. D., Kothe, D. B., Sicilian, J. M. & Williams, M. W. 2006 A balanced-force algorithm for continuous and sharp interfacial surface tension models within a volume tracking framework. *J. Comput. Phys.* **213**, 141–173.

Gachechiladze, G. A. 1970 Design of a circular hydraulic jump. *Power technology and engineering* **4**, 949–951.

Gajjar, J. S. B. & Smith, F. T. 1983 On hypersonic self-induced separation, hydraulic jumps and boundary-layers with algebraic growth. *Mathematika* **30**, 77–91.

Genady, E., Grimshaw, R. H. J. & Smyth, N. F. 2006 Unsteady undular bores in fully nonlinear shallow-water theory. *Phys. Fluids* **18**.

Gerlach, D., Tomar, G., Biswas, G. & Durst, F. 2006 Comparison of volume-of-fluid methods for surface-tension dominated two-phase flows. *Int. J. Heat Mass Transfer* **49**, 740–754.

Gharangik, A. M. & Chaudhry, M. H. 1991 Numerical simulation of hydraulic jump. *Journal of Hydraulic Engineering* **117**, 1195–1210.

Godwin, R. 1993 The hydraulic jump ("shocks" and viscous flow in the kitchen sink). *American Journal of Physics* **61**, 829–832.

Gradeck, M., Kouachi, A., Dani, A. & ad J. L. Borean, D. A. 2006 Experimental and numerical study of the hydraulic jump of an impinging jet on a moving surface. *Experimental Thermal and Fluid Science* **30**, 193–201.

Gribbon, P. W. F. & Cope, J. A. 1963 Radial flow of superfluid helium over a horizontal plate. *Phil. Mag.* **8**, 2047–2053.

Gumkowski, S. 2008 Modelling and experimental investigation of the hydraulic jump in liquid film formed by impinging two-phase air-water jet. *Heat Transfer Engg.* **29**, 816–821.

Hager, W. H. 1992 *Energy dissipators and hydraulic jump*. Water Science and Tech. Lib., Kluwer Academic Publishers.

Hansen, J. L. 2001 Pattern formation of sand ripples and polygons in the hydraulic jump. PhD thesis, Copenhagen University.

Hansen, K. S., Jorgensen, D., Pederson, J. R. & Toldobd, B. 2002 Polygonformede hydrauliske spring - et modelleringsprojekt. Website, `www.roenby.com/DHS`.

Hansen, S. H., Horluck, S., Zaunner, D., Dimon, P., Ellegaard, C. & Creagh, S. C. 1997 Geometric orbits of surface waves from a circular hydraulic jump. *Phys. Rev. E* **55**, 7048–7061.

Hasson, D. & Peck, R. E. 1964 Thickness distribution in a sheet formed by impinging jets. *A.I.Ch.E. Journal* **752**, 754.

Henley, S. J., Ashfold, M. N. R. & Pearce, S. R. J. 2003 The structure and composition of lithium fluoride films grown by off-axis pulsed laser ablation. *Applied surface science* **217**, 68–77.

Higuera, F. J. 1994 The hydraulic jump in a viscous laminar flow. *J. Fluid Mech.* **274**, 69–92.

Higuera, F. J. 1997 The circular hydraulic jump. *Phys. Fluids* **9**, 1476–1478.

Hirt, C. W. & Nichols, B. D. 1981 Volume of fluid method (vof) for the dynamics of free boundaries. *Journal of computational physics* **39**, 201–225.

Hoefer, M. & Ablowitz, M. 2009 Dispersive shock waves. Website, `http://www.scholarpedia.org/article/Dispersive_shock_waves`.

Holland, D. M., Rosales, R. R., Stefanica, D. & Tabak, E. 2002 Internal hydraulic jumps and mixing in two-layer flows. *J. Fluid Mech.* **470**, 63–83.

Homann, F. 1936 Der einfluss grosset zhigkeit bei der strmung um den zylinder and um die kugel. *Z. angew Math. Mech.* **16**, 153–164.

Hsieh, D.-Y. 1967 On the shock transition, the hydraulic jump and vortex breakdown. *Tech. Rep.* 85-39. California Institute Of Technology.

Ishigai, S., Nakanishi, S., Mizuno, M. & Imamura, T. 1977 Heat transfer of the impinging round water jet in the interference zone of flim flow along the wall. *Bull. of the J.S.M.E* **20**, 85–92.

Jannes, G., Piquet, R., Maissa, P., Mathis, C. & Rousseaux, G. 2010 The circular jump is a white hole. *eprint arXiv:1010.1701v1* .

John, N. S. 2007 Investigations of metal and metal organic bilayer nanostructures employing atomic force microscopy and related techniques. PhD thesis, Jawaharlal Nehru Center for Advanced Scientific Research, Bangalore.

John, N. S., Selvi, N. R., Mathur, M., Govindarajan, R. & Kulkarni, G. U. 2006 A facile method of producing femtoliter metal cups by pusled laser ablation. *J. Phys. Chem. B* .

Johnson, R. S. 1972 Shallow-water waves on a viscous fluid - the undular bore. *Phys. Fluids* **15**, 1693.

Johnson, R. S. 1997 *A modern introduction to the mathematical theory of water-waves*. Cambridge University Press.

Kasa, I. A. 1976 A circle fitting procedure and its error analysis. *IEEE Transactions on Instrumentation and Measurement* **25**, 8–14.

Kasimov, A. 2008 A stationary circular hydraulic jump, the limits of its existence and its gasdynamic analogue. *J. Fluid Mech.* **601**, 189–198.

Kate, R. P., Das, P. K. & Chakraborty, S. 2007*a* An experimental investigation on the interaction of hydraulic jumps formed by two normal impinging circular liquid jets. *J. Fluid Mech.* **590**, 355–380.

Kate, R. P., Das, P. K. & Chakraborty, S. 2007*b* Hydraulic jumps due to oblique impingement of circular liquid jets on a flat horizontal surface. *J. Fluid Mech.* **573**, 247–263.

Kate, R. P., Das, P. K. & Chakraborty, S. 2007*c* Hydraulic jumps with corners due to obliquely inclined circular liquid jets. *Phys. Rev. E* **75**.

Kate, R. P., Das, P. K. & Chakraborty, S. 2008 An investigation on non-circular hydraulic jumps formed due to obliquely impinging circular liquid jets. *Experimental Thermal and Fluid Science* **32**, 1429–1439.

Kate, R. P., Das, P. K. & Chakraborty, S. 2009 Effect of jet obliquity in hydraulic jumps formed by impinging circular liquid jets on a moving horizontal plate. *ASME, Journal of Fluids Engg.* **131**, 034502–1–5.

Khalifa, A. A. M. & McCorquodale, J. A. 1979 Radial hydraulic jump. *ASCE, J. Hydraulics Division* **105**.

Khalifa, A. A. M. & McCorquodale, J. A. 1992 Simulation of the radial hydraulic jump. *Journal of hydraulic research* **30**, 149–163.

Khavari, M., Fard, M. P. & Teymourtash, I. A. R. 2009 A parametric study on the formation of a circular hydraulic jump by volume-of-fluid method. In *The 6th International Chemical Engineering Congress and Exhibition*.

Kluwick, A., Cox, E. A., Exner, A. & Grinschgl, C. 2009 on the laminar structure of weakly nonlinear bores in laminar high reynolds number flow. *Acta Mech.* **210**, 135–157.

Koloseus, H. J. & Ahmad, D. 1969 Circular hydraulic jump. *Proc. of the ASCE, Journal of the hydraulic division* **95**, 409–422.

Kurihara, M. 1946 On hydraulic jumps. *Report of the Research Institute for Fluid Engineering* **3**, 11–33.

Labus, T. L. 1977 Liquid jet impingement normal to a disk in zero gravity. *Tech. Rep.* NASA Technical Paper 1017. NASA.

Labus, T. L. & DeWitt, K. J. 1978 Liquid jet impingement normal to a disk in zero gravity. *ASME, Transactions, Journal of Fluids Engineering* **100**, 204–209.

Larras, J. 1962 Ressaut circulaire sur fond parfaitemenr lisse. *C.R. Acad. Sci. Paris* **225**, 837.

Lawson, J. D., ASCE, M. & Phillips, B. C. 1983 Circular hydraulic jump. *Journal of hydraulic engineering, ASCE* **109**, 505–518.

Lemos, C. M. 1996 Higher-order schemes for free surface flows with arbitrary configurations. *International Journal For Numerical Methods In Fluids* **23**, 545–566.

Li, J. 1995 Calcul d'interface affine par morceaux (piecewise linear interface calculation). *C. R. Acad. Sci. Paris, série IIb, (Paris)* **320**, 391–396.

Liu, X. 1992 Liquid jet impingement heat transfer and its potential applications at extremely high heat fluxes. PhD thesis, Massachussets Institute of Technology, Massachussets.

Liu, X. & Lienhard, J. H. 1993 The hydraulic jump in circular jet impingement and in other thin liquid films. *Experiments in Fluids* **15**, 108–116.

Mathur, M., Dasgupta, R., Selvi, N. R., John, N. S., Kulkarni, G. U. & Govindarajan, R. 2007 Gravity-free hydraulic jumps and metal femtoliter cups. *Phys. Rev. Lett.* **98**, 164502.

Michell, J. H. 1890 On the theory of free stream lines. *Phil. Trans. Roy. Soc. London, Series A* **181**, 389–431.

Middleman, S. 1995 *Modelling Axisymetric Flows*. Academic Press.

Mikielewicz, J. 2003 Analogy between hydraulic jump in films formed by impinging liquid jet and critical flow in internal flows. *Journal of Thermal Science* **12**, 171–175.

Mikielewicz, J. & Gumkowski, S. 2005 Modelling and experimental investigation of the hydraulic jump in liquid film formed by an impinging jet. In *SPRAY-05: International symposium on heat and mass transfer in spray systems*. Anatalya, Turkey.

Mikielewicz, J. & Mikielewicz, D. 2009 A simple dissipation model of circular hydraulic jump. *Int. J. Heat Mass Trans.* **52**, 17–21.

Moncada, A. T., Aguirre-Pe, J. & Olivero, M. L. 1999 Imperfect circular hydraulic jump. In *Proceedings XXVIII Congreso IAHR*.

Murtuza, L. 1996 Wave evolution on thin film flows. Master's thesis, Indian Institute Of Science.

Nakoryakov, V. E., Pokusaev, V. G. & Troyan, E. N. 1978 Impingement of an axisymmetric liquid jet on a barrier. *Int. J. Heat Mass Transfer* **21**, 1175–1184.

Naraghi, M. N., Moallemi, M. K., Naraghi, M. H. N. & Kumar, S. 1999 Experimental modeling of circular hydraulic jump by the impingement of a water column on a horizontal disk. *Journal of Fluids Engg.* **121**, 86–92.

Nettleton, P. C. 1983 The forced radial hydraulic jump. Master's thesis, University of Windsor.

Nirapathdongporn, S. 1968 Circular hydraulic jump. Master's thesis, Asian Institute of Technology.

Olsson, R. G. & Turkdogan, E. T. 1964 Radial spread of a liquid stream on a horizontal plate. *Nature* **211**, 813–816.

Ozar, B., Cetegen, B. M. & Faghri, A. 2003 Experiments on the flow of a thin liquid film over a horizontal stationary and rotating disk surface. *Expts. Fluids* **34**, 556–565.

Pacheco, J. R. 1999 On the numerical solution of liquid film film and jet flows. *J. Fluids Engg.* **125**, 365–374.

Pacheco, J. R. 2003 Pattern formation of sand ripples and polygons in the hydraulic jump. PhD thesis, Copenhagen University.

Pelzer, J. 2002 Effect of jet structure on hydraulic jump. `http://facweb.eths.k12.il.us/chemphys/research%20papers/Justin%20-%20Hydraulic%20Jump.htm`.

Phillips, K. 2008 Investigation of circular hydraulic jump behaviour in microgravity. In *38th Fluid Dynamics Conference and Exhibit*. Seattle, Washington, USA.

Pilliod, J. E. & Puckett, E. G. 2004 Second-order accurate volume-of-fluid algorithms for tracking material interfaces. *Journal of computational physics* **199**, 465–502.

Pirat, C., Lebon, L., Fruleux, A., Roche, J.-S. & Limat, L. 2010 Gyroscopic instability of a drop trapped inside an inclined circular hydraulic jump. *Phys. Rev. Lett.* .

Popinet, S. 2003 Gerris a tree-based adaptive solver for the incompressible euler equations in complex geometries. *J. Compt. Phys.* **190**, 572–600.

Popinet, S. 2009 An accurate adaptive solver for surface tension driven interfacial flows. *J. Comput. Phys.* **228**, 5838–5868.

Popinet, S. 2010 Gerris. Website, `http://gfs.sourceforge.net/wiki/index.php/Main_Page`.

Preiswerke, E. 1938 Applications of the methods of gas dynamics to water flows with free surfaces: Part i. *Tech. Rep.* NACA TM 934. NACA.

Preiswerke, E. 1940 Applications of the methods of gas dynamics to water flows with free surfaces: Part ii. *Tech. Rep.* NACA TM 935. NACA.

Puckett, E. G., Almgren, A. S., Bell, J. B., Marcus, D. L. & Rider, W. J. 1997 A higher-order projection method for tracking fluid interfaces in variable density incompressible flows. *Journal of computational physics* **130**, 269–282.

Putkaradaze, V. 1997 Local structures in extended systems. PhD thesis, Neils Bohr Institute.

Rahman, M. M., Faghri, A. & Hankey, W. L. 1991*a* Computation of turbulent flow in a thin liquid layer of fluid involving a hydraulic jump. *Journal of Fluids Engineering* **113**, 411–418.

Rahman, M. M., Hankey, W. L. & Faghri, A. 1991*b* Analysis of the fluids flow and heat transfer in a thin liquid film in the presence and absence of gravity. *Int. J. Heat Mass Transfer* **34**, 103–114.

Rai, A., Dandapat, B. S. & Poria, S. 2008 Circular hydraulic jump in generalized-newtonian fluids. Available at Arxiv.

Rajaratnam, N. 1967 *Hydraulic Jumps, Advances in hydroscience*. Academic Press.

Ramadurgam, S. 2010 Private communication.

Rao, A. & Arakeri, J. 1998 Integral analysis applied to radial film flows. *Int. J. Heat Mass Transfer* **41**, 2757–2767.

Rao, A. & Arakeri, J. H. 2001 Wave structure in the radial film flow with a circular hydraulic jump. *Experiments in Fluids* **31**, 542–549.

Rao, K. P. A. 1994 Thin film flows: Integral methods and experiments on the circular hydraulic jump. Master's thesis, Indian Institute Of Science, Bangalore.

Ray, A. K. & Bhattacharya, J. K. 2007 Standing and travelling waves in the shallow-water circular hydraulic jump. *Phys. Lett. A* **371**, 241–248.

Rayleigh, L. 1908 Note on tidal bores. *Porc. R. soc. Lond. A* **81**, 448–449.

Rayleigh, L. 1914 On the theory of long waves and bores. *Proc. Roy. Soc. Lond. A*. **90**, 324–328.

Rhines, P. 2010 Hydraulic jumps. Website, `http://www.ocean.washington.edu/research/gfd/hydraulics.html`.

Riabouchinsky 1932 Sur l'analogie hydraulic des movements d'un fluid compressible. *C. R. Acad. Sci.* **195-22**, 998–999.

de Riet, E. V., Nellsen, C. J. C. M. & Dieleman, J. 1993 Reduction of droplet emission and target roughening in laser ablation and deposition of metals. *Journal of applied physics* **74**, 2008–2012.

Rojas, N. O., Argentina, M., Cerda, E. & Tirapegu, E. 2010 Inertial lubrication theory. *Phys. Rev. Lett.* **104**, 187801–1–4.

Rolley, E., Guthmann, C. & Pettersen, M. S. 2007 The hydraulic jump and ripples in liquid helium. *Physica B* **394**, 46–55.

Rondelezl, Y., Tresset, G., Kazuhito V. Tabata, H. A., Fujita, H., Takeuchi, S. & Noji, H. 2005 Microfabricated arrays of femtoliter chambers allow single molecule enzymology. *Nature Biotechnology* **23**, 361–365.

Saddler, C. D. & Higgins, M. S. 1963 Radial free surface flows. PhD thesis, Massachussetts Institute of Technology.

Schiaffino, S. & Sonin, A. A. 1997 Molten droplet deposition and solidification at low weber numbers. *Physics of fluids* **9**, 3172–3187.

Shapiro, A. 2008 Film notes for waves in fluids. Website, `http://web.mit.edu/html/ncfmf.html`.

Shen, M. C. 1961 On the radial spreading of bores. *Tech. Rep.* AD0259442. Brown University.

Silverstein, D. 2002 Properties of hydraulic jump on inclines. `http://facweb.eths.k12.il.us/chemphys/research%20papers/DJ's%20-%20Hydraulic%20Jump%20on%20Incline.htm`.

Singha, S. B., Bhattacharya, J. K. & Ray, A. K. 2005 Hydraulic jump in one-dimensional flow. *Eur. J. Phys. B* **48**, 417–426.

Siwon, B. 1993 Experimental investigation of the liquid film by a gas-liquid spray jet impinging onto a flat surface. *Int. Comm. Heat Mass Transfer* **20**, 665–674.

Sreenivas, K. R., De, P. K. & Arakeri, J. H. 1999 Levitation of a drop over a film flow. *J. Fluid Mech.* **380**, 297–397.

Stevens, J. 1991 Measurements of local fluid velocities in an axisymmetric, free liquid jet impinging on a flat plate. PhD thesis, Brigham Young University.

Stevens, J. & Webb, B. W. 1992 Measurements of the free surface flow structure under an impinging, free liquid jet. *Transactions of the ASME - Journal of heat transfer* **114**, 79–84.

Stevens, J. & Webb, B. W. 1993 Measurements of flow structure in the radial layer of impinging free-surface liquid jets. *Int. J. Heat Mass Transfer* **36**, 3751–3758.

Stoker, J. J. 1992 *Water Waves - The mathematical theory with applications*. Wiley-Interscience.

Tani, I. 1949 Water jump in the boundary layer. *J. Phys. Soc. Japan* **4**, 212–215.

Taylor, G. 1966 Oblique impact of a jet on a plane surface. *Phil. Trans. Roy. Soc. London, Series A* **260**, 96–100.

Terrones, M., Grobert, N., Olivares, J., Zhang, J. P., Terrones, H., Kordatos, K., Hsu, W. K., Hare, J. P., Townsend, P. D., Prassides, K., Cheetham, A. K., Kroto, H. W. & Walton, D. R. M. 1997 Controlled production of aligned-nanotubes bundles. *Nature* **388**, 52–55.

Thandaveswara, B. S. 2010 Normal hydraulic jumps. Website, `http://nptel.iitm.ac.in/courses/IIT-MADRAS/Hydraulics/`.

Thiffeault, J.-L. & Belmonte, A. 2010 Hydraulic jumps on an incline. *eprint arXiv:1009.0083* .

Thomas, S., Hankey, W., Faghri, A. & Swanson, T. 1990 One-dimensional analysis of the hydrodynamic and thermal characteristics of thin flim flows including the hydraulic jump. *Transactions of the ASME - Journal of Heat Transfer* **112**, 728–735.

Thorpe, S. A. & Kavcic, I. 2008 The circular internal hydraulic jump. *J. Fluid Mech.* **610**, 99–129.

Varella, A. D. 1992 Nonlinear waves on the surface of a radially flowing film. Master's thesis, Massachussetts Institute of Technology.

Vasista, V. K. 1989 Experimental study of the hydrodynamics of an impinging liquid jet. Master's thesis, Massachussets Institute of Technology, Massachussets.

Vishwanath, K. P. 2010 An experimental investigation of the effects of momentum flux on the jump radius and film height in a circular hydraulic jump. Unpublished Report, Engineering Mechanics Unit, Jawaharlal Nehru Center for Advanced Scientific Research, Bangalore, India.

Watanabe, S., Putkaradze, V. & Bohr, T. 2003 Integral methods for shallow free-surface flows with separation. *J. Fluid Mech.* **480**, 233–265.

Watson, E. J. 1964 The radial spread of a liquid jet over a horizontal plane. *J. Fluid Mech.* **20**, 481–499.

Wikipedia 2010 Tidal bore. Website, `http://en.wikipedia.org/wiki/Tidal_bore`.

Yih, C. S. & Guha, C. R. 1955 Hydraulic jump in a fluid system of two layers. *Tellus* **7**, 358–366.

Yokoi, K. & Xiao, F. 1999 A numerical study of the transition in the circular hydraulic jump. *Phys. Lett. A* **257**, 153–157.

Yokoi, K. & Xiao, F. 2000*a* Numerical studies of hydraulic jump phenomenon with largely deformed interfaces. *Prog. Theoretical Physics Supplement* **138**, 708–709.

Yokoi, K. & Xiao, F. 2000*b* Relationship between a roller and a dynamic pressure distribution on circular hydraulic jumps. *Phys. Rev. E* **61**, 1016–1019.

Yokoi, K. & Xiao, F. 2002 Mechanism of structure formation in circular hydraulic jumps: numerical studies of strongly deformed free-surface shallow flows. *Physica D* **161**, 202–219.